©Copyright 2012

Michael J. Stebbins

Obtaining Material Properties of the Plantar Soft Tissue for a Patient-Specific Finite Element Model of the Foot

Michael J. Stebbins

A thesis submitted in partial fulfillment of the requirements for the degree of

Master of Science in Mechanical Engineering

University of Washington

2012

Committee:

William R. Ledoux

Peter R. Cavanagh

Randal P. Ching

David R. Haynor

Per G. Reinhall

Program Authorized to Offer Degree:

Mechanical Engineering

University of Washington

Abstract

Obtaining Material Properties of the Plantar Soft Tissue for a
Patient-Specific Finite Element Model of the Foot

Michael J. Stebbins

Chair of the Supervisory Committee:
Affiliate Associate Professor William R. Ledoux
Departments of Mechanical Engineering and Orthopaedics & Sports Medicine

Background

People with diabetes account for just over 8% of the US population, but they undergo approximately 63% of all non-traumatic lower limb amputations, or 65,700 amputations per year. Eighty-five percent of those amputations are preceded by a foot ulcer. Diabetes has been shown to increase the stiffness of the plantar soft tissue in cadaveric samples, which could cause shifting of the magnitude and/or location of peak stresses within the foot.

The purpose of this research project was to develop a magnetic resonance imaging (MRI) compatible, dynamic loading device that used cardiac-gated MRI imaging to obtain in vivo force versus deformation data for the plantar soft tissue. The resulting data will be used as inputs to an inverse finite element (FE) analysis to solve for soft tissue material properties in a patient-specific FE model

Methods

A computer-controlled, MRI-compatible loading device was designed, built, and tested in the laboratory to quantify performance parameters and ensure safe operation of the device before proceeding to pilot human studies. A test subject was loaded by the device while tissue thickness changes were measured via an ultrasound transducer attached to the

loading device. Finally, an MRI pilot study was completed in which the heel of a test subject was dynamically loaded in compression at a 0.2 Hz rate inside an MRI while three-dimensional (3-D) images were obtained.

Results

The amount of test subject movement and shift within the apparatus under loading were determined during ultrasound testing, as was a displacement calibration curve for normal human soft tissue. Force on the foot and displacement of the soft tissue during 12 phases of loading and unloading were obtained from the MRI pilot study, from which the stiffness of the plantar skin and adipose tissue was calculated to be 55 N/mm.

Conclusion

An MRI-compatible, computer-controlled loading device was successfully designed, built, and used in a pilot human study. As the first device of its kind, it will prove beneficial to the research and medical communities by increasing understanding of the initiation of foot ulcers in people with diabetes.

TABLE OF CONTENTS

1 Introduction....1
1.1 Purpose....1
1.2 Background....1
1.3 Summary Of This Thesis....4
2 An MRI-Compatible Device For Obtaining Patient-Specific Plantar Soft Tissue Properties 5
2.1 Introduction....5
2.2 Methods....7
2.2.1 Device Overview....7
2.2.2 Verification Testing....12
2.3 Results....16
2.4 Discussion....20
2.5 Acknowledgements....22
3 Ultrasound Testing....23
3.1 Introduction....23
3.2 Methods....24
3.2.1 Test Set Up....24
3.2.2 Test Procedure....25
3.2.3 Data Processing....26
3.3 Results....30
3.4 Discussion....33
3.5 Conclusion....35
4 MRI Pilot Testing....36
4.1 Introduction....36
4.2 Methods....36
4.2.1 Test Procedure....36
4.2.2 Data Processing....39
4.3 Results....42
4.4 Discussion....49
5 Conclusion....52
5.1 Purpose....52

5.2 Research 52
5.3 Findings 53
5.4 Future Work 55
5.5 Summary 55
References 56
Appendix A. Hydraulic Plantar Soft Tissue Reducer (HyPSTR) User's Manual……..60
Appendix B. Reduction of Electromagnetic Interference Noise in Data Signal Acquisition.176
Appendix C. Plantar Tissue Thickness and Strain Under Body Weight Review……...206

LIST OF FIGURES

Figure 2.1. Schematic of displacement system..... 8

Figure 2.2. CAD assembly of human loading apparatus.....10

Figure 2.3. Two cycles (of six total cycles performed per fill/bleed test).....13

Figure 2.4. Six loading cycles from one fill/bleed test. 14

Figure 2.5. Summary plot of repeatability testing.....16

Figure 2.6. Example of encoder to LVDT displacement calibration curves. 18

Figure 2.7. Example of pressure to force calibration curves and equations 18

Figure 2.8. MRI-compatibility testing of a phantom.. 20

Figure 3.1. Ultrasound transducer mounting fixture.. 25

Figure 3.2. Test subject in human loading apparatus. 25

Figure 3.3. (left) An example ultrasound image of the heel pad.....27

Figure 3.4. A schematic depiction of the calculation of calcaneus movement.....28

Figure 3.5. (left) Pressure versus load data obtained during the 3.0 mm. 29

Figure 3.6. (left) Pressure versus load data with modified calibration curve 29

Figure 3.7. Peak displacement of the loading platen, tissue thickness.....30

Figure 3.8. Force on the loading platen (derived from system pressure) 31

Figure 3.9. Platen displacement, test subject displacement and distance.....32

Figure 3.10. Force on loading platen (derived from system pressure) 32

Figure 3.11. Force vs. displacement for a barefoot heel pad loaded with increasing. 34

Figure 4.1. The test subject's foot just prior to the high-resolution static scan.....37

Figure 4.2. MRI image (sagittal view) of the test subject’s heel.. 40

Figure 4.3. (left) Pressure versus force data obtained during the 3.0 mm.....41

Figure 4.4. Example image from T1-weighted high-resolution scan to be used for FE.....42

Figure 4.5. Example image from T2-weighted high-resolution scan to be used for FE.....43

Figure 4.6. Twelve images, from unloaded (phase 1) to fully loaded (phase 6). 44

Figure 4.7. Position of the calcaneus relative to the imaging volume.....45
Figure 4.8. Average thickness and standard deviation of the plantar fat pad.....46
Figure 4.9. Average strain in the plantar skin versus phase.. 47
Figure 4.10. Average strain in the plantar fat pad versus phase......47
Figure 4.11. Derived average platen load for each phase.. 48
Figure 4.12. Average load on the platen versus total average soft tissue displacement. 48
Figure 4.13. Force vs. displacement for a barefoot heel pad loaded 50

LIST OF TABLES

Table 2.1 Cyclic displacement testing summary 17

Table 2.2. Calibration curve fit equations and RMS errors.....19

Table 2.3. PPU signal generation testing summary 19

ABBREVIATIONS

3-D	Three Dimensional
AC	Alternating Current
ADC	Analog to Digital Converter
AVI	Audio Video Interleave
BMI	Body Mass Index
BMIC	Bio Molecular Imaging Center
BMP	Bitmap image file
BPM	Beats Per Minute
BTU	Basic Triggering Unit
c	Control Patient
CAD	Computer-Aided Design
CCD	Charge-Coupled Device
CCW	Counter-Clockwise
CDAS	Control and Data Acquisition System
CDC	Centers for Disease Control and Prevention
CI	Compressibility Index
d	Diabetic Patient
DAQ	Data Acquisition
DC	Direct Current
DFT	Discrete Fourier Transform
DICOM	Digital Imaging and Communications in Medicine file
DPST	Double Pole Single Throw
EKG	Electrocardiography
EMI	Electromagnetic Interference
ET	Echo Train

FEA	Finite Element Analysis
f_c	Cutoff Frequency
f_s	Sampling Frequency
FEM	Finite Element Model
FFE	Fast Field Echo
GRF	Ground Reaction Force
GUI	Graphical User Interface
HyPSTR	Hydraulic Plantar Soft Tissue Reducer
IC	Integrated Circuit
ID	Internal Diameter
IRB	Institutional Review Board
LT	Loaded Thickness
LVDT	Linear Variable Displacement Transducer
M1-5	Submetatarsal Heads 1-5
MRI	Magnetic Resonance Imaging
OD	Outer Diameter
PN	Part Number
PPU	Peripheral Pulse Unit
PVC	Polyvinyl chloride
RC	Resistive-Capacitive
RF	Radio Frequency
RMS	Root Mean Square
SC	Switched Capacitor
SSR	Solid State Relay
TE	Echo Time

TR	Repetition Time
US	Ultrasound
USD	United States Dollars
UT	Unloaded Thickness
UW	University of Washington
VDC	Voltage Direct Current
VI	Virtual Instrument

ACKNOWLEDGEMENTS

This work was funded by VA Rehabilitation Research and Development Service grant A6973R.

I would like to express my appreciation to all of the people that make up the Veterans Affairs Rehabilitation Research and Development Center of Excellence for Limb Loss Prevention and Prosthetic Engineering. The collective knowledge and skills of the members makes it a wonderful place to learn; the good-natured attitude of everyone there makes it a fantastic place to work. I'd like to especially thank Wesley Edmundson for rushing to fill a large number of "I-needed-this-part-yesterday" or "one-more-part-should-get-the-device-working" types of orders for me.

To the graduate students and engineers that I shared a lab space with: thank you for all of your help and for your understanding; without both, loading the device into cargo vans and running hydraulic tubing throughout the lab would have been difficult. Mike Fassbind (Mike F.), your design of the components inside the MRI room and your inputs/suggestions to the project on an almost weekly occurrence were critical to my success; after all, you were the one who brought up "slippage in the actuator"!

My thanks goes out to Shruti Pai for the many little pieces of advice/knowledge you shared with me, and for the plantar tissue thickness literature review you gave me as a starting point for my own review of tissue strain.

To an old co-worker and a dear friend, Tim Dardis; I owe you one. Discussing the intricacies of this particular hydraulic system with you over beers on multiple instances brought forth several of the solutions used on the device today.

I would like to thank Greg Wilson, Jinnan Wang, and Lawrence Pallozola, from Philips Healthcare. Because of your assistance, the triggering of the MRI from software worked without issue the first time.

Thank you also to Dr. Baocheng Chu, Associate Director of the UW Bio Molecular Imaging Center. Your ability to explain difficult MRI concepts in simple terms made learning the basics of MRI easier. Your devotion to the project was a life-saver when it was 9pm and the eighth hour of a scheduled four hour meeting, and we were still working to obtain gated images.

Thank you very much to my committee members. Your knowledge about biomechanics, shared with me over many meetings and emails were invaluable. Your flexibility in giving me extra time to complete my thesis meant I was able to write about the important data collected at the very end.

I am deeply indebted to my advisor, Bil Ledoux. You taught me an unbelievable amount in the time I have known you, from biomechanics and research to how to keep a smile when it feels like it might all be crashing down. Saying that 'getting to where we did with the project wouldn't have been possible without you' would be one of the largest understatements ever uttered. Instead, I'll just say thank you very much for everything.

I would also like to thank my parents. Mom and dad, I owe you so incredibly much for teaching me the importance of hard work and determination, and for instilling in me a love of learning; I could never have finished this project without you.

Finally, to my wife Emily, thank you from the very bottom of my heart. Your support through difficult times, encouragement to take a well-needed break now and again, advice offered when it was needed most, and your unfaltering belief in my ability to succeed when I was sure that I couldn't were more important to me than you'll ever know. I am so incredibly lucky to have you as a part of my life, thank you.

DEDICATION

To Emily, my wife, my LOML, and my best friend

1 Introduction

1.1 Purpose

People with diabetes in the United States currently account for 8.3% of the population, but they undergo over 60% of all non-traumatic lower-limb amputations, or approximately 65,700 amputations per year (Centers for Disease Control and Prevention, 2011b). The CDC estimates that if current trends continue, one in three adult Americans will have diabetes by 2050 (Centers for Disease Control and Prevention, 2011a). The epidemic is not contained to the United States; the number of people worldwide with diabetes has risen from 30 million in 1985 (International Diabetes Federation, 1997) to 366 million in 2011 (International Diabetes Federation, 2011).

In addition to the 4.6 million deaths caused by diabetes in 2011, worldwide diabetes-related healthcare expenditures in that year were estimated at USD 465 billion (International Diabetes Federation, 2011). It is estimated that 85% of all non-traumatic lower limb amputations in people with diabetes are preceded by a foot ulcer (Reiber, 1995). Direct costs of diabetic foot ulcerations in 2001 were estimated to be USD 11 billion for the US alone (Gordois, 2003).

Despite two recent studies showing a downward trend in diabetic lower limb amputations (Li, 2012; Tseng, 2011), with the explosive worldwide growth in new cases of diabetes, foot ulcers and lower limb amputations will continue to be a huge problem for the diabetic population. Developing a better understanding of the pathomechanics behind foot ulcers in people with diabetes and then devising solutions to prevent ulcer formation is of paramount importance to an increasing segment of the world's population.

1.2 Background

Diabetes has been shown to increase the stiffness of the plantar soft tissue in cadaveric samples (Pai, 2010). This stiffening would presumably cause shifts in the location and/or magnitude of peak stresses internal to the foot due to the tissue's decreased ability to elastically deform and redistribute pressure under a given load (Gefen, 2003). Experimental observation of *in vivo* stress distribution internal to the foot is not feasible; instead, computational models are used to understand how changes in soft tissue stiffness might lead to load redistribution, and ultimately, to ulcer formation.

A number of groups have built noteworthy computational foot models. Gefen (2003) used a finite element (FE) model to compare loading underneath the first and second metatarsal heads of normal feet and simulated diabetic feet. A review of the literature showed that peak contact stress under the medial metatarsal heads of people with diabetes during standing was approximately 1.5 – 2.3 times higher than that of normal feet. The FE model showed that for a contact stress increase of 1.5 times, average internal stresses were 4.1 times higher. The author concludes that ulcer formation initiates deep to the plantar surface, most likely under stress risers such as the bony prominences of the metatarsals. Cheung et al. (2008) have combined an FE foot model with a multi-material orthosis model in order to determine the sensitivity of orthosis design parameters on the reduction of peak plantar contact stress. Using the model and a Taguchi sensitivity analysis (Taguchi, 2005), the group determined that insole stiffness was the second most important factor in reducing peak plantar pressure after the use of an arch-conforming orthosis. Chen et al. (2010) constructed a detailed three-dimensional (3-D) FE model to study the hypothesis that foot ulceration is initiated internally. The model was validated against an F-Scan plantar pressure measurement with an average difference in plantar pressure predictions under the M2, M3, and M4 metatarsal heads of 14.1%. Under a standing load, the model showed an average internal stress magnification factor of 3.01 under the forefoot using soft tissue material properties from the literature representing normal feet. An FE model of the first ray of the foot by Budhabhatti et al (2007) used material properties generated in a separate inverse FE analysis study for the lumped soft tissue. The orientation of the model against a rigid plate and of the bones to one another was adjusted using an optimization algorithm designed to minimize the error between the model-predicted plantar pressure and experimentally-measured pressures. The pressure distribution under the first ray was then calculated for three case studies representing hallux limitus, surgical arthrodesis of the first ray, and a footwear intervention.

The computer models discussed thus far all use lumped-material models for the soft tissue; that is, there is no distinction made between muscle, fat, tendon, etc. Members of our group (Isvilanonda, In Review) have developed a complex 3D explicit FE model of the foot complete with detailed cartilage, plantar fascia, plantar fat, nonlinear ligament properties, and extrinsic muscle tendons that wrap around bones in a physiological manner. The fascia, ligaments and tendons are currently discrete elements, with future work to include 3-D representations of the intrinsic musculature and skin.

The magnitude and location of peak stresses in the soft tissue of the foot are dependent upon the soft tissue material properties in conjunction with the patient-specific anatomy. Using patient-specific FE models is a means to avoid using averaged tissue material properties and anatomy to represent the large variability inherent to biological tissues. In order to derive patient-specific material properties, an inverse FE analysis can be solved; force and displacement are used as inputs to the model, and an optimization algorithm iterates until it has converged on material properties that satisfy the input conditions to within a user-defined tolerance. Multiple analyses are generally conducted using randomized starting points for the properties to ensure that the converged-upon properties are not dependent upon the starting point (Halloran, 2011).

Previous groups have tested devices capable of generating patient-specific material properties of the foot. Petre et al. (2008) designed a device that was able to apply either a compressive or a shear load to the plantar surface of the forefoot while internal deformations were measured via MRI. Individual images of the foot were obtained via standard MRI imaging for five separate loading conditions, from zero to 100% ground reaction force (GRF). The resulting properties did not include strain rate dependent effects due to the static loading used. Erdemir et al. (2006) utilized ultrasound imaging and dynamic loading to provide inputs for an inverse FE analysis. They were able to develop hyperelastic material properties of the plantar fat, but the simplified inverse FE model approximated the fat pad as an axi-symmetric, flat disc with a patient-specific thickness. Anatomical boundary conditions for the tissue were not included.

The purpose of this thesis research project was to develop an MRI-compatible, dynamic loading device that uses cardiac-gated MRI imaging to obtain force vs. deformation data. These data will be used as inputs in conjunction with the group's existing 3-D FE model to conduct an inverse FE analysis that will solve for patient-specific material properties. Cardiac-gated MRI enables static imaging of the dynamically-loaded foot, beneficial for both the increased level of safety for test subjects with insensate feet and for the ability to generate viscoelastic material properties. *In vivo* material stiffness measurements and patient-specific FE models of controls, people with diabetes, people with diabetes and foot deformities, and people with diabetes and a history of ulceration will allow our group to study stress redistribution in the diabetic foot. This will help to increase what is currently known about the pathomechanics of foot ulcer formation in the diabetic population and enable researchers and clinicians to design ulcer preventative measures.

1.3 Summary of this Thesis

The structure of this thesis is meant to align with the progression of the research. The document begins with a chapter that will be submitted as an article that details the designing, building and testing of the MRI-compatible loading device. Descriptions of the devices subsystems, components, and functional parameters are followed by results of the completed testing to quantify the performance of the device and to ensure its safe operation during future human studies.

The second chapter describes an *in vivo* test performed with an ultrasound transducer attached to the loading device. This study was conducted for two reasons: 1) to test the performance of the loading device and the human loading apparatus before proceeding to MRI testing and 2) to ensure that cyclic loading of the heel pad would not have any long-term viscoelastic effect whereby the loaded thickness would change over time. These changes would lead to undesirable artifacts in the gated MRI images obtained in future testing.

The third chapter describes an *in vivo* pilot test of the loading device inside of the MRI. One test subject was MRI imaged with a high-resolution scan and then imaged using cardiac gating while the foot was loaded in compression at a 0.2 Hz rate. The force vs. deformation data presented in this chapter are the same that will be used as inputs to the inverse FEA which will ultimately determine patient-specific material properties of the plantar soft tissue.

The final chapter is a conclusion of the work.

There are also three appendices to the thesis. The first is a user's manual written for the loading device. The second summarizes the author's experiences and lessons learned in dealing with electromagnetic interference (EMI) and the device. The third appendix is a review of the literature of unloaded and loaded plantar soft tissue thickness, and strain of the soft tissue under body weight.

2 An MRI-Compatible Device For Obtaining Patient-Specific Plantar Soft Tissue Material Properties

2.1 Introduction

People with diabetes in the United States currently account for 8.3% of the population, but they undergo over 60% of all non-traumatic lower-limb amputations, or approximately 65,700 amputations per year (Centers for Disease Control and Prevention, 2011b). The CDC estimates that if current trends continue, one in three adult Americans will have diabetes by 2050 (Centers for Disease Control and Prevention, 2011a). Diabetes has been shown to increase the stiffness of the plantar soft tissue in cadaveric samples (Pai, 2010), which would presumably cause shifts in the location and/or magnitude of peak stresses internal to the foot.

Computational modeling by Gefen (2003) has shown that for a 150% increase in contact stress (the low end of the increase range for diabetic patients as compared to non-diabetic patients), average internal stress under the second metatarsal rises by approximately 400%. This supports the hypothesis that foot ulcers initiate deep to the plantar surface at stress concentration points, such as bony prominences (Delbridge, 1985). Computational models are the only feasible means to better understand the correlation between increased stiffness deep in the plantar soft tissue and ulcer initiation in people with diabetes. Using patient-specific anatomy and material properties in computational foot models, as opposed to using averaged tissue material properties and anatomy, allows for the most accurate interactions between variable-stiffness soft tissue and subject-specific stress concentration points. Given force vs. tissue deformation data and anatomical geometry, an inverse finite element analysis (FEA) can be solved to determine patient-specific material properties to within a user-specified tolerance. Multiple analyses are conducted using randomized starting points for the properties to ensure the converged-upon properties are not dependent upon the starting point (Halloran, 2011).

Previous groups have proposed devices capable of generating patient-specific models of the foot. Petre et al. (2008) tested a device that was able to apply either a compressive or a

shear load to the plantar surface of the foot while internal deformations were measured via magnetic resonance imaging (MRI). The soft tissue deformation was observed under five separate loads, from zero force up to 100% vertical ground reaction force (GRF) using testing sequences lasting approximately 3.5 minutes each. Due to the static imaging, the resulting material properties did not include strain rate-dependent effects. Erdemir et al. (2006) utilized ultrasound imaging in conjunction with dynamic loading and inverse FEA to develop hyperelastic material properties of the plantar fat pad. The material properties included strain rate dependent effects, but the inverse FE model approximated the fat pad as axi-symmetric with idealized boundary conditions (albeit with patient-specific thickness). Several other groups (Cheung, 2008; Chen, 2010; Budhabhatti, 2007), have created FEA models capable of quantifying various types of load distribution within the foot, but a patient-specific foot model does not yet exist.

Peak stress magnitude and location in the soft tissue of the foot is dependent upon the soft tissue material properties in conjunction with the patient-specific anatomy. Using patient-specific FE models is a means to avoid using averaged tissue material properties and anatomy to represent the large variability inherent to biological tissues.

Patient-specific FE models of controls, people with diabetes, people with diabetes and foot deformities, and people with diabetes and a history of ulceration will be studied by this group to quantify *in vivo* changes in soft tissue stress redistribution in the diabetic foot. The purpose of this study was to develop an MRI-compatible loading device capable of obtaining patient-specific plantar soft tissue material properties using dynamic, *in vivo* loading in conjunction with cardiac-gated MRI imaging. Cardiac-gated MRI enables static imaging of the dynamically-loaded foot, beneficial for both the increased level of safety for test subjects with insensate feet and for the ability to generate viscoelastic material properties.

2.2 Methods

2.2.1 Device Overview

A cyclic, displacement-controlled, compressive load will be applied to either the forefoot or hindfoot while gated MRI images of the internal tissue deformation data are obtained at sixteen total points on the loading and unloading curve. A single-acting, master/slave hydraulic loading device was designed to produce a sine wave-shaped displacement curve of maximum amplitude 13mm at a loading rate of 0.1 Hz with a maximum load output of 1500N. The displacement requirement was chosen to represent the maximum displacement necessary to approximate strain under body weight of the greatest plantar fat pad thickness expected (Appendix C). The force requirement was chosen to ensure that the device would have the ability to apply a force representative of GRF of all potential test subjects. Displacement requirements called for a triangle wave cycling at 1.0 Hz, but early testing showed large pressure surges so the frequency and shape of the displacement wave were modified. The device will record hydraulic system pressure, actuator displacement, and MRI gating trigger output. To enable plantar foot force measurement in an MRI machine, the force on the foot corresponding to each three-dimensional (3-D) MRI image will be correlated to the hydraulic system pressure. Deformation of the soft tissue will be determined from the segmented MRI images. The force versus deformation data will be used as inputs to an inverse FEA to solve for the patient-specific material properties of the plantar skin, adipose tissue, and muscle tissue. To ensure MRI-compatibility, all equipment inside the MRI imaging room (save for several small hardware items) is non-metallic. MRI-compatibility testing showed no appreciable loss in image quality with the metallic hardware. Equipment located inside the MRI control room, including all actuation, control and data acquisition components, is able to be metallic, but all electronic components utilize electromagnetic interference (EMI) best practices (e.g., twisted-pair shielded wiring, metal enclosures, and analog filtered signal lines) to reduce EMI impacts to the obtained signals from the MRI machine.

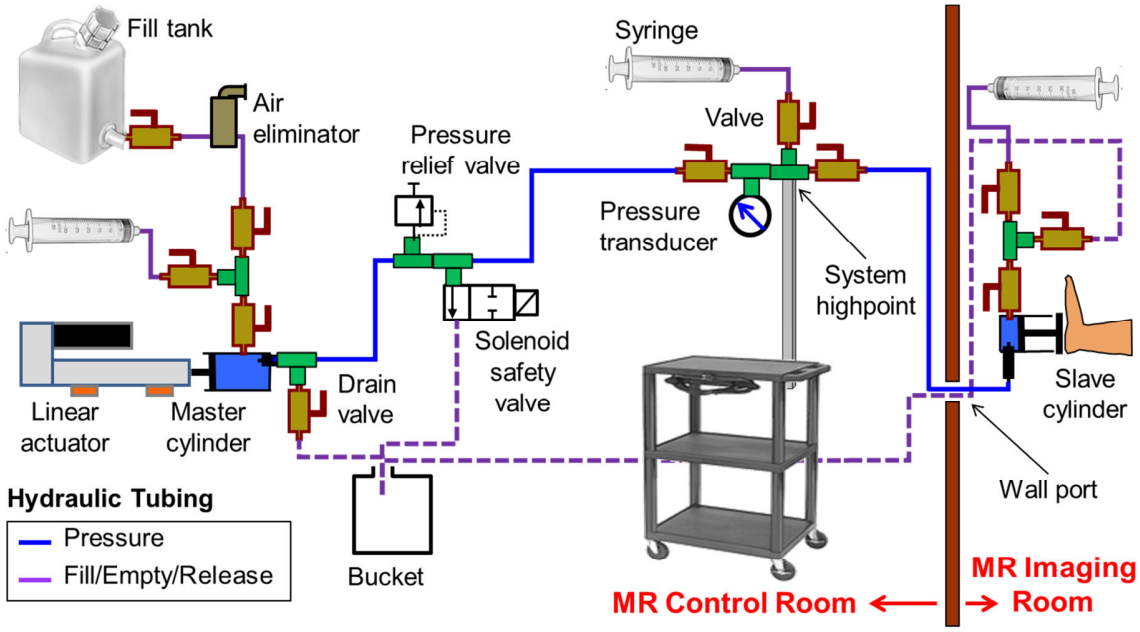

Figure 2.1. Schematic of displacement system

2.2.1.1 Displacement system

The displacement control system (Figure 1.1) is comprised of a stepper motor-driven linear actuator (Ultra Motion, Cutchogue, NY) controlled by a stand-alone stepper driver (Applied Motion Products, Inc., Watsonville, CA). Attached to the actuator is a custom-designed, single-acting, aluminum piston/cylinder (42.85mm bore diameter). The slave piston/cylinder is a similarly custom-designed, single-acting hydraulic cylinder with equal bore diameter, but is made of acetal plastic. The load is applied to the plantar surface of the foot through a polycarbonate loading platen threaded onto the end of the slave piston shaft. The master cylinder and slave cylinder are connected via ~9 meters of 9.65mm ID, vacuum-rated nylon tubing (McMaster Carr, Aurora, OH). Vacuum-rated tubing was chosen due to the system undergoing a small negative pressure (-10 to -20 kPa) at full retraction under cycling. Room-temperature tap water is used as the hydraulic fluid due to its lower dissolved air content as compared to mineral oil (approximately 0.1% vs. 0.4% at room temperature and atmospheric pressure, Yousheng, 2009) and the ease with which the hydraulic system can be quickly disassembled. The fluid is passed through a hydronic heating air eliminator (Spirotherm, Glendale Heights, IL) in order to reduce dissolved air in the fluid. A system of valves, auxiliary tubing and syringes are placed above both the master and slave cylinders

and at the high point of the hydraulic system. Air remaining in the system fluid after filling is bled from individual segments of the systems by tapping components and displacing the master piston to move bubbles to high points, and then transferred out of the system via a syringe.

2.2.1.2 Human Loading Apparatus

The test subject is held in an MRI-compatible loading apparatus that is designed to support the slave cylinder and loading platen, to restrain the leg and the foot being loaded, and to restrain the subject's torso in order to minimize movement of the imaged volume. The slave cylinder can be adjusted in the anterior/posterior direction to align the loading platen with the center of the hindfoot or forefoot, and in the medial/lateral direction to adjust for left or right foot testing. In order to minimize motion of the foot during imaging, the leg and lower leg of the foot being tested are supported in foam-covered cradles and restricted from moving via nylon webbing. The webbing is clamped into place by a cam-mechanism designed to allow for minute adjustments for test subject comfort. To further minimize motion, the subject's torso is held in place with adjustable straps over the shoulders and around the waist connected to a backboard that is integrated into the apparatus. The components of the apparatus are all modular, to allow for subject-specific adjustments and for easy disassembly and storage. For MRI-compatibility, all components of the apparatus are either machined polycarbonate or acetal plastics, or are nylon, fiberglass-reinforced nylon, polypropylene, polyethylene or particle board hardware.

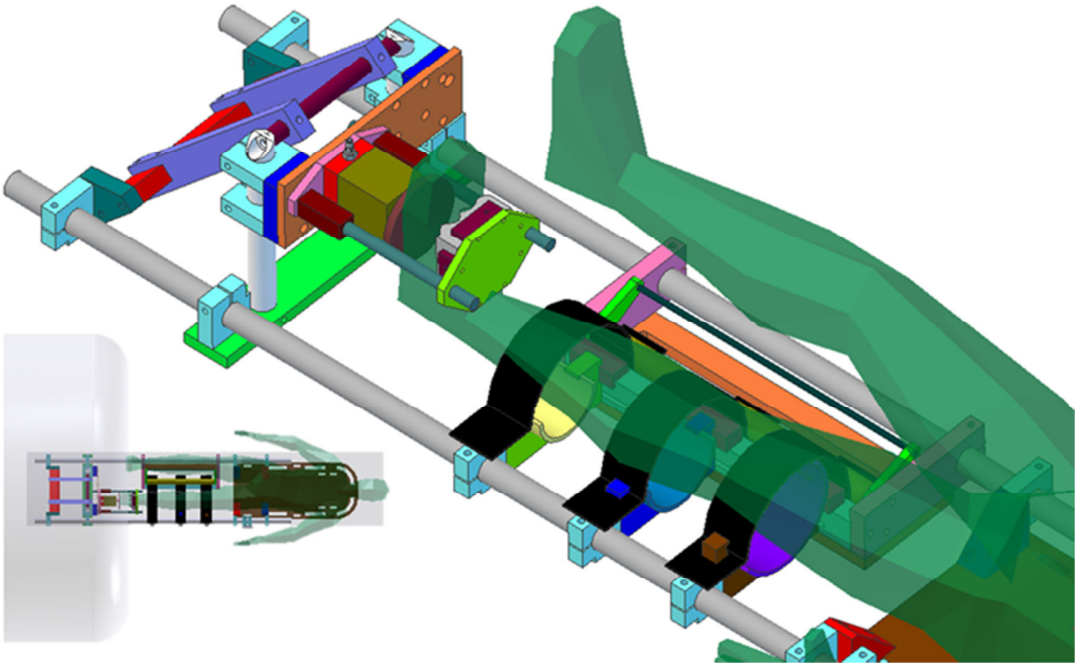

Figure 2.2. CAD assembly of human loading apparatus (inset shows assembly entering MRI bore)

2.2.1.3 Device Control and Data Acquisition

The stepper driver (Model: ST5-Si, Applied Motion Products, Inc., Watsonville, CA) is controlled via manufacturer-provided software. Custom LabVIEW software acquires and logs data, sends the displacement-synchronized trigger signal to the MRI control center, and controls the solenoid hydraulic safety valve. The software runs on a laptop computer (Intel Pentium M, 1.6 GHz, 2.0 GB RAM) which hosts an external data acquisition board (Model: USB-6212, 400 kS/s, 16-bits, National Instruments, Austin, TX). All signals are acquired at 2500 Hz to allow for digital smoothing in post-processing. The position of the linear actuator vs. time is determined from a rotary encoder (resolution = 0.18° of stepper motor rotation or 0.0008 mm of actuator displacement) affixed to the stepper motor. The load applied to the foot is measured via a pressure transducer (Model: PX209-200, Omega Engineering, Stamford, CT) installed in the hydraulic system. Frictional losses at the O-rings and fluid/tubing boundary, along with the compressibility of any air remaining in the fluid after bleeding, require the pressure data to be calibrated. Calibration is achieved via testing while simultaneously acquiring hydraulic fluid pressure data and the force being transmitted by the loading platen. A 2224 N loadcell (Model: MC3A-1000, Advanced Mechanical Technology,

Inc., Watertown, MA) was placed in series with the platen and the loading apparatus. With these data, the actual load on the foot along with the appropriate temporal shift can be determined.

2.2.1.4 MRI Gating

A gated MRI-protocol, similar to that used in cardiac MRI, will be used to obtain sixteen static 3-D images of the foot while the loading platen translates dynamically from zero to the patient-specific maximum displacement and then back to zero repeatedly. Cardiac gating techniques use a physiological signal from the patient to trigger the MRI machine to acquire all MRI signals at a time when the position of the dynamically-displacing heart is the same. Only objects with a periodic or quasi-periodic motion can be imaged in this manner (Van de Walle, 1997). In gated-imaging, the MRI Control and Data Acquisition System (CDAS) is triggered via the Basic Triggering Unit (BTU), which converts various analog physiologic signals into a digital data stream. For use with this device, the BTU is replaced by data meant to mimic that of a square wave peripheral pulse unit (PPU) signal. A simulated PPU pulse is generated and sent once per loading cycle by LabVIEW via an RS-232 serial port and is then converted to a fiber optic signal via an RS-232-to-HP Versalink fiber optic converter (Electro Standards Laboratories, Cranston, RI) to interface with the CDAS. In addition, five separate required status messages are included with the PPU signal every twenty milliseconds. An Achieva 3.0T MRI system (Philips Healthcare, Best, the Netherlands) is used for all MRI testing.

2.2.1.5 Safety System

The loading device incorporates several redundant safety measures to protect the subject from over-loading and/or painful loading. An electronic, solenoid-operated hydraulic valve (Model: 71295SN2KNJ1N0C111C2, Parker Hannifin, Cleveland, OH) is installed in the hydraulic system. When power is removed from the solenoid, the valve opens and the pressurized hydraulic fluid exits the system into a waste container, thereby removing load from the loading platen. Power to the solenoid can be removed by any of the following: 1) an emergency stop (E-stop) button near the test operator, 2) an E-stop button at the test subject's side inside the MRI, 3) by the system software if a patient-specific not-to-exceed

pressure is exceeded and 4) by a virtual button on the LabVIEW front panel. The not-to-exceed pressure is the system pressure at the subject's GRF increased by a factor of 1.2 to account for pressure surges. The E-stop button inside the MRI is fiber-optic and interfaces with a controller (both from Banner Engineering, Minneapolis, MN) inside the MRI control room. The button was modified so as to remove all metal inside of it except for several small hardware pieces, and is securely mounted to the loading frame near one of the test subject's hands. The hydraulic system also includes an adjustable mechanical pressure relief valve. This valve is set to release any pressure greater than the patient-specific not-to-exceed pressure. As a final measure, the master piston is positioned in the master cylinder such that if it were to extend past a failed electronic limit switch, it could travel less than 1 mm before contacting the rigid aluminum cylinder bottom. The 1 mm buffer is a result of setting the location of the electronic limit switch by hand so as not to accidentally bottom-out the piston during cycling, which could damage the actuator.

2.2.2 Verification Testing

A series of verification tests were conducted to quantify the device's performance, maximum operating capabilities, PPU signal generation timing, MRI-compatibility and safety system performance. All data post-processing was performed in MATLAB (The MathWorks, Inc., Natick, MA).

2.2.2.1 Hydraulic System Fill/Bleed Repeatability Testing

The repeatability of the device was tested by conducting three separate fill/bleed/displacement test cycles of the hydraulic system at room temperature on two separate days. For each test, the empty hydraulic system was filled with fluid and air bubbles were bled from the system per the developed protocol (see Appendix A). After bleeding, the system was cycled six times against a piece of silicone gel between the platen and a rigid backstop. The silicone gel measured approximately 75 cm^2 with a thickness of 2 cm, and was chosen due to its viscoelastic similarity to biological soft tissue. For each of the six cycles, the actuator was advanced in 2.0 mm moves from 0 to 20 mm with a three second pause after each move. 20 mm of actuator displacement was required to compensate for the non-linear displacement loss of the system, a function of the compliance

of the hydraulic tubing and of residual air in the hydraulic fluid. After pausing at 20 mm, the actuator was returned to 0 mm of displacement in one continuous move and then the next cycle commenced (Figure 1.3). After each 2.0 mm move, the position of the loading platen was measured via a linear variable displacement transducer (LVDT) attached to the slave piston. The three second pause allowed for a moving-average filter of the LVDT signal to stabilize and for the value to be recorded by hand. For each set of six cycles, the actuator vs. LVDT displacement for the last five cycles was averaged. The first cycle was eliminated due to it consistently showing less LVDT displacement than subsequent cycles (Figure 1.4). Upon its first retraction from maximum extension in the first cycle, the slave piston comes to rest at a position where the force resisting movement due to friction between the O-rings and the cylinder is greater than that of the pressure of the retracting hydraulic fluid. This position is slightly extended from the initial start position, explaining why the five subsequent cycles move further for a given actuator displacement.

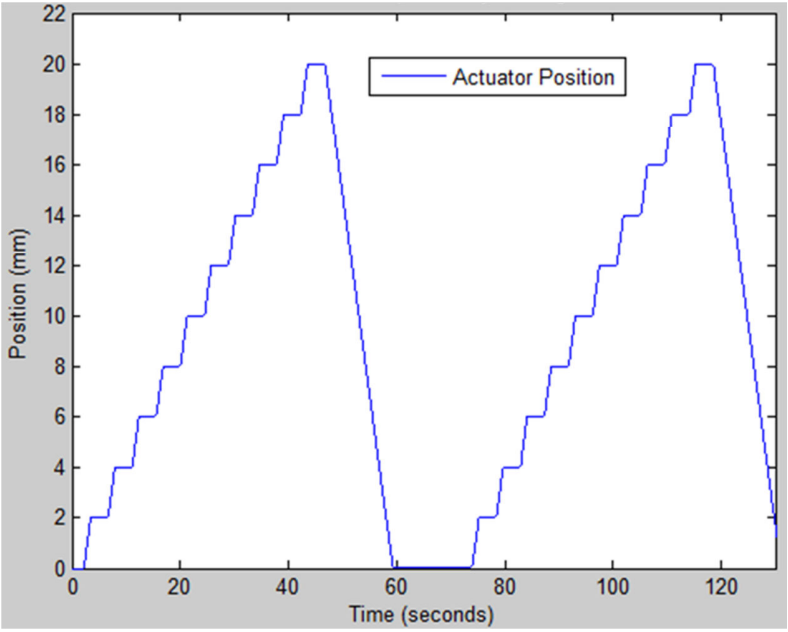

Figure 2.3. Two cycles (of six total cycles performed per fill/bleed test) showing incremental actuator movement used for repeatability testing.

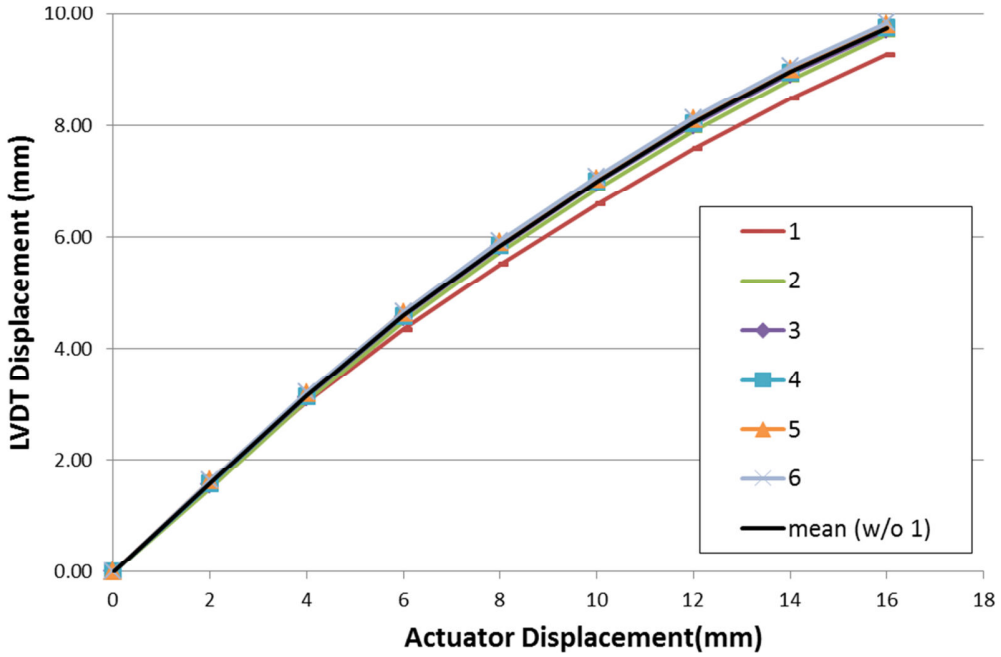

Figure 2.4. Six loading cycles from one fill/bleed test.

2.2.2.2 Cyclic Displacement Testing

Sine wave displacement profiles with a frequency equal to 0.1 Hz and peak amplitudes of 3.0, 5.0, 7.0, and 9.0 mm (as determined by the LVDT) were cycled for 30 minutes each. The same piece of silicone gel discussed previously was placed between the loading platen and the load cell. A literature review (Appendix C) found that unloaded adult plantar soft tissue thickness under the calcaneus and metatarsals generally falls between 8.3 and 26.5mm, and that the strain in the soft tissue beneath either location under body weight is approximately 0.45. The range of displacements chosen to test was meant to encompass as much of the range as was expected for *in vivo* testing while not exceeding the maximum pressure of the hydraulic system (1034 kPa). For each test, the actual displacement of the loading platen vs. the prescribed displacement was analyzed at maximum extension for each cycle. The first 10 cycles' worth of data were excluded from that analysis due to preconditioning of the silicone gel. The root mean square (RMS) error between a best-fit curve to the actual platen displacement and the prescribed displacement was calculated using the MATLAB Curve Fitting toolbox. The time delay of the displacement occurring at the loading platen as compared to the actuator's encoder signal was calculated in order to determine the temporal shift necessary to correct the pressure and rotary encoder data.

Calibration curves were calculated to correlate platen displacement with actuator displacement for both loading and unloading for each displacement test. Similar calibration curves correlating load on the platen to pressure in the system during loading and unloading were also calculated for each displacement test. The temporal shifts are incorporated into the respective calibration curves.

2.2.2.3 PPU Signal Testing

For each of the four sinusoidal displacement tests, the PPU serial signal output was recorded and compared to the actual displacement. The timing of the PPU signal generation was compared to the displacement of the actuator in order to calculate how closely synchronized the two were.

2.2.2.4 Maximum Hydraulic Pressure Testing

The hydraulic system was tested at the maximum design pressure for the system (1034 kPa). A coil spring was slowly loaded by the platen until the maximum design pressure was attained. The system was held at that displacement for a period of 10 minutes.

2.2.2.5 MRI-Compatibility Testing

The MRI-compatibility of the system was tested following a common MRI-compatibility test procedure (Tsekos, 2007) in order to quantify the impact of the loading device upon the obtained images. A fluid-filled MRI phantom was imaged in four separate conditions: a) The control condition, with the loading device not present on the MRI table. b) The device in place, not electrically powered and not displacing. c) The device in place, with electrical power, but not displacing. d) The device in place, with electrical power, and displacing at a 0.1 Hz rate. An equivalent slice was taken from each condition and the MRI-compatibility was calculated by computing the delta between the control condition image (a) and each of the other three conditions (b, c, and d) images.

2.2.2.6 Safety System Testing

Finally, each element of the safety system was tested while the system was under maximum design pressure to ensure operation at the most critical condition.

2.3 Results

The device was shown to be repeatable between fill and bleed cycles of the hydraulic system to a standard deviation of +/- 0.24mm at a maximum slave extension of 10.8mm. The system's non-linear response under increasing load (Figure 1.5) is believed to be a function of the compliance of both the nylon hydraulic tubing and the air remaining in the fluid after filtering and bleeding.

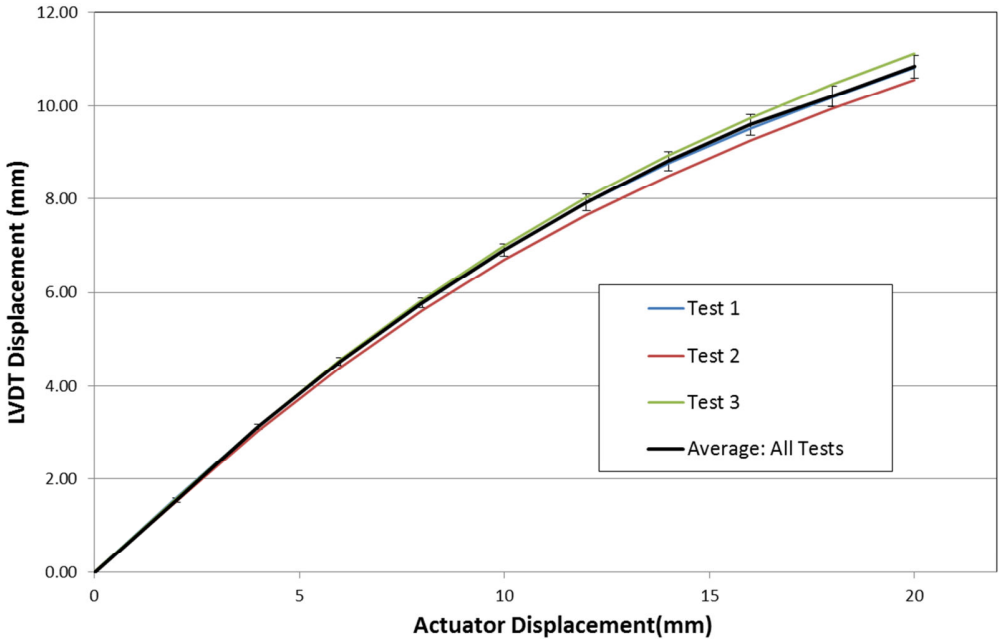

Figure 2.5. Summary plot of repeatability testing.

Once initial stepwise calibration testing had been performed to quantify the non-linear response of the system to various actuator displacements, sinusoidal target peak displacements of the platen were achieved to within 2.8% error (Table 1.1). As the displacement increased, and therefore the load on the platen from the compressed silicone gel increased, the standard deviation of the platen position at maximum extension increased

from 0.003 mm at a 3.0 mm target peak displacement, to 0.117 mm at a 9.0 mm target peak displacement.

The frequency of the platen displacement was within 0.3% of the target frequency of 0.1 Hz. The RMS error of the encoder data to a curve fit sine wave showed the encoder precisely followed the target displacement profile. The platen's RMS error, at approximately an order of magnitude greater, showed more variability. This is due in large part to the slave piston not returning precisely to the initial zero position, as mentioned in the Methods section.

Table 2.1 Cyclic displacement testing summary

	Displacement (mm)			Platen Displacement Frequency (Hz)		RMS Error: Displacement to Target Sine (mm)		Time Lag: Platen Relative to Actuator
	Actuator	Platen						
Test #		Target	Measured	Target	Measured	Actuator	Platen	(seconds)
1	4.072	3.000	3.065 ± 0.003	0.1000	0.1002	0.036	0.324	0.461 ± 0.227
2	7.625	5.000	5.015 ± 0.005	0.1000	0.0997	0.039	0.361	0.439 ± 0.189
3	11.943	7.000	7.198 ± 0.047	0.1000	0.0999	0.046	0.658	0.380 ± 0.127
4	17.974	9.000	9.119 ± 0.117	0.1000	0.0998	0.073	0.869	0.316 ± 0.112

Note: Actuator displacement is measured by encoder

The calibration curves between actuator (encoder) displacement and platen (LVDT) displacement (Figure 1.6) and between hydraulic pressure and platen load (Figure 1.7) are required to determine conditions at the loading platen while in the MRI bore, where instrumentation (the LVDT and the load cell) will not be available. The non-linearity of the system performance requires second and third order polynomial curve fits. Table 1.2 provides the curve fit equations and RMS errors for all four displacement tests.

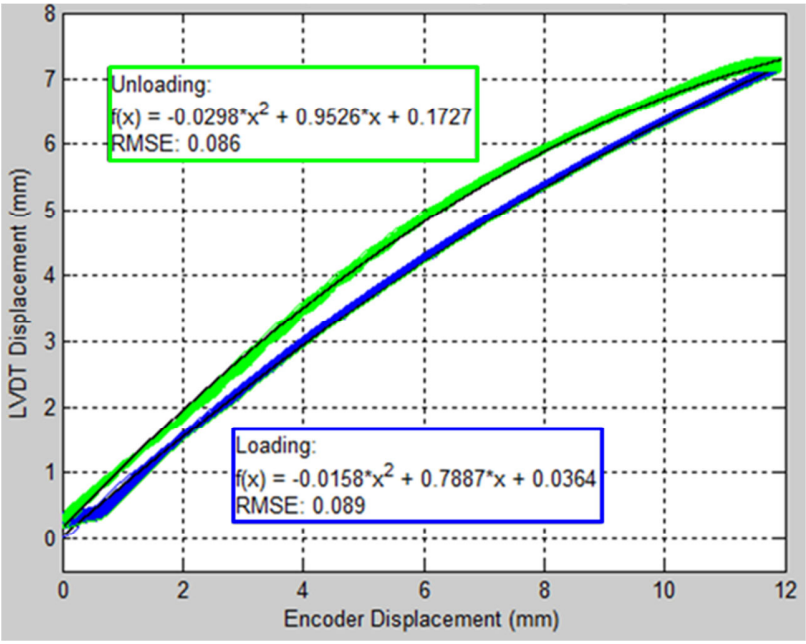

Figure 2.6. Example of encoder to LVDT displacement calibration curves and equations for loading and unloading (7.0 mm displacement test, against silicone gel).

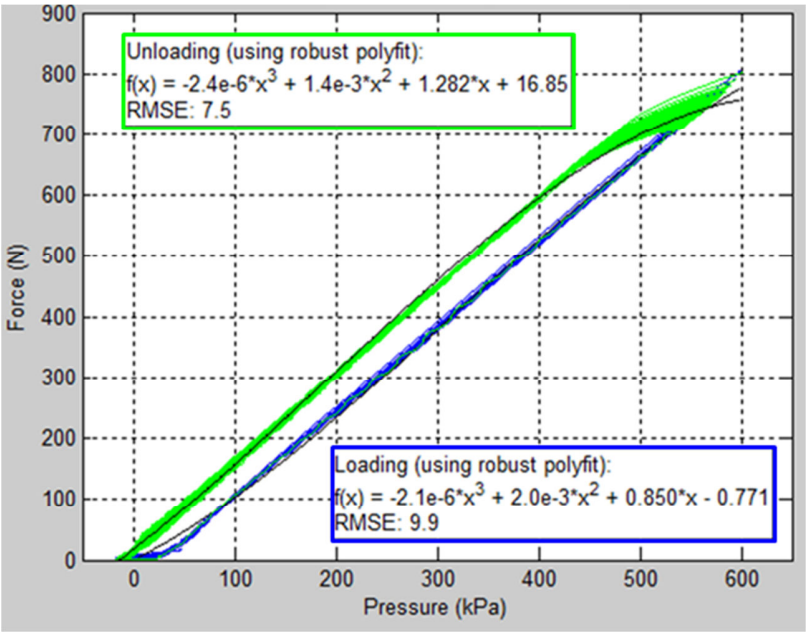

Figure 2.7. Example of pressure to force calibration curves and equations for loading and unloading (7.0 mm displacement test, against silicone gel).

Table 2.2. Calibration curve fit equations and RMS errors

Test #	Disp. (mm)	Loading Direction	Displacement (mm) f(x) : LVDT x : Encoder	RMS Error	Pressure to Force (kPa, N) f(x): Platen Force x: Hydraulic Pressure	RMS Error
1	3.000	Loading	$f(x) = -0.034x^3 + 0.244x^2$ 0.205x + 0.4619	0.037	$f(x) = -5.3E\text{-}5x^3 + 1.6E\text{-}2x^2$ - 0.133x + 6.173	2.2
		Unloading	$f(x) = -0.028x^3 + 0.116x^2 + 0.623x + 0.5294$	0.026	$f(x) = -2.6E\text{-}5x^3 + 1.3E\text{-}4x^2 + 1.43x + 16.60$	3.8
2	5.000	Loading	$f(x) = -0.0068x^2 + 0.6894x + 0.1890$	0.089	$f(x) = -1.2E\text{-}5x^3 + 6.3E\text{-}3x^2 + 0.391x + 4.227$	5.5
		Unloading	$f(x) = -0.0385x^2 + 0.9266x + 0.3043$	0.086	$f(x) = -1.0E\text{-}5x^3 + 3.0E\text{-}3x^2 + 1.262x + 16.92$	4.9
3	7.000	Loading	$f(x) = -0.0158x^2 + 0.7887x + 0.0364$	0.089	$f(x) = -2.1E\text{-}6x^3 + 2.0E\text{-}3x^2 + 0.850x$ - 0.771	9.9
		Unloading	$f(x) = -0.0298x^2 + 0.9526x + 0.1727$	0.086	$f(x) = -2.4E\text{-}6x^3 + 1.4E\text{-}3x^2 + 1.282x + 16.85$	7.5
4	9.000	Loading	$f(x) = -0.0147x^2 + 0.7840x$ - 0.2869	0.123	$f(x) = -3.8E\text{-}8x^3 + 4.9E\text{-}5x^2 +$ 01.385x - 32.26	2.4
		Unloading	$f(x) = -0.0218x^2 + 0.9113x$ - 0.1781	0.127	$f(x) = -4.6E\text{-}7x^3 + 4.7E\text{-}4x^2 + 1.349x + 17.32$	8.5

Testing of the software-generated PPU signal used to trigger the MRI–gating showed an inconsistent error in the initial signal sent after detecting movement of the actuator (Table 1.3). However, once the initial signal is sent, subsequent signals are sent with high precision (error ≤ 0.0004%).

Table 2.3. PPU signal generation testing summary

Test #	Initial PPU Signal (seconds) Encoder movement	Target Time	Actual	Error (msecs)	Delta Between Signals (seconds) Target	Actual Mean	Actual St. Dev. (msecs)
1	0	10.000	9.5579	-442.1	10.000	10.0000	0.11
2	0	10.000	10.0022	2.2	10.000	10.0000	0.42
3	0	10.000	9.9948	-5.2	10.000	10.0000	0.15
4	0	10.000	9.8023	-197.7	10.000	10.0000	0.15

MRI-compatibility testing showed only a slight degradation of signal with the device inside the MRI bore, regardless of power or displacement occurring (Figure 1.8). The degradation may be due to the small metallic screws in the hydraulic valve handles above the slave cylinder or the metal spring embedded inside the test subject E-stop button. Images (b), (c), and (d) all clearly show the vitamin E capsule used as a platen marker (small circle in the upper-left corners). Image (b) was obtained at a different time than (a), (c), and (d); although care was taken to place the phantom in the same location, a slight movement is apparent in the delta image.

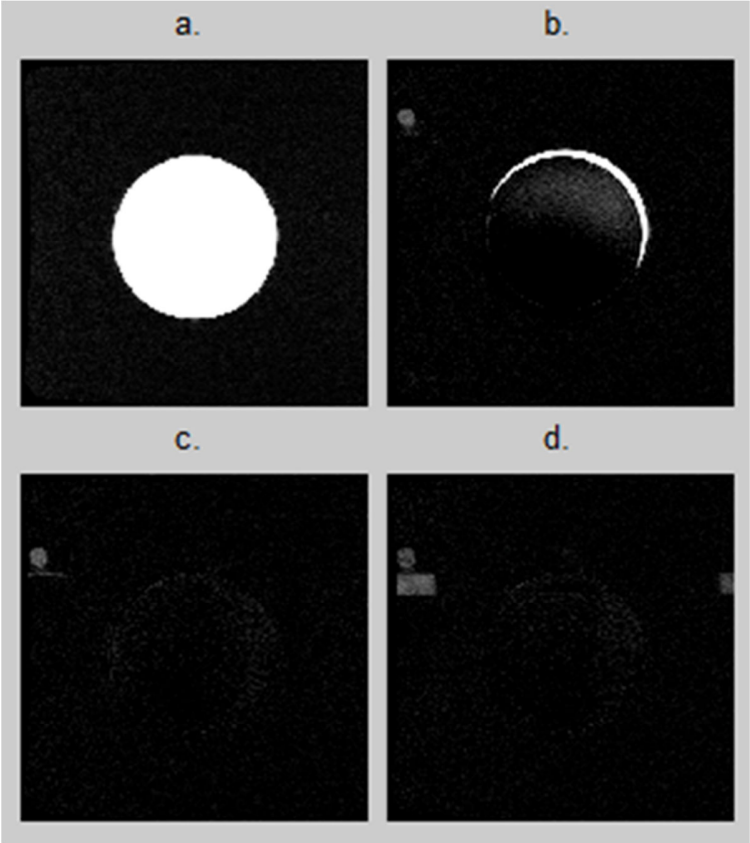

Figure 2.8. MRI-compatibility testing of a phantom. a) Image of phantom alone in MRI bore b) Device in place in the MRI bore but not powered or displacing c) Device in the MRI bore and powered, but not displacing d) Device in the MRI bore, powered and displacing at 0.1 Hz. Note: Images b-d are all delta images from image a; Vitamin E capsule used for platen marker is visible in b, c, and d; Image b also shows slight movement of phantom from initial position.

2.4 Discussion

This study sought to develop and test an MRI-compatible loading device capable of using dynamic, *in vivo* loading in conjunction with gated MRI imaging to obtain patient-specific plantar soft tissue material properties. Verification testing of the device shows that it has promise in achieving the study goals.

The device showed displacement repeatability to ±0.24 mm at a peak platen displacement of 10.8 mm between multiple fill/bleed cycles. Using the calibration curve generated to account for displacement non-linearity, the peak displacement of the loading platen was accurate to with 2.8% of the target displacement. The displacement of the loading platen

was only able to be tested to a maximum of 9.1 mm, instead of the design requirement of 13.0 mm. This was due to the system reaching the maximum design pressure at 9.1 mm, due to the stiffness of the silicone gel material used to simulate soft tissue. The frequency of the displacement was within 0.3% of the target rate of 0.1 Hz. MRI-compatibility imaging with the device in place did not show appreciable loss in image quality. The PPU signal showed an inconsistent error in its initial generation, but precise generation for all subsequent signals. The initial generation error should not prove to be an issue during MRI testing, as the pressure data can be temporally shifted by the error amount to align the pressure data with the imaging phases that occurred.

A comparable MRI loading device by Petre et al. (2008) used a hand hydraulic pump to apply a force-controlled load to a test subject's foot in the MRI. Device performance comparisons are difficult to make, but the computer-driven displacement control of this device is more precise. The loading device by Erdemir et al. (2006) featured an automated loading mechanism, but since the imaging modality used was ultrasound, 3-D tissue deformation data were not obtained. By designing this device to be MRI-compatible, our group will be able to generate data for a full 3-D inverse FE analysis.

It is possible that the MRI-compatible loading device has more potential uses than just foot loading. Fitting various other attachments to the hydraulic slave end in order to take advantage of the high force output possible with the device might lead to other novel uses. Possibilities include dynamic joint loading during gated-MRI imaging to investigate joint laxity, or prosthetic socket loading while imaging to quantify soft tissue response to socket fit.

There are several limitations of the device and the test method worth noting. In order to create a loading device easily capable of fitting inside the MRI bore, the device is only capable of loading ½ of the foot in compression. Designing a compressive and shear loading device capable of physiologic loading to the whole foot while being small enough to position inside the MRI bore would be challenging. The loading frequency that the device is capable of is not representative of the 6-8 Hz rate that heel strike occurs in during normal

gait (Antonsson, 1985). 1.0 Hz was the initial design frequency, but that was decreased after it was determined that pressure shock waves were causing large amounts of pressure data noise at that frequency. A sine displacement wave is used instead of a triangle wave for the same reason; the sine wave proved much better at reducing pressure shock waves for any given cycle frequency.

Additionally, for a given cycle rate and experiment displacement, a sine displacement wave features a higher peak velocity than a triangle wave. This could potentially add artifacts to the images obtained at locations in the loading cycle where the peak velocity occurs. Cardiac-gating was chosen to create a safer test for diabetic test subjects with potentially insensate feet and/or existing foot conditions; however, the need to minimize all motion of the subject's body while at the same time precisely displacing the plantar surface of the foot to ensure aberration-free images could prove difficult. *In vivo* testing inside of the MRI will ultimately prove the current device design appropriate or not.

Future work on the device will include investigation of MRI-compatible transducers to enable precise control of the platen via a feedback mechanism, testing of hydraulic oils to determine the reduction in pressure surge effects at higher loading frequencies, and the inclusion of shear loading into the device.

2.5 Acknowledgements

This work was supported by the Department of Veterans Affairs RR&D Grant A6973R. Technical support for triggering of the MRI was provided by Philips Healthcare, Cleveland.

3 Ultrasound Testing

3.1 Introduction

Ultrasound imaging (sometimes known as sonography) is a relatively low-cost, increasingly portable, inherently-safe means of imaging musculoskeletal tissues. It has been used in previous studies as an effective means to measure the thickness of the heel pad and second metatarsal head, in both loaded and unloaded states (Rome, 1998; Cavanagh, 1999; Uzel, 2006; Kwan, 2010). This study sought to use an ultrasound system in conjunction with the loading device detailed in Chapter 1 to perform pilot human studies with the device, conducted as a precursor to using the device inside the magnetic resonance imaging (MRI) scanner.

Ultrasound testing was conducted in two sets. The first set of testing was performed in order to determine: 1) if the plantar soft tissue experienced a change in peak strain during the twenty minute duration of cyclic compressive loading and 2) if the test subject shifted in the loading apparatus over the duration of the test. Cardiac-gated MRI, for which the device will ultimately be used, requires any motion within the imaged-volume to be periodic or quasi-periodic, in order to capture images without artifacts (Van de Walle, 1997). If the plantar soft tissues strain rates changed over the test duration, or if the subject's foot displaced within the human loading apparatus in a non-consistent manner, the MRI images obtained may contain artifacts.

The second set of testing was conducted in order to develop a calibration curve to be used to correlate displacement of the actuator with displacement of the loading platen during loading of a healthy foot. Verification testing of the loading device showed that the ratio of platen displacement to actuator displacement was dependent upon the force against the loading platen, and was therefore specific to the material being loaded (Chapter 1). In order to proceed with *in vivo* pilot testing in the MRI, a calibration curve correlating displacement of the actuator to displacement of the loading platen while loading normal plantar soft tissue was necessary.

3.2 Methods

3.2.1 Test Set Up

All ultrasound imaging was conducted with a portable, variable 5-12 MHz ultrasound transducer system (Model: T3000, Terason Ultrasound, Burlington, MA) used in B-mode with settings optimized for musculoskeletal imaging. One subject (male, age = 42 years, weight = 913 N) was tested. A rapid-prototyped fixture was designed in order to: 1) grip the compound-curved transducer, 2) attach to the threaded slave piston shaft, 3) adjust the height of an acrylic plastic loading platen over the transducer head and 4) react the compressive load through the fixture instead of through the transducer head (Figure 3.1). Ultrasound acoustic coupling gel was applied between the transducer head and the platen, after which the platen was lowered onto the transducer head until contact between the two had been made. Acoustic coupling gel was also applied between the platen and the plantar heel skin.

The test subject was placed in the human loading apparatus (Figure 3.2, detailed in Chapter 1) and all straps were tightened to the point of being taut without causing discomfort to the subject. An additional strap (Figure 3.1, right) was placed under the subject's forefoot and secured to a strap superior to it in an effort to keep the loaded foot neutrally-aligned and to prevent plantar flexion during loading.

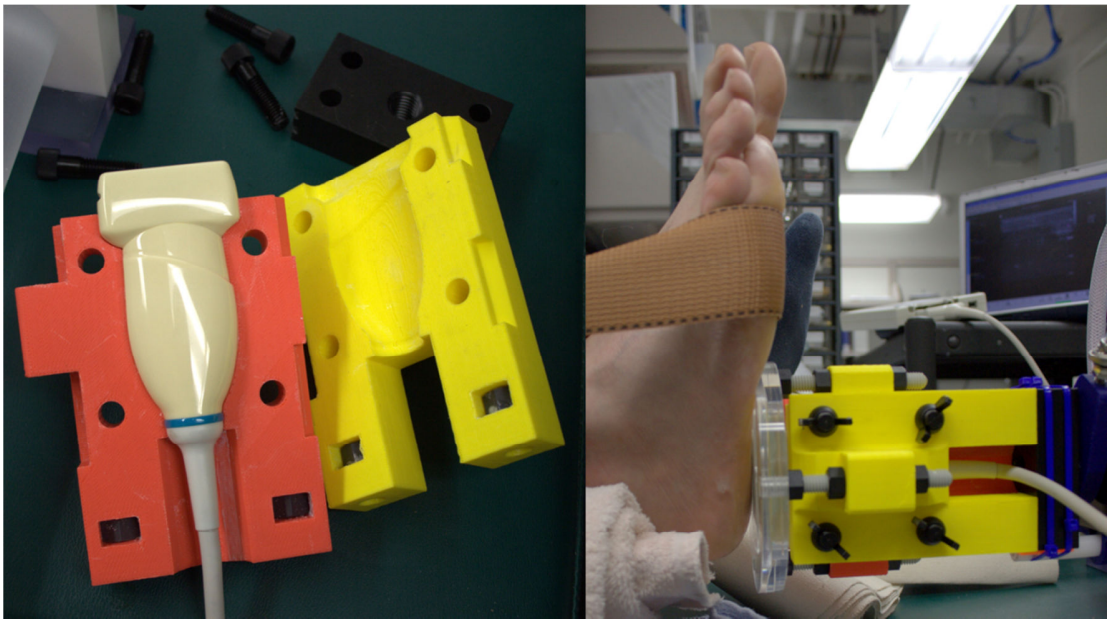

Figure 3.1. Ultrasound transducer mounting fixture. (left) Transducer resting in open fixture, (right) Fixture shown with platen mounted and in loading position against the heel of the test subject's foot.

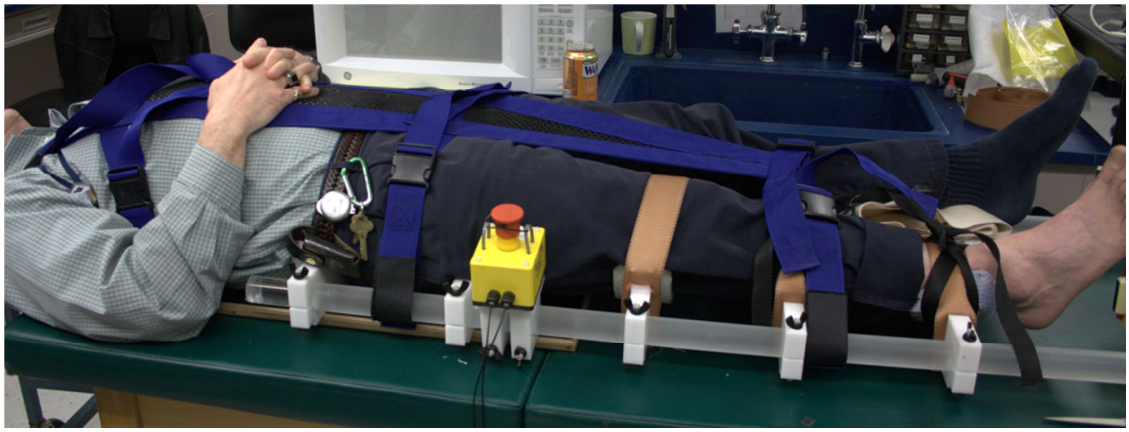

Figure 3.2. Test subject in human loading apparatus.

3.2.2 Test Procedure

Two sets of testing were performed. The first set of testing involved applying a sine wave displacement profile compressive load to the test subject's heel pad with an actuator total displacement equal to 14.62 mm at a rate of 0.1 Hz. Preliminary displacement tests, starting with a conservative displacement of 5.0 mm and incrementally-increasing the displacement while monitoring system pressure, showed a pressure much smaller than was predicted

based on the verification testing. At 14.62 mm, the peak pressure had only reached a level of approximately 130 kPa (~5 times lower than predicted). The test subject also said that he felt himself moving in the device and that the load on his foot felt much smaller than GRF. It was decided to proceed at this displacement level for a twenty minute duration test in order to analyze the data and attempt to quantify the test subject movement. During that test, ultrasound images showing the distance between the platen and the inferior-most point in the calcaneus were obtained. The images were recorded at 14 frames per second using BB Flashback Express Recorder screen capture software (Blueberry Software, Birmingham, U.K.) and output to an .AVI file. The displacement of the actuator was measured via a rotary encoder attached to the stepper motor of the linear actuator, the displacement of the loading platen was measured via a linear variable displacement transducer (LVDT) attached to the slave piston, and the hydraulic system pressure was measured via a pressure transducer. These data were sampled and recorded via custom-written LabVIEW software (Appendix A).

The second set of testing involved seven separate tests each composed of five cycles of a sine wave displacement compressive load at 0.1 Hz applied to the test subject's heel pad. The peak displacement of the actuator was increased from 7.6 mm to 19.6 mm in 2.0 mm increments for the seven tests. For each test, ultrasound images, encoder and LVDT displacements, and system pressure were measured and recorded in the same manner as described above.

3.2.3 Data Processing

Data processing was conducted in MATLAB (The MathWorks, Inc., Natick, MA). For both sets of testing, the .AVI file of ultrasound images was down-sampled to include only frames in which motion of the calcaneus was observed when compared to the previous frame. The mean value of the delta image obtained by subtracting the current frame from the previous frame was calculated, and changes in movement were captured as non-zero pixel values in the delta image. Delta images with a mean value less than 0.5 (to allow for some noise between images in which no motion actually occurred) were removed from the analysis. The down-sampled frames were reviewed individually and down-sampled again to include

only those frames in which the maximum soft tissue displacement had occurred. For each of these resulting frames, the inferior-most visible point of the calcaneus was marked and the distance between it and the surface of the loading platen calculated (Figure 3.3). The resolution of this analysis method (the smallest distance able to be selected by the user) was tested and found to be 0.0994 mm. The movement of the calcaneus during testing (Figure 3.4) was calculated using the following equation:

$$Calcaneus\ Movement = (Loaded\ Thickness + Platen\ Displacement) - Unloaded\ Thickness \quad (1)$$

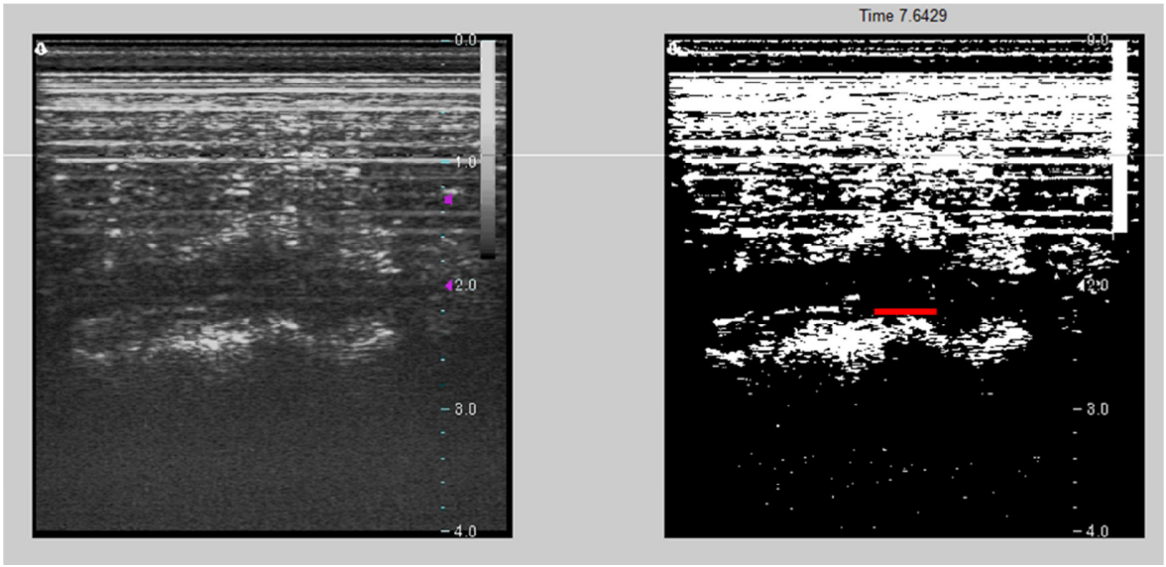

Figure 3.3. (left) An example ultrasound image of the heel pad under compressive load. (right) The same image with a binary threshold applied to aid in selection of the lowest point of the calcaneus (highlighted in this image with a red line). Note the reverberation of the transducer signal through the acrylic plastic loading platen, visible as horizontal lines in the upper half of both images.

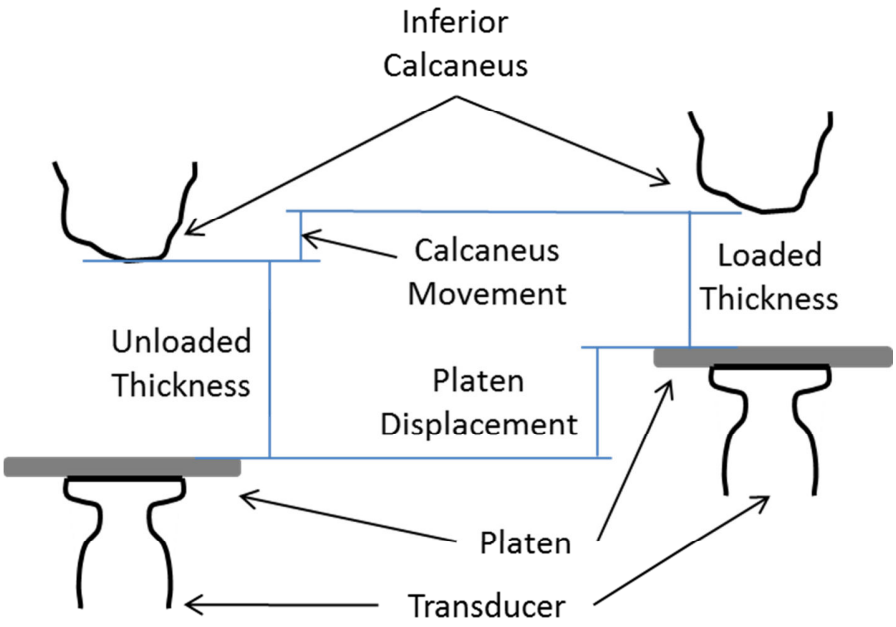

Figure 3.4. A schematic depiction of the calculation of calcaneus movement.

The force on the loading platen during testing was calculated from the experiment system pressure and the pressure-to-load calibration data obtained during verification testing against silicone gel at 3.0 mm displacement (Figure 3.5, left). The 3.0 mm displacement test was chosen due to the comparability of the maximum pressure during that test and the maximum pressure during the ultrasound test. Other silicone calibration data available included curves to 5, 7 and 9 mm, but the pressures were higher than during the ultrasound testing.

The pressure at peak displacement was not exactly the same between the ultrasound experiment and the verification test from which the calibration data were obtained. Thus, when using the two separate calibration equations to derive force on the platen during loading and unloading, discontinuities in the derived force occurred at maximum and minimum displacement locations (Figure 3.5, right). To correct this non-physical phenomenon, at peak displacement locations when shifting from the loading curve to the unloading curve, force was held constant until the pressure had decreased to a value that fell upon the unloading curve (Figure 3.6, left). This had the effect of flattening the peaks of the force curve (Figure 3.6, right), which was similar to the observed behavior in the system

during verification testing. Similarly, at locations of minimum displacement where the calibration curves calculated a force less than zero, the force data were set equal to zero. This reflected the fact that the loading platen had no means of applying a tensile load to the foot.

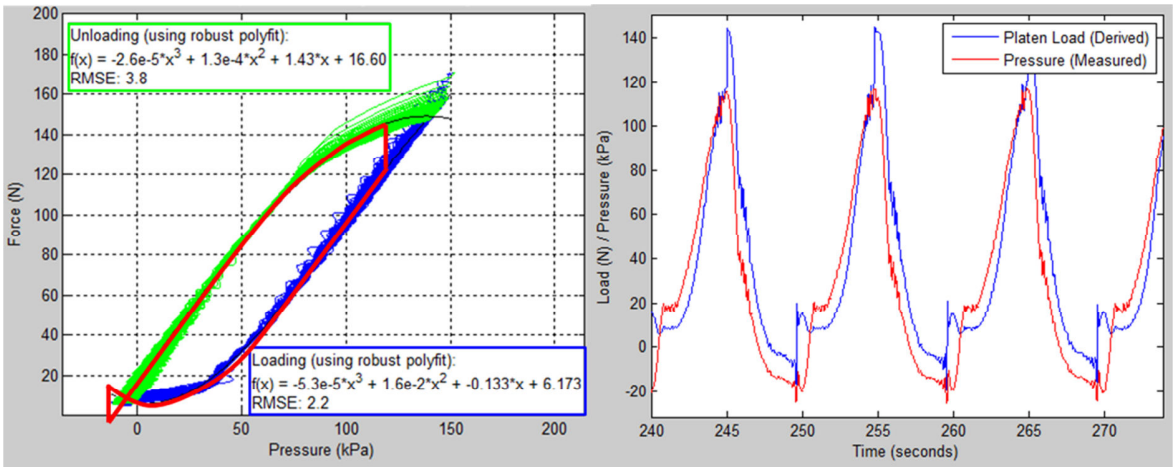

Figure 3.5. (left) Pressure versus load data obtained during the 3.0 mm displacement test against silicone gel, the calculated equations for both portions of the displacement cycle, and a solid red line indicating an example path up and down the curves when calculating force from pressure. (right) Measured pressure from the ultrasound test and force derived from the equations. Note the discontinuities in force at maximum and minimum displacement due to the shift from one equation to the other at that point.

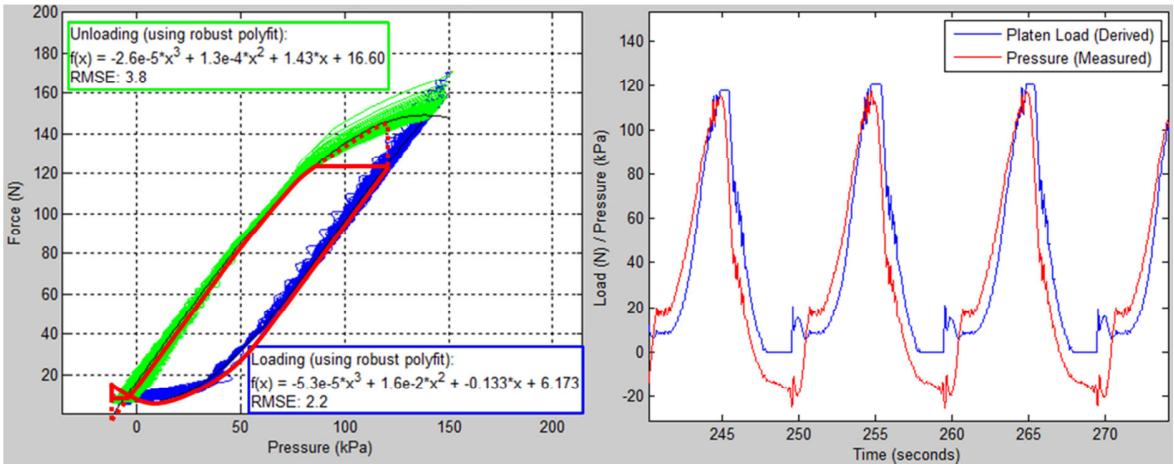

Figure 3.6. (left) Pressure versus load data with modified calibration curve fits for both portions of the loading cycle. The solid red line demonstrates holding the force at a constant value at peak displacement until pressure decreases to a point on the unloading curve and setting all forces to be greater than or equal to zero. (right) Measured pressure from the ultrasound test and derived force updated using methodology demonstrated in left image. Note discontinuities in force at maximum and minimum displacement have been eliminated.

3.3 Results

The first set of testing showed that there was no significant change in the loaded thickness of the soft tissue under peak cyclic load over time, but that the test subject did shift in the loading apparatus (Figure 3.7, Eq. 1). The shift was consistent with a small change of approximately 1.0 mm at approximately 200 seconds into the test. It was hypothesized that this small change reflected a shift in the position of the test subject in the loading apparatus. The movement of the calcaneus at peak displacement measured 7.0 ± 0.2 mm.

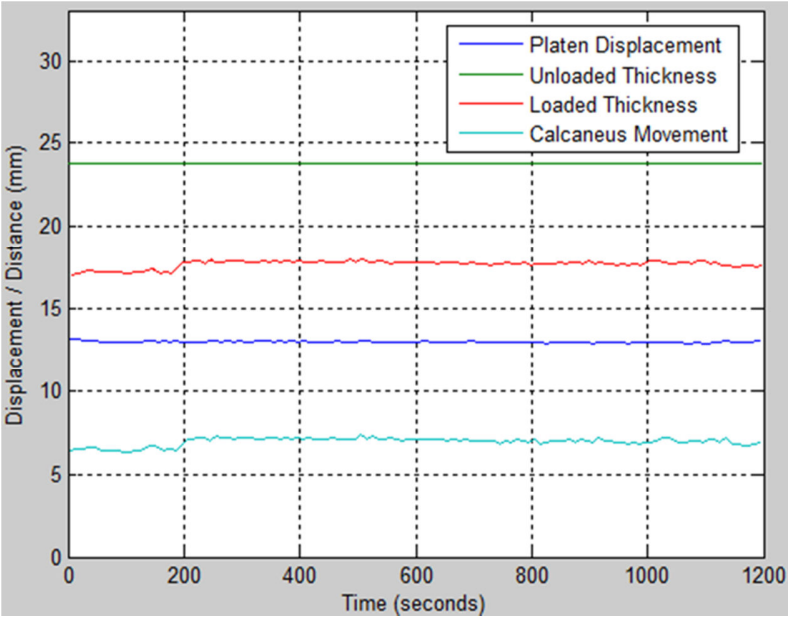

Figure 3.7. Peak displacement of the loading platen, tissue thickness (distance between the inferior-most point of the calcaneus and the platen) at unloaded and peak loaded positions, and the movement of the calcaneus at peak displacement, all versus test time.

Peak force during testing (derived from the system pressure as described above) measured approximately 140 N at a maximum displacement of the platen of approximately 13.0 mm (Figure 3.8). Since the displacements in these data are from the LVDT attached to the loading platen, they include the movement of the test subject in the loading apparatus in addition to the compressive displacement of the soft tissue.

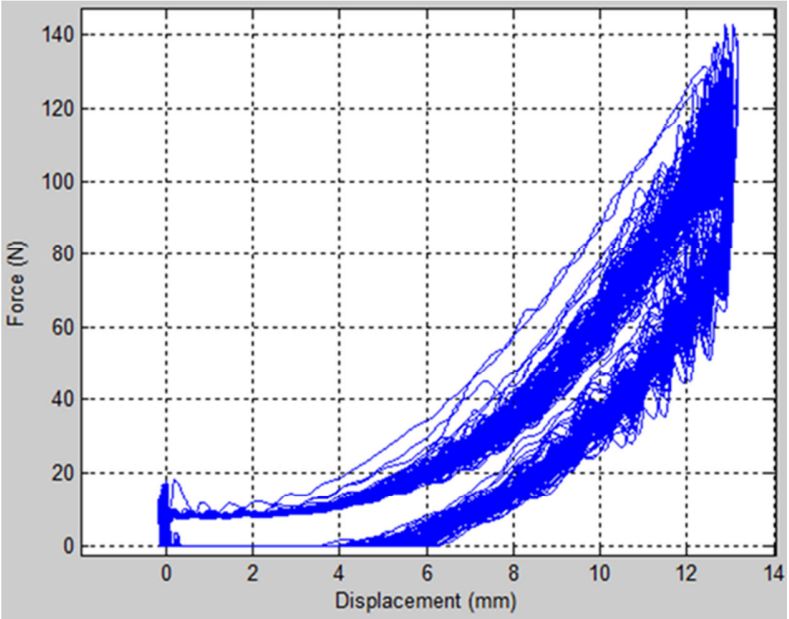

Figure 3.8. Force on the loading platen (derived from system pressure) versus displacement of the platen (from LVDT). Note that the displacement includes calcaneus movement (test subject movement in the loading apparatus.)

The second set of tests involving seven different peak displacements showed that the amount of test subject movement in the loading apparatus was a function of the loading platen displacement. Test subject movement for each test was calculated by the equation:

$$\Delta p - \Delta c = \Delta TS \tag{2}$$

Where Δp = the change in platen displacement, Δc = the change in distance from the inferior-most point of the calcaneus to the loading platen, and ΔTS = the displacement of the test subject, all measured from one displacement test to the next. The values of platen displacement and calcaneus to platen distance were averaged over all five cycles for each displacement test. Increasing the displacement of the platen caused only a slightly larger compression of the soft tissue; most of the increased displacement caused the test subject to shift further superiorly in the loading apparatus at peak displacement (Figure 3.9). As was expected, the increase in compression of the soft tissue from one displacement amount to the next caused an increase in the force on the platen (Figure 3.10).

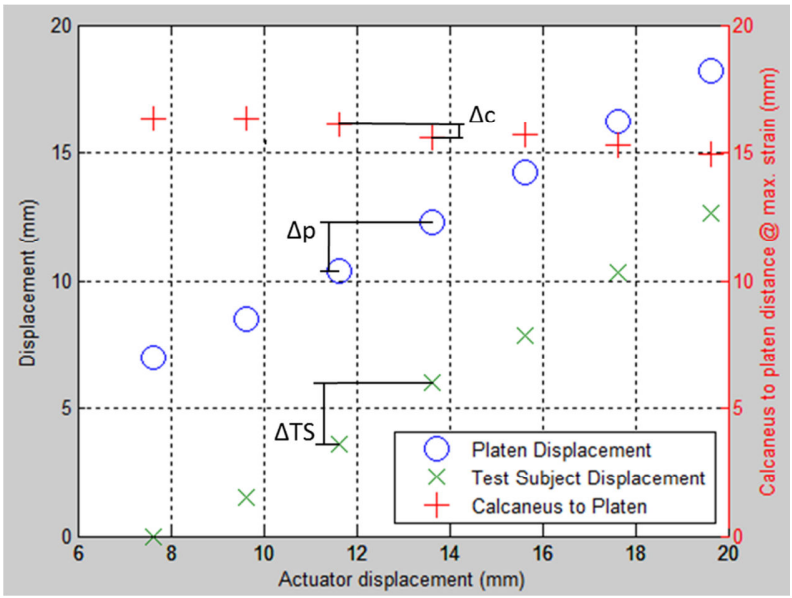

Figure 3.9. Platen displacement, test subject displacement and distance from the inferior-most point of the calcaneus to the loading platen versus average peak actuator displacement for seven displacement tests ($\Delta\, p$ = change in platen displacement, $\Delta\, c$ = change in distance from the inferior-most point of the calcaneus to the loading platen, and $\Delta\, TS$ = displacement of the test subject, all measured from one displacement test to the next, Eq. 2).

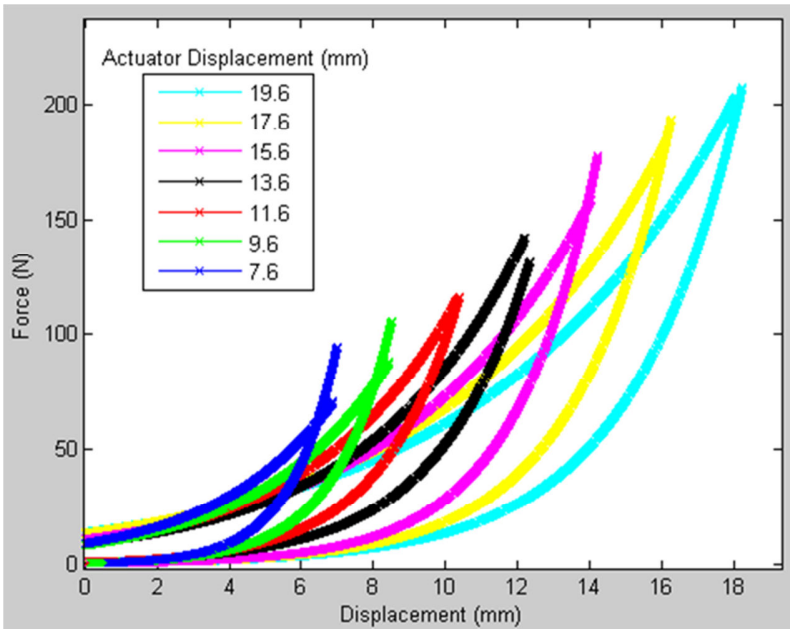

Figure 3.10. Force on loading platen (derived from system pressure) versus displacement of the platen for seven displacement tests. Note that the displacement includes calcaneus movement (test subject movement in apparatus.)

3.4 Discussion

The testing of the loading device with an ultrasound transducer attached to the slave piston was successful in answering the questions posed. It was determined that the plantar soft tissue does not experience any significant change in strain over a twenty minute cyclic compressive loading. It was also determined that the test subject does move in the loading apparatus, but that the movement remains consistent from cycle to cycle. However, the test was susceptible to test subject shifts, as occurred once. Finally, a calibration curve of actuator displacement to platen displacement under loading of a normal foot was calculated for use in future *in vivo* testing.

The force versus displacement curve obtained during this experiment shows a similar shape to the data from a pendulum impact test by Aerts and De Clercq (1993). The highest force seen during our testing was approximately 200 N, while the lowest force seen by Aerts was approximately 250 N. The pendulum impact testing involved placing the knee of the limb being loaded against a rigid surface parallel to the plantar surface of the foot. Thus, the pendulum experiment had less potential for displacement of the test subject's leg and foot, and a rigid backstop to react load out of the test subject. Our experiment allowed for movement of the ankle, lower leg, and knee (similar to Aerts' test), and additionally, movement in the leg, hip, and torso, with non-rigid straps reacting load out of the shoulders. It is understandable that our test featured lower peak loads and greater displacements.

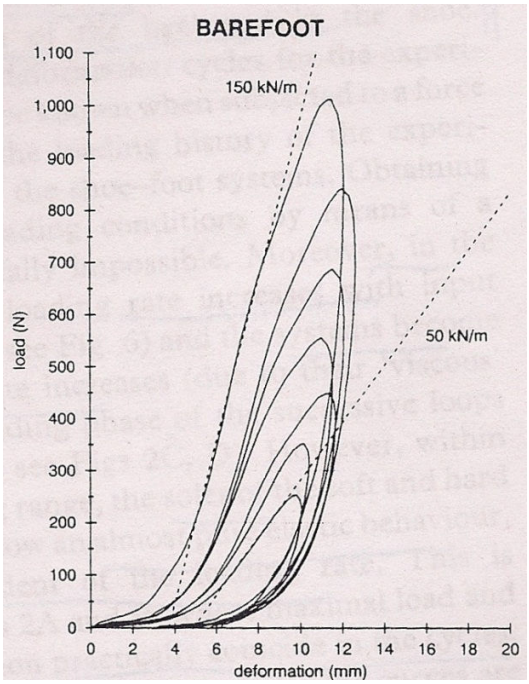

Figure 3.11. Force vs. displacement for a barefoot heel pad loaded with increasing impact velocities during pendulum impact testing (Aerts, 1993).

The testing and data processing had several limitations. The noise added to the ultrasound images due to wave reverberation through the acrylic loading platen made finding the inferior-most point of the calcaneus in an unloaded state challenging. Another limitation was that the distance of the inferior-most point of the calcaneus to the loading platen was only calculated at peak displacement due to a lack of time in which to develop a fully-automated software analysis program to track the calcaneus location throughout the entire loading cycle. The lowest point of the calcaneus was manually chosen for each loading cycle. If automated software was used to determine how the test subject shifted in the loading apparatus for all points on the loading curve, that displacement could be subtracted from the platen displacement to determine the displacement of the soft tissue alone. Another limitation of the study was the discontinuities apparent in the force data at peak force locations still remaining after the modifications to eliminate those discontinuities had been performed (Figure 3.10). A different methodology will be investigated from which to obtain force on the platen as a function of pressure in the hydraulic fluid.

3.5 Conclusion

Overall, the testing of the loading device provided valuable insight into the device's performance while loading normal plantar soft tissue and was an important step to take before proceeding with pilot testing inside the MRI. It was determined that there was no long-term viscoelastic effect in the soft tissue, so data collection could commence with initial loading, and the test subject movement was near-constant throughout all cycles, so no MRI image artifacts due to non-periodic motion were expected. This testing validated the proposed MRI pilot testing protocol.

4 MRI Pilot Testing

4.1 Introduction

Magnetic Resonance Imaging (MRI) is a commonly-used medical imaging modality. The ability to delineate soft tissue types in the acquired images, the three dimensional (3-D) format of the data obtained and the lack of any ionizing radiation to the subject are several reasons why MRI is regularly used for musculoskeletal imaging.

Several groups have used MRI imaging in conjunction with a loading mechanism to observe *in vivo* internal soft tissue deformation under load. Gefen et al. (2001) employed a custom-built indentation device in conjunction with MRI imaging to measure load vs. localized displacement of the plantar soft tissue in locations between submetatarsal heads. Then et al. (2007) designed a device to statically load the buttock with an indentor while MRI images were obtained. The resulting data were used as inputs to an inverse finite element analysis (FEA) which solved for material properties of the combined gluteal skin/fat tissues and muscle tissue. Petre et al. (2008) used a custom-built loading device to apply a test subject-specific compressive load equivalent to the subject's ground reaction force (GRF) to the plantar forefoot while the foot was imaged inside an MRI machine. All three of these studies used static loading while MRI images were acquired due to the length of time required for a standard scan (on the order of several minutes for an imaging volume the size of the foot). Subsequently, the material properties derived were not representative of dynamic loading.

The intent of this pilot study was to dynamically load the heel of a test subject's foot while MRI images representing twelve phases (six points up and six points down the loading curve) were obtained via cardiac-gated MRI imaging.

4.2 Methods

4.2.1 Test Procedure

All MRI imaging was performed on a 3.0T Philips Achieva MRI system (Philips Healthcare, Best, the Netherlands) on one test subject (male, age = 42 years, weight = 913 N). High-resolution, static images of the foot to be tested were obtained prior to dynamic loading.

These images were obtained to create the unloaded soft tissue geometry for the FEA model. Bone tissue geometry for this test subject will be obtained from CT images collected at an earlier time. The leg of the tested foot was supported and elevated slightly with pillows and foam pads (Figure 4.1). Nothing was touching the foot, except for the MRI coils held in place on the medial and lateral sides of the foot with a strap, so as not to load the foot. The first high-resolution scan obtained was a T1-weighted 3-D Fast Field Echo (FFE) sequence (Echo Train (ET): 1, Repetition Time (TR): 10.7, Echo Time (TE): 2.3, Frequency: 128, Phase Encoding Steps (Phase): 426, Flip Angle (Flip): 35) to be used for muscle, adipose tissue and skin anatomy. The second high-resolution scan was a T2-weighted 2-D sequence (ET: 15, TR: 13436, TE: 80, Frequency: 128, Phase: 480, Flip: 90) to be used for cartilage anatomy.

Figure 4.1. The test subject's foot just prior to the high-resolution static scan.

Several attempts were made to acquire dynamic scans with sixteen individual phases while loading the test subject's foot at 0.1 Hz. This loading rate matched verification testing, both non-human and human, that had previously been performed (Chapters 1 and 2). However, due to the required minimum heart rate input to the MRI system of ten beats per minute (BPM), or a rate of 0.167 Hz, we were unable to image at 0.1 Hz, which equated to 6 BPM. Instead, scanning was performed with the loading device cycling at 0.1 Hz and the MRI

system imaging at a 50% duty cycle with an input heart rate of twelve BPM. This would enable the MRI system to obtain all of the images pertaining to the loading portion of the loading/unloading cycle in one scan sequence, and then collect all of the images pertaining to the unloading portion of the cycle in a subsequent scan sequence. Using this methodology, the MRI system failed with indeterminate errors before a full set of images could be obtained during two attempts. No data were collected for the failed tests and a restart and continuation of the tests after failure was not possible. Since both tests had failed after a relatively long duration (~40 minutes for the first and ~30 minutes for the second), the group decided to reduce the test duration. This was accomplished by raising the cycling rate from 0.1 Hz to 0.2 Hz in order to scan at a 100% duty cycle instead of a 50% duty cycle. Voxel size was increased from 0.6 mm^3 to 1.0 mm^3, and the number of phases obtained reduced from sixteen to twelve in order to reduce the scan time. These parameters allowed the group to successfully complete a dynamic scan in approximately eleven minutes without any MRI system failures.

A T1-weighted 3-D FFE sequence was used to obtain 70 transverse slices of the heel, with each slice having a thickness of 2 mm with a slice spacing of 1 mm. A volume equal to 92 x 56 x 70 mm (A/P x M/L x S/I) was imaged with a voxel size of 1.0 mm^3 (ET: 36, TR: 11.4, TE: 5.0, Frequency: 128, Phase: 89, Flip: 35). The trigger delay, a required input responsible for setting the delay between the PPU trigger signal being received by the MRI Control and Data Acquisition System (CDAS) and the imaging occurring, was set to 152 milliseconds.

During imaging, the loading device actuator was set to displace with a sine wave displacement profile at 0.2 Hz and peak amplitude of 15.625 mm. Using the calibration data obtained during ultrasound testing (Chapter 2), an actuator displacement of 15.625 mm would result in a loading platen displacement of approximately 14.22 mm. Hydraulic system pressure data and actuator encoder data were acquired during testing at a 2500 Hz sampling rate.

4.2.2 Data Processing

MRI images from gated-imaging were provided as one set of DICOM files in a transverse-slice orientation. Using the slice information contained in each DICOM file header, the data were split into twelve stacks of images, each representing one phase of the cardiac-gated MRI imaging. ImageJ (National Institutes of Health) was used to open the stacks, reslice the data into a sagittal-slice orientation, and output each image of the resliced stack into a .BMP file. Custom-written MATLAB software (The MathWorks, Inc., Natick, MA) was used to open the individual .BMP files of the first phase, adjust the contrast to aid in differentiation of the musculoskeletal components, and then apply a binary threshold image adjustment to enable edge-finding of the calcaneus. The inferior-most point on the calcaneus for each image was calculated. It was determined that slice number 49 of the 91 slices in each stack contained the inferior-most point of the calcaneus. For each of the twelve phases, the image corresponding to slice 49 was displayed in MATLAB and the inferior-most point of the calcaneus, the boundary between the plantar fat pad and deep plantar skin surface, and the superficial skin surface were selected along a vertical line extending from the inferior-most point of the calcaneus (Figure 4.2). These measurements were converted into plantar fat pad thickness and plantar skin tissue thickness for each phase of the loading/unloading cycle. This process was conducted three separate times to reduce the effect of user-input error in selecting points in the low resolution images.

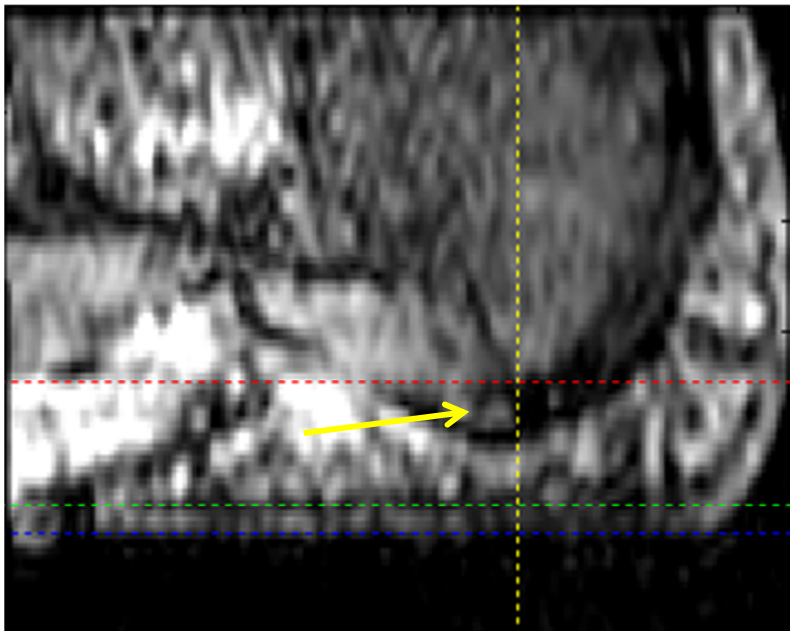

Figure 4.2. MRI image (sagittal view) of the test subject's heel. Red line denotes inferior-most point of the calcaneus, green line denotes boundary between the fat pad and skin, and blue line denotes the superficial surface of the plantar skin. Note, object identified by yellow arrow is not part of the calcaneus, as it appears to be in this image; it is thought to be ligament tissue.

The force on the loading platen over the duration of the test was calculated from the system hydraulic pressure using the pressure-to-force calibration data obtained during verification testing (Figure 4.3). The cycling rate during all verification testing was 0.1 Hz, half as fast as that of MRI pilot testing. Since the dynamic-component of the hydraulic fluid load is assumed to still be relatively small at this low rate, it was decided to proceed with the 0.1 Hz test data and to check the data with additional verification testing at 0.2 Hz. As was done during ultrasound testing (Chapter 2), discontinuities in the calibrated force data were corrected by holding the force constant at maximum displacement and holding the force to be greater than or equal to zero throughout the test.

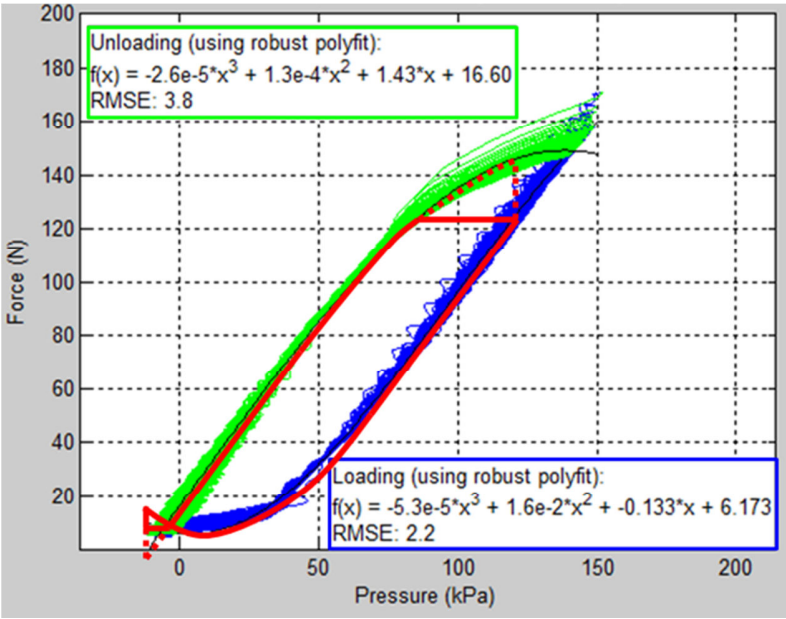

Figure 4.3. (left) Pressure versus force data obtained during the 3.0 mm verification displacement test with modified calibration curve fits for both portions of the loading cycle. The solid red line demonstrates holding the force at a constant value at peak displacement until pressure decreases to a point on the unloading curve and holding all forces to be greater than or equal to zero in order to eliminate discontinuities at maximum and minimum displacements.

The average force on the platen over each of the twelve phases was calculated by grouping the force data over all cycles into the appropriate twelve windows representing the periods over which the twelve images had been acquired. The actual generation of the PPU trigger signal in relation to the initial movement of the actuator was determined by reviewing the rotary encoder output data collected for the experiment in order to determine the point in time that the actuator had initially displaced. That time was compared to the recorded PPU signal timestamp in order to relate the PPU signal generation to actuator movement. The PPU signal occurred 1.3 milliseconds before the start of each loading cycle. That offset, combined with the MRI trigger delay parameter of 152 milliseconds, meant that phase one of the twelve phases was centered about a point in time 150.7 milliseconds after the beginning of the loading cycle. The duration of each phase was equal to 1/12 of the total cycle time of five seconds, or 0.417 seconds per phase. Starting 150.7 milliseconds after the initial movement of the actuator, the force data for all the cycles were grouped by phase. The data for each phase were averaged to represent the mean force on the platen for the duration of that phase over all cycles of the experiment. The stiffness of the soft tissue was

calculated by fitting a first order curve to the high stiffness region of the force versus displacement curve.

4.3 Results

One stack of T1-weighted high-resolution images of the unloaded foot was acquired in a scan lasting approximately thirty-one minutes (Figure 4.4).

Figure 4.4. Example image from T1-weighted high-resolution scan to be used for FE soft tissue geometry.

Another stack of T2-weighted high-resolution images of the unloaded foot was acquired in a scan lasting approximately 15 minutes (Figure 4.5).

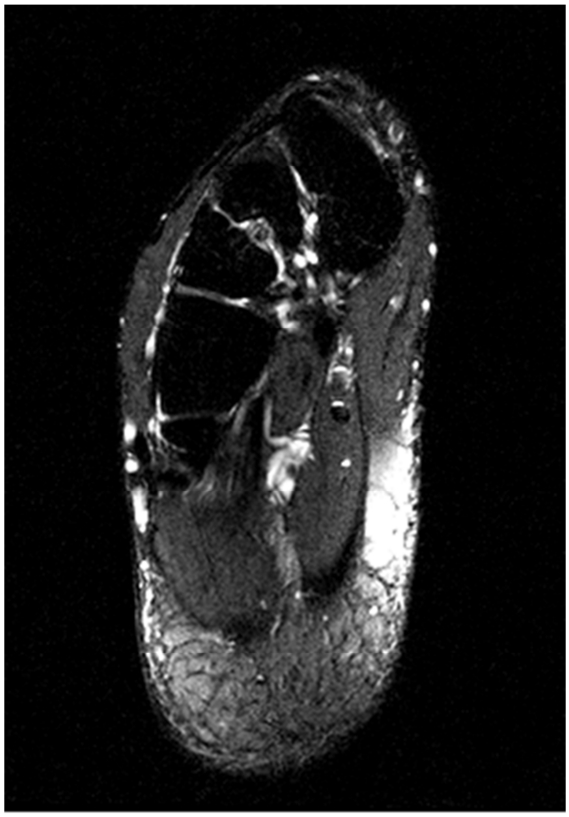

Figure 4.5. Example image from T2-weighted high-resolution scan to be used for FE soft tissue geometry.

Twelve stacks of images of the dynamically-loaded foot were obtained and processed as described above (Figure 4.6). Compression of the soft tissue and the tissue's return to an unloaded state can clearly be witnessed during the twelve phases.

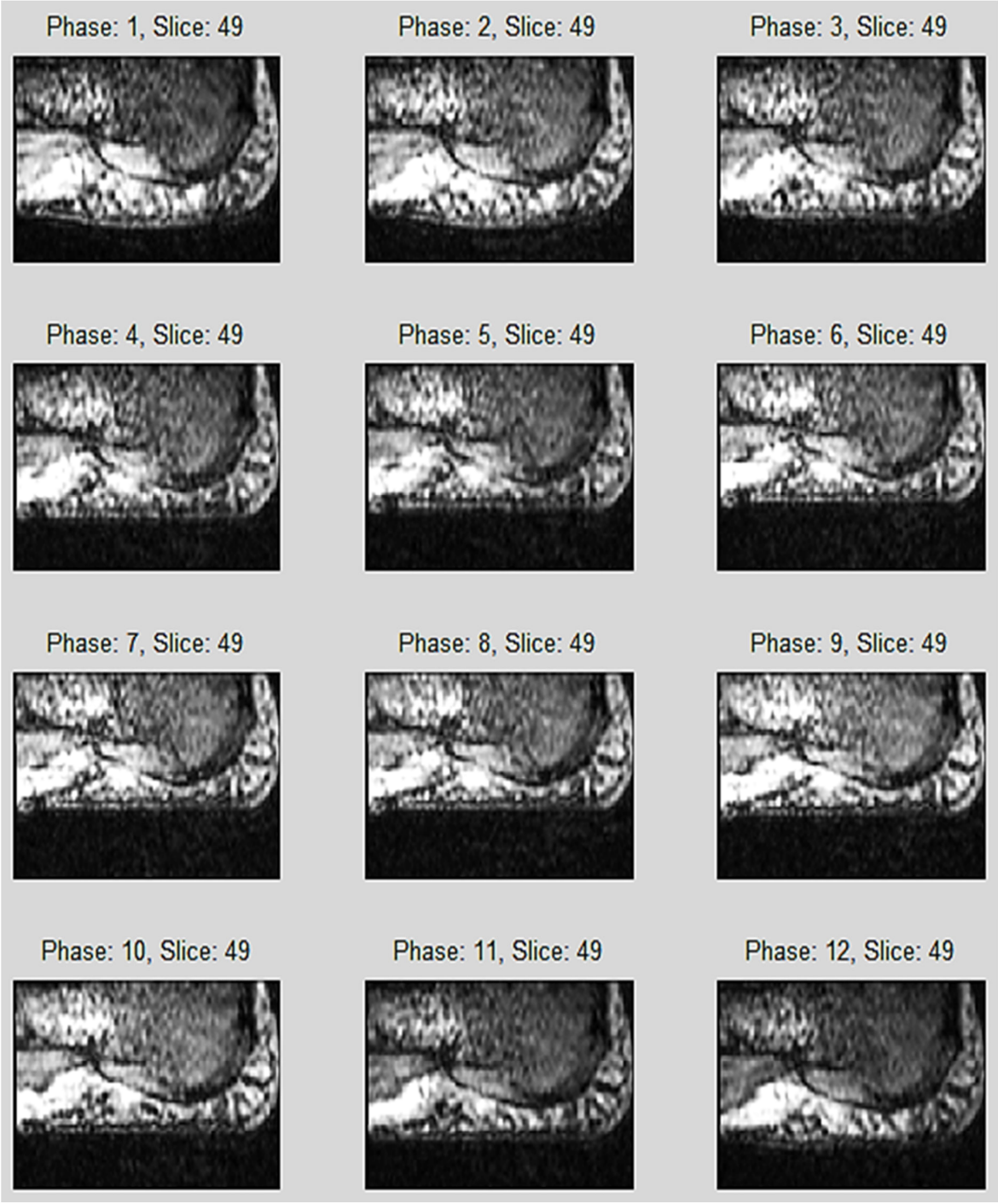

Figure 4.6. Twelve images, from unloaded (phase 1) to fully loaded (phase 6) to unloaded (phase 12) corresponding to the loading and unloading portions of the loading cycle. Each image is the same slice of the MRI stack, which was determined to contain the inferior-most point of the test subject's calcaneus.

The inferior-most point of the test subject's calcaneus was tracked through the twelve phases in order to determine how the test subject shifted in the loading apparatus over the loading cycle (Figure 4.7). The maximum shift was calculated to be 6.2 mm during the 8th phase of imaging.

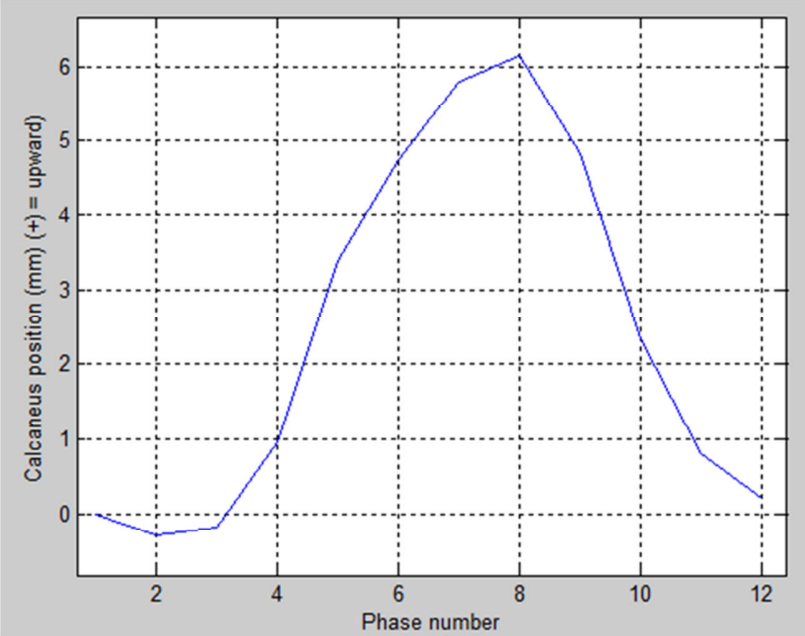

Figure 4.7. Position of the calcaneus relative to the imaging volume. Positive values reflect a shift in the direction of load application (superior direction).

Due to the relative thickness of the skin and low resolution of the dynamic images, there was significant variability in the calculated thickness of the skin between the three separate edge selections. The average value of the thickness of the plantar skin varied from a maximum of 3.4 mm to a minimum of 2.7 mm. The average value of the plantar fat pad thickness varied from a maximum of 16.0 mm to a minimum of 10.2 mm (Figure 4.8).

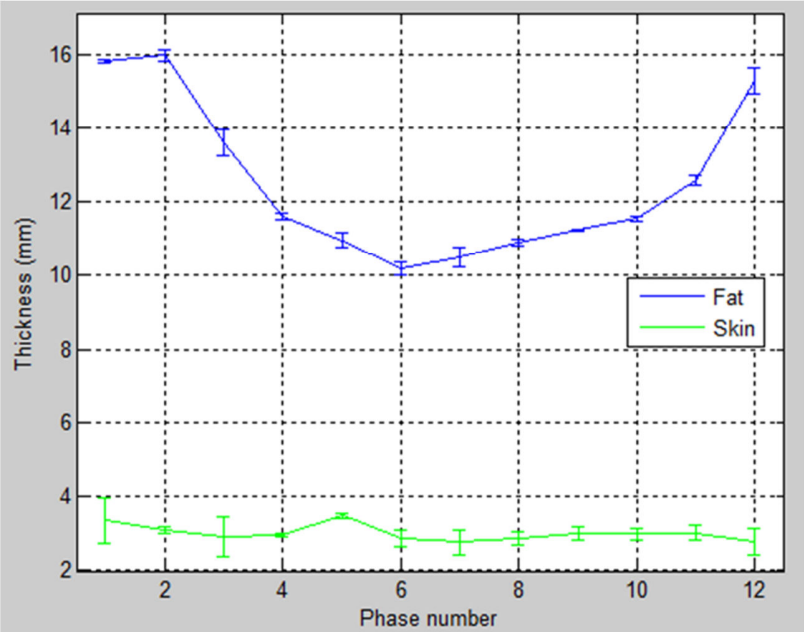

Figure 4.8. Average thickness and standard deviation of the plantar fat pad and the plantar skin at each phase of imaging for all three separate edge selections.

The calculated strain in the plantar skin shows a large range within one standard deviation from average of the three edge selection trials (Figure 4.9). The calculated strain in the plantar fat pad shows a maximum strain of 36.3% compressive strain occurring at phase 6 (Figure 4.10).

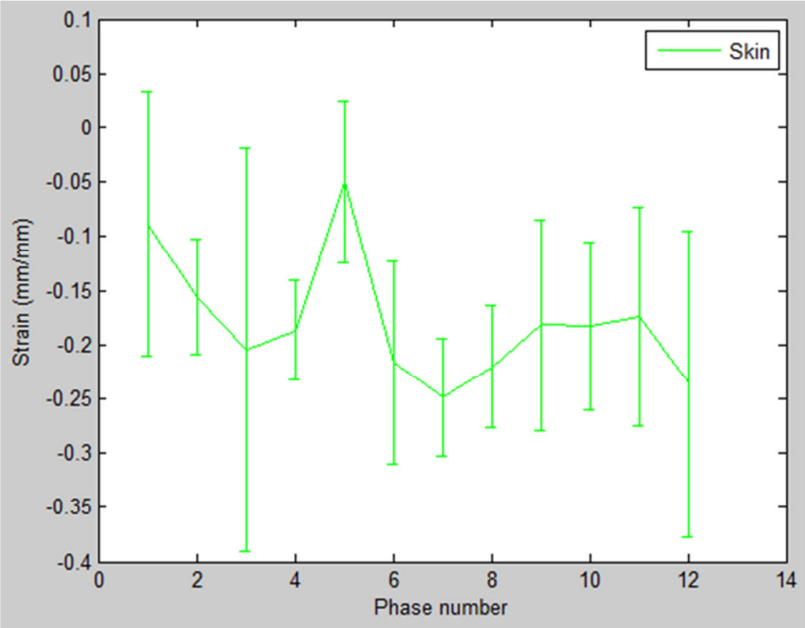

Figure 4.9. Average strain in the plantar skin versus phase. Error bars show one standard deviation.

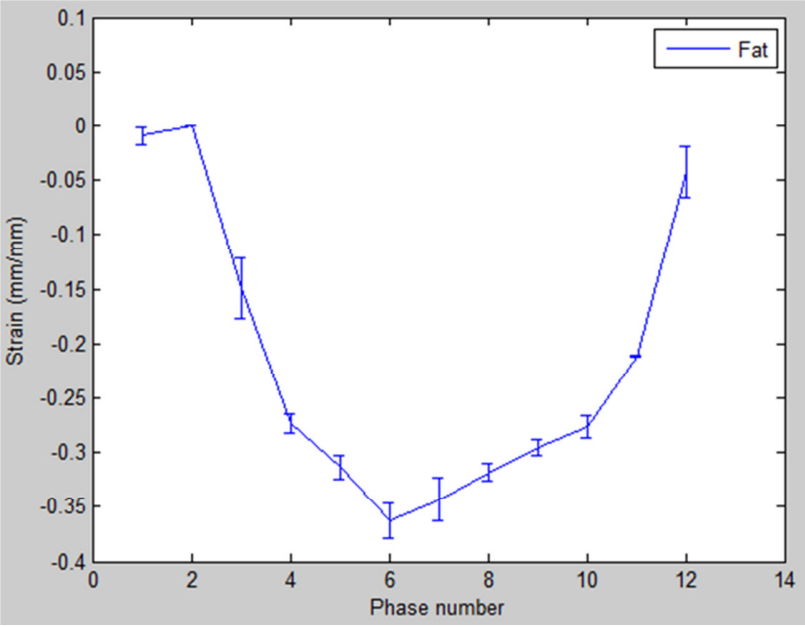

Figure 4.10. Average strain in the plantar fat pad versus phase. Error bars show one standard deviation.

Derived load on the platen showed a maximum of 141.8 N, occurring at phase 7 (Figure 4.11). Derived load on the platen versus total average displacement of the soft tissue was

calculated, as was the stiffness of the soft tissue in the high-stiffness region of the curve (Figure 4.12). The stiffness was calculated to be 55 N/mm.

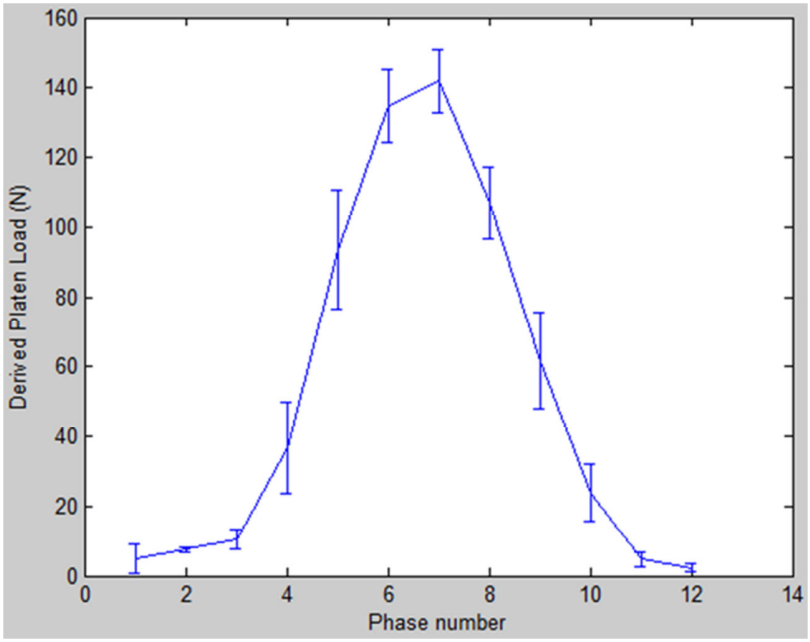

Figure 4.11. Derived average platen load for each phase. Error bars show one standard deviation.

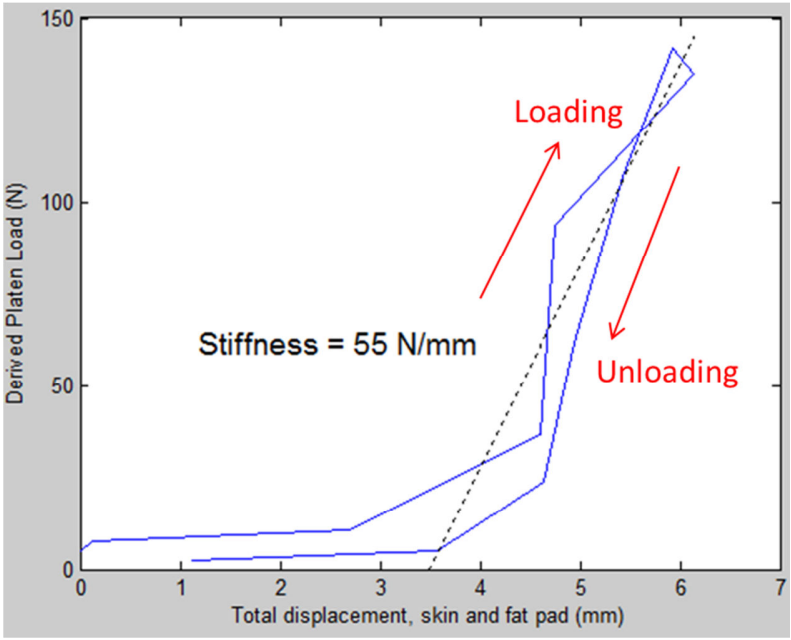

Figure 4.12. Average load on the platen versus total average soft tissue displacement (plantar fat pad plus plantar skin).

4.4 Discussion

This study obtained twelve MRI images of the heel of a test subject while the heel was dynamically-loaded in compression. The images obtained were of a high enough resolution that calculating plantar fat pad thickness and strain under load was possible, while the same calculations for the plantar skin showed large standard deviations. This was due to the thinness of the skin tissue relative to the 1 mm resolution in the images.

The movement of the test subject in the human loading apparatus at peak load, referred to as calcaneus movement, was very similar to that obtained using the same loading apparatus and loading device with an ultrasound transducer affixed to the loading device (Chapter 2). In that study, the calcaneus movement was approximately 7.0 mm at peak displacement, while the calcaneus moved a maximum of approximately 6.2 mm in this test.

The heel fat pad underwent a maximum strain of approximately 36% at a load equal to approximately 15% of the test subject's body weight. A literature review was conducted to determine average plantar soft tissue strain under body weight (Appendix C). That review showed a mean strain of the heel soft tissue under body weight of 43%. This suggests that the peak load level in this test was not far into the high-stiffness region of the typical soft tissue force versus displacement curve (possibly even still in the low-stiffness region, commonly referred to as the "toe"), as the results show a relatively high strain but relatively low peak force.

The stiffness of the soft tissue was calculated for the high-stiffness region of the force versus displacement curve to be 55 N/mm. The calculated stiffness is comparable to the lowest impact velocity in a barefoot heel pendulum impact test by Aerts et al. (1993, Figure 4.13). At the slowest velocity (0.37 $m*s^{-1}$), a stiffness of 50 kN/m (50 N/mm) was calculated. This velocity is almost two orders of magnitude greater than our loading rate. This difference might explain the greater peak forces they observed in testing, as the strain rate

dependence of the tissue would cause it to be stiffer at a faster loading rate, while the structural testing and *in vivo* loading of the entire heel in the two tests are comparable.

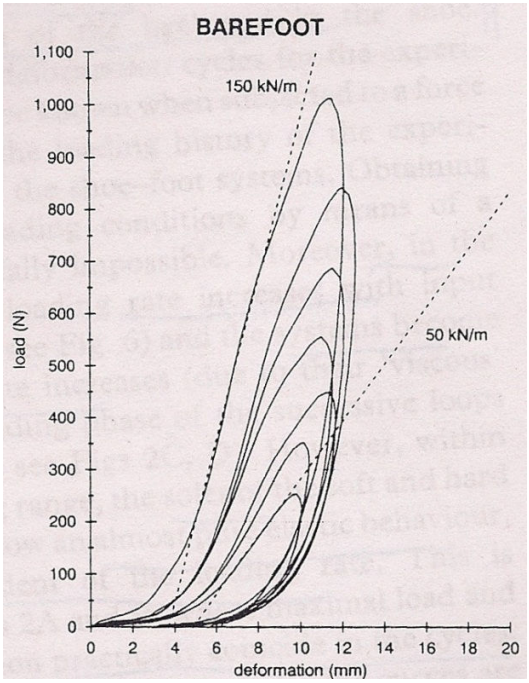

Figure 4.13. Force vs. displacement for a barefoot heel pad loaded with increasing impact velocities during pendulum impact testing. The dashed lines represent the final stiffness of the 0.37 and 0.96 $m*s^{-1}$ tests (from Aerts, 1993).

There were several limitations in this study. The frequency content of the loading curve (0.2 Hz) was significantly slower than the frequency content of gait (6-8 Hz) (Antonsson, 1985). This frequency was also twice as high as the frequency used in the verification testing from which the pressure-to-force calibration curve fits were obtained. It is not known how the greater loading frequency would affect the pressure-to-force calibration data, as the data were not obtained for any frequencies but 0.1 Hz. Future verification testing will be used to validate the assumption that the pressure-to-force calibration curve fits are similar between 0.2 and 0.1 Hz.

Another limitation is that the loading was only compressive, and as such, did not mimic the physiological combined compressive and shear loading that the plantar foot undergoes during gait. The movement of the test subject in the human loading apparatus meant that a

force approximating that of body weight was not able to be applied to the foot. Finally, the resolution and number of phases collected by the MRI system were less than was desired. Increased resolution would provide additional insight into the strain of the plantar skin tissue under load and additional phases would allow for more points from which to build a curve and less deviation from the average load during each phase.

Future work will include investigating methods to increase the loading rate and the possible addition of shear loading to the device. Methods to restrict movement of the loaded foot, including a modified ankle-foot orthosis, are also currently being considered. The imaging parameters used during gated MRI will be tuned to optimize both the data collected and the time the test subject spends under loading. To compare plantar pressure attained during loading to that during posture and gait, a pedar pressure sensor will be placed between the plantar foot and the loading platen in a test performed outside of the MRI scanner. Finally, a comprehensive error analysis to quantify accuracy and repeatability of calculating the force upon the foot via the pressure in the system will be conducted. A sensitivity analysis to quantify the sensitivity of the test results to the temporal shifting that occurs due to the PPU signal initiation and the MRI PPU trigger delay will also be a part of that error analysis.

5 Conclusion

5.1 Purpose

The purpose of this research project was to develop an MRI-compatible, dynamic loading device that used cardiac-gated MRI imaging to obtain *in vivo* force versus deformation data for the plantar soft tissue. These data will be used as inputs, in conjunction with our group's existing three-dimensional (3-D) finite element (FE) model, to conduct an inverse FE analysis that will solve for patient-specific material properties of the soft tissue. Peak stress magnitude and location in the soft tissue is dependent upon the material properties in addition to the patient-specific anatomy. Using patient-specific FE models is a means to avoid using averaged tissue material properties and anatomy to represent the large variability inherent to biological tissues. The *in vivo* stiffness measurements obtained with this device will enable our group to create patient-specific FE foot models of controls and people with diabetes. These models will enable 3-D visualization and quantification of the stress fields within the tissue and allow for the differences in those stress fields from normals to people with diabetes to be determined. This will help to further the understanding of the pathomechanics of foot ulcers in the diabetic population. Ultimately, results from these patient-specific FE models could aid in designing new orthoses or clinical techniques that aid in the prevention of foot ulcers.

5.2 Research

The majority of the research involved the designing, building and bench top verification testing of a computer-controlled, MRI-compatible loading device (Chapter 1, Appendix A). The initial design specifications for the device were to produce a triangle displacement wave with maximum amplitude of 13 mm at a 1.0 Hz rate and the capability of outputting a 1500 N load. Due to a lack of similar devices in the literature, the device was designed and assembled from a low level, including the component-by-component design of an MRI-compatible, single-acting hydraulic system. Safety of the test subject during loading was paramount, and as such, a redundant safety system was incorporated. Verification testing in the laboratory was conducted in order to quantify the performance of the device and to ensure its safe operation before proceeding to human studies.

Initial *in vivo* testing was conducted in the laboratory with an ultrasound transducer affixed to the loading device (Chapter 2). This study was conducted for two reasons: 1) to test the performance of the loading device and the human loading apparatus before proceeding to MRI testing and 2) to ensure that cyclic loading of the heel would not have any long-term viscoelastic effects whereby the loaded tissue thickness would change over time. After successful completion of that testing, an *in vivo* pilot test of the loading device inside of the MRI was conducted (Chapter 3). One test subject was successfully imaged using cardiac-gating while the device loaded the plantar heel in compression at a 0.2 Hz rate.

While soft tissue deformation under load has been studied using MRI imaging in the past, a review of the literature did not find a system that combined triggered cardiac-gated MRI with dynamic loading in order to generate *in vivo* soft tissue material properties. It is believed that this work represents the first instance of this methodology. Due to the fact that there may be commercialization potential for the device (for more uses than just foot loading), the device is currently patent-pending.

5.3 Findings

The hydraulic loading device provided several difficult challenges throughout its design and testing. Turn-key hydraulic systems without metallic components were not found during initial searches. Designing the system component-by-component with MRI-compatible pieces was hampered mainly by limited availability of high-pressure rated plastic fittings. The electromagnetic interference (EMI) emitted by several of the motion-control components required an entire electrical system re-design and retrofit in order to maintain an acceptable level of noise on crucial data signal lines (Appendix B). The open-loop nature of the control system, due to a lack of any MRI-compatible transducers for use in the scanning room, combined with the non-linear displacement of the slave piston as a function of master piston displacement due to hydraulic system compliance, combined to create a formidable challenge in making the system displace precisely as intended. Finally, the propensity of the test subject's body to move in the human loading apparatus made it impossible to attain

the levels of force and tissue strain that had been initially sought without further modifications to the apparatus.

Ultimately, using step-by-step procedures to bleed air from the hydraulic fluid (Appendix A), a cycling rate reduction, and a great deal of trial and error testing, most of the initial design specifications were able to be achieved. During benchtop verification testing against a piece of silicone gel (Chapter 1), the device was repeatable to ± 0.24 mm at 10.8 mm of slave displacement at 0.1 Hz, with a sine wave displacement profile over a 30 minute duration. The displacement profile was changed from a 1.0 Hz triangle wave to a 0.1 Hz sine wave in order to reduce pressure surges occurring in the system caused by rapid inertial changes in the hydraulic fluid. The maximum load output by the device was measured at 1541 N, attained during maximum pressure testing. The device is capable of a displacement greater than 10.8 mm, but the maximum design pressure of 1034 kPa was reached at this displacement. It was determined during testing that the non-linearity of the slave piston displacement was a function of the load on the slave piston; for all intents and purposes, this meant that a different displacement calibration curve would be necessary for all materials tested. The device worked reliably and safely enough that the team was comfortable moving forward with pilot human loading studies.

Testing the device in the laboratory with an ultrasound transducer affixed to the slave piston provided critical data before attempting to test in the MRI. The amount of test subject movement and shift within the apparatus were determined, as was a displacement calibration curve for normal human tissue.

After some initial protocol development trials, a successful dynamic MRI scan was acquired while the device loaded a test subject's heel at 0.2 Hz. The stiffness of the combined plantar skin and adipose tissue was calculated to be 55 N/mm, which was similar in stiffness to a pendulum-impact test of the barefoot heel conducted by Aerts (1993).

5.4 Future Work

Additional verification testing to check the validity of using pressure-to-force calibration data generated from 0.1 Hz testing for 0.2 Hz tests will be conducted, and a revised means to convert pressure-to-force will be determined. The data obtained during the pilot MRI study will then be used by another member of the group as inputs to an inverse FE analysis. The analysis will be used to determine the patient-specific material properties of the test subject's plantar soft tissues. The device will be used in its existing form to test both controls and people with diabetes within the year. Potential improvements to be incorporated in a second-generation design of the device include: an oil-based hydraulic fluid; hydraulic pump(s) and electronically-controlled valves for increased cycling rate capability and more precise displacements; combination compressive and shear loading capability to more closely mimic loading under gait; intra-MRI force and/or displacement sensors to refine loading accuracy; and MRI scan parameter tuning for higher-resolution images and more phases from which to create a force versus displacement curve.

5.5 Summary

This thesis has detailed the designing, building and testing of an MRI-compatible, computer-controlled loading device. As the first device of its kind, it has proven to be a challenging project for the author, one that he hopes will help the research and medical communities to better understand the pathomechanics behind foot ulcers in people with diabetes, and ultimately, to design methods of prevention for this costly (fiscally and emotionally) public health concern.

References

Aerts P & De Clercq D 1993, "Deformation characteristics of the heel region of the shod foot during a simulated heel strike: the effect of varying midsole hardness.", *Journal of sports sciences,* vol. 11, no. 5, pp. 449-61.

Antonsson, E.K. & Mann, R.W. 1985, "The frequency content of gait", *Journal of Biomechanics,* vol. 18, no. 1, pp. 39-47.

Budhabhatti SP, Erdemir A, Petre M, Sferra J, Donley B & Cavanagh PR 2007, "Finite element modeling of the first ray of the foot: a tool for the design of interventions.", *Journal of Biomechanical Engineering,* vol. 129, no. 5, pp. 750-6.

Cavanagh, P.R. 1999, "Plantar soft tissue thickness during ground contact in walking", *Journal of Biomechanics,* vol. 32, no. 6, pp. 623-628.

Centers for Disease Control and Prevention. 2011a, *Diabetes: At A Glance 2011*, U.S. Department of Health and Human Services, Centers for Disease Control and Prevention, Atlanta, GA.

Centers for Disease Control and Prevention. 2011b, *National diabetes fact sheet: national estimates and general information on diabetes and prediabetes in the United States, 2011.*, U.S. Department of Health and Human Services, Centers for Disease Control and Prevention, Atlanta, GA.

Chen, W.M., Lee, T., Lee, P.V.S., Lee, J.W. & Lee, S.J. 2010, "Effects of internal stress concentrations in plantar soft-tissue-A preliminary three-dimensional finite element analysis", *Medical Engineering and Physics,* vol. 32, no. 4, pp. 324-331.

Cheung J.T.-M. & Zhang M. 2008, "Parametric design of pressure-relieving foot orthosis using statistics-based finite element method", *Med.Eng.Phys.Medical Engineering and Physics,* vol. 30, no. 3, pp. 269-277.

Delbridge L, Ctercteko G, Fowler C, Reeve TS & Le Quesne LP 1985, "The aetiology of diabetic neuropathic ulceration of the foot.", *The British journal of surgery,* vol. 72, no. 1, pp. 1-6.

Erdemir, A., Viveiros, M.L., Ulbrecht, J.S. & Cavanagh, P.R. 2006, "An inverse finite-element model of heel-pad indentation", *Journal of Biomechanics,* vol. 39, no. 7, pp. 1279-1286.

Gefen, A., Megido-Ravid, M., Azariah, M., Itzchak, Y. & Arcan, M. 2001, "Integration of plantar soft tissue stiffness measurements in routine MRI of the diabetic foot", *Clinical Biomechanics,* vol. 16, no. 10, pp. 921-925.

Gefen A 2003, "Plantar soft tissue loading under the medial metatarsals in the standing diabetic foot.", *Medical engineering & physics,* vol. 25, no. 6, pp. 491-9.

Gordois A, Scuffham P, Shearer A, Oglesby A & Tobian JA 2003, "The health care costs of diabetic peripheral neuropathy in the US.", *Diabetes care,* vol. 26, no. 6, pp. 1790-5.

Halloran, J.P. & Erdemir, A. 2011, "Adaptive Surrogate Modeling for Expedited Estimation of Nonlinear Tissue Properties Through Inverse Finite Element Analysis", *Annals of Biomedical Engineering,* vol. 39, no. 9, pp. 2388-2397.

International Diabetes Federation 2011, "IDF Diabetes Atlas, 5th edition", .

International Diabetes Federation 1997, "Diabetes health economics: facts, figures, and forecasts", .

Isvilanonda, V., Dengler, E., Iaquinto, J.M., Sangeorzan, B.J. & Ledoux, W.R. In Review, "Finite element analysis of the foot: Model validation and comparison between two common treatments of the clawed hallux deformity", *Clinical Biomechanics,* .

Kwan, R.L.C., Zheng, Y.P. & Cheing, G.L.Y. 2010, "The effect of aging on the biomechanical properties of plantar soft tissues", *Clinical Biomechanics,* vol. 25, no. 6, pp. 601-605.

Li Y, Burrows NR, Gregg EW, Albright A & Geiss LS 2012, "Declining rates of hospitalization for nontraumatic lower-extremity amputation in the diabetic population aged 40 years or older: u.s., 1988-2008.", *Diabetes care,* vol. 35, no. 2, pp. 273-7.

Pai, S. & Ledoux, W.R. 2010, "The compressive mechanical properties of diabetic and non-diabetic plantar soft tissue", *Journal of Biomechanics,* vol. 43, no. 9, pp. 1754-1760.

Petre M., Erdemir A. & Cavanagh P.R. 2008, "An MRI-compatible foot-loading device for assessment of internal tissue deformation", *J.Biomech.Journal of Biomechanics,* vol. 41, no. 2, pp. 470-474.

Reiber, G.E., Boyko, E.J. & Smith, D.G. 1995, "Lower Extremity Foot Ulcers and Amputations in Diabetes" in *Diabetes in America*, 2nd edition edn, National Institutes of Health, , pp. 409.

Rome K, Campbell RS, Flint AA & Haslock I 1998, "Ultrasonic heel pad thickness measurements: a preliminary study.", *The British journal of radiology,* vol. 71, no. 851, pp. 1149-52.

Taguchi, G., Chowdhury, S., Wu, Y., Taguchi, S. & Yano, H., 2005, *Taguchi's quality engineering handbook,* John Wiley & Sons ; ASI Consulting Group, Hoboken, N.J.; Livonia, Mich.

Then C, Menger J, Benderoth G, Alizadeh M, Vogl TJ, Hübner F & Silber G 2007, "A method for a mechanical characterisation of human gluteal tissue.", *Technology and health care : official journal of the European Society for Engineering and Medicine,* vol. 15, no. 6, pp. 385-98.

Tsekos, N.V., Khanicheh, A., Christoforou, E. & Mavroidis, C. 2007, "Magnetic Resonance--Compatible Robotic and Mechatronics Systems for Image-Guided Interventions and Rehabilitation: A Review Study.", *Annual Review of Biomedical Engineering,* vol. 9, no. 1.

Tseng C.-L., Rajan M., Pogach L., Miller D.R. & Lafrance J.-P. 2011, "Trends in initial lower extremity amputation rates among veterans health administration health care system users from 2000 to 2004", *Diabetes Care Diabetes Care,* vol. 34, no. 5, pp. 1157-1163.

Uzel M, Cetinus E, Ekerbicer HC & Karaoguz A 2006, "Heel pad thickness and athletic activity in healthy young adults: a sonographic study.", *Journal of clinical ultrasound : JCU,* vol. 34, no. 5, pp. 231-6.

Van de Walle R, Lemahieu I & Achten E 1997, "Magnetic resonance imaging and the reduction of motion artifacts: review of the principles.", *Technology and health care : official journal of the European Society for Engineering and Medicine,* vol. 5, no. 6, pp. 419-35.

Yousheng Yang, Semini, C., Guglielmino, E., Tsagarakis, N.G. & Caldwell, D.G. 2009, "Water vs. oil hydraulic actuation for a robot leg", pp. 1940-1946.

Appendix A. Hydraulic Plantar Soft Tissue Reducer (HyPSTR) User's Manual

TABLE OF CONTENTS

1.1 Device Description 66
1.1.1 Hardware 68
1.1.1.1 Hydraulic System 68
1.1.1.2 Displacement System 73
1.1.1.3 Human Loading Jig 74
1.1.1.4 Electrical System 76
1.1.2 Software 81
1.1.2.1 Excel (Pre-Processing) 81
1.1.2.2 Q Programmer 84
1.1.2.3 Master LabVIEW VI 88
1.1.2.4 MATLAB (Post-Processing) 116
1.1.2.5 ST Configurator 147
1.2 Testing Patients with the Device 148
1.2.1 Pre-test step 148
1.2.2 Device set-up 148
1.2.3 User-specific test parameters 150
1.2.4 Power-on 152
1.2.5 Setup and test the safety system 153
1.2.6 Fill system and bleed 154
1.2.7 Obtain high-resolution, static scan of the subject 160
1.2.8 Position test subject 160
1.2.9 Position loading platen 162
1.2.10 Testing 163
1.2.11 Test completion 164

1.3 Lessons Learned 165
1.4 Future Work 172
1.5 References 173
1.5.1 Component User's Manuals 173
1.5.2 Works Cited 174

LIST OF FIGURES

Figure 1.1. (left) Components that will go into the MRI control room.....67

Figure 1.2. Hydraulic schematic showing components and location in regards to MRI 68

Figure 1.3. Spreadsheet used in the initial design of the displacement system.....72

Figure 1.4. Linear actuators force vs. speed capability plot 74

Figure 1.5. CAD mockup of test subject held in human loading jig. 75

Figure 1.6. Device electronics wiring schematic 76

Figure 1.7. View inside the main (larger) project box showing several electrical.....77

Figure 1.8. View of DAQ and wiring inside of the smaller project box 78

Figure 1.9. Wiring schematic of solenoid valve.....80

Figure 1.10. Excel spreadsheet used to obtain Q Programmer stepper motor settings.....82

Figure 1.11. Excel spreadsheet plot displaying constant acceleration, peak velocity. 83

Figure 1.12. Subject-specific safety parameters calculator in Excel.....84

Figure 1.13. Q Programmer GUI with example cyclic, sine displacement wave. 85

Figure 1.14. Q Programmer GUI while actuator is displacing. Stop button highlighted. 87

Figure 1.15. LabVIEW Master VI front panel, main view.....92

Figure 1.16. LabVIEW Master VI front panel, device settings view 92

Figure 1.17. LabVIEW Master VI block diagram with individual loops labeled (a-f) 93

Figure 1.18. PPU Signal Generator subVI and code comments 94

Figure 1.19. PPU Signal Generator subVI expanded, entire VI view 94

Figure 1.20. Left-hand side zoom of Figure 1.19 95

Figure 1.21. Right-hand side zoom of Figure 1.19.....95

Figure 1.22. Alternate case structures from portion of VI shown in Figure 1.21. 96

Figure 1.23. Code comments corresponding to PPU Signal Generator subVI 97

Figure 1.24. PPU Signal Trigger VI, entire view.....98

Figure 1.25. Alternate case structures for VI shown in Figure 1.24. 98

Figure 1.26. Additional case structure for VI shown in Figure 1.24. 99
Figure 1.27. Code comments corresponding to PPU Signal Trigger VI 99
Figure 1.28. Acquired Signals VI, entire view 100
Figure 1.29. Alternate case structure for VI shown above 100
Figure 1.30. Additional case structures for VI shown in Figure 1.28. 101
Figure 1.31. Code comments corresponding to Acquired Signals VI 102
Figure 1.32. Datalogger VI, entire view 103
Figure 1.33. Alternate case structures for VI shown in Figure 1.32. 104
Figure 1.34. Additional case structures for VI shown in Figure 1.32. 104
Figure 1.35. Code comments corresponding to Datalogger VI 105
Figure 1.36. Stop VI, Front Panel updates and Solenoid Control VI 105
Figure 1.37. Alternate case structures for VI shown in Figure 1.36. 105
Figure 1.38. Alternate case structure for VI shown in Figure 1.36. 106
Figure 1.39. Code comments corresponding to Stop VI, Front Panel and Solenoid 106
Figure 1.40. Op-amp power supply VI, entire view 107
Figure 1.41. Alternate case structures for VI shown in Figure 1.40. 107
Figure 1.42. Code comments corresponding Op-amp Power Supply VI 107
Figure 1.43. PPU Signal Counter subVI block diagram, front panel, and VI properties 108
Figure 1.44. PPU Status Message Starter subVI block diagram, front panel 108
Figure 1.45. Checksum Calculator subVI block diagram, front panel, and VI properties 109
Figure 1.46. Checksum Bitwise Inverter subVI block diagram, front panel 109
Figure 1.47. Initialize Press Transducer kPa subVI front panel and block diagram 110
Figure 1.48. Initialize LVDT subVI front panel and block diagram 110
Figure 1.49. Initialize Encoder Analog Inputs subVI front panel and block diagram 111
Figure 1.50. Initialize Load Cell subVI front panel and block diagram 112

Figure 1.51. Generate Data Acquisition Sample Clock subVI front panel and block 112

Figure 1.52. Initialize Encoder subVI front panel and block diagram.....113

Figure 1.53. Elapsed Time subVI front panel and block diagram.....113

Figure 1.54. Waveform Data Queue to File TDMS subVI front panel and block diagram...114

Figure 1.55. PPU Data Queue to File subVI front panel and block diagram.....115

Figure 1.56. Datalog File to Text File subVI front panel and block diagram 115

Figure 1.57. Example plot from MATLAB showing locations of master piston.....117

Figure 1.58. ST Configurator user interface.....147

Figure 1.59. Connection to CDAS (picture from Phillips) 149

Figure 1.60. Mechanical pressure relief valve and solenoid pressure release valve 154

Figure 1.61. Hydraulic schematic showing componentry and location in regards 155

Figure 1.62. From left to right: master cylinder, slave cylinder, and system high point.....155

Figure 1.63. Static scan arrangement showing leg supported but only MRI coils.....160

Figure 1.64. Gantt chart of Master's degree (both thesis and classes) 166

Figure 1.65. Test setup that proved that the linear actuator was not displacing.....167

Figure 1.66. Example of water hammer effects in this hydraulic system.....169

Figure 1.67. Several iterations of LVDT to slave cylinder mounting mechanisms 170

1.1 Device Description

The Hydraulic Plantar Soft Tissue Reducer (HyPSTR) (Figure 1.1) is a computer-controlled, single-acting, master/slave, cyclic, hydraulic loading device. It is used in conjunction with gated MRI to generate force vs. deformation data of the plantar soft tissue, which are then used as inputs to an inverse finite element analysis (FEA) model, from which soft tissue material properties are derived. Following is a description of the sub-systems, both hardware and software, their function in the device, and how they operate.

A great deal of information pertaining to the individual components and sub-system functions can be found in the first chapter of this thesis, “An MRI-Compatible Device for Obtaining Patient-Specific Plantar Soft Tissue Material Properties”. As such, this appendix will attempt to include only relevant information that was not already covered in that document.

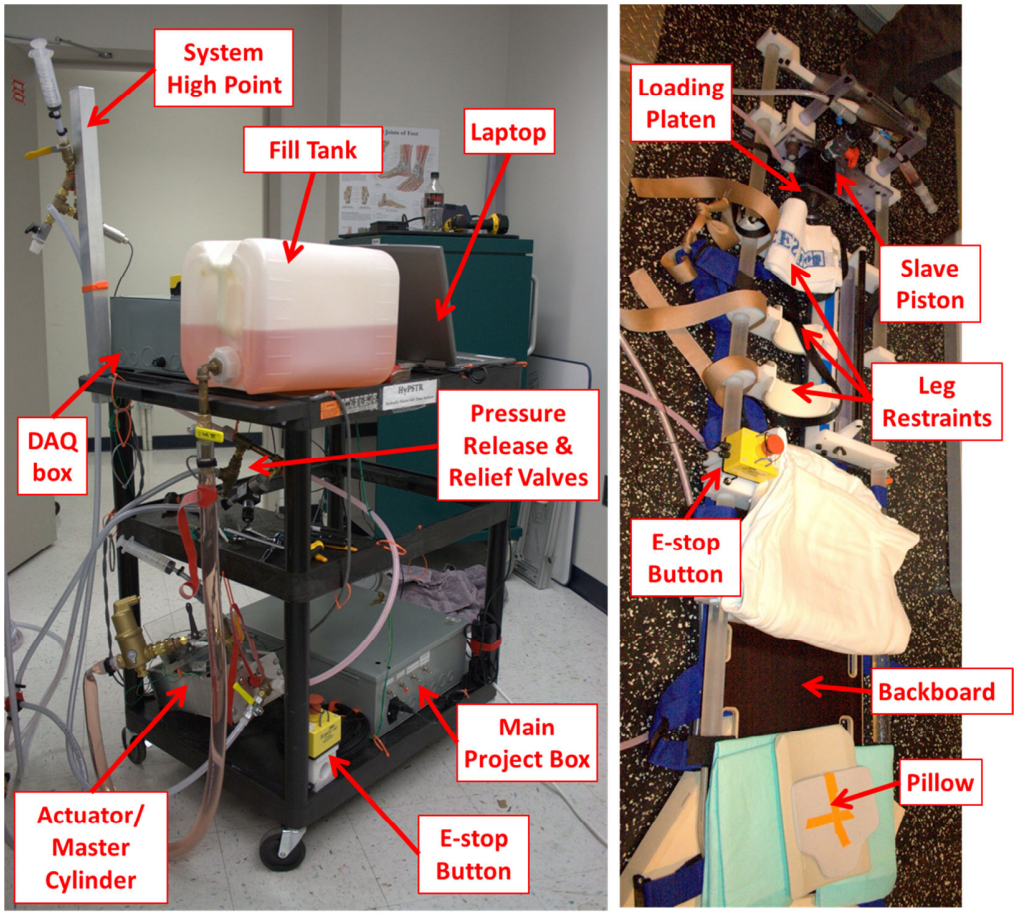

Figure 1.1. (left) Components that will go into the MRI control room (right) Components that will go into the MRI imaging room

1.1.1 Hardware

1.1.1.1 Hydraulic System

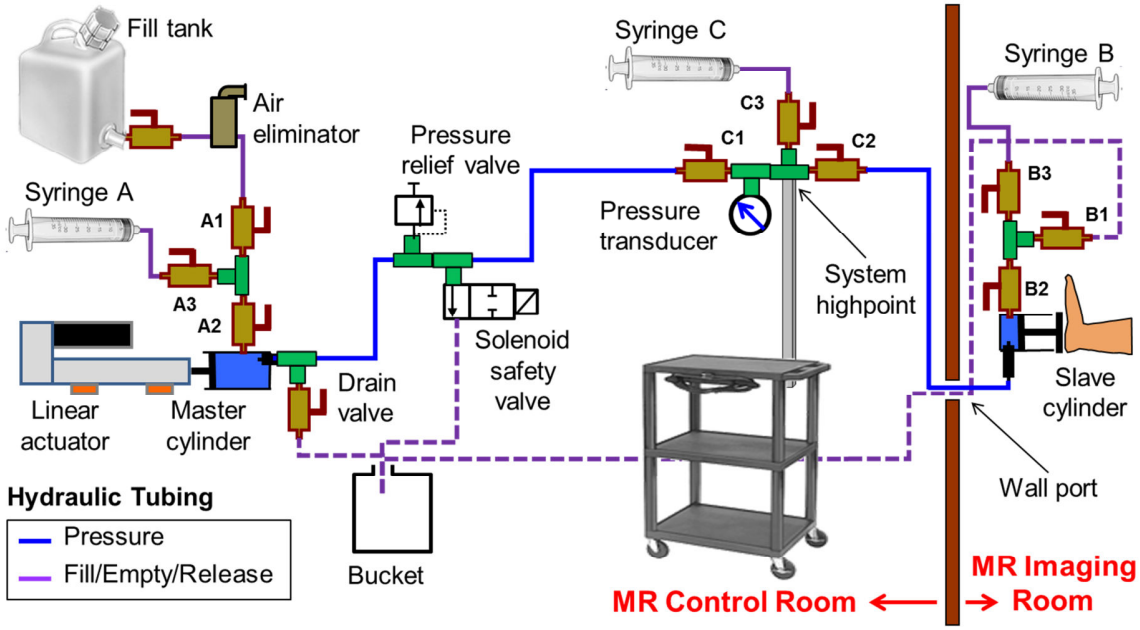

Figure 1.2. Hydraulic schematic showing components and location in regards to MRI bore

The master cylinder and linear actuator driving it are situated in the MRI control room, where ferrous metals are allowed. The necessary displacement to be applied to the foot is carried via the hydraulic fluid residing in tubing that passes through small ports in the wall between the control room and the imaging room. There, the slave piston/cylinder converts hydraulic energy into piston displacement which applies a compressive load to the plantar surface of the foot.

The hydraulic system includes all components under pressure during cycling, all fill and drain lines, and bleed syringes (Figure 1.2). The main pressure line is nylon 6 vacuum-rated tubing (McMaster-Carr PN5173K47, OD of 0.5", ID of 0.38"). It has a maximum pressure rating of 503 psi, and is vacuum-rated to 29.9" Hg. It was the second type of tubing purchased; the first was reinforced PVC tubing that was not vacuum-rated. It was thought to be deforming when the retraction of the master piston caused a slight negative pressure in the line; that assumption was not verified, but the tubing change was inexpensive with no real downsides.

The tubing is connected to all other hydraulic components through nylon compression fittings (McMaster-Carr PN 50775K337) with a maximum pressure rating of 1379 kPa (200 psi). These fittings are composed of a body and a nut assembly including a plastic nut, a stainless steel grasping ring that grips the tubing, and a Buna-Nitrile O-ring. **Once disassembled, the entire nut assembly should be replaced, as the fittings are not designed to be reused.** This was determined after one fitting that had been disassembled and then reassembled released the tubing it was holding at approximately 427 kPa (62 psi), or less than half of the maximum design pressure.

The maximum design pressure of the device is set at 1034 kPa (150 psi). The lowest rated component is the mechanical pressure relief valve, which has a range of relief pressures from 172-1207 kPa (25-175 psi). The valve is a sturdy bronze fitting; it is assumed that at a pressure higher than 1207 kPa, the relief valve would activate, relieving the excess pressure and not catastrophically-failing. Several of the other components of the hydraulic system have a maximum design pressure of 1379 kPa (200 psi). Hence, setting the system maximum design pressure to 1034 kPa may be slightly conservative, but without being able to predict the exact failure mode of the system and without knowing what kind of safety factors have been applied to each individual component's maximum pressure, being conservative is the only safe option. As detailed in the initial chapter of this thesis, a maximum pressure test was conducted in which the maximum pressure seen by the system was 1075 kPa (156 psi).

Multiple configurations and materials of O-rings and X-rings were tested for the master and slave pistons before settling on a soft Buna-N O-ring (McMaster-Carr PN AS568A) for both components. These O-rings feature a durometer hardness of A50, giving them better sealability and less friction under the relatively low pressure load they encounter during service (Parker Hannifin Corporation, 2007). Another step taken to reduce friction, increase sealability, and prolong O-ring useful lifetime was to use Chemplex 710 Silicone Compound (Fuchs Lubritech) O-ring lubricant on O-rings when installing them, for both the master and slave pistons.

Additionally, when assembling any pressurized hydraulic fitting that is metal-to-metal, Loctite 545 Thread Sealant is applied to the male threads in order to ensure a leak-proof connection. When either one or both of the pieces being connected is plastic, Loctite No More Leaks Plastic Pipe Thread Sealant is applied in a similar manner for the same reason.

Tap water was chosen over mineral oil for a hydraulic fluid in the initial design phase of the project for several reasons:

- Near-incompressibility: according to one group, water has an undissolved air content that is approximately four times lower than that of mineral oil at 20℃ and atmospheric pressure (Yousheng, 2009). Undissolved air in this device's closed hydraulic system would result in less movement of the slave piston than the input movement of the master piston, leading to inaccurate displacements.
- Ease of availability: the laboratory where the device was built and tested has access to a sink, as does the MRI control room at the facility where tests will be conducted.
- Ease of cleanup: if a spill of some sort were to occur, the easy cleanup of tap water is a strong advantage.

In an effort to remove as much air from the tap water as is possible before testing, several steps are taken. Water is put into the fill tank and allowed to sit for a period of time that is at least 12 hours. Through the same process whereby dissolved oxygen and nitrogen gases come out of solution and coalesce to form bubbles on the inside of a glass of water left to sit for some time, dissolved air is extracted from the hydraulic fluid as it stabilizes to room temperature. Additionally, a hydronic air eliminator is installed in-line between the fill tank and the hydraulic system. The air eliminator (Spirotherm, Inc.) is used to remove free air (bubbles seen by the eye), entrained air (bubbles small enough that the force of buoyancy acting on them isn't enough to overcome the viscosity of the fluid, so they do not rise), and dissolved air (dissolved in solution) from hydronic (radiant-heat) home heating systems. Finally, food coloring is added to the water before filling the system. This makes it easier to find and bleed out air bubbles inside the semi-opaque white nylon tubing.

An Excel spreadsheet (Figure 1.3) was used to calculate many of the parameters of the hydraulic displacement system in the initial design phase of the project, such as: required

cylinder diameters, actuator speeds, and hydraulic tubing ID's. The spreadsheet was linked so that the effect on the system of a change to one parameter would be apparent throughout all other affected parameters.

Hydraulic calcs	Metric		English	
= input cell				
Slave cylinder				
Force:	1500	N	337.5	lbf
Cylinder diam:	42.850	mm	1.687	in
Cylinder area:	1442.1	mm^2	2.235	in^2
Displacement:	10	mm	0.394	in
Master Cylinder				
Force:	1500	N	337.5	lbf
Cylinder diam:	42.85	mm	1.687	in
Cylinder area:	1442.1	mm^2	2.235	in^2
Displacement:	10	mm	0.394	in
Loading Rate:	0.1	Hz	0.1	Hz
Displacement Rate:	2.0	mm/sec	0.08	in/sec
Displacement Rate:	120.0	mm/min	4.72	in/min
Flowrate:	173049	mm^3/min	10.6	in^3/min
Hydraulic hose/Pressure				
System pressure:	1040	kPa (kN/m^2)	150.9	psi
Area ratio:	1.00	mm/mm	1.00	in/in
Flowrate:	0.17	liter/min	0.05	gallon/min
Desired Max Velocity:	3.00	m/sec	10.00	feet/sec
Hose Inner Diameter, minimum calced:	1.11	mm	0.04	in
Hose Inner Diameter, minimum:	6.30	mm	0.25	in
Hose ID, actual used:	9.652	mm	0.380	in
Hose area, actual:	73.17	mm^2	0.11	in^2
H20 Temperature (estimate):	10	degrees C	50	degrees F
u, velocity in tube:	0.04	m/sec	0.13	ft/sec
v, kinematic viscosity:	1.3070E-06	m^2/sec	1.407E-05	ft^2/sec
dh, hydraulic diameter:	0.009652	m	0.03167	ft
k, roughness of tube:	0.0000015	m	0.000005	ft
Re, Reynolds number:	2.91E+02		2.91E+02	
k/dh:	0.00016		0.00016	
λ, D'Arcy-Weisbach friction coeff:	0.0360	n/a	0.0360	n/a
ρ, density:	1000.00	kg/m^3	62.40	lb/ft^3
Length of tubing:	9.14	m	30.00	ft
Pressure loss due to fluid friction:	26	Pa (N/m^2)	0.004	psi
Actuator/Screw				
Degree/Step:	1.8	deg/step		
Steps/Rev:	200.0	steps/rev		
Displacement/rev (screw):	3.17500	mm/rev	0.1250	in/rev
Belt ratio:	2		2	
Rev (motor) / Displacement (screw)	0.629921	rev/mm	16.0000	rev/in
Displacement (screw) / rev (motor)	1.587500	mm / rev	0.0625	in / rev
Displacement (screw) / full step:	0.0158750	mm/step	0.0006250	in/step
Encoder counts/step	10	counts/step	10	counts/step
Steps/Displacement:	125.9843	full steps/mm	3200.0	full steps/in
Counts/Displacement:	1259.8	counts/mm	32000	counts/in
Microstepping:	25,400	steps/rev	20,000	steps/rev
	16,000	microsteps/mn	320,000	microsteps/in

Figure 1.3. Spreadsheet used in the initial design of the displacement system

1.1.1.2 Displacement System

The linear actuator (Ultra Motion, 2-2B.125-HT23) that forms the basis of the displacement system consists of a 0.125”/revolution ball bearing lead screw with a two inch stroke length. It is driven through a belt-drive system with a 2:1 ratio (stepper motor: actuator revolutions) by a NEMA 23 stepper motor with 200 full steps/revolution. The actuator includes magnetic reed-type limit switches that are wired to the stepper motor driver. Upon closing of the limit switch circuit, the actuator is stopped nearly-instantaneously in order to prevent accidental over-extension/retraction of the screw, which could lead to failure of the actuator and/or stepper motor.

Initially, the actuator belt drive system incorporated a slip clutch to prevent overloading of the screw. After months of testing and troubleshooting of the system, it was determined that the actuator was not displacing the amount that the rotary encoder reported that it was. Upon sending the actuator back to the manufacturer, it was determined that the slip clutch was slipping under a minimal load, much less than the 400 lbf load it was supposed to be set at when initially purchased. The manufacturer recommended locking the slip clutch for this application, in order to ensure the greatest displacement precision and accuracy.

Since the actuator no longer has the protection of a slip-clutch, it is imperative that the actuator is not allowed to travel past the limit switches, as destruction of the ball screw, belt drive system, and/or stepper motor are all possible outcomes.

The actuator was initially specified to be able to apply a 1500 N load at a peak velocity of 20 mm/second, in order to enable a 10 mm peak displacement triangle wave cycling at 1.0 Hz. It is capable of up to 63.5 mm/second velocity and a load of 2225N (Figure 1.4).

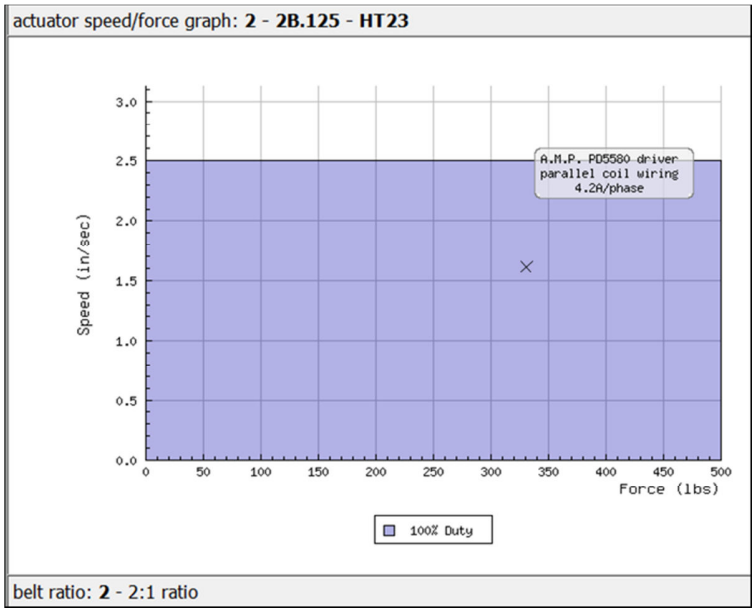

Figure 1.4. Linear actuators force vs. speed capability plot ("X" marks the approximate maximum design force of 1500N and maximum design displacement speed of 20 mm/second)

1.1.1.3 Human Loading Jig

The human loading jig was designed by Michael Fassbind, an engineer in our laboratory. It is constructed of several modular components, all of which are made of entirely non-metallic parts. The modularity serves several purposes:

- Near-infinite adjustment for different test subjects
- Ease of transport from location to location
- Ease of storage at the MRI facility

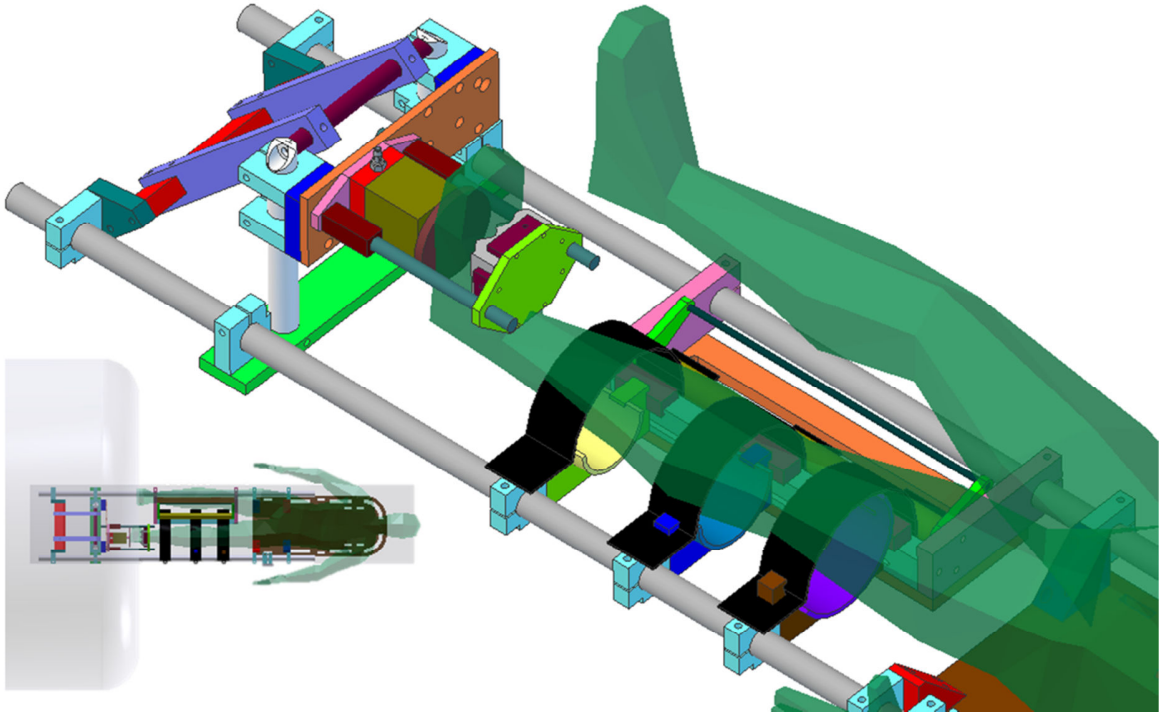

Figure 1.5. CAD mockup of test subject held in human loading jig (top view including size relative to MRI bore, inset).

The only part of the jig containing any metal components is the fiber optic emergency stop button (E-stop button). The button contains several non-ferrous metal screws for which plastic replacements could not be obtained, and one ferrous metal spring that was not accessible for replacement without possible damage to the button. An MRI-compatibility test was performed on the button to ensure that the spring would be both safe and not affect the image quality. No compatibility problems were detected at that time. The button housing is attached to one of the main rails that form the backbone of the jig using large, rigid plastic mounting brackets. Additionally, the part of the button containing the spring is safety-wired to the housing using redundant plastic zip-ties. It was approved as being MRI-safe by the radiologist responsible for all of the team's MRI imaging.

1.1.1.4 Electrical System

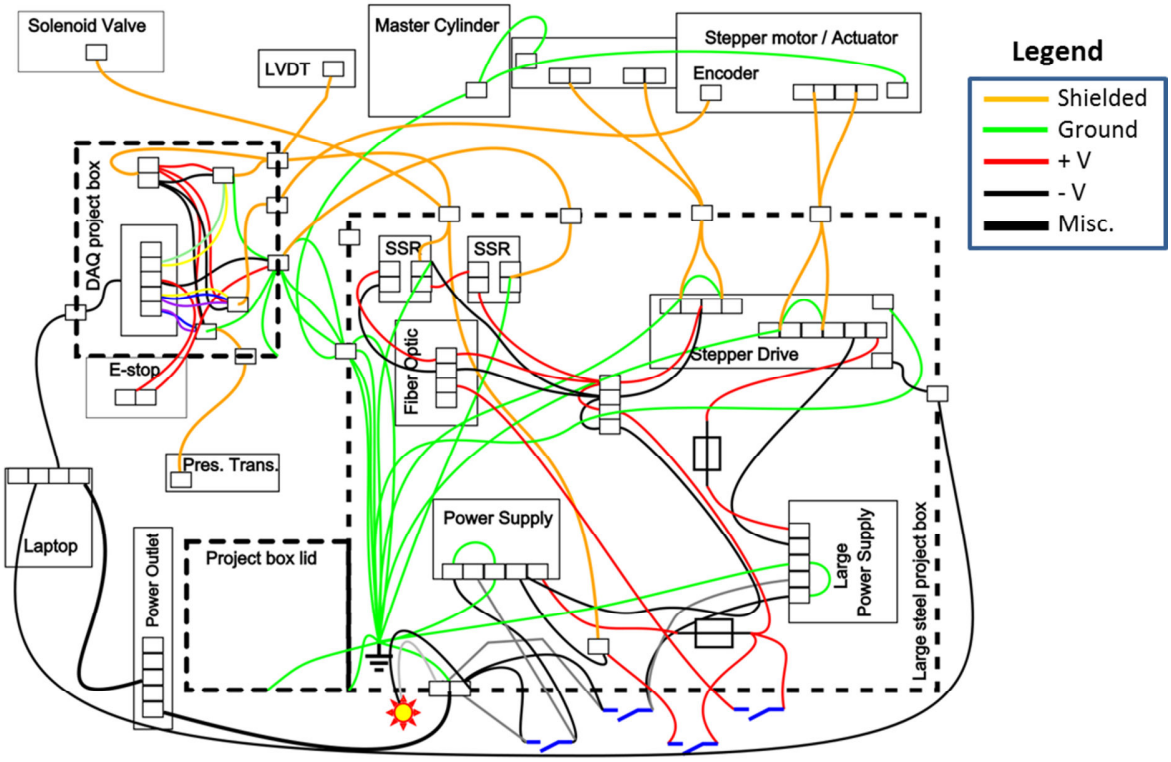

Figure 1.6. Device electronics wiring schematic

Designing, testing, and revising the electronics of the device proved to be a substantial portion of the project. Detailed information regarding the electrical system is located in Appendix B of this thesis. This section will only seek to introduce topics that are not covered or expand on topics that are only minimally covered in that section.

The electronic system has several responsibilities:

- Provide a thorough grounding scheme incorporating a single-point (“star”) ground and no ground loops
- Provide power to the stepper motor driver
- Provide control signals to the stepper motor that powers the linear actuator
- Power limit switches on the linear actuator
- Power the fiber optic control box that detects the state of the test subject’s E-stop button
- Control the safety circuit responsible for powering the solenoid valve (details below)

- Power the laptop used to conduct the experiment
- Power the rotary encoder and pressure transducer used during MRI testing
- Power the Linear Variable Displacement Transducer (LVDT) and load cell used during verification testing
- Power the active analog filters used to filter acquired data signals

A 28 volt, 224 watt, AC-to-DC power supply is solely responsible for powering the stepper motor driver. An auxiliary, 24 volt, 60 watt AC-to-DC power supply is responsible for powering all other components in the device (Figure 1.7), save for the USB-powered data acquisition (DAQ) board (Figure 1.8).

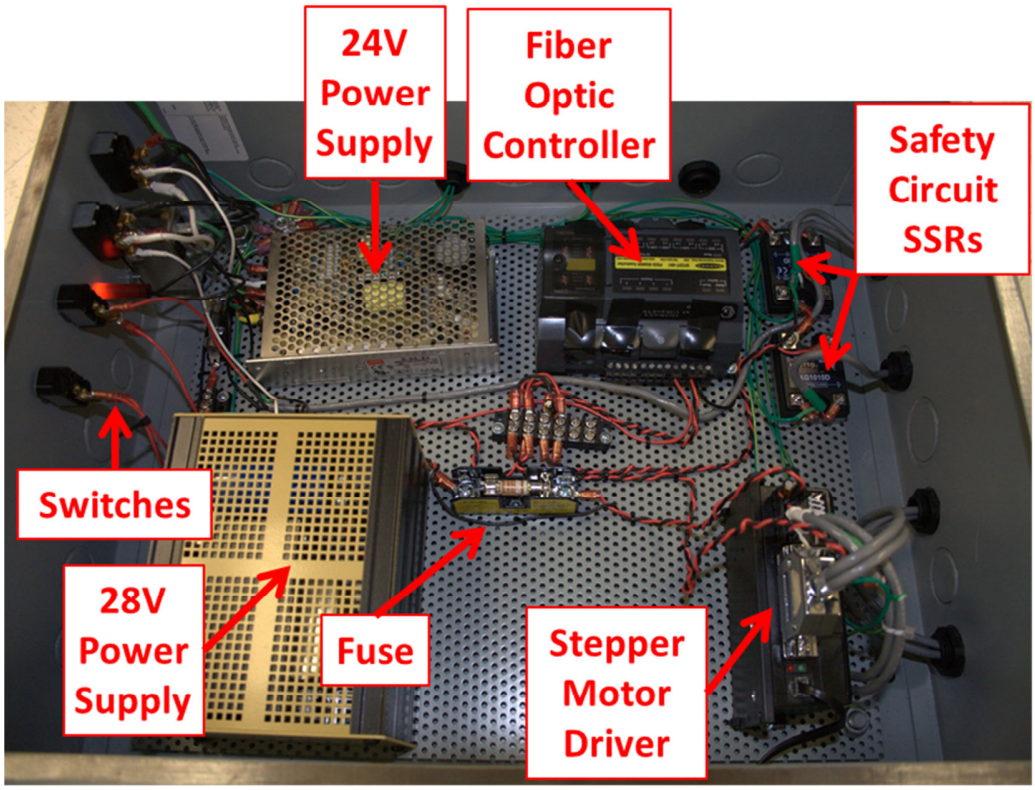

Figure 1.7. View inside the main (larger) project box showing several electrical components

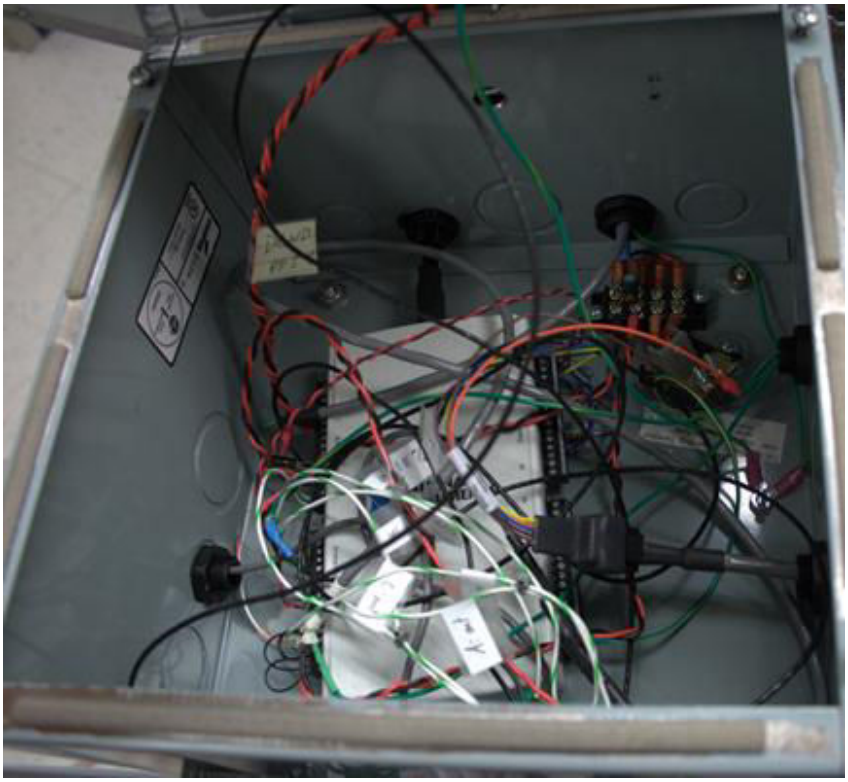

Figure 1.8. View of DAQ and wiring inside of the smaller project box

Best-practices in wiring were attempted. This includes:

- An EMI line filter with built-in switch and fuse at the point that the 110V mains voltage enters the main project box
- Fuses rated at 50-75% of the maximum design amperage of the wires they are in-line with (to prevent the wiring from catching fire before a fuse trips)
- Strain-relief for all wires/cables passing into the project boxes
- Soldered/heat-shrink wrapped connections at all locations where signal integrity is important or where wire-strain might be able to occur
- Use of Double Pole Single Throw (DPST) switches to connect 110V mains power to the AC-to-DC power supplies

The device was tested by the UW Scientific Instruments division on February 8th, 2012, as is required per IRB requirements. The device passed a leakage current test with a value of

670 μA. It also passed a test measuring the resistance of the path to ground. It was approved for human testing at UW facilities.

One keenly important aspect of the electronics system is the solenoid valve and the circuitry used to power that valve. The solenoid valve is a “normally-open” type, meaning that until power is applied, the valve is open and fluid is allowed to pass through it. The valve is placed in-line with the pressure hydraulic line (Figure 1.2). The idea behind this design is that if the solenoid stops receiving electrical power, for any reason, the entire pressurized portion of the hydraulic system will be near-instantaneously brought down to atmospheric pressure, thereby removing any load being applied to the test subject’s foot. The solenoid valve wiring (Figure 1.9) allows for five possible scenarios that will remove power from the solenoid valve:

- The test subject E-stop button is depressed.
- The test operator E-stop button is depressed.
- A virtual button on the front panel of the LabVIEW master VI is clicked.
- The LabVIEW master VI detects a pressure reading greater than the operator-input not-to-exceed pressure.
- Any loss of electrical power to the device (such as the MRI facility losing electrical power or a malfunction of the 24VDC power supply) will also open the solenoid valve.

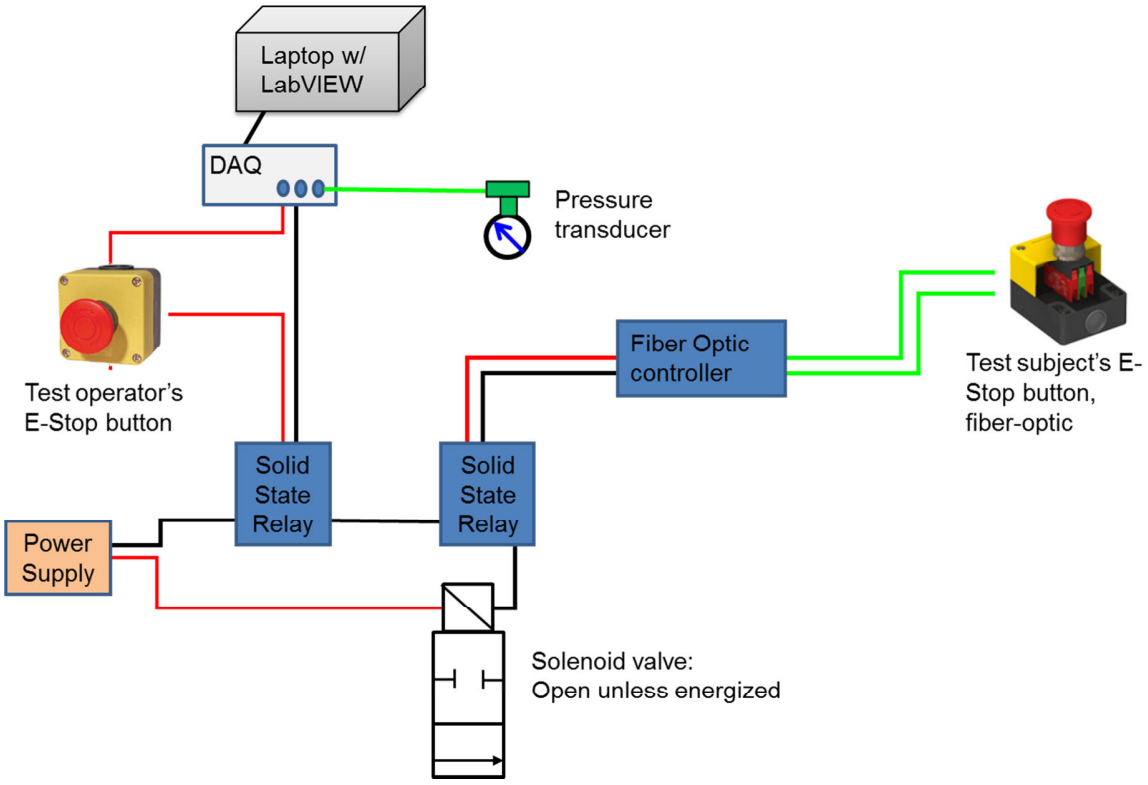

Figure 1.9. Wiring schematic of solenoid valve

When the test subject fiber optic E-stop button is depressed, a mechanism inside the button blocks the path of light traveling from one of the fiber optic cables routed from the control room into the imaging room from being passed through to the other cable, and routed back to the control room. The two cables originate from inside the main project box at the fiber optic controller. When the controller senses that the light path has been broken, a low-current 24 VDC output is stopped. That output is wired to the sensor side of one of two solid state relays (SSRs) placed in serial; cutting power to sensor side of the SSR effectively opens the SSR switch and thus, opens the circuit to the solenoid valve.

Similarly, a low-current 5 VDC digital output from the DAQ board is routed through the test operator's E-stop button, and then into the sensor side of the second SSR. Cutting the power in that circuit by either the DAQ outputting a Digital LOW value (~0V) or the E-stop button breaking the circuit when depressed will open the SSR switch and open the circuit to the solenoid valve.

1.1.2 Software

The device uses several different software packages during MRI testing and several additional software packages for pre- and post-processing. The following sections describe the software's function, design, and usage. It should be noted that the descriptions and images all refer to the code revision used for verification testing, with an LVDT and a load cell as part of the configuration. During testing in the MRI machine, the LVDT and load cell will not be part of the configuration, so the code will be modified only to remove the LVDT and load cell portions from data acquisition, data display, data logging, and data post-processing.

1.1.2.1 Excel (Pre-Processing)

An Excel spreadsheet (Figure 1.10.) is used to determine the input parameters for the Q Programmer software (Section 1.1.2.2) and also to determine settings for the safety system. From the unloaded static MRI scan of the test subject's foot, an unloaded thickness of the plantar fat pad is determined. A literature review (Appendix C) showed that strain in the plantar soft tissue under body weight is approximately 45%. From the patient's unloaded thickness and the desired strain, a total necessary displacement of the loading platen can be determined. That displacement is combined with the cycling rate desired for the experiment and a correction factor (determined during verification testing to account for compliance in the hydraulic tubing and air in the hydraulic fluid) to determine the required displacement of the actuator and master piston.

Q Programmer (Section 1.1.2.2) is capable of one constant acceleration rate, one constant deceleration rate, and a peak velocity for any single actuator displacement. By adjusting these parameters (always holding the deceleration rate to be equal to the acceleration rate), an approximated sine wave is produced. Excel's built-in optimization engine (found under Data/Solver, in Excel 2010) is used to iterate over values for the acceleration/deceleration rate and peak velocity to find a best-fit approximate sine displacement wave. The stepper motor driver has a finite resolution for both parameters, so integer constraints are placed on the two variables adjusted in the optimization (Figure 1.10. , right-hand side). The minimization of the root mean square (RMS) error between the approximated sine wave and a true sine wave of the same frequency and peak amplitude is the objective function of the

optimization. Both the GRG Nonlinear and Evolutionary algorithms are used along with reasonable constraints on the variables and several iterations in order to minimize the RMS error. The values in orange are the parameters that are then fed as inputs to Q Programmer.

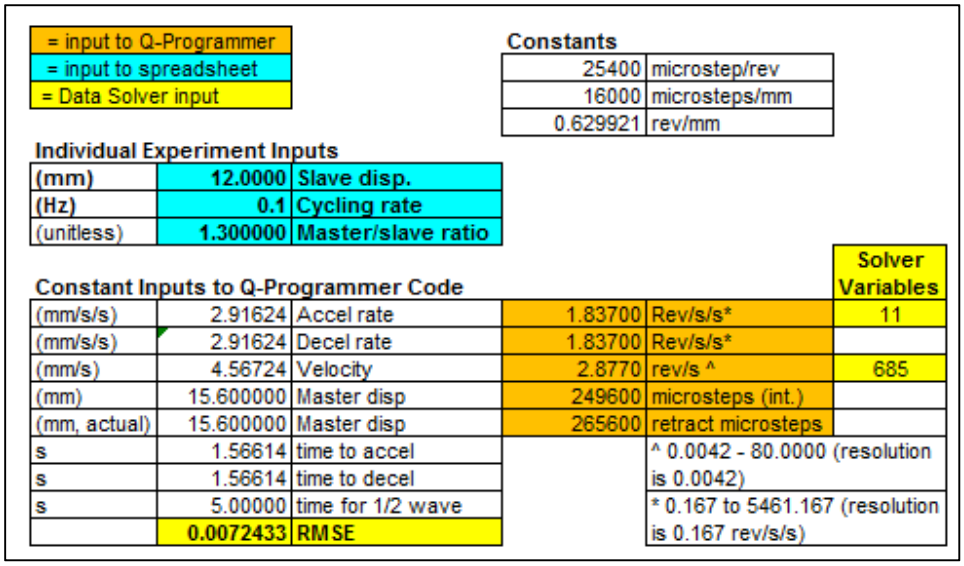

= input to Q-Programmer
= input to spreadsheet
= Data Solver input

Constants

25400	microstep/rev
16000	microsteps/mm
0.629921	rev/mm

Individual Experiment Inputs

(mm)	**12.0000**	**Slave disp.**
(Hz)	**0.1**	**Cycling rate**
(unitless)	**1.300000**	**Master/slave ratio**

Constant Inputs to Q-Programmer Code

					Solver Variables
(mm/s/s)	2.91624	Accel rate	1.83700	Rev/s/s*	11
(mm/s/s)	2.91624	Decel rate	1.83700	Rev/s/s*	
(mm/s)	4.56724	Velocity	2.8770	rev/s ^	685
(mm)	15.600000	Master disp	249600	microsteps (int.)	
(mm, actual)	15.600000	Master disp	265600	retract microsteps	
s	1.56614	time to accel		^ 0.0042 - 80.0000 (resolution is 0.0042)	
s	1.56614	time to decel			
s	5.00000	time for 1/2 wave		* 0.167 to 5461.167 (resolution is 0.167 rev/s/s)	
	0.0072433	**RMSE**			

Figure 1.10. Excel spreadsheet used to obtain Q Programmer stepper motor settings.

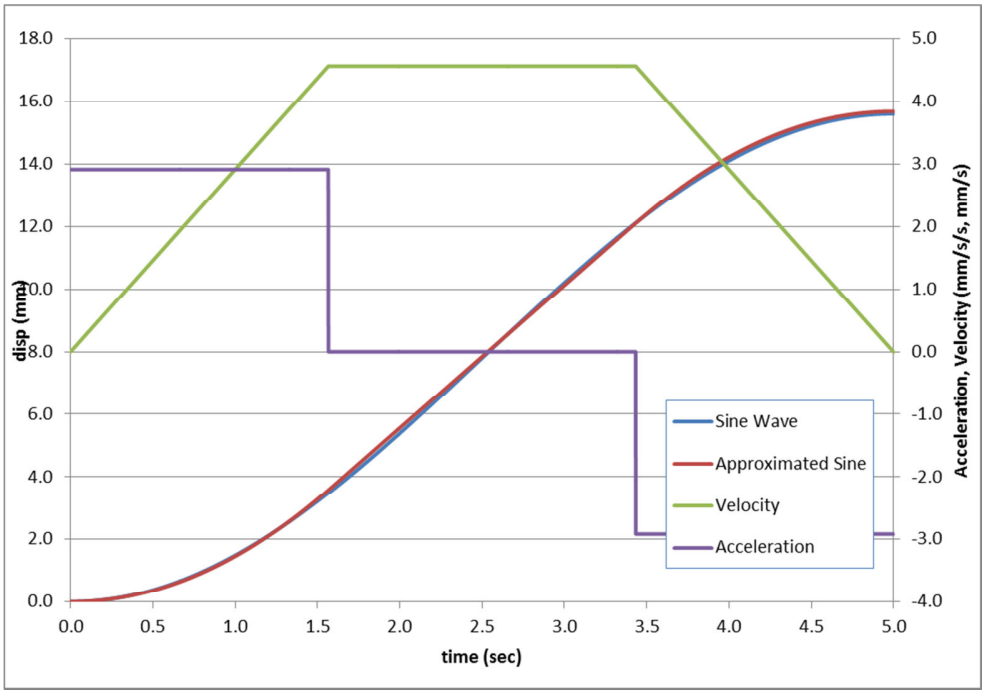

Figure 1.11. Excel spreadsheet plot displaying constant acceleration, peak velocity, and approximate sine wave obtained from both compared to a true sine wave.

An additional feature in the Excel pre-processing worksheet is a simple calculator used to determine appropriate values to use for the patient-specific not-to-exceed pressure and the setting to use for the mechanical pressure relief valve. The not-to-exceed pressure is the subject's body weight factored by 1.2 times and converted to a pressure via the area of the slave cylinder. The factor of 1.2 is just an engineering assumption based off of the pressure overages seen during some faster cycling tests, and knowing that the vertical ground reaction force at heel strike is approximately 1.2 times body weight; this factored pressure should be safe for test subjects. The calculated mechanical pressure relief valve setting has a scaling factor of 1.1, but the value is rounded up to the nearest 25 psi incremental setting on the valve (because the adjustments on the valve are not precise). It isn't envisioned that this device will ever be relied upon for subject safety, so it is set to be just above the solenoid valve not-to-exceed pressure, in order not to release pressure at the peaks of a cycling test or during pressure surges at higher velocity moves.

Safety system settings:	
205	Test Subject body weight (lbf)
1.2	Factor: estimate, based on water hammer, friction
759	**Not-to-Exceed pressure (kPa)**
1.1	Factor (ensure solenoid has chance to act before mechanical valve
150	**Mechanical Pressure Relief Valve Setting (psi)**

Figure 1.12. Subject-specific safety parameters calculator in Excel pre-processing worksheet.

1.1.2.2 Q Programmer

Q Programmer is a stand-alone program provided by Applied Motion Products, (manufacturer of the stepper motor driver) for use in controlling the linear actuator displacements. It allows for semi-complex displacement profiles to be generated and executed by the actuator, along with the ability to adjust many different configuration settings. Programs are stored in text files which are editable in any text editor or in the Q Programmer graphical user interface (GUI). The program files are then downloaded to the stepper motor driver memory through a USB-to-serial device, the program is executed, and if need be, stopped using the GUI. For a full description of the software, and a list of all possible program commands, please see “Host Command Reference: Q and SCL commands for servo and stepper drives” from Applied Motion Products.

Figure 1.13. The Q Programmer GUI with an example cyclic sine displacement wave program loaded and some highlighted areas (Figure 1.13) is discussed below.

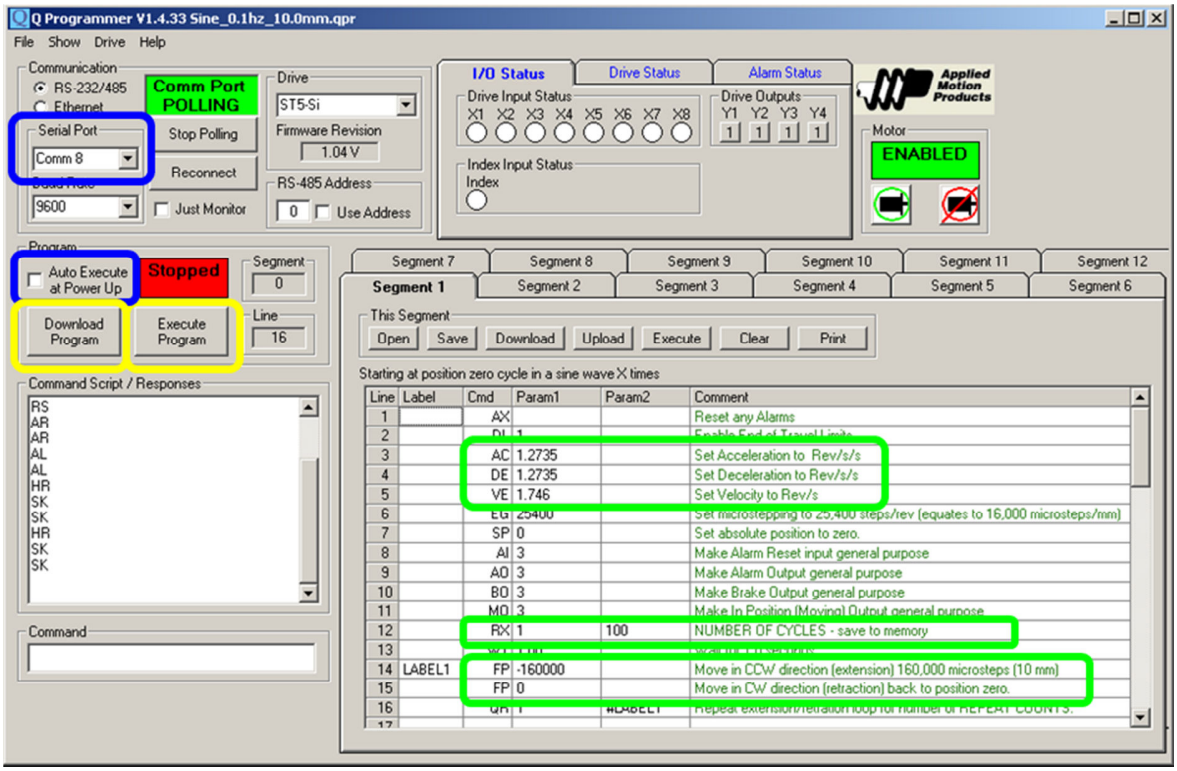

Figure 1.13. Q Programmer GUI with example cyclic, sine displacement wave program loaded.

Highlighted in green are several important parameters for this program. Any sine displacement wave program used during testing will look similar to this one, but with these highlighted fields tailored to the specific displacement amount, cycling rate, and number of cycles to execute. At the top are AC, DE, and VE, which stand for Acceleration, Deceleration, and Velocity. These parameters are in either Revs/second^2 or Revs/second, and are obtained from the pre-processing Excel worksheet described above. The next highlighted parameter is RX. This is the number of times the commands below it will be repeated. The last highlighted box shows FP -160000 and FP 0. FP stands for Feed to Position. In line 7 of the code, SP 0 sets the position at whatever point the actuator is currently located to Absolute position zero. Feed to Position -160,000 tells the actuator to displace 160,000 microsteps (16,000 microsteps / mm of displacement for the device) or 10mm in the CCW (extension) direction.

Highlighted in blue are two selections to take note of. If the USB-to-serial adaptor is plugged into the proper USB port on the laptop and is connected before the laptop is

powered-on, Q Programmer should locate the stepper motor driver on Comm port 8 without issue. If that is not the case, the Serial Port option should be changed to Comm port 8, and Q Programmer restarted, after which it should locate the stepper driver. The next blue highlight shows the Auto Execute at Power Up checkbox UNCHECKED. This box should NEVER BE CHECKED, as it sets the actuator to start executing whatever displacement profile is stored in memory as soon as power is supplied to the driver. If this was unexpected, it could be dangerous. If the device begins auto-executing upon power-on, type the command "PM" into the Command Script/Responses box and press Enter. If it returns “PM=7”, the drive is set to auto-execute the stored Q program. Type “PM=2” into the Command Script/Responses box and press Enter, then type “PM” and Enter. This should confirm that PM has been set to PM = 2. You can find more details in the Host Command Reference under the PM command.

Highlighted in yellow are the Download Program and Execute Program buttons. As mentioned above, the program is first downloaded into the stepper motor driver’s memory. After the program is downloaded, a dialog box pops up alerting the user that it completed successfully. Clicking OK dismisses the popup, after which the Execute Program button is used to commence movement of the actuator.

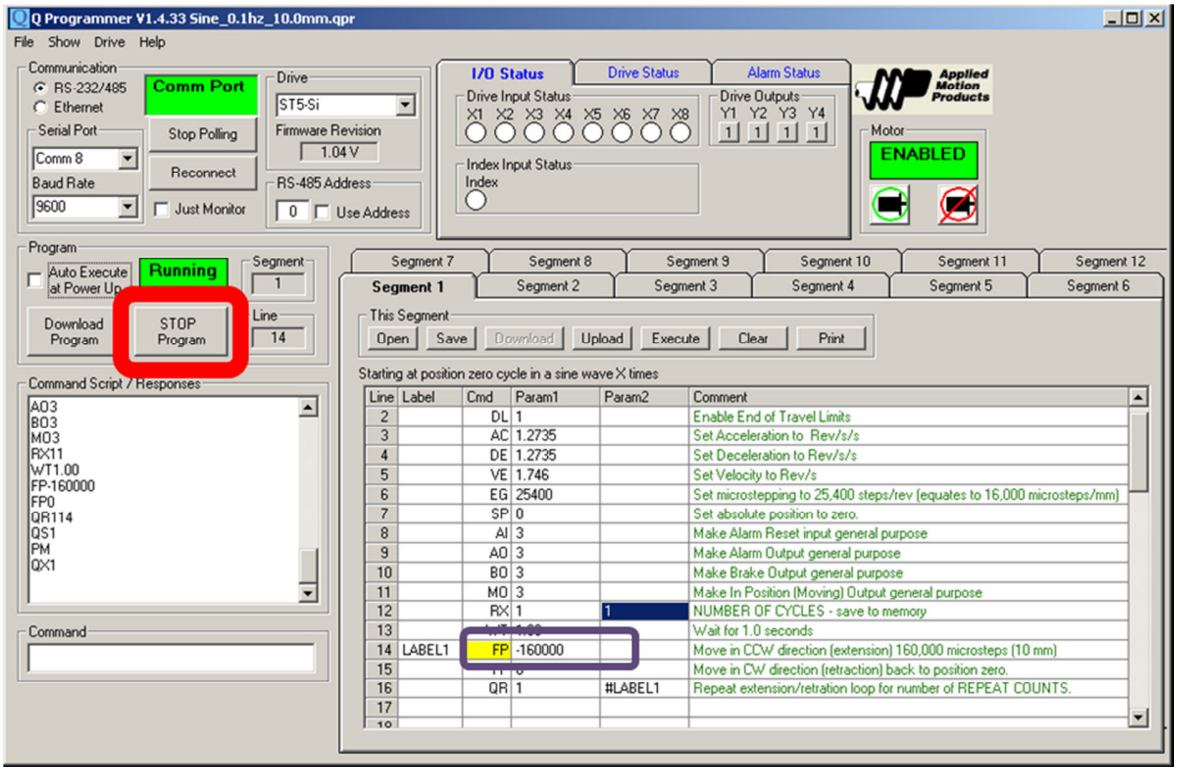

Figure 1.14. Q Programmer GUI while actuator is displacing. Stop button highlighted in red.

The Q Programmer GUI during actuator movement (Figure 1.14. is discussed next. The yellow cell highlighted in a purple box is the program line item that is currently being executed.

Highlighted in red is the STOP Program button, which will freeze the actuator in its displacement profile wherever it may be at the time the button is clicked. It is because of this fact that this button is NOT the button to press in an emergency situation during human testing. If the load on the foot of the test subject is painful, pressing this button would effectively hold the pressure at whatever level it is currently at, and not reduce the pressure on the foot. Pressure is only released by removing power to the solenoid valve (near-instantaneous) or by loading a different program into Q Programmer, downloading it to the drive, and then executing it to retract the actuator. Obviously, this would take drastically longer than using an E-stop button to release the pressure.

1.1.2.3 Master LabVIEW VI

All software tasks involved in operating the device besides the driving of the linear actuator are performed in the Master LabVIEW VI (Virtual Instrument, the LabVIEW file extension). The Master VI is responsible for all of the following:

- Acquiring, converting (using calibration tables), displaying and recording to a datafile the signals from:
    - the rotary encoder attached to the stepper motor that drives the linear actuator
    - the pressure transducer used to determine the force upon the foot during testing
    - the LVDT used to determine the displacement of the slave piston and loading platen during verification testing
    - the load cell used to determine the actual force generated by the loading platen during verification testing
- Detecting the initial movement of the linear actuator in order to synchronize the generation of the MRI trigger signal
- Generating and sending via RS-232 serial connection the messages to the MRI Control and Data Acquisition System (CDAS). These messages trigger the gated MRI along with sending required periodic status messages to the CDAS.
- Comparing the pressure in the hydraulic system to the not-to-exceed pressure set for each individual test
- Removing power from the solenoid valve circuit if the not-to-exceed pressure is exceeded
- Generating +/- 10 VDC signals used to power the supply rails of the op-amp used to actively filter sensor signals
- Providing a user interface panel from which the test operator can adjust device parameters, start and stop data collection, visualize the state of the sensor data, and release pressure from the system in an emergency situation

The software follows a multi-loop producer/consumer architecture, implemented using Classic State Machines. This is a popular LabVIEW architectural format outlined very

clearly in Blume (2007). This particular architecture was chosen over others for its applicability to the serial flow through different states of the device (Initialize, Start, Read Data, Shut-Down, etc.), for its clean look and ease of readability for future users of the code, and for the efficiency that can be realized from it. Several tasks of the code are time-critical (especially generation of the MRI trigger signal and acquisition of all sensor data) and must be given priority in the execution of the code. Producer/consumer loops allow for the producer loop (generally the more time-critical of two tasks involving acquired data) to run at a higher frequency and enqueue the data to then be used at a later time by a less-critical, lower frequency consumer loop (generally something like data logging or data display).

The front panel (Figure 1.15.) features experiment-specific settings for the not-to-exceed pressure and data file name, in addition to graphical and numerical displays of the various sensor readings. There are also several user-input buttons/switches, including a large, red emergency pressure release button. Finally, in the device settings view (Figure 1.16), specific parameters that don't generally require changing are set, such as DAQ board channel wiring, data collection rate, and PPU signal parameters.

The laptop used for the device is a Dell, Intel Pentium M, 1.6 GHz PC running Windows XP. Since Windows is a non-deterministic operating system, maintaining accurate task completion down to a several millisecond precision can be challenging, if not impossible. The documentation regarding the MRI signal stated that a message needed to be sent every 2 milliseconds to the CDAS, with only a small margin for late or dropped messages. To ensure the MRI triggering was properly synced to the displacement of the loading platen, great care was taken to optimize the laptop hardware, software, and LabVIEW code in order to meet the time-critical messaging scheme. Several online LabVIEW forums have posts on improving the execution speed and reliability of LabVIEW on a non-real time operating system. The following is a list of steps taken (based on De Clue, 2002):

Hardware:

- The laptop was "flattened" (Windows XP re-installed over a formatted hard disc) to remove all traces of old software from the machine.

- The RAM of the computer was increased from 512 MB to 2 GB, the maximum the motherboard was capable of using.

General software:

- Windows was set to optimize background services to ensure that LabVIEW background threads were not de-prioritized.
- Windows indexing services were stopped, as this process might use CPU clock cycles at inopportune moments.
- The anti-virus program on the laptop was removed. At the very least, it should be ensured that the anti-virus program is not allowed to run while critical LabVIEW code is operating. Since it was impossible to completely disable the anti-virus used on the laptop, and since the machine is not ever connected to the internet, the program was completely removed to ensure it would not disrupt LabVIEW's execution.

LabVIEW software:

- LabVIEW's priority in Task Manager was permanently raised to High by creating a shortcut to the labview.exe file with a target of "C:\WINDOW\system32\cmd.exe /c start /high labview.exe". Starting the program via this shortcut is equivalent to starting it as usual and then going into Task Manager via Ctrl+Alt+Delete, and choosing Set Priority and High. Setting the priority to High ensures that the LabVIEW CPU requests will out-prioritize those of any other non-Windows program that might be running at the Normal priority level. Setting the priority to Realtime (the highest priority) might "lock up" the computer, as Windows-based tasks critical to system operation (such as interrupt service routines) might not have an opportunity to use the CPU due to LabVIEW dominating it.
- The most time-critical VI, the PPU signal generation loop, was created as a subVI inside of the Master VI. This was done because every subVI can have its execution priority set separately in its properties field. This execution priority determines how the parallel-threads inside of a running LabVIEW program are prioritized during execution. The PPU Signal Generation Loop subVI was given a priority of "Time Critical" (the highest priority). Additionally, a Timed Loop was used for the code inside the subVI, instead of a standard

While Loop, as the rest of the code uses. In testing, these steps were the only way found to ensure a precise 2 millisecond interval between subsequent PPU messages.

- Tasks in the code were separated based upon their functionality. Time-critical tasks were whittled down to be as small and efficient as possible, with no extraneous code to hold-up the entire loop.
- All loops contain a Wait (milliseconds) VI. The various loops used within the Master VI are prioritized by the LabVIEW compiler based on each loop's Wait VI, with those having a smaller wait time out-prioritizing those with a larger wait time.
- Data is logged to LabVIEW-specific binary file formats (.TDMS and Datalog). This drastically decreases the time taken to record data as compared to logging it to a text file or Excel spreadsheet file in ASCII format. After the testing has completed, these binary data files can be converted to more "human-friendly" ASCII file formats.
- The Front Panel (LabVIEW's user interface) is set to update via its own, low-priority loop. Data that is collected at 2500 Hz is updated on the front panel once every 100 milliseconds. The human eye cannot easily detect occurrences much faster than this, so updating graphs and numerical displays any more frequently is wasted. Similarly, user-inputs such as button clicks don't occur much faster than this, either, so checking for user-inputs can also be put in a low-priority loop.
- The LabVIEW profiler was used to identify parts of the code that were being called frequently and/or that were using a large amount of CPU time when called. From this, I learned that the Moving Average VIs that I was using to digitally smooth noisy data were slowing down the code execution. These VIs are now disabled once the actuator starts moving, as their usefulness then is trivial anyway.
- Once all aspects of the VI were working appropriately, the Enable Debugging setting in each VI was disabled. This speeds execution up, but eliminates the ability to debug using dataflow, probes, and other debug techniques specific to LabVIEW.

Following are figures of the LabVIEW Master VI code in its entirety, the individual block diagram loops responsible for various tasks (marked with a letter identifier), the comments embedded in the code, and finally, the various subVIs used within the Master VI.

These figures were taken from "Master_rev_17f.vi".

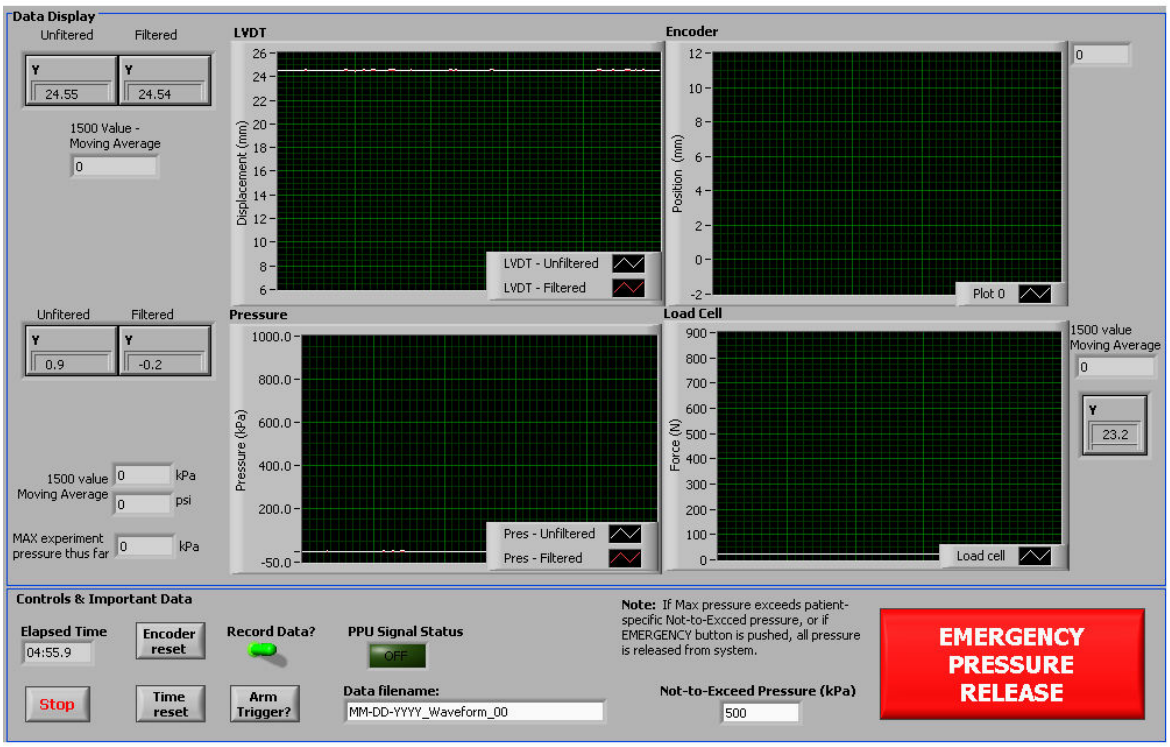

Figure 1.15. LabVIEW Master VI front panel, main view

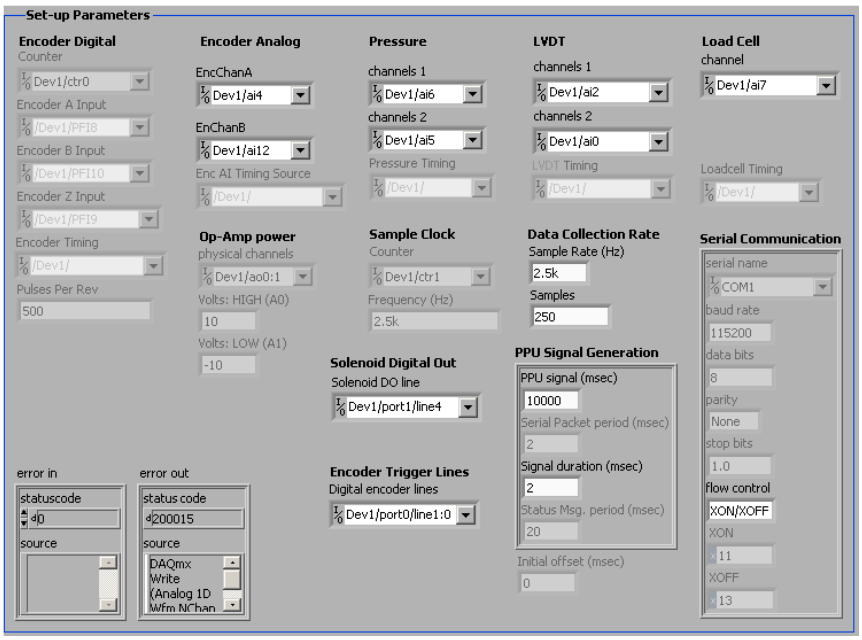

Figure 1.16. LabVIEW Master VI front panel, device settings view

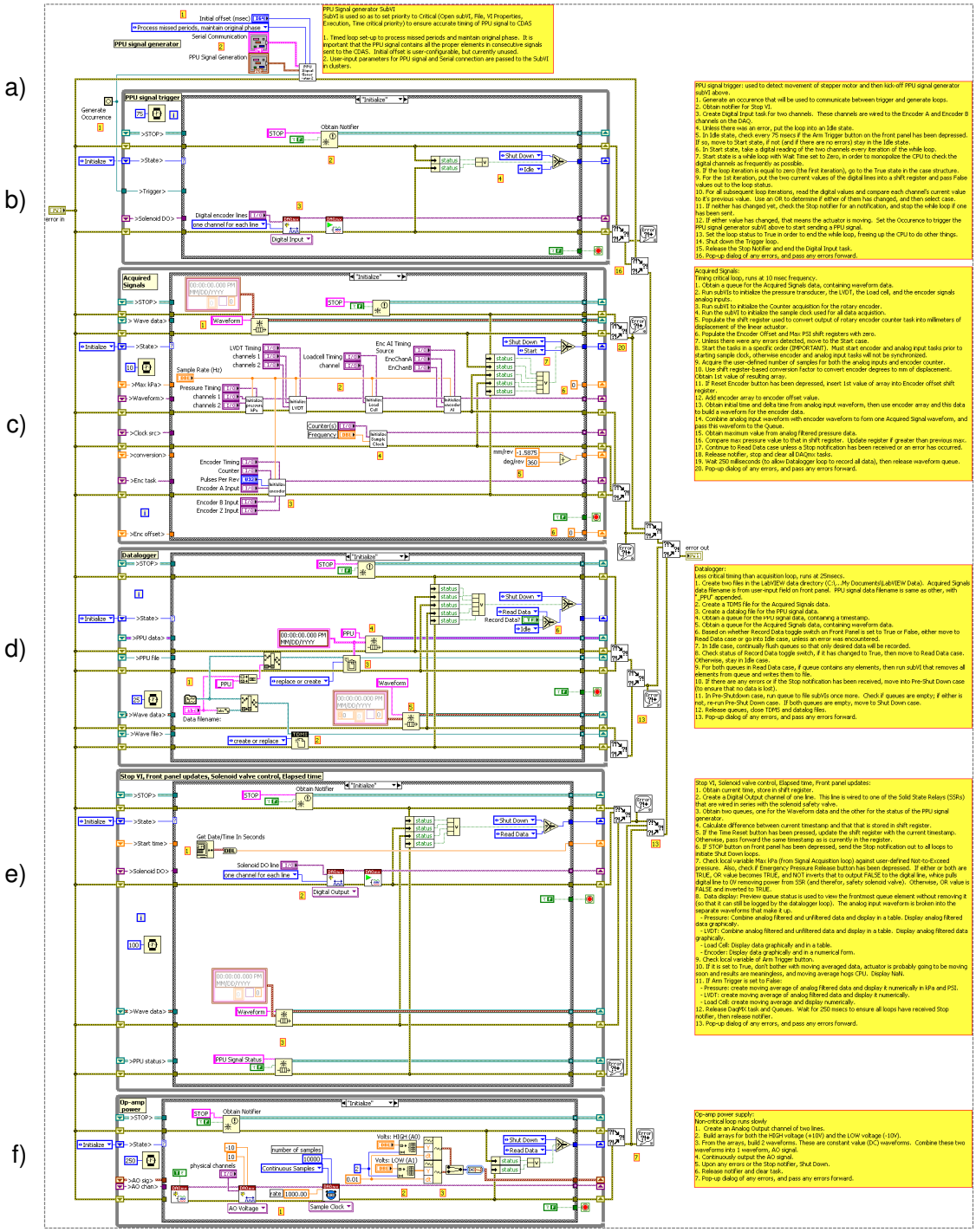

Figure 1.17. LabVIEW Master VI block diagram with individual loops labeled (a-f)

a) PPU Signal Generator

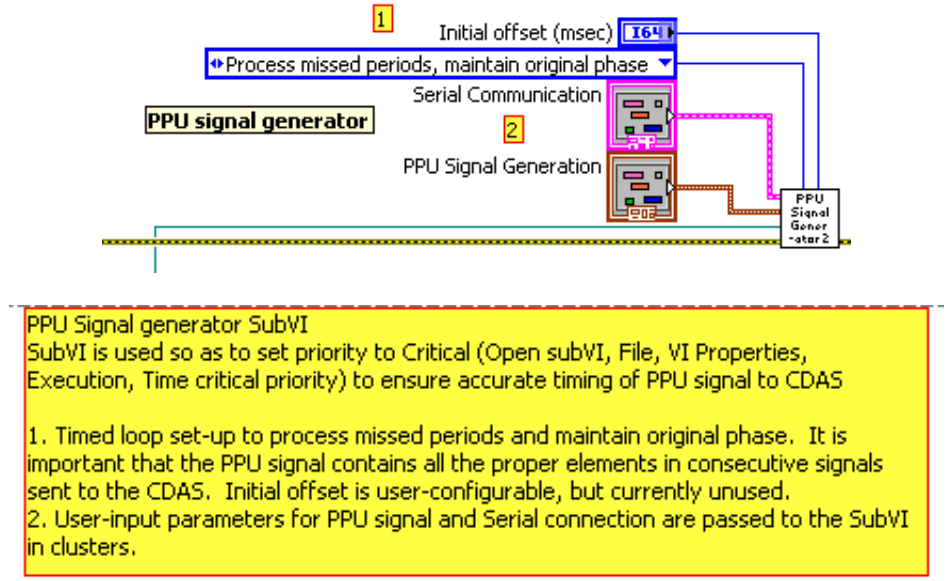

Figure 1.18. PPU Signal Generator subVI and code comments

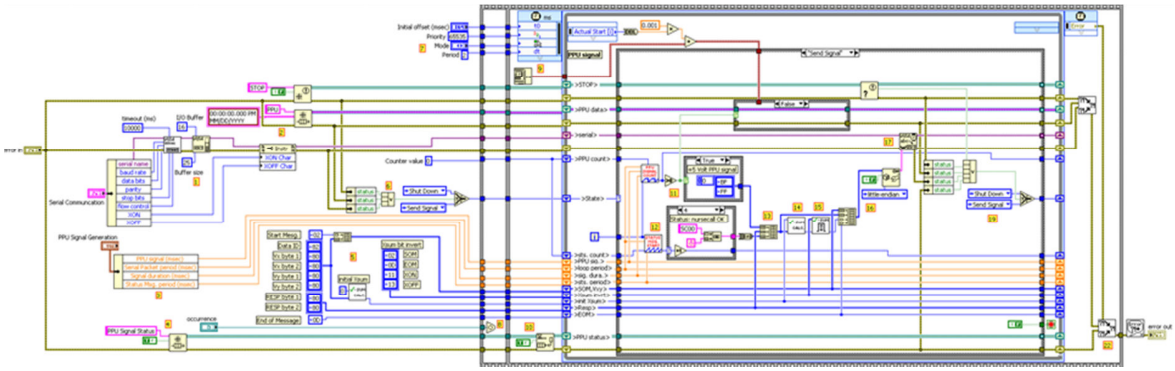

Figure 1.19. PPU Signal Generator subVI expanded, entire VI view

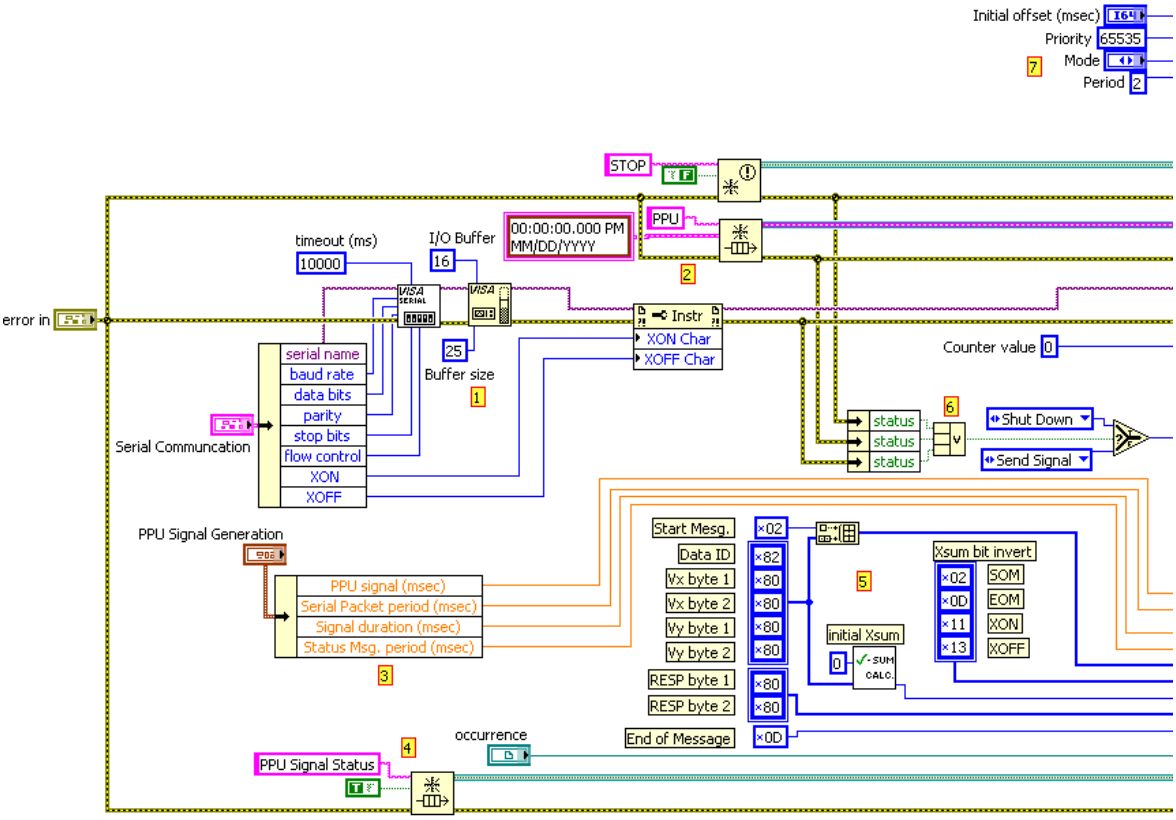

Figure 1.20. Left-hand side zoom of Figure 1.19

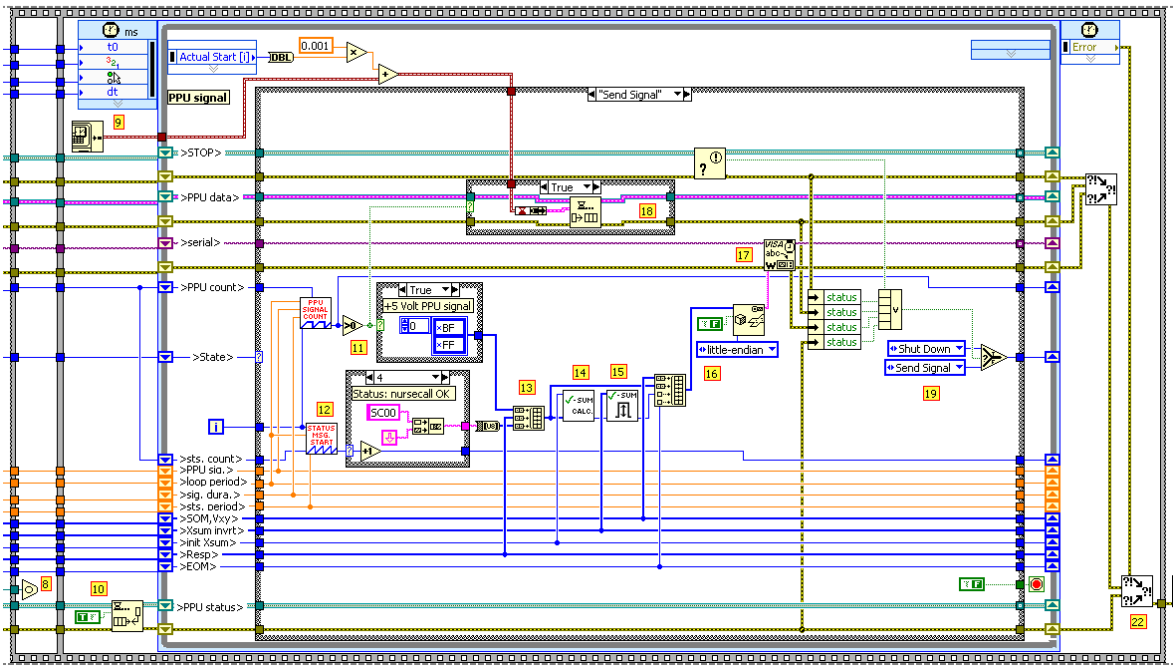

Figure 1.21. Right-hand side zoom of Figure 1.19

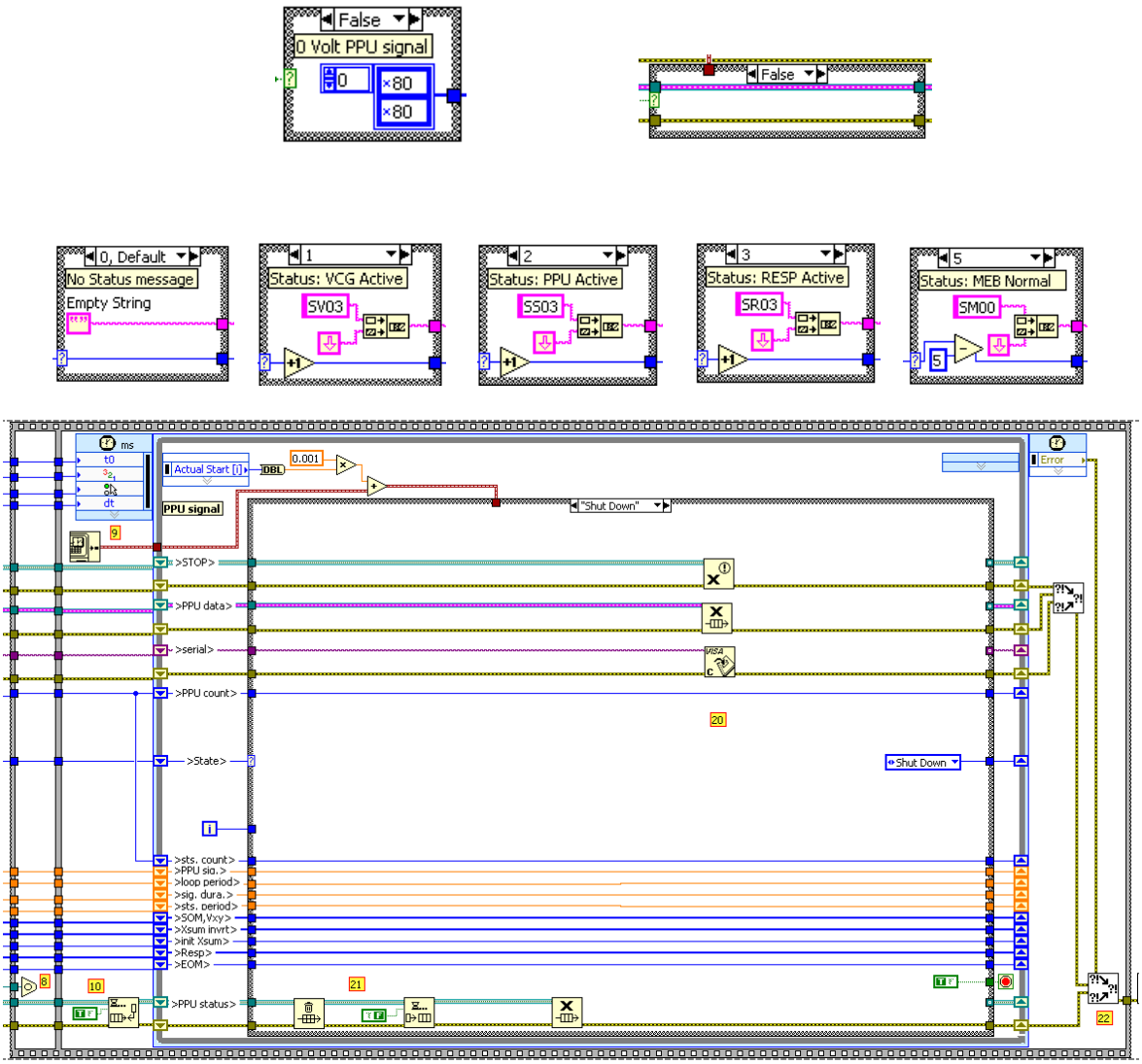

Figure 1.22. Alternate case structures from portion of VI shown in Figure 1.21.

PPU signal: (based on information packet from Philips Corporation)
Timing critical loop, runs at 2 msec period.

1. Initialize RS-232 serial connection.
2. Obtain a queue for the PPU signal data, and a notification for the Stop notifier.
3. Populate shift registers with components of user-defined PPU signal parameters.
4. Create queue to show LED indicator on main.vi front panel when PPU signal is actively being sent.
5. Populate shift registers with individual components of CDAS-expected signal.
6. Unless there was an error in the setup, proceed to the sequence with a state of Send Singal.
7. Initialize timed-loop parameters.
8. Wait on Occurence coming from Trigger loop (inside of Main VI). Proceed to 2nd frame of sequence after it's received.
9. Obtain initial timestamp.
10. Input True value into PPU Signal status queue to change front panel LED to TRUE.
11. Keep track of number of loop iterations that have passed. Based on user-input parameters for PPU signal, generate a HI or LO PPU signal to add to signal.
12. Keep track of number of loop iterations that have passed. Based on requirements of CDAS, generate one of 5 status messages or no status message to add to signal.
13. Combine PPU signal, RESP message (constant), and Status messages.
14. Perform checksum of values.
15. If the previously generated checksum value is equal to a start/end of message, or bit-flow value, then the checksum value is bitwise inverted. Otherwise, it is passed on as-is.
16. Messages and checksum are combined into one serial signal.
17. Serial signal is sent to CDAS via COM port.
18. Timestamp added to PPU queue only when PPU signal is high (cuts down on I/O operations, as only 1 signal out of every 10,000 is High (for 0.1 Hz loading rate).
19. Unless Stop notification has been received or some VI encounters an error, continue to next Send Signal case.
20. Serial connection is closed, notifier is released, PPU queue is released.
21. Empty the PPU signal status queue and put a false value in.
22. Pop-up dialog of any errors, and pass any errors forward.

Figure 1.23. Code comments corresponding to PPU Signal Generator subVI

b) PPU Signal Trigger

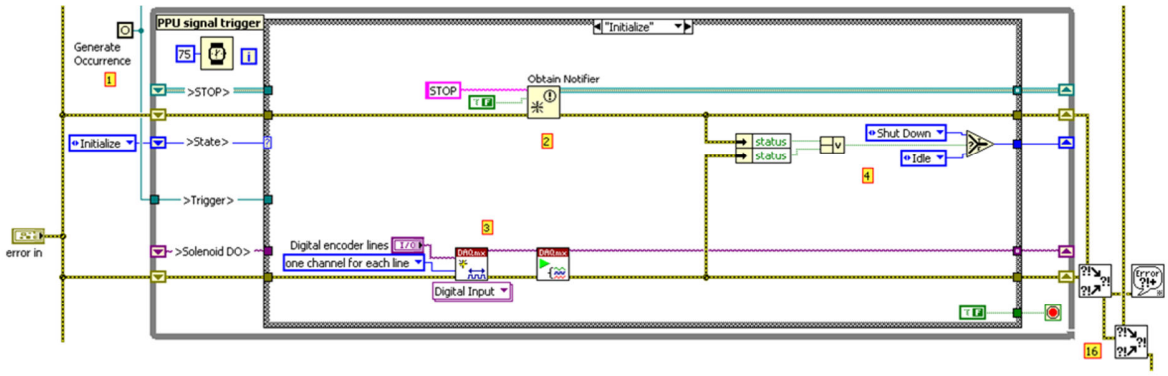

Figure 1.24. PPU Signal Trigger VI, entire view

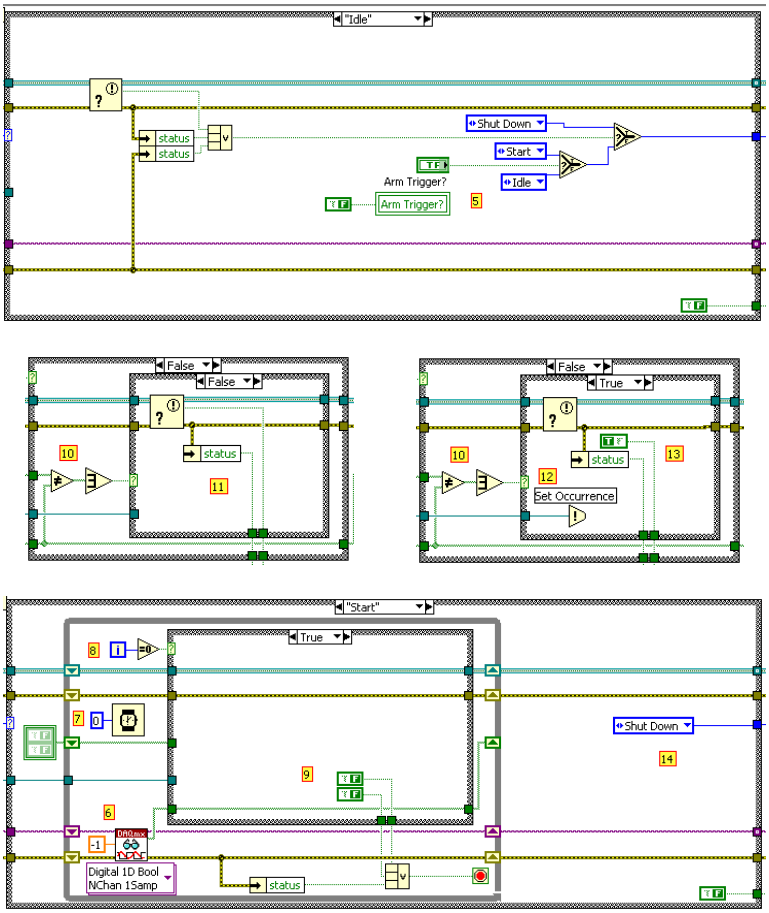

Figure 1.25. Alternate case structures for VI shown in Figure 1.24.

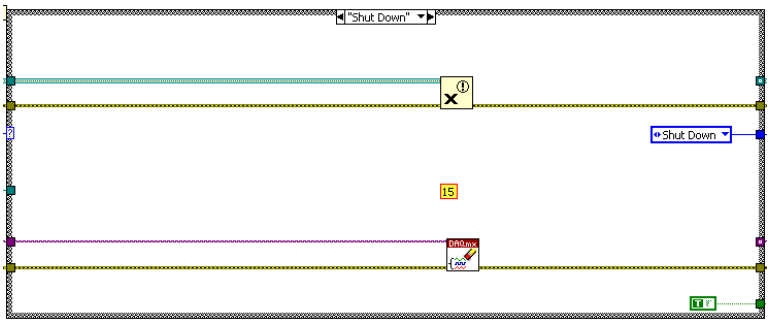

Figure 1.26. Additional case structure for VI shown in Figure 1.24.

PPU signal trigger: used to detect movement of stepper motor and then kick-off PPU signal generator subVI above.
1. Generate an occurence that will be used to communicate between trigger and generate loops.
2. Obtain notifier for Stop VI.
3. Create Digital Input task for two channels. These channels are wired to the Encoder A and Encoder B channels on the DAQ.
4. Unless there was an error, put the loop into an Idle state.
5. In Idle state, check every 75 msecs if the Arm Trigger button on the front panel has been depressed. If so, move to Start state, if not (and if there are no errors) stay in the Idle state.
6. In Start state, take a digital reading of the two channels every iteration of the while loop.
7. Start state is a while loop with Wait Time set to Zero, in order to monopolize the CPU to check the digital channels as frequently as possible.
8. If the loop iteration is equal to zero (the first iteration), go to the True state in the case structure.
9. For the 1st iteration, put the two current values of the digital lines into a shift register and pass False values out to the loop status.
10. For all subsequent loop iterations, read the digital values and compare each channel's current value to it's previous value. Use an OR to determine if either of them has changed, and then select case.
11. If neither has changed yet, check the Stop notifier for an notification, and stop the while loop if one has been sent.
12. If either value has changed, that means the actuator is moving. Set the Occurence to trigger the PPU signal generator subVI above to start sending a PPU signal.
13. Set the loop status to True in order to end the while loop, freeing up the CPU to do other things.
14. Shut down the Trigger loop.
15. Release the Stop Notifier and end the Digital Input task.
16. Pop-up dialog of any errors, and pass any errors forward.

Figure 1.27. Code comments corresponding to PPU Signal Trigger VI

c) Acquired Signals

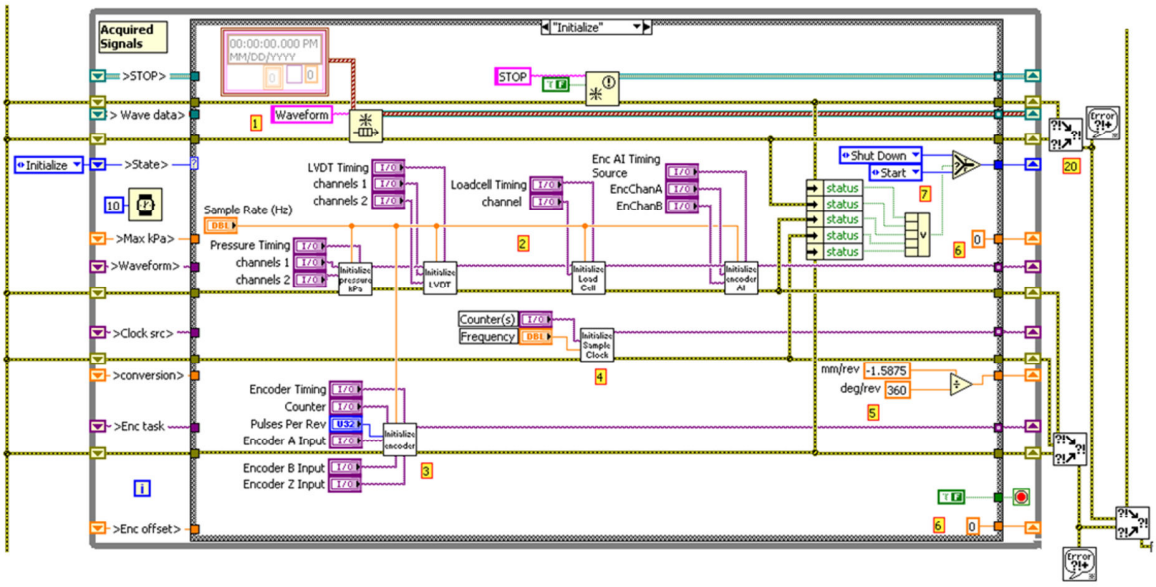

Figure 1.28. Acquired Signals VI, entire view

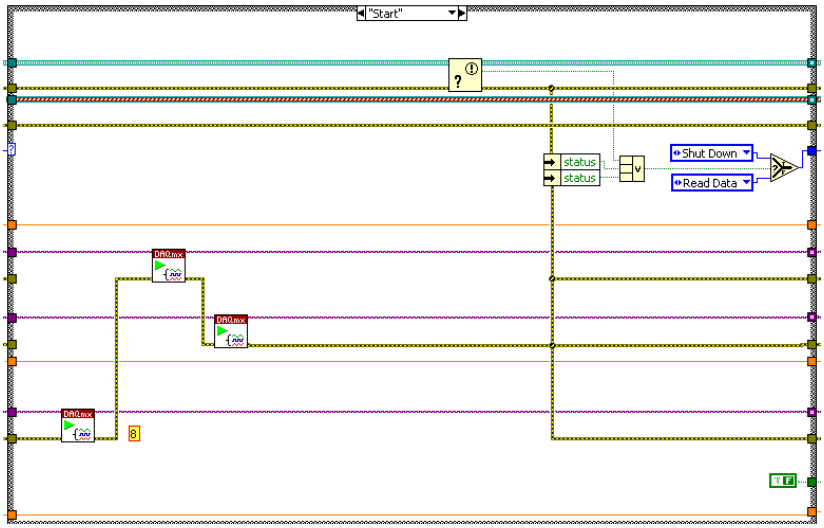

Figure 1.29. Alternate case structure for VI shown above

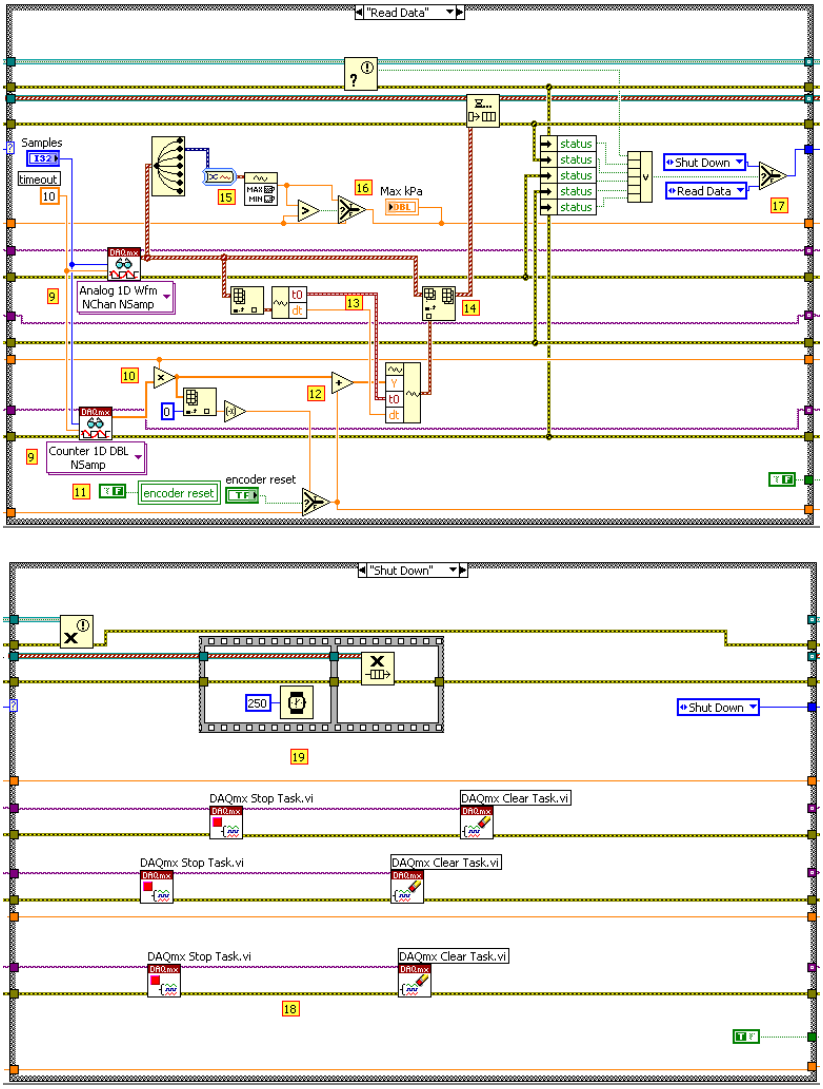

Figure 1.30. Additional case structures for VI shown in Figure 1.28.

Acquired Signals:
Timing critical loop, runs at 10 msec frequency.
1. Obtain a queue for the Acquired Signals data, containing waveform data.
2. Run subVIs to initialize the pressure transducer, the LVDT, the Load cell, and the encoder signals analog inputs.
3. Run subVI to initialize the Counter acquisition for the rotary encoder.
4. Run the subVI to initialize the sample clock used for all data acquistion.
5. Populate the shift register used to convert output of rotary encoder counter task into millimeters of displacement of the linear actuator.
6. Populate the Encoder Offset and Max PSI shift registers with zero.
7. Unless there were any errors detected, move to the Start case.
8. Start the tasks in a specific order (IMPORTANT). Must start encoder and analog input tasks prior to starting sample clock, otherwise encoder and analog input tasks will not be synchronized.
9. Acquire the user-defined number of samples for both the analog inputs and encoder counter.
10. Use shift register-based conversion factor to convert encoder degrees to mm of displacement. Obtain 1st value of resulting array.
11. If Reset Encoder button has been depressed, insert 1st value of array into Encoder offset shift register.
12. Add encoder array to encoder offset value.
13. Obtain initial time and delta time from analog input waveform, then use encoder array and this data to build a waveform for the encoder data.
14. Combine analog input waveform with encoder waveform to form one Acquired Signal waveform, and pass this waveform to the Queue.
15. Obtain maximum value from analog filtered pressure data.
16. Compare max pressure value to that in shift register. Update register if greater than previous max.
17. Continue to Read Data case unless a Stop notification has been received or an error has occurred.
18. Release notifier, stop and clear all DAQmx tasks.
19. Wait 250 milliseconds (to allow Datalogger loop to record all data), then release waveform queue.
20. Pop-up dialog of any errors, and pass any errors forward.

Figure 1.31. Code comments corresponding to Acquired Signals VI

d) Datalogger

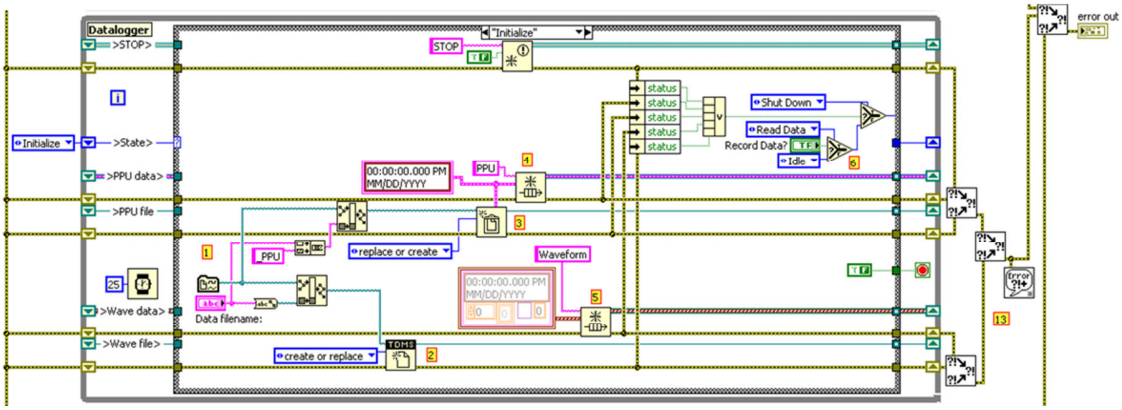

Figure 1.32. Datalogger VI, entire view

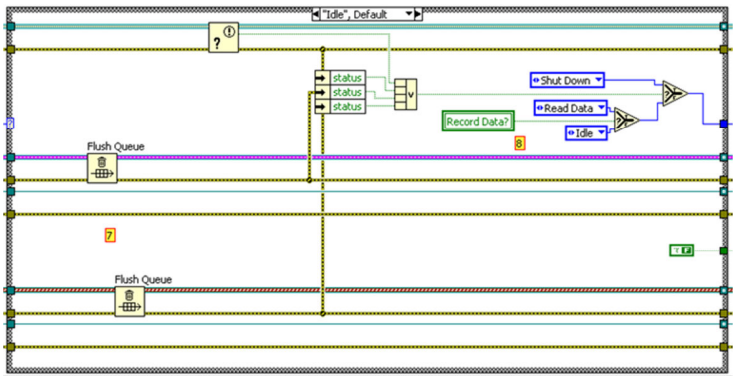

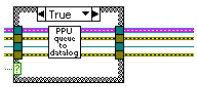

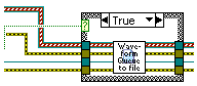

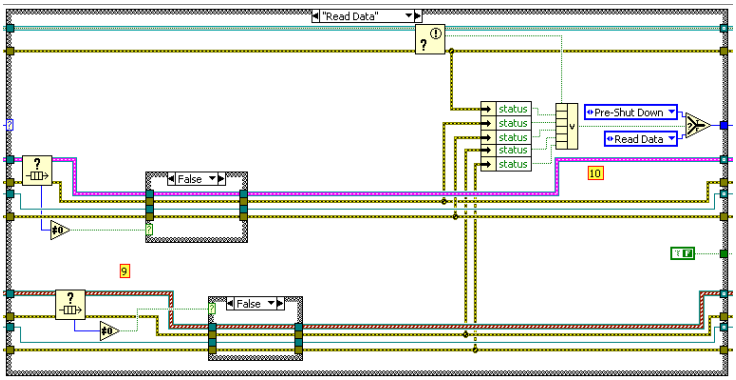

Figure 1.33. Alternate case structures for VI shown in Figure 1.32.

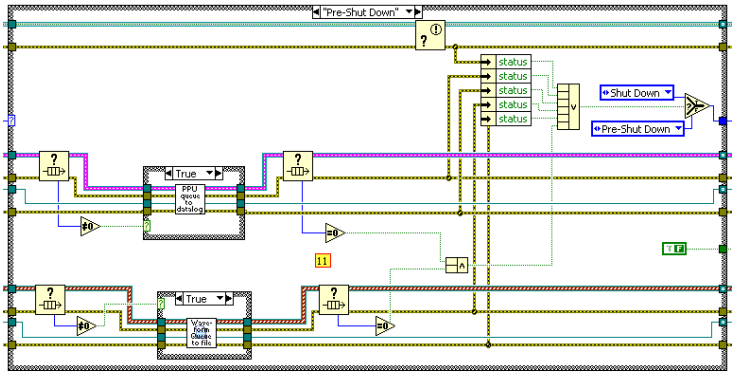

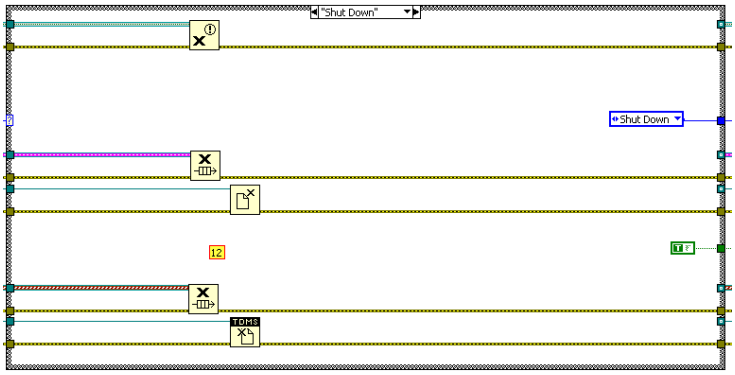

Figure 1.34. Additional case structures for VI shown in Figure 1.32. .

Datalogger:
Less critical timing than acquisition loop, runs at 25msecs.
1. Create two files in the LabVIEW data directory (C:\...My Documents\LabVIEW Data). Acquired Signals data filename is from user-input field on front panel. PPU signal data filename is same as other, with "_PPU" appended.
2. Create a TDMS file for the Acquired Signals data.
3. Create a datalog file for the PPU signal data.
4. Obtain a queue for the PPU signal data, containing a timestamp.
5. Obtain a queue for the Acquired Signals data, containing waveform data.
6. Based on whether Record Data toggle switch on Front Panel is set to True or False, either move to Read Data case or go into Idle case, unless an error was encountered.
7. In Idle case, continually flush queues so that only desired data will be recorded.
8. Check status of Record Data toggle switch, if it has changed to True, then move to Read Data case. Otherwise, stay in Idle case.
9. For both queues in Read Data case, if queue contains any elements, then run subVI that removes all elements from queue and writes them to file.
10. If there are any errors or if the Stop notification has been received, move into Pre-Shut Down case (to ensure that no data is lost).
11. In Pre-Shutdown case, run queue to file subVIs once more. Check if queues are empty; if either is not, re-run Pre-Shut Down case. If both queues are empty, move to Shut Down case.
12. Release queues, close TDMS and datalog files.
13. Pop-up dialog of any errors, and pass any errors forward.

Figure 1.35. Code comments corresponding to Datalogger VI

e) Stop VI, Front Panel updates, and Solenoid control

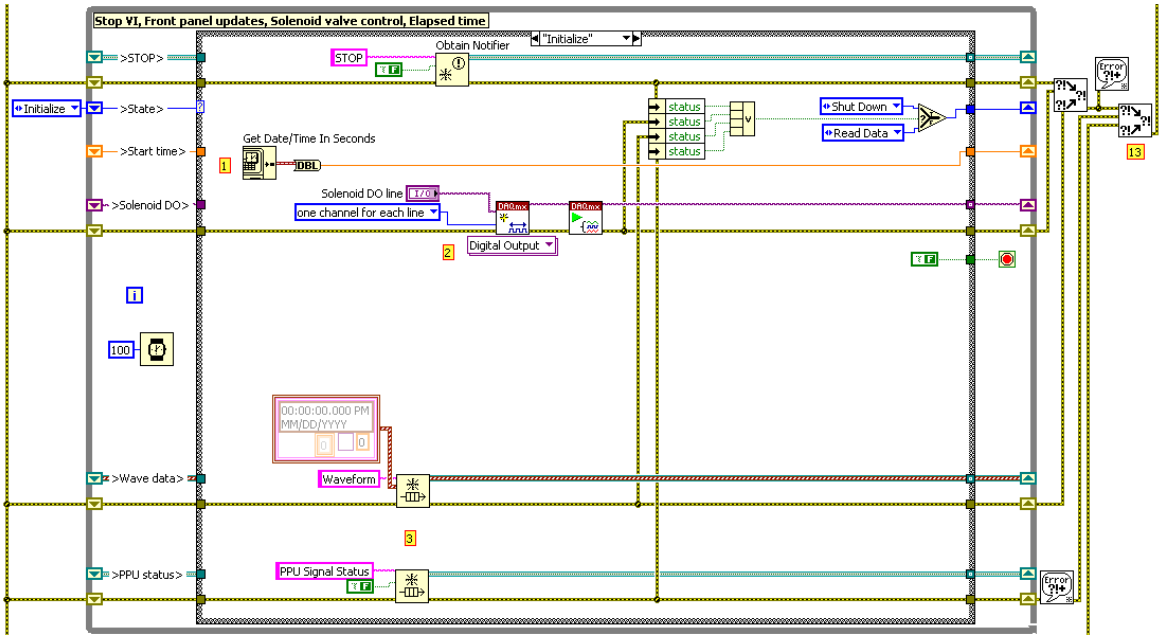

Figure 1.36. Stop VI, Front Panel updates and Solenoid Control VI

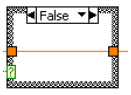

Figure 1.37. Alternate case structures for VI shown in Figure 1.36.

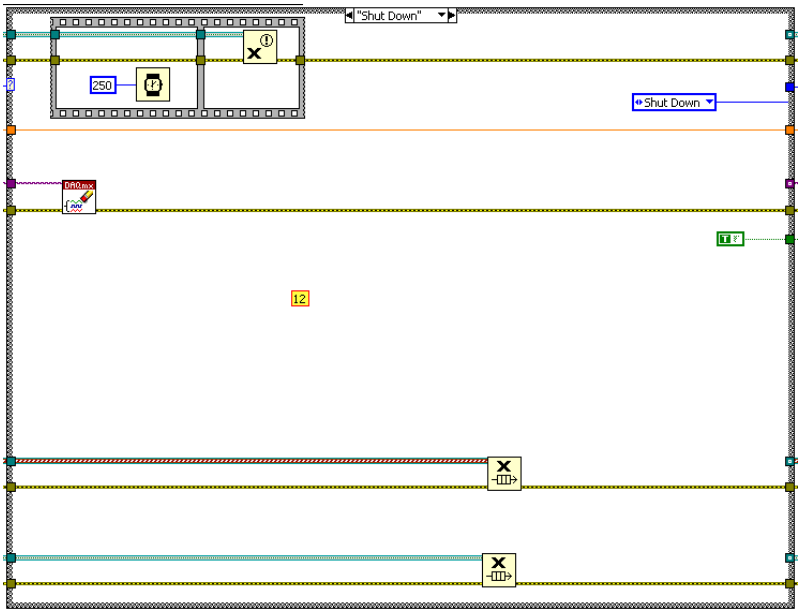

Figure 1.38. Alternate case structure for VI shown in Figure 1.36.

Stop VI, Solenoid valve control, Elapsed time, Front panel updates:
1. Obtain current time, store in shift register.
2. Create a Digital Output channel of one line. This line is wired to one of the Solid State Relays (SSRs) that are wired in series with the solenoid safety valve.
3. Obtain two queues, one for the Waveform data and the other for the status of the PPU signal generator.
4. Calculate difference between current timestamp and that that is stored in shift register.
5. If the Time Reset button has been pressed, update the shift register with the current timestamp. Otherwise, pass forward the same timestamp as is currently in the register.
6. If STOP button on front panel has been depressed, send the Stop notification out to all loops to initiate Shut Down loops.
7. Check local variable Max kPa (from Signal Acquisition loop) against user-defined Not-to-Exceed pressure. Also, check if Emergency Pressure Release button has been depressed. If either or both are TRUE, OR value becomes TRUE, and NOT inverts that to output FALSE to the digital line, whice pulls digital line to 0V removing power from SSR (and therefor, safety solenoid valve). Otherwise, OR value is FALSE and inverted to TRUE.
8. Data display: Preview queue status is used to view the frontmost queue element without removing it (so that it can still be logged by the datalogger loop). The analog input waveform is broken into the separate waveforms that make it up.
- Pressure: Combine analog filtered and unfiltered data and display in a table. Display analog filtered data graphically.
- LVDT: Combine analog filtered and unfiltered data and display in a table. Display analog filtered data graphically.
- Load Cell: Display data graphically and in a table.
- Encoder: Display data graphically and in a numerical form.
9. Check local variable of Arm Trigger button.
10. If it is set to True, don't bother with moving averaged data, actuator is probably going to be moving soon and results are meaningless, and moving average hogs CPU. Display NaN.
11. If Arm Trigger is set to False:
- Pressure: create moving average of analog filtered data and display it numerically in kPa and PSI.
- LVDT: create moving average of analog filtered data and display it numerically.
- Load Cell: create moving average and display numerically.
12. Release DaqMX task and Queues. Wait for 250 msecs to ensure all loops have received Stop notifier, then release notifier.
13. Pop-up dialog of any errors, and pass any errors forward.

Figure 1.39. Code comments corresponding to Stop VI, Front Panel and Solenoid control VI

f) Op-amp power supply

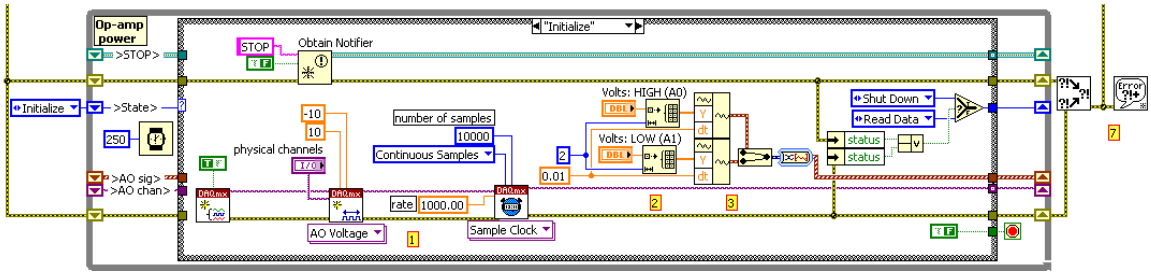

Figure 1.40. Op-amp power supply VI, entire view

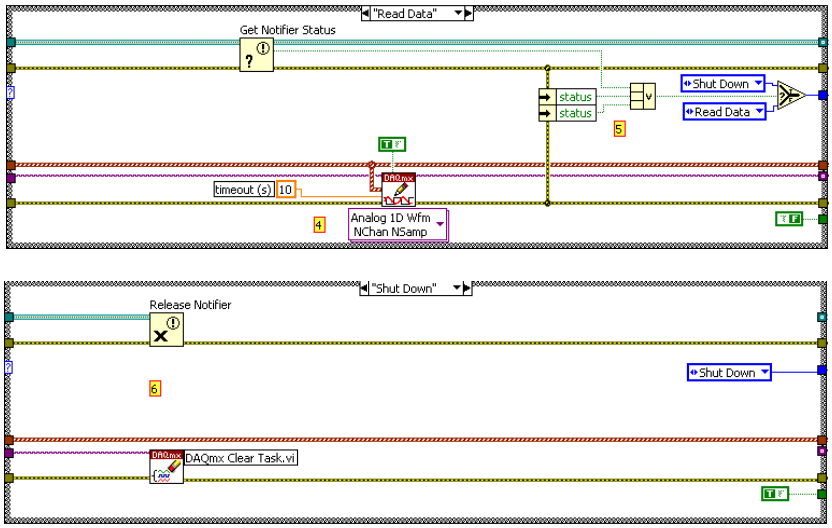

Figure 1.41. Alternate case structures for VI shown in Figure 1.40.

Op-amp power supply:
Non-critical loop runs slowly
1. Create an Analog Output channel of two lines.
2. Build arrays for both the HIGH voltage (+10V) and the LOW voltage (-10V).
3. From the arrays, build 2 waveforms. These are constant value (DC) waveforms. Combine these two waveforms into 1 waveform, AO signal.
4. Continuously output the AO signal.
5. Upon any errors or the Stop notifier, Shut Down.
6. Release notifier and clear task.
7. Pop-up dialog of any errors, and pass any errors forward.

Figure 1.42. Code comments corresponding Op-amp Power Supply VI

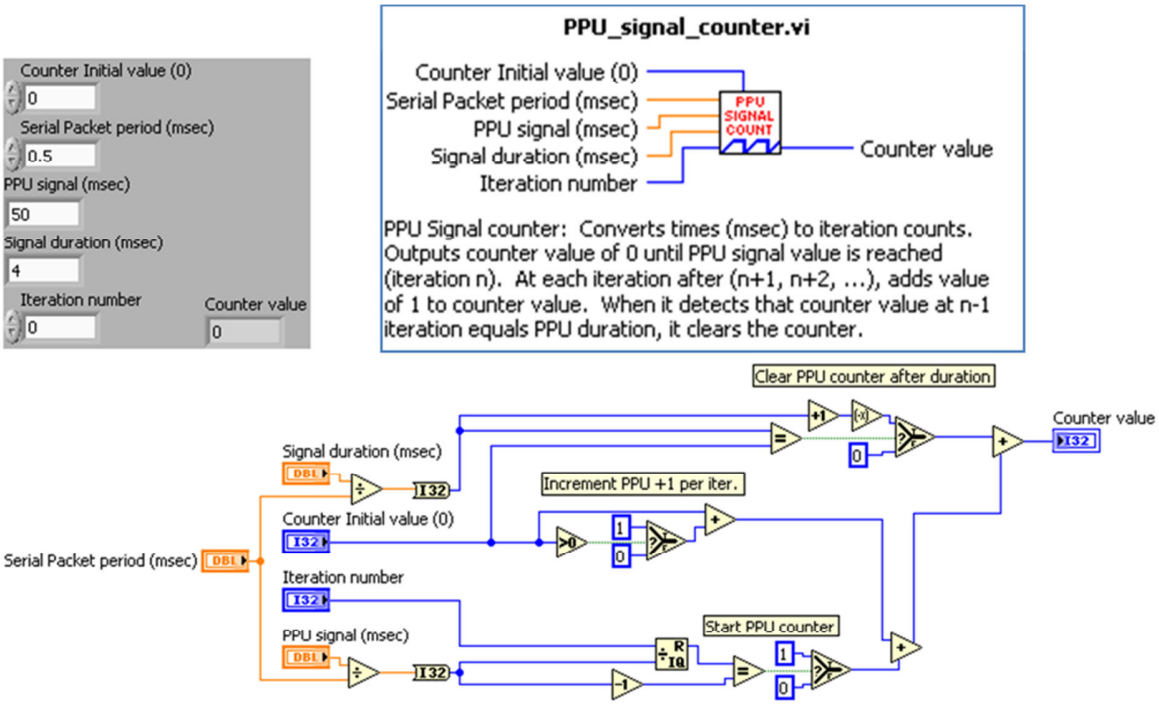

Figure 1.43. PPU Signal Counter subVI block diagram, front panel, and VI properties

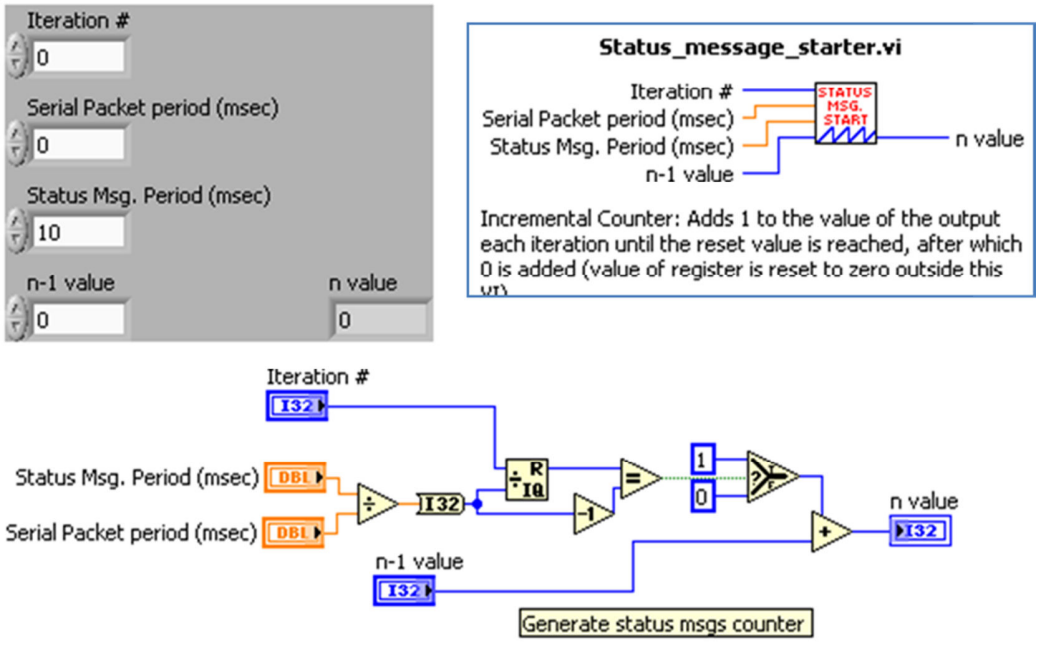

Figure 1.44. PPU Status Message Starter subVI block diagram, front panel, and VI properties

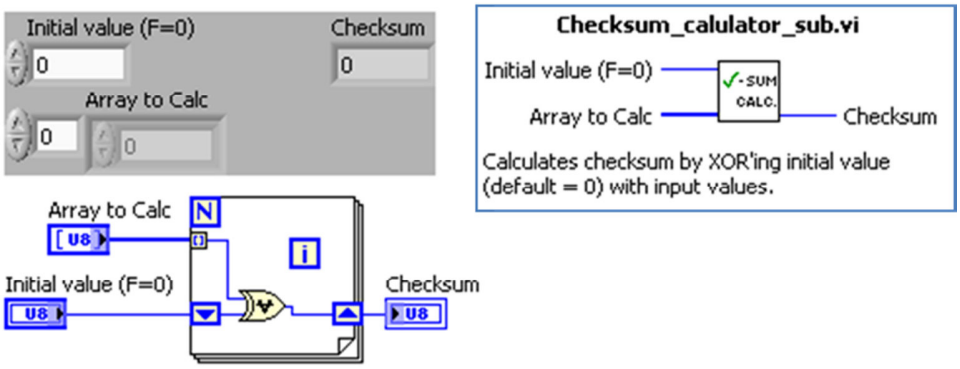

Figure 1.45. Checksum Calculator subVI block diagram, front panel, and VI properties

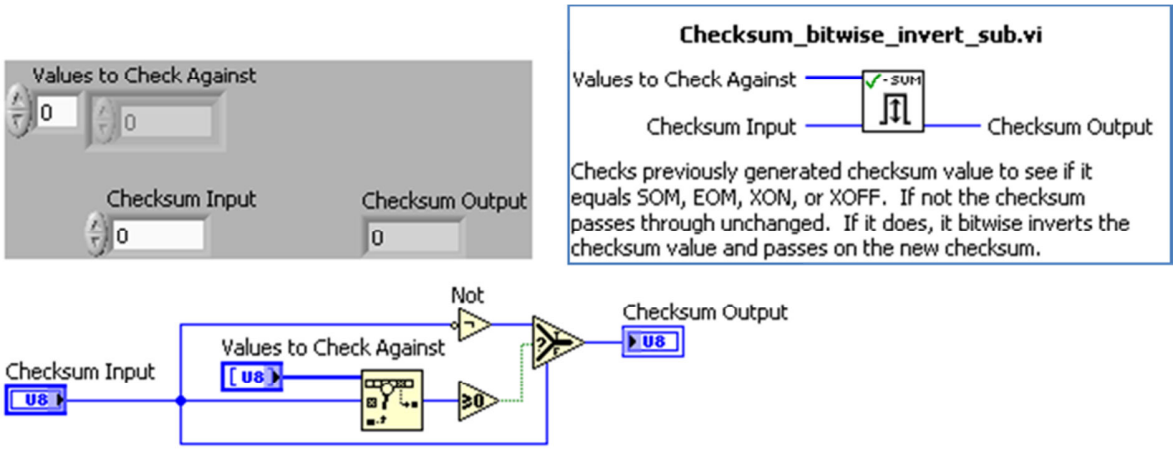

Figure 1.46. Checksum Bitwise Inverter subVI block diagram, front panel and VI properties

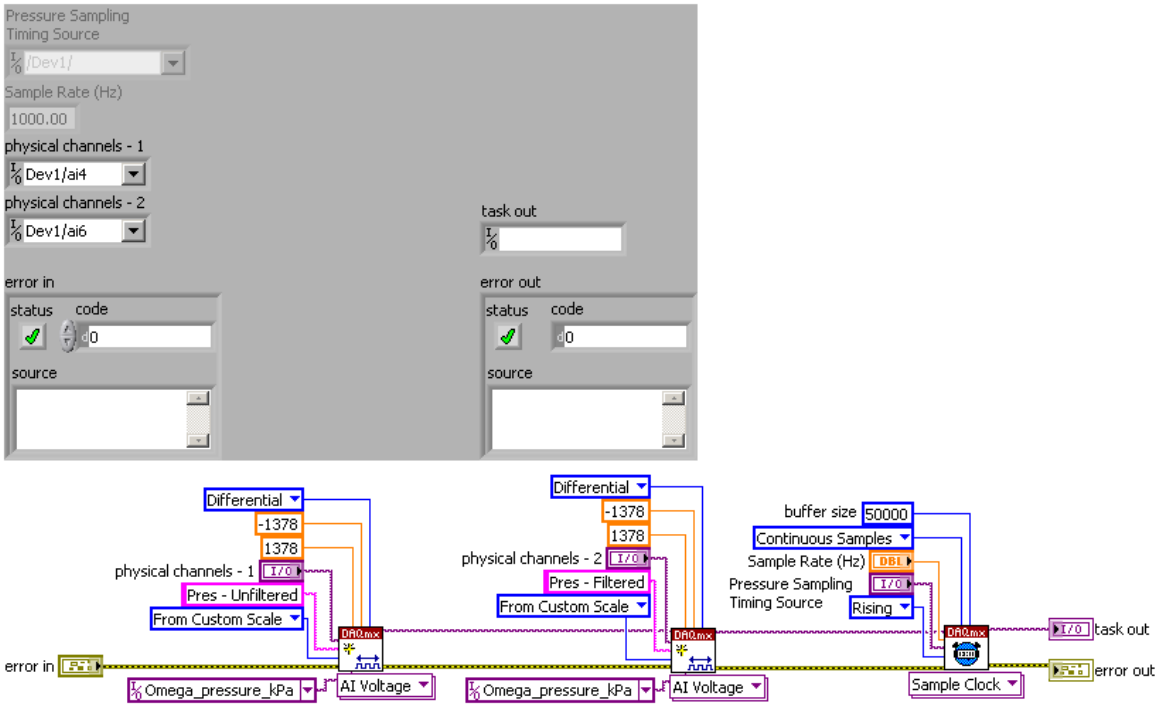

Figure 1.47. Initialize Press Transducer kPa subVI front panel and block diagram

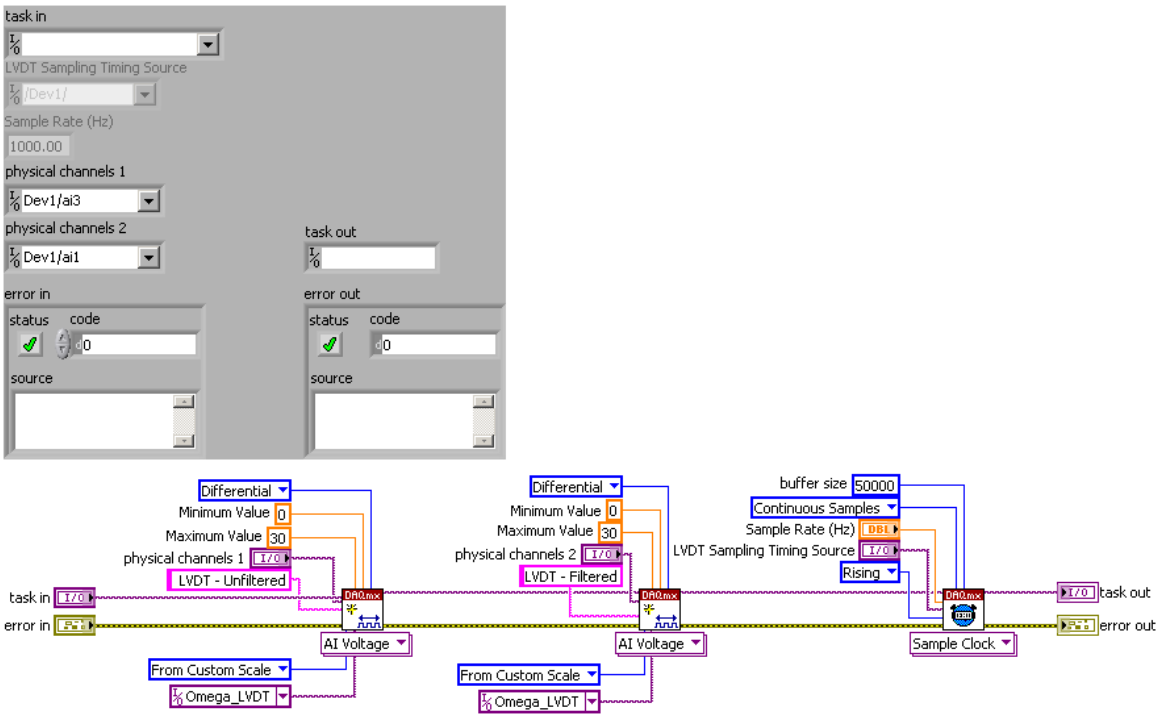

Figure 1.48. Initialize LVDT subVI front panel and block diagram

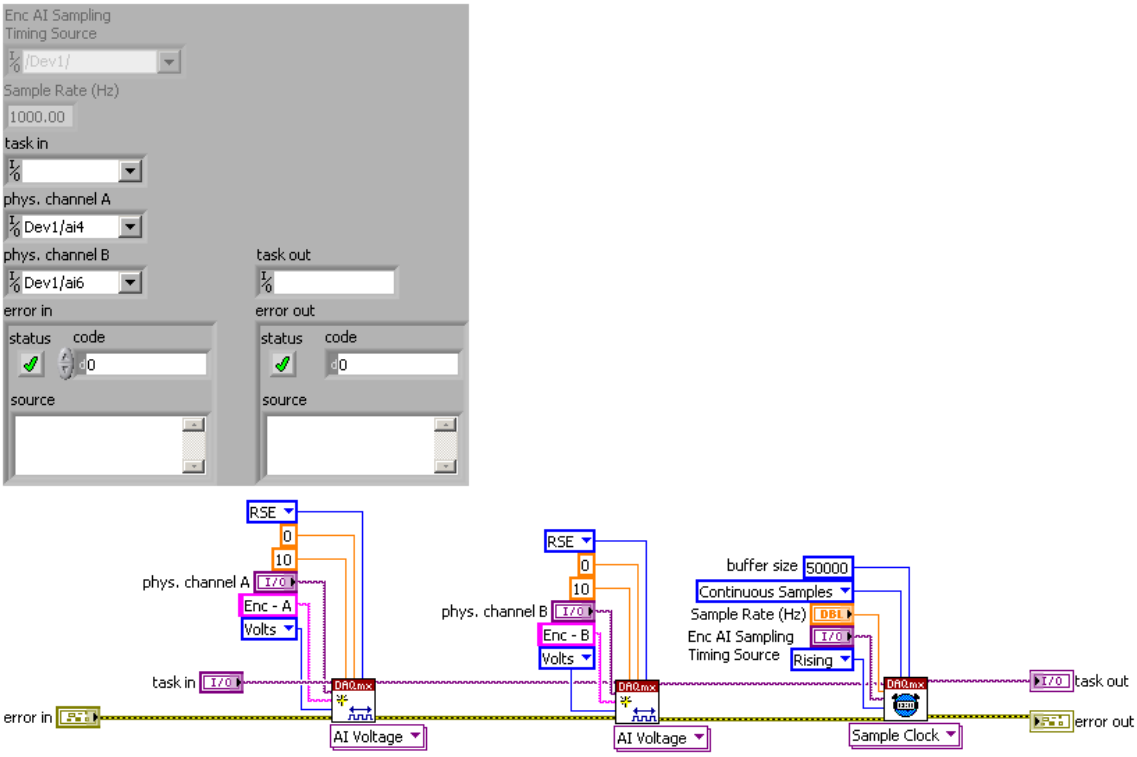

Figure 1.49. Initialize Encoder Analog Inputs subVI front panel and block diagram

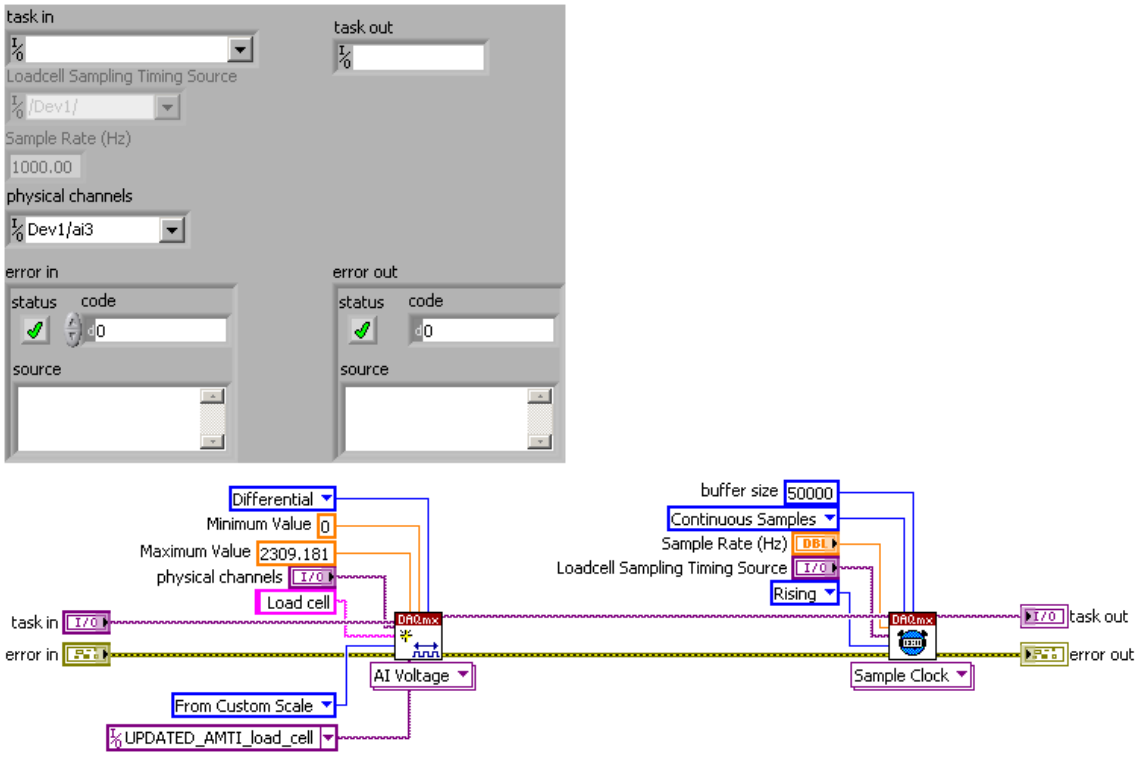

Figure 1.50. Initialize Load Cell subVI front panel and block diagram

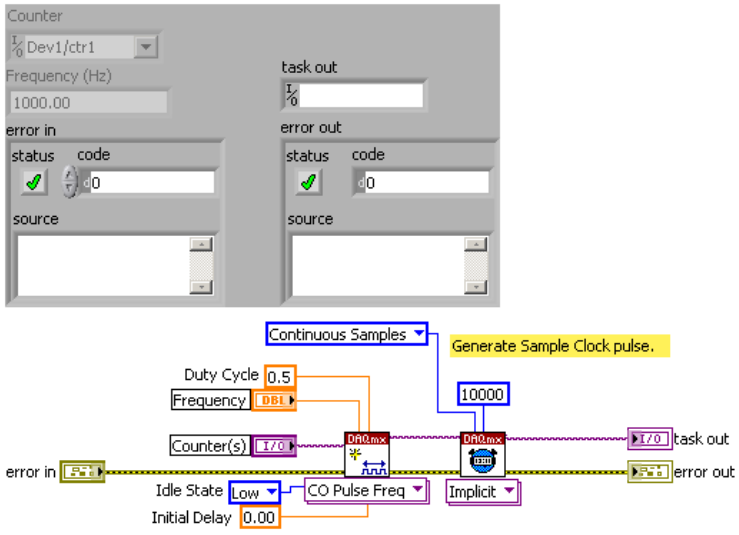

Figure 1.51. Generate Data Acquisition Sample Clock subVI front panel and block diagram

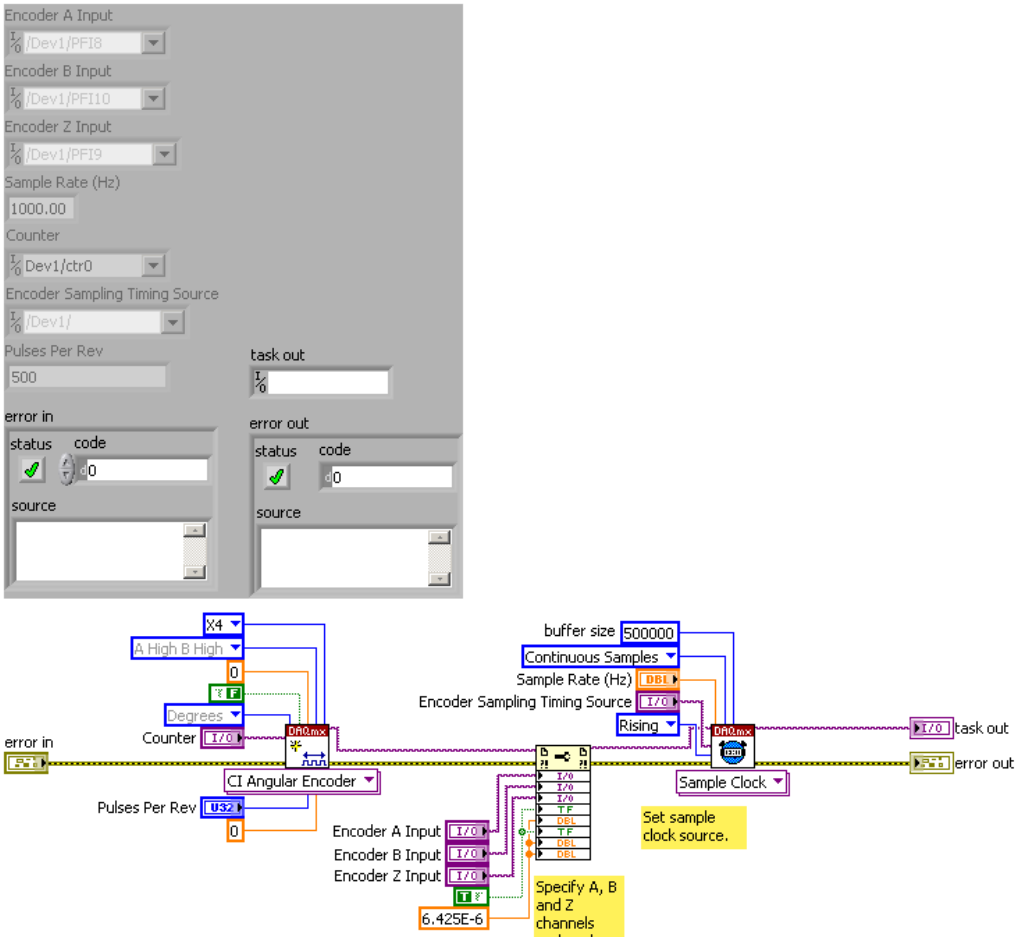

Figure 1.52. Initialize Encoder subVI front panel and block diagram

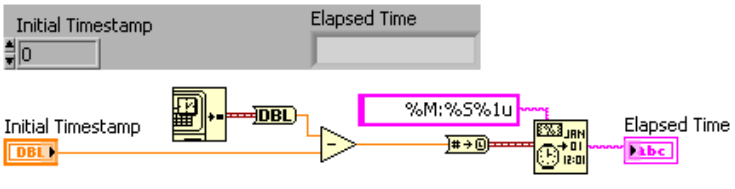

Figure 1.53. Elapsed Time subVI front panel and block diagram

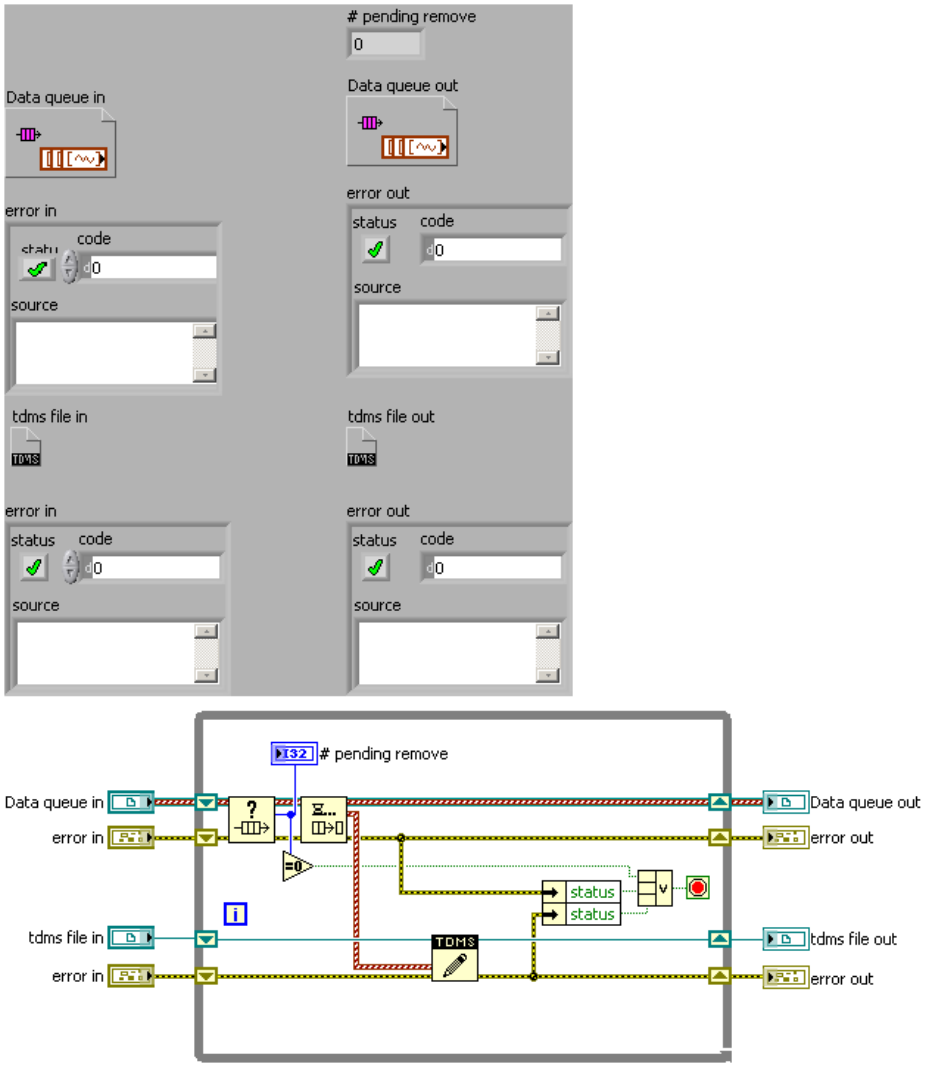

Figure 1.54. Waveform Data Queue to File TDMS subVI front panel and block diagram

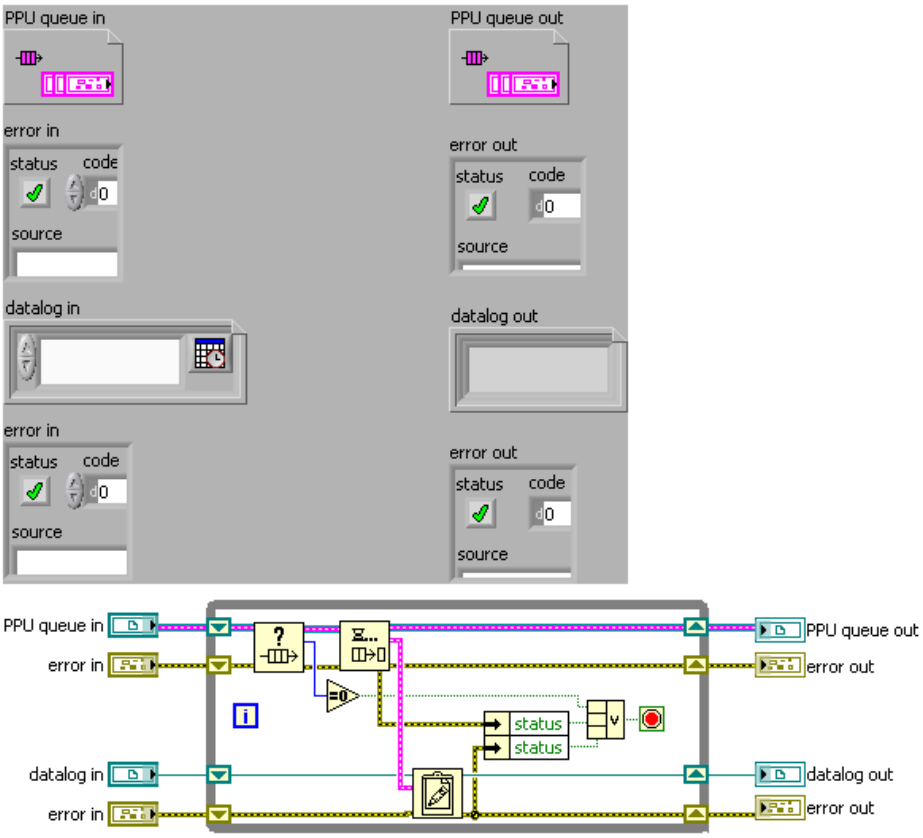

Figure 1.55. PPU Data Queue to File subVI front panel and block diagram

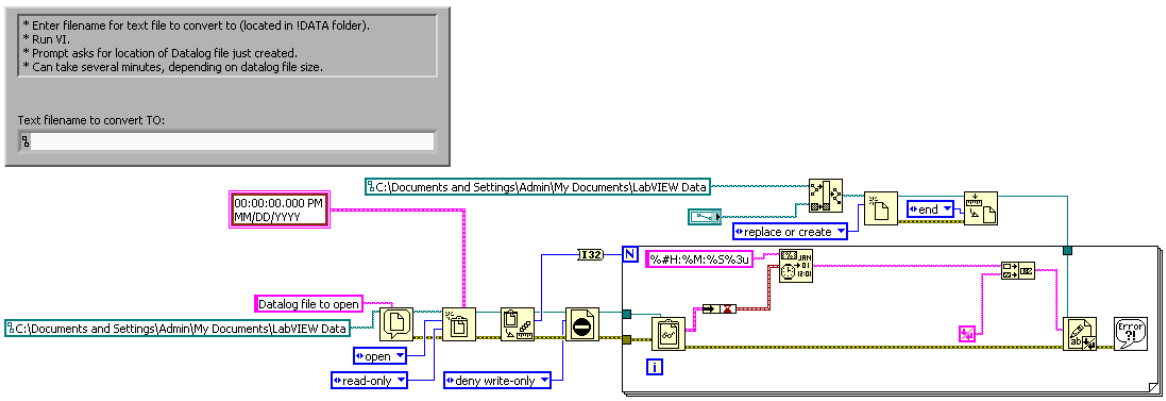

Figure 1.56. Datalog File to Text File subVI front panel and block diagram

1.1.2.4 MATLAB (Post-Processing)

MATLAB (The Mathworks, Inc.) is used exclusively for post-processing of the experimental data due to its ability to easily manipulate the large data files (50+ MB) generated during testing.

The main functions of the post-processing code are as follows:

- Read in the .TDMS (LabVIEW-specific binary file format) that the experiment data is saved in and convert that data to arrays
- Request user-input to define the approximate beginning and ending time points of the test
- Convert the absolute LVDT position measurements into relative displacements
- Apply a user-selectable digital smoothing filter to the analog-filtered signal data
- Find the minimum and maximum amplitudes and temporal positions for each cycle of sensor data
- Apply linear curve-fits to those minimum/maximum data
- Report out all data in graphical and numerical form for review by the user (Figure 1.57.).

Note: the MATLAB code used to convert LabVIEW TDMS files into MATLAB array data is named “convertTDMS.m”. It can be downloaded from the MATLAB File Exchange at this address: http://www.mathworks.com/matlabcentral/fileexchange/28771-converttdms-v9.

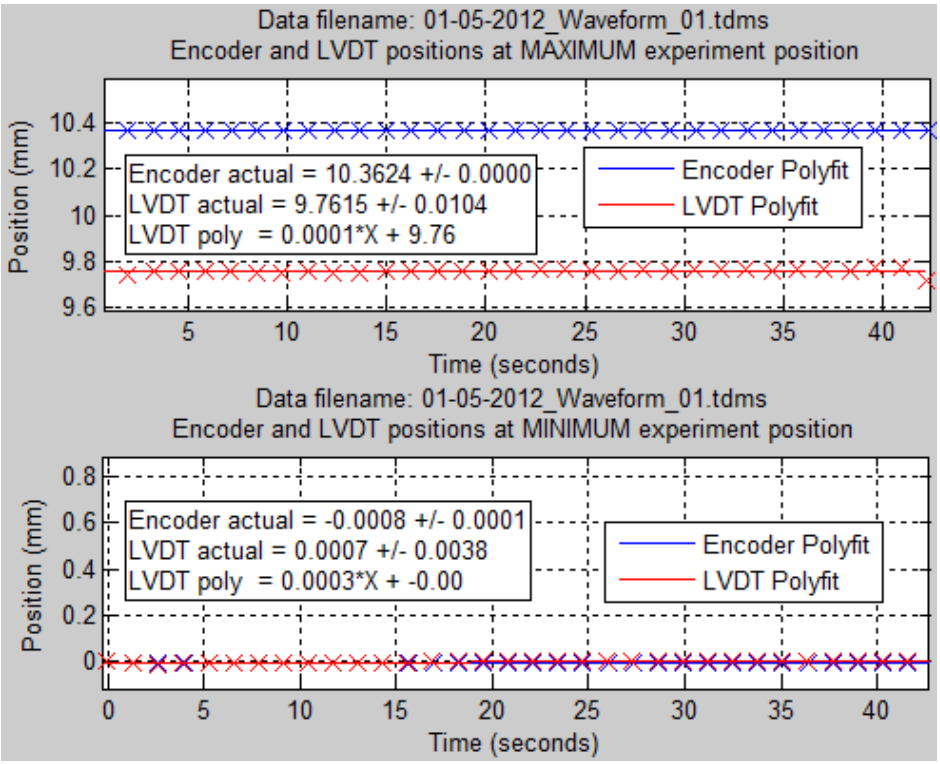

Figure 1.57. Example plot from MATLAB showing locations of master piston (from actuator encoder, blue) and slave piston (from LVDT, red) at minimum and maximum points during sine displacement wave cycling, along with linear curve fits of those points.

The code block below is the main post-processing file. This is revision "WaveformOutputTDMS_03d.m". This code was written by myself and includes substantial explanatory comments. It should be fairly easy for anyone needing to understand the details behind the data post-processing to walk through the code.

```
% Filename: WaveformOutputTDMS_03d.m”
%
% Last modification: 01-31-2012
% - Change all pressure values from psi to kPa to reflect changes made in
% Labview
% - Incorporate standard pressure and load cell figures, smoothing, and peak
% calculations.
% - Read in one TDMS waveform file(which now contains all analog input
% waveforms and an Encoder waveform), ask the user to pick points
% representing the beginning and ending of the cycling and the LVDT zero
% position. Truncate the data, shift all data to begin at zero,
% transcribe and mirror the LVDT data so that it lies on top of Encoder
% data, find maximum and minimum values and times for Encoder and LVDT data.
% Calculate lag of LVDT behind Encoder, actual period of cycling, actual
% displacement of both and duration of Time spent at maxs and mins.
% Calculate similar data for pressure and load cell data.

close all
clear all
clc

% User inputs - DOUBLE-CHECK ALL OF THESE OR THINGS MIGHT NOT WORK!!!
% % % % % % % % % % % % % % % % % % % % % % % % % % % % % % % % % % % % % %
WaveformFile = '02-10-2012_Waveform_03.tdms'; % TDMS file to process
SampleRate = 2500; % Hz, rate of sensor sampling
EncMax = 6.911000; % approximate maximum Encoder value
EncMin = 0; % aproximate minimum Encoder value
TolFactor = 5; % unitless, number of standard deviations away from average to not exclude data
CycleRate = 0.1; % Hz, rate of cycle
SecondsToView = 10; % number of seconds of beginning and ending of data to view for choosing data to analyze
M = 'MarkerSize'; % shorthand for plotting marking
MS = 10; % size of markers on plots (default value is very small)
```

```
% Data smoothing filter parameters
LvdtWindow = 101; % window size used for LVDT smoothing filter
LvdtDegree = 2; % only used in the sgolay smoothing algorithm
LvdtSmoothMethod = 'sgolay';
LoadWindow = 101; % window size used for load cell smoothing filter
LoadDegree = 2; % only used in the sgolay smoothing algorithm
LoadSmoothMethod = 'sgolay';
PressWindow = 101; % window size used for pressure trans. smoothing filter
PressDegree = 2; % only used in the sgolay smoothing algorithm
PressSmoothMethod = 'sgolay';
%   'moving'; %center-based moving average filter, size = window
%   'lowess'; %local regression, 1st degree poly, size = window
%   'loess'; %local regression, 2nd degree poly, size = window
%    'sgolay'; %Savitzky-Golay filter, moving average w/ linear least squares regression,
polynomial = degree , size = window
%      'smoothn'; %optimizes splined smoothing parameter via a minimization of the
generalized cross-validation (GCV) method, size = window


% % % % % % % % % % % % % % % % % % % % % % % % % % % % % % % % % % %
% % %
% Read and plot Pressure, Encoder and LVDT data from text file:
[Time,Encoder,PressRaw,PressFilt,LvdtRaw,LvdtFilt,LoadRaw,EncA,EncB] =
WaveformInputTDMS_02_EncAI(WaveformFile);


FilenameAdapted = strrep(WaveformFile,'_','\_');
TitleStr = sprintf('Data filename: %s',FilenameAdapted);
Encoder = Encoder - Encoder(1,1); % only affects if encoder doesn't come in
% starting at ZERO.
aqua = [0,0.75,0.75];
green = [0,0.5,0];
red = [1,0,0];
blue = [0,0,1];


figure; % Figure 1
```

```
subplot(221),plot(Time,Encoder);
xlabel('Time (seconds)');
ylabel('Encoder position (mm)');
title(TitleStr);

subplot(222),plot(Time,PressRaw,Time,PressFilt);
xlabel('Time (seconds)');
ylabel('Pressure (kPa)');
legend('Raw data','Analog filtered')
title(TitleStr);

subplot(223),plot(Time,LvdtRaw,'g-',Time,LvdtFilt,'r-');
xlabel('Time (seconds)');
ylabel('LVDT position (mm)');
legend('Raw data','Analog filtered')
title(TitleStr);

subplot(224),plot(Time,LoadRaw);
xlabel('Time (seconds)');
ylabel('Load Cell (N)');
legend('Raw data')
title(TitleStr);


% % % % % % % % % % % % % % % % % % % % % % % % % % % % % % % % % % %
% % %
% Truncate Encoder, lvdt, load cell and pressure data to include only perinent
% Plot beginning of data and ask user to click 1 point for cycle beginning
figure;  % Figure 2 (temporary, deleted after user makes selections)
plot(Time,Encoder,Time,LvdtRaw,'g-');
xlabel('Time (seconds)');
ylabel('position (mm)');
legend('Encoder','LVDT-Raw','Location','Best')
title({'Pick one X point for beginning Time point of cycle analysis:'});
```

```
axis([Time(1,1) Time((SecondsToView*SampleRate),1) -inf inf])
% User-input click on filtered data to pick X locations to analyze
[Bx By] = ginput(1);

% % % % % % % % % % % % % % % % % % % % % % % % % % % % % % % % % % %
% % %
% Plot end of data and ask user to click 1 point to use for end of Cycles
figure;  % Figure 3 (temporary, deleted after user makes selections)
plot(Time,Encoder,Time,LvdtRaw,'g-');
xlabel('Time (seconds)');
ylabel('position (mm)');
legend('Encoder','LVDT-Raw','Location','Best')
title({'Pick one X point for ending Time point of cycle analysis:'});
axis([Time((end-(SecondsToView*SampleRate)),1) Time(end,1) -inf inf])

% User-input click on filtered data to pick X locations to analyze
[Ex Ey] = ginput(1);
close;  close;  % close 2 windows opened up for user input

% % % % % % % % % % % % % % % % % % % % % % % % % % % % % % % % % % %
% % %
% Use user-selected timepoints to define zero positions
BeginTime = Bx(1,1);
EndTime = Ex(1,1);
BeginIndex = find(Time >= BeginTime,1);
EndIndex = find(Time >= EndTime,1);
EncInitial = Encoder(BeginIndex) ;
EncFinal = Encoder(EndIndex) ;
LvdtInitial = mean(LvdtFilt((BeginIndex-LvdtWindow):BeginIndex));
LvdtFinal = mean(LvdtFilt(EndIndex:(EndIndex+LvdtWindow)));
LoadInitial = mean(LoadRaw((BeginIndex-LoadWindow):BeginIndex));
LoadFinal = mean(LoadRaw(EndIndex:(EndIndex+LoadWindow)));
PressInitial = mean(PressFilt((BeginIndex-PressWindow):BeginIndex));
PressFinal = mean(PressFilt(EndIndex:(EndIndex+PressWindow)));
```

```
% Use user-selected timepoints to define data to analyze
TimeTrnc = Time(BeginIndex:EndIndex,1);
EncTrnc = Encoder(BeginIndex:EndIndex,1);
LvdtRawTrnc = LvdtRaw(BeginIndex:EndIndex,1);
LvdtFiltTrnc = LvdtFilt(BeginIndex:EndIndex,1);
PressRawTrnc = PressRaw(BeginIndex:EndIndex,1);
PressFiltTrnc = PressFilt(BeginIndex:EndIndex,1);
LoadRawTrnc = LoadRaw(BeginIndex:EndIndex,1);
EncATrnc = EncA(BeginIndex:EndIndex,1);
EncBTrnc = EncB(BeginIndex:EndIndex,1);

% Shift Time vector to start at zero
StartTime = TimeTrnc(1,1);
TimeTrnc = TimeTrnc - StartTime;

%%%%%%%%%%%%%%%%%%%%%%%%%%%%%%%%%%%
%%%
% shift LVDT data to zero point and mirror about the X-axis
LvdtRawTrnc = -(LvdtRawTrnc - LvdtInitial);
LvdtFiltTrnc = -(LvdtFiltTrnc - LvdtInitial);
LvdtFinal = -(LvdtFinal - LvdtInitial);
LvdtInitial = LvdtInitial - LvdtInitial;

% Plot flipped and shifted data
figure;  % Figure 3
plot(TimeTrnc,EncTrnc,TimeTrnc,LvdtRawTrnc,TimeTrnc,LvdtFiltTrnc);
xlabel('Time (seconds)');
ylabel('Position (mm)');
legend('Encoder','LVDT - Raw','LVDT - Filtered','Location','Best')
title('Shifted and Mirrored LVDT data, UNSMOOTHED');
grid on
```

```
% % % % % % % % % % % % % % % % % % % % % % % % % % % % % % % % % % %
% % %
% Smooth LVDT data
if strcmp(LvdtSmoothMethod,'moving') == 1;
   LvdtSmooth = smooth(LvdtFiltTrnc,LvdtWindow,'moving');
elseif strcmp(LvdtSmoothMethod,'lowess') == 1;
   LvdtSmooth = smooth(LvdtFiltTrnc,LvdtWindow,'lowess');
elseif strcmp(LvdtSmoothMethod,'loess') == 1;
     LvdtSmooth = smooth(LvdtRawTrnc,LvdtWindow,'loess');
elseif strcmp(LvdtSmoothMethod,'sgolay') == 1;
   LvdtSmooth = smooth(LvdtFiltTrnc,LvdtWindow,'sgolay',LvdtDegree);
elseif strcmp(LvdtSmoothMethod,'smoothn') == 1;
   LvdtSmooth = smoothn(LvdtFiltTrnc,'robust'); % robust removes outliers
end
LvdtSmoothMethod  %write out method used to command window

% Plot raw, analog filtered, and smoothed-analog filtered data
figure;   % Figure 4
plot(TimeTrnc,LvdtFiltTrnc,TimeTrnc,LvdtSmooth);
xlabel('Time (seconds)');
ylabel('Position (mm)');
legend('Analog Filtered','Filtered + Smoothed','Location','Best');
title(TitleStr);
grid on

% % % % % % % % % % % % % % % % % % % % % % % % % % % % % % % % % % %
% % %
% Smooth Load Cell data
if strcmp(LoadSmoothMethod,'moving') == 1;
   LoadSmooth = smooth(LoadRawTrnc,LoadWindow,'moving');
elseif strcmp(LoadSmoothMethod,'lowess') == 1;
   LoadSmooth = smooth(LoadRawTrnc,LoadWindow,'lowess');
elseif strcmp(LoadSmoothMethod,'loess') == 1;
     LoadSmooth = smooth(LoadRawTrnc,LoadWindow,'loess');
```

```
elseif strcmp(LoadSmoothMethod,'sgolay') == 1;
   LoadSmooth = smooth(LoadRawTrnc,LoadWindow,'sgolay',LoadDegree);
elseif strcmp(LoadSmoothMethod,'smoothn') == 1;
   LoadSmooth = smoothn(LoadRawTrnc,'robust'); % robust removes outliers
end
LoadSmoothMethod  %write out method used to command window

% Plot raw and smoothed load cell data
figure;   % Figure 5
plot(TimeTrnc,LoadRawTrnc,TimeTrnc,LoadSmooth);
xlabel('Time (seconds)');
ylabel('Force (N)');
legend('Raw Data','Smoothed','Location','Best');
title(TitleStr);
grid on

% % % % % % % % % % % % % % % % % % % % % % % % % % % % % % % % % % %
% % %
% Smooth pressure transducer data
if strcmp(PressSmoothMethod,'moving') == 1;
   PressSmooth = smooth(PressFiltTrnc,PressWindow,'moving');
elseif strcmp(PressSmoothMethod,'lowess') == 1;
   PressSmooth = smooth(PressFiltTrnc,PressWindow,'lowess');
elseif strcmp(PressSmoothMethod,'loess') == 1;
     PressSmooth = smooth(PressRawTrnc,PressWindow,'loess');
elseif strcmp(PressSmoothMethod,'sgolay') == 1;
   PressSmooth = smooth(PressFiltTrnc,PressWindow,'sgolay',PressDegree);
elseif strcmp(PressSmoothMethod,'smoothn') == 1;
   PressSmooth = smoothn(PressFiltTrnc,'robust'); % robust removes outliers
end
PressSmoothMethod  %write out method used to command window

% Plot raw, analog filtered, and smoothed-analog filtered data
figure;   % Figure 6
```

```
plot(TimeTrnc,PressFiltTrnc,TimeTrnc,PressSmooth);
xlabel('Time (seconds)');
ylabel('Pressure (kPa)');
legend('Analog Filtered','Filtered + Smoothed','Location','Best');
title(TitleStr);
grid on

% % % % % % % % % % % % % % % % % % % % % % % % % % % % % % % % % % %
% % %
% Find min/max values and locations of Encoder signal

% Calculate how many Cycles occurred during the analyzed Time period
Cycles = floor(( TimeTrnc(end,1) - TimeTrnc(1,1) ) * CycleRate);
Cycles % write out number of Cycles to command window

% Iterate through each cycle, starting 1/2 way through the first
% displacement in order to avoid picking trivial min/maxes in the
% beginning area finding the min/max locations and values
MidEncMax = zeros(Cycles,1);
MaxEncDuration = zeros(Cycles,1);
MidEncTimeMax = zeros(Cycles,1);
MidEncMin = zeros(Cycles,1);
MinEncDuration = zeros(Cycles,1);
MidEncTimeMin = zeros(Cycles,1);
a = 1;
for i = 1:Cycles
   if i == 1; % for the first iteration, BeginInd = the first value
      BeginInd = (1/4)*(1/CycleRate)*SampleRate;
   end

   if i == Cycles; %for the last cycle, make the last value = EndInd
      EndInd = length(TimeTrnc);
   else EndInd = BeginInd + (SampleRate * (1 / CycleRate)) - 1;
   end   %otherwise, EndInd = BeginInd plus one cycle's worth of data
```

```
    %   create temporary Time and Encoder arrays to search for max/min
    TimeTemp = TimeTrnc(BeginInd:EndInd,1);
    EncTemp = EncTrnc(BeginInd:EndInd,1);

    % Find maximum value of temporary Encoder array
    MidEncMax(a,1) = max(EncTemp);
    MaxIndices = find(EncTemp == (MidEncMax(a,1)));
    TimeMax = (TimeTemp(MaxIndices));

    % if there are multiples Time points that the max occurred at, find the
    % duration there.  Else, use 1/sample rate as the duration.
    if length(MaxIndices) > 1
        MaxEncDuration(a,1) = TimeMax(end,1) - TimeMax(1,1);
    else MaxEncDuration(a,1) = 1/SampleRate;
    end

    MidEncTimeMax(a,1) = ((MaxEncDuration(a,1)) / 2) + TimeMax(1,1);

    MidEncMin(a,1) = min(EncTemp);
    MinIndices = find(EncTemp == (MidEncMin(a,1)));
    TimeMin = TimeTemp(MinIndices);
    if length(MinIndices) > 1
        MinEncDuration(a,1) = TimeMin(end,1) - TimeMin(1,1);
    else MinEncDuration(a,1) = 1/SampleRate;
    end
    MidEncTimeMin(a,1) = ((MinEncDuration(a,1)) / 2) + TimeMin(1,1);
    a = a + 1;
    BeginInd = EndInd + 1;
end

% % % % % % % % % % % % % % % % % % % % % % % % % % % % % % % % % % %
% % %
% Incorporate previously determined Initial and Final positions into Min's
```

```
Temp = zeros(length(MidEncMin)+1,1);
Temp(2:end,1) = MidEncMin;
Temp(1,1) = EncInitial;
Temp(end,1) = EncFinal;
MidEncMin = Temp;

Temp = zeros(length(MinEncDuration)+1,1);
Temp(2:end,1) = MinEncDuration;
Temp(1,1) = 1/SampleRate;
Temp(end,1) = 1/SampleRate;
MinEncDuration = Temp;

Temp = zeros(length(MidEncTimeMin)+1,1);
Temp(2:end,1) = MidEncTimeMin;
Temp(1,1) = BeginTime - StartTime;
Temp(end,1) = EndTime - StartTime;
MidEncTimeMin = Temp;

% % % % % % % % % % % % % % % % % % % % % % % % % % % % % % % % % % %
% % %
% Find min/max locations and values of LVDT-smoothed signal, code should be
% the same as Encoder code above, obviously with different variable names.
a = 1;
MidLvdtMax = zeros(Cycles,1);
MaxLvdtDuration = zeros(Cycles,1);
MidLvdtTimeMax = zeros(Cycles,1);
MidLvdtMin = zeros(Cycles,1);
MinLvdtDuration = zeros(Cycles,1);
MidLvdtTimeMin = zeros(Cycles,1);
% Iterate through each cycle, finding the min/max locations and values
for i = 1:Cycles
   if i == 1;
      BeginInd = (1/4)*(1/CycleRate)*SampleRate;
   end
```

```
    if i == Cycles;
        EndInd = length(TimeTrnc);
    else EndInd = BeginInd + (SampleRate * (1 / CycleRate)) - 1;
    end

    TimeTemp = TimeTrnc(BeginInd:EndInd,1);
    LvdtTemp = LvdtSmooth(BeginInd:EndInd,1);

    MidLvdtMax(a,1) = max(LvdtTemp);
    MaxIndices = find(LvdtTemp == (MidLvdtMax(a,1)));
    TimeMax = TimeTemp(MaxIndices);

    if length(MaxIndices) > 1
        MaxLvdtDuration(a,1) = TimeMax(end,1) - TimeMax(1,1);
    else MaxLvdtDuration(a,1) = 1/SampleRate;
    end

    MidLvdtTimeMax(a,1) = ((MaxLvdtDuration(a,1)) / 2) + TimeMax(1,1);

    MidLvdtMin(a,1) = min(LvdtTemp);
    MinIndices = find(LvdtTemp == (MidLvdtMin(a,1)));
    TimeMin = TimeTemp(MinIndices);

    if length(MinIndices) > 1
        MinLvdtDuration(a,1) = TimeMin(end,1) - TimeMin(1,1);
    else MinLvdtDuration(a,1) = 1/SampleRate;
    end

    MidLvdtTimeMin(a,1) = ((MinLvdtDuration(a,1)) / 2) + TimeMin(1,1);

    a = a + 1;
    BeginInd = EndInd + 1;
end
```

```
% % % % % % % % % % % % % % % % % % % % % % % % % % % % % % % % % % %
% % %
% Incorporate previously determined Initial and Final positions into Min's
Temp = zeros(length(MidLvdtMin)+1,1);
Temp(2:end,1) = MidLvdtMin;
Temp(1,1) = LvdtInitial;
Temp(end,1) = LvdtFinal;
MidLvdtMin = Temp;

Temp = zeros(length(MinLvdtDuration)+1,1);
Temp(2:end,1) = MinLvdtDuration;
Temp(1,1) = 1/SampleRate;
Temp(end,1) = 1/SampleRate;
MinLvdtDuration = Temp;

Temp = zeros(length(MidLvdtTimeMin)+1,1);
Temp(2:end,1) = MidLvdtTimeMin;
Temp(1,1) = BeginTime - StartTime;
Temp(end,1) = EndTime - StartTime;
MidLvdtTimeMin = Temp;

% % % % % % % % % % % % % % % % % % % % % % % % % % % % % % % % % % %
% % %
% Find min/max locations and values of Load Cell smoothed.
a = 1;
MidLoadMax = zeros(Cycles,1);
MaxLoadDuration = zeros(Cycles,1);
MidLoadTimeMax = zeros(Cycles,1);
MidLoadMin = zeros(Cycles,1);
MinLoadDuration = zeros(Cycles,1);
MidLoadTimeMin = zeros(Cycles,1);
% Iterate through each cycle, finding the min/max locations and values
for i = 1:Cycles
```

```
if i == 1;
   BeginInd = (1/4)*(1/CycleRate)*SampleRate;
end

if i == Cycles;
   EndInd = length(TimeTrnc);
else EndInd = BeginInd + (SampleRate * (1 / CycleRate)) - 1;
end

TimeTemp = TimeTrnc(BeginInd:EndInd,1);
LoadTemp = LoadSmooth(BeginInd:EndInd,1);

MidLoadMax(a,1) = max(LoadTemp);
MaxIndices = find(LoadTemp == (MidLoadMax(a,1)));
TimeMax = TimeTemp(MaxIndices);

if length(MaxIndices) > 1
   MaxLoadDuration(a,1) = TimeMax(end,1) - TimeMax(1,1);
else MaxLoadDuration(a,1) = 1/SampleRate;
end

MidLoadTimeMax(a,1) = ((MaxLoadDuration(a,1)) / 2) + TimeMax(1,1);

MidLoadMin(a,1) = min(LoadTemp);
MinIndices = find(LoadTemp == (MidLoadMin(a,1)));
TimeMin = TimeTemp(MinIndices);

if length(MinIndices) > 1
   MinLoadDuration(a,1) = TimeMin(end,1) - TimeMin(1,1);
else MinLoadDuration(a,1) = 1/SampleRate;
end

MidLoadTimeMin(a,1) = ((MinLoadDuration(a,1)) / 2) + TimeMin(1,1);
```

```
    a = a + 1;
    BeginInd = EndInd + 1;
end

Temp = zeros(length(MidLoadMin)+1,1);
Temp(2:end,1) = MidLoadMin;
Temp(1,1) = LoadInitial;
Temp(end,1) = LoadFinal;
MidLoadMin = Temp;

Temp = zeros(length(MinLoadDuration)+1,1);
Temp(2:end,1) = MinLoadDuration;
Temp(1,1) = 1/SampleRate;
Temp(end,1) = 1/SampleRate;
MinLoadDuration = Temp;

Temp = zeros(length(MidLoadTimeMin)+1,1);
Temp(2:end,1) = MidLoadTimeMin;
Temp(1,1) = BeginTime - StartTime;
Temp(end,1) = EndTime - StartTime;
MidLoadTimeMin = Temp;

% % % % % % % % % % % % % % % % % % % % % % % % % % % % % % % % % % %
% % %
% Find min/max locations and values of Pressure smoothed.
a = 1;
MidPressMax = zeros(Cycles,1);
MaxPressDuration = zeros(Cycles,1);
MidPressTimeMax = zeros(Cycles,1);
MidPressMin = zeros(Cycles,1);
MinPressDuration = zeros(Cycles,1);
MidPressTimeMin = zeros(Cycles,1);
% Iterate through each cycle, finding the min/max locations and values
for i = 1:Cycles
```

```
if i == 1;
   BeginInd = (1/4)*(1/CycleRate)*SampleRate;
end

if i == Cycles;
   EndInd = length(TimeTrnc);
else EndInd = BeginInd + (SampleRate * (1 / CycleRate)) - 1;
end

TimeTemp = TimeTrnc(BeginInd:EndInd,1);
PressTemp = PressSmooth(BeginInd:EndInd,1);

MidPressMax(a,1) = max(PressTemp);
MaxIndices = find(PressTemp == (MidPressMax(a,1)));
TimeMax = TimeTemp(MaxIndices);

if length(MaxIndices) > 1
   MaxPressDuration(a,1) = TimeMax(end,1) - TimeMax(1,1);
else MaxPressDuration(a,1) = 1/SampleRate;
end

MidPressTimeMax(a,1) = ((MaxPressDuration(a,1)) / 2) + TimeMax(1,1);

MidPressMin(a,1) = min(PressTemp);
MinIndices = find(PressTemp == (MidPressMin(a,1)));
TimeMin = TimeTemp(MinIndices);

if length(MinIndices) > 1
   MinPressDuration(a,1) = TimeMin(end,1) - TimeMin(1,1);
else MinPressDuration(a,1) = 1/SampleRate;
end

MidPressTimeMin(a,1) = ((MinPressDuration(a,1)) / 2) + TimeMin(1,1);
```

```
    a = a + 1;
    BeginInd = EndInd + 1;
end

Temp = zeros(length(MidPressMin)+1,1);
Temp(2:end,1) = MidPressMin;
Temp(1,1) = PressInitial;
Temp(end,1) = PressFinal;
MidPressMin = Temp;

Temp = zeros(length(MinPressDuration)+1,1);
Temp(2:end,1) = MinPressDuration;
Temp(1,1) = 1/SampleRate;
Temp(end,1) = 1/SampleRate;
MinPressDuration = Temp;

Temp = zeros(length(MidPressTimeMin)+1,1);
Temp(2:end,1) = MidPressTimeMin;
Temp(1,1) = BeginTime - StartTime;
Temp(end,1) = EndTime - StartTime;
MidPressTimeMin = Temp;

% % % % % % % % % % % % % % % % % % % % % % % % % % % % % % % % % % %
% % %
% % % % % % % % % % % % % % % % % % % % % % % % % % % % % % % % % % %
% % %
% Plot calculated values of signals':
%  - Value of Max/Min location
%  - Max/Min along with polyfit to look for drift over Cycles
%  - Calculated period (Time from Max to Max or Min to Min)
%  - Duration of Time spent at Max or Min location
%  - Displacement per cycle
%  - Time lag between Encoder Max and LVDT Max (and Min/Min)
% % % % % % % % % % % % % % % % % % % % % % % % % % % % % % % % % % %
% % %
```

```
%%%%%%%%%%%%%%%%%%%%%%%%%%%%%%%%%%%
%%%

MidEncTime = vertcat(MidEncTimeMin,MidEncTimeMax);
MidEnc = vertcat(MidEncMin,MidEncMax);
MidLvdtTime = vertcat(MidLvdtTimeMin,MidLvdtTimeMax);
MidLvdt = vertcat(MidLvdtMin,MidLvdtMax);
MidLoadTime = vertcat(MidLoadTimeMin,MidLoadTimeMax);
MidLoad = vertcat(MidLoadMin,MidLoadMax);
MidPressTime = vertcat(MidPressTimeMin,MidPressTimeMax);
MidPress = vertcat(MidPressMin,MidPressMax);

% Plot Encoder and LVDT data of min/max locations together
figure;  % Figure 7
plot(TimeTrnc,EncTrnc,'b-');
hold on
plot(MidEncTime,MidEnc,'Bx',M,MS)
hold on
plot(TimeTrnc,LvdtSmooth,'r-');
hold on
plot(MidLvdtTime,MidLvdt,'rx',M,MS)
xlabel('Time (seconds)');
ylabel('Position (mm)');
legend('Encoder','Encoder Max/Min',...
   'LVDT-Smoothed','LVDT Max/Min','Best')
TxtStr_1 = ('Encoder and LVDT: data points used for Min/Max calculations');
title({TitleStr,TxtStr_1});
grid on

% Calc 1st order polyfits of Enc and LVDT maxes and min
MidEncMaxPoly = polyfit(MidEncTimeMax,MidEncMax,1);
MidEncMinPoly = polyfit(MidEncTimeMin,MidEncMin,1);
MidLvdtMaxPoly = polyfit(MidLvdtTimeMax,MidLvdtMax,1);
MidLvdtMinPoly = polyfit(MidLvdtTimeMin,MidLvdtMin,1);
```

```
MidEncMaxFit = polyval(MidEncMaxPoly,MidEncTimeMax);
MidEncMinFit = polyval(MidEncMinPoly,MidEncTimeMin);
MidLvdtMaxFit = polyval(MidLvdtMaxPoly,MidLvdtTimeMax);
MidLvdtMinFit = polyval(MidLvdtMinPoly,MidLvdtTimeMin);

% Plot polyfits of maxs along with actual maxs
figure;  % Figure 8
subplot(211)
h(1) = plot(MidEncTimeMax,MidEncMaxFit,'b-');
hold on
h(2) = plot(MidEncTimeMax,MidEncMax,'Bx',M,MS);
h(3) = plot(MidLvdtTimeMax,MidLvdtMaxFit,'r-');
h(4) = plot(MidLvdtTimeMax,MidLvdtMax,'rx',M,MS);
xlabel('Time (seconds)');
ylabel('Position (mm)');
hasbehavior(h(2),'legend',false);
hasbehavior(h(4),'legend',false);
legend('Encoder Polyfit','LVDT Polyfit','Location','Best');
TxtStr_1 = ('Encoder and LVDT positions at MAXIMUM experiment position');
title({TitleStr,TxtStr_1});
grid on

clear TxtStr
TxtStr(1) = cellstr(sprintf('Encoder actual = %6.4f +/- %6.4f',...
   mean(MidEncMax),std(MidEncMax)));
TxtStr(2) = cellstr(sprintf('LVDT actual = %6.4f +/- %6.4f',...
   mean(MidLvdtMax),std(MidLvdtMax)));
TxtStr(3) = cellstr(sprintf('LVDT poly  = %6.4f*X + %4.2f',...
   MidLvdtMaxPoly(1,1),MidLvdtMaxPoly(1,2)));
textbp(TxtStr,'BackgroundColor',[1 1 1],'EdgeColor','black','LineStyle','-')
axis([-inf inf 9.1 10.1])

% Plot polyfits of mins along with actual mins
subplot(212)
```

```matlab
h(1) = plot(MidEncTimeMin,MidEncMinFit,'b-');
hold on
h(2) = plot(MidEncTimeMin,MidEncMin,'Bx',M,MS);
h(3) = plot(MidLvdtTimeMin,MidLvdtMinFit,'r-');
h(4) = plot(MidLvdtTimeMin,MidLvdtMin,'rx',M,MS);
xlabel('Time (seconds)');
ylabel('Position (mm)');
hasbehavior(h(2),'legend',false);
hasbehavior(h(4),'legend',false);
legend('Encoder Polyfit','LVDT Polyfit','Location','Best');
TxtStr_1 = ('Encoder and LVDT positions at MINIMUM experiment position');
title({TitleStr,TxtStr_1});
grid on

TxtStr(1) = cellstr(sprintf('Encoder actual = %6.4f +/- %6.4f',...
   mean(MidEncMin),std(MidEncMin)));
TxtStr(2) = cellstr(sprintf('LVDT actual = %6.4f +/- %6.4f',...
   mean(MidLvdtMin),std(MidLvdtMin)));
TxtStr(3) = cellstr(sprintf('LVDT poly  = %6.4f*X + %4.2f',...
   MidLvdtMinPoly(1,1),MidLvdtMinPoly(1,2)));
textbp(TxtStr,'BackgroundColor',[1 1 1],'EdgeColor','black','LineStyle','-')
axis([-inf inf -0.5 0.5])

% % % % % % % % % % % % % % % % % % % % % % % % % % % % % % % % % % %
% % %
% Plot Max/Min points of Load Cell along with data
figure;  % Figure 8
plot(TimeTrnc,LoadSmooth,'b-');
hold on
plot(MidLoadTime,MidLoad,'Bx',M,MS)
xlabel('Time (seconds)');
ylabel('Force (N)');
legend('Load Cell - Smoothed','Load Cell Max/Min','Best')
TxtStr_1 = ('Load Cell: Min/Max points');
```

```
title({TitleStr,TxtStr_1});
grid on

%%%%%%%%%%%%%%%%%%%%%%%%%%%%%%%%%%%%%%%
% Plot Max/Min point of Pressure along with data
figure;  % Figure 8
plot(TimeTrnc,PressSmooth,'b-');
hold on
plot(MidPressTime,MidPress,'Bx',M,MS)
xlabel('Time (seconds)');
ylabel('Pressure (kPa)');
legend('Pressure - Smoothed','Pressure Max/Min','Best')
TxtStr_1 = ('Pressure Tranducer: Min/Max points');
title({TitleStr,TxtStr_1});
grid on

%%%%%%%%%%%%%%%%%%%%%%%%%%%%%%%%%%%%%%%
% Calculate the actual period of the Encoder signal
DeltaEncMax = zeros(Cycles-1,1);
DeltaEncMin = zeros(Cycles-1,1);
DeltaLvdtMax = zeros(Cycles-1,1);
DeltaLvdtMin = zeros(Cycles-1,1);

for i = 1:(length(MidEncTimeMax)-1)
   DeltaEncMax(i,1) = MidEncTimeMax(i+1,1) - MidEncTimeMax(i,1);
end;

for i = 1:(length(MidEncTimeMin)-1)
   DeltaEncMin(i,1) = MidEncTimeMin(i+1,1) - MidEncTimeMin(i,1);
end;

% Calculate the actual period of the LVDT signal
```

```
for i = 1:(length(MidLvdtTimeMax)-1)
    DeltaLvdtMax(i,1) = MidLvdtTimeMax(i+1,1) - MidLvdtTimeMax(i,1);
end;

for i = 1:(length(MidLvdtTimeMin)-1)
    DeltaLvdtMin(i,1) = MidLvdtTimeMin(i+1,1) - MidLvdtTimeMin(i,1);
end;

% Stats for the periods of the Encoder and lvdt:
MeanPeriodEncMax = mean(DeltaEncMax);    MeanPeriodEncMax
StdevPeriodEncMax = std(DeltaEncMax);    StdevPeriodEncMax
MeanPeriodEncMin = mean(DeltaEncMin);    MeanPeriodEncMin
StdevPeriodEncMin = std(DeltaEncMin);    StdevPeriodEncMin
MeanPeriodLvdtMax = mean(DeltaLvdtMax);  MeanPeriodLvdtMax
StdevPeriodLvdtMax = std(DeltaLvdtMax);  StdevPeriodLvdtMax
MeanPeriodLvdtMin = mean(DeltaLvdtMin);  MeanPeriodLvdtMin
StdevPeriodLvdtMin = std(DeltaLvdtMin);  StdevPeriodLvdtMin

% Plot the periods together:
figure;  % Figure 7
plot(DeltaEncMax,'b-');
hold on
plot(DeltaEncMin,'k-');
hold on
plot(DeltaLvdtMax,'r-');
hold on
plot(DeltaLvdtMin,'m-');
xlabel('Cycle number');
ylabel('Time (seconds)');
legend('Encoder: Max positions','Encoder: Min positions',...
    'LVDT: Max positions','LVDT: Min positions','Location','Best')
TxtStr_1 = ('Max-to-max and Min-to-min times of Encoder and LVDT signals');
title({TitleStr,TxtStr_1});
grid on
```

```
clear TxtStr
TxtStr(1) = cellstr(sprintf('Encoder at Max = %6.4f +/- %6.4f',...
   MeanPeriodEncMax,StdevPeriodEncMax));
TxtStr(2) = cellstr(sprintf('Encoder at Min = %6.4f +/- %6.4f',...
   MeanPeriodEncMin,StdevPeriodEncMin));
TxtStr(3) = cellstr(sprintf('LVDT at Max = %6.4f +/- %6.4f',...
   MeanPeriodLvdtMax,StdevPeriodLvdtMax));
TxtStr(4) = cellstr(sprintf('LVDT at Min = %6.4f +/- %6.4f',...
   MeanPeriodLvdtMin,StdevPeriodLvdtMin));
textbp(TxtStr,'BackgroundColor',[1 1 1],'EdgeColor','black','LineStyle','-')

% % % % % % % % % % % % % % % % % % % % % % % % % % % % % % % % % % %
% % %
% Stats on duration of Time at min or max location
MeanDurationEncMax = mean(MaxEncDuration);    MeanDurationEncMax
StdevDurationEncMax = std(MaxEncDuration);    StdevDurationEncMax
MeanDurationEncMin = mean(MinEncDuration);    MeanDurationEncMin
StdevDurationEncMin = std(MinEncDuration);    StdevDurationEncMin
MeanDurationLvdtMax = mean(MaxLvdtDuration);  MeanDurationLvdtMax
StdevDurationLvdtMax = std(MaxLvdtDuration);  StdevDurationLvdtMax
MeanDurationLvdtMin = mean(MinLvdtDuration);  MeanDurationLvdtMin
StdevDurationLvdtMin = std(MinLvdtDuration);  StdevDurationLvdtMin

% Plot the duration of Time at min or max location
figure;  % Figure 8
plot(MaxEncDuration,'b-');
hold on
plot(MinEncDuration,'k-');
hold on
plot(MaxLvdtDuration,'r-');
hold on
plot(MaxLvdtDuration,'m-');
xlabel('Cycle number');
ylabel('Time (seconds)');
```

```
legend('Encoder: Max positions','Encoder: Min positions',...
    'LVDT: Max positions','LVDT: Min positions','Location','Best')
TxtStr_1 = ('Duration of Time spent at Max/Min position');
title({TitleStr,TxtStr_1});
grid on
clear TxtStr
TxtStr(1) = cellstr(sprintf('Encoder @ Max = %6.4f +/- %6.4f',...
    MeanDurationEncMax,StdevDurationEncMax));
TxtStr(2) = cellstr(sprintf('Encoder @ Min = %6.4f +/- %6.4f',...
    MeanDurationEncMin,StdevDurationEncMin));
TxtStr(3) = cellstr(sprintf('LVDT @ Max = %6.4f +/- %6.4f',...
     MeanDurationLvdtMax,StdevDurationLvdtMax));
 TxtStr(4) = cellstr(sprintf('LVDT @ Min = %6.4f +/- %6.4f',...
     MeanDurationLvdtMin,StdevDurationLvdtMin));
textbp(TxtStr,'BackgroundColor',[1 1 1],'EdgeColor','black','LineStyle','-')


% % % % % % % % % % % % % % % % % % % % % % % % % % % % % % % % % % %
% % %
% Displacement per cycle
% Calculate Encoder displacements:
EncDisp = zeros(((Cycles-1)*2),1);
for i = 1:((length(MidEncMax) + length(MidEncMin)) - 1);
    if (MidEncTimeMax(1,1) < (MidEncTimeMin))
        if(mod(i,2) == 0)
            EncDisp(i,1) = abs(MidEncMax(((ceil(i/2))+1),1)-...
                MidEncMin(((ceil(i/2))),1));
        else EncDisp(i,1) = abs(MidEncMax(((ceil(i/2))),1) - ...
                MidEncMin(((ceil(i/2))),1));
        end
    else if(mod(i,2) == 0)
            EncDisp(i,1) = abs(MidEncMin(((ceil(i/2))+1),1) -...
                MidEncMax(((ceil(i/2))),1));
        else EncDisp(i,1) = abs(MidEncMin(((ceil(i/2))),1) -...
                MidEncMax(((ceil(i/2))),1));
```

```
        end
    end
end

DeleteDisp = find((EncDisp > (mean(EncDisp) + TolFactor*std(EncDisp))|...
    (EncDisp < (mean(EncDisp) - TolFactor*std(EncDisp))));
if isempty(DeleteDisp) ~= 0
else
    EncDisp(DeleteDisp,:) = [];
end

% Calculate LVDT displacements:
LvdtDisp = zeros(((Cycles-1)*2),1);
for i = 1:((length(MidLvdtMax) + length(MidLvdtMin)) - 1);
    if (MidLvdtTimeMax(1,1) < (MidLvdtTimeMin))
        if(mod(i,2) == 0)
            LvdtDisp(i,1) = abs(MidLvdtMax(((ceil(i/2))+1),1)-...
                MidLvdtMin(((ceil(i/2))),1));
        else LvdtDisp(i,1) = abs(MidLvdtMax(((ceil(i/2))),1) - ...
                MidLvdtMin(((ceil(i/2))),1));
        end
    else if(mod(i,2) == 0)
            LvdtDisp(i,1) = abs(MidLvdtMin(((ceil(i/2))+1),1) -...
                MidLvdtMax(((ceil(i/2))),1));
        else LvdtDisp(i,1) = abs(MidLvdtMin(((ceil(i/2))),1) -...
                MidLvdtMax(((ceil(i/2))),1));
        end
    end
end

DeleteDisp = find((LvdtDisp > (mean(LvdtDisp) + TolFactor*std(LvdtDisp))|...
    (LvdtDisp < (mean(LvdtDisp) - TolFactor*std(LvdtDisp))));
if isempty(DeleteDisp) ~= 0
else
```

```
    LvdtDisp(DeleteDisp,:) = [];
end

% linear polyfit the displacement
X = transpose(1:length(LvdtDisp));
LvdtDispPoly = polyfit(X,LvdtDisp,1);

% Calculate statistics on actual displacment values
MeanEncoderDisplacement = mean(EncDisp);   MeanEncoderDisplacement
StDevEncoderDisplacement = std(EncDisp);   StDevEncoderDisplacement
MeanLvdtDisplacement = mean(LvdtDisp);     MeanLvdtDisplacement
StDevLvdtDisplacement = std(LvdtDisp);     StDevLvdtDisplacement
PolyLvdtDisplacement = LvdtDispPoly(1,1);  PolyLvdtDisplacement

% Plot the actual displacements/ 1/2 cycle of the Encoder and LVDT
figure;  % Figure 9
plot(EncDisp,'b-');
hold on
plot(X,LvdtDisp,'r-',X,polyval(LvdtDispPoly,X),'r:');
xlabel('1/2 Cycle number');
ylabel('Displacment (mm)');
legend('Encoder: actual displacement','LVDT: actual displacement',...
    'LVDT: linear fit','Location','Best')
TxtStr_1 = ('Displacement per 1/2 cycle for Encoder and LVDT');
title({TitleStr,TxtStr_1});
grid on
clear TxtStr
TxtStr(1) = cellstr(sprintf('Encoder = %6.4f +/- %6.4f',...
    MeanEncoderDisplacement,StDevEncoderDisplacement));
TxtStr(2) = cellstr(sprintf('LVDT actual = %6.4f +/- %6.4f',...
    MeanLvdtDisplacement,StDevLvdtDisplacement));
TxtStr(3) = cellstr(sprintf('LVDT poly  = %6.4f*X + %4.2f',...
    LvdtDispPoly(1,1),LvdtDispPoly(1,2)));
textbp(TxtStr,'BackgroundColor',[1 1 1],'EdgeColor','black','LineStyle','-')
```

```
axis([-inf +inf EncMax-0.8 EncMax+0.2])

% % % % % % % % % % % % % % % % % % % % % % % % % % % % % % % % % % %
% % %
% Time lag between Encoder Max and LVDT Max (and Min/Min)
TimeLagMax = MidLvdtTimeMax - MidEncTimeMax;
TimeLagMin = MidLvdtTimeMin - MidEncTimeMin;

% 1st order curve fit both difference vectors
XMax = transpose(1:length(TimeLagMax));
XMin = transpose(1:length(TimeLagMin));
TimeLagMaxPoly = polyfit(XMax,TimeLagMax,1);
TimeLagMinPoly = polyfit(XMin,TimeLagMin,1);
MaxPolyFit = polyval(TimeLagMaxPoly,XMax);
MinPolyFit = polyval(TimeLagMinPoly,XMin);

MeanTimeLagMax = mean(TimeLagMax);   MeanTimeLagMax
StDevTimeLagMax = std(TimeLagMax);   StDevTimeLagMax
MeanTimeLagMin = mean(TimeLagMin);   MeanTimeLagMin
StDevTimeLagMin = std(TimeLagMin);   StDevTimeLagMin

% Plot Time lag results
figure;   % Figure 10
plot(XMax,TimeLagMax,'b',XMax,MaxPolyFit,'b:')
hold on
plot(XMin,TimeLagMin,'r',XMin,MinPolyFit,'r:')
legend('Lag @ Max','Max Polyfit','Lag @ Min','Min Polyfit','Location','Best')
ylabel('Lag Time (seconds)')
xlabel('Cycle number')
TxtStr_1 = ('Lag Time of LVDT max/min behind Encoder max/min, By cycle');
title({TitleStr,TxtStr_1});

% % Plot all four signals overlaid upon one another, on two axis, scale PSI
% % to kPa
```

```
% PressScale = 6.89475729; % 1 psi = 6.89475729 kPa
% PressSmoothScaled = PressScale * PressSmooth;
% PressFiltScaled = PressScale * PressFiltTrnc;

% Smoothed data
figure
X1 = [TimeTrnc,TimeTrnc];
Y1 = [EncTrnc,LvdtSmooth];
X2 = [TimeTrnc,TimeTrnc];
Y2 = [LoadSmooth,PressSmooth];
[AX,H1,H2] = plotyy(X1,Y1,X2,Y2);
set(AX(1),'YLim',[0,7]);
points = 8;
ticks = get(AX(1),'YLim');
ticks = round(linspace(ticks(1),ticks(2),points));
set(AX(1),'YTick',ticks);
set(AX(2),'YLim',[-50 300]);
ticks = get(AX(2),'YLim');
ticks = round(linspace(ticks(1),ticks(2),points));
set(AX(2),'YTick',ticks);
ylabel(AX(1),'Position (mm)');
ylabel(AX(2),'Force (N) and Pressure (kPa)');
xlabel('time (seconds)');
legend('Encoder','LVDT','Load Cell','Pressure');
clear TxtStr_1;
TxtStr_1 = ('Combined data, Digitally filtered');
title({TitleStr,TxtStr_1});
grid on;

% Analog filtered, but not smoothed data
figure
X1 = [TimeTrnc,TimeTrnc];
Y1 = [EncTrnc,LvdtFiltTrnc];
X2 = [TimeTrnc,TimeTrnc];
```

```
Y2 = [LoadRawTrnc,PressFiltTrnc];
[AX,H1,H2] = plotyy(X1,Y1,X2,Y2);
set(AX(1),'YLim',[0,7]);
points = 8;
ticks = get(AX(1),'YLim');
ticks = round(linspace(ticks(1),ticks(2),points));
set(AX(1),'YTick',ticks);
set(AX(2),'YLim',[-50 300]);
ticks = get(AX(2),'YLim');
ticks = round(linspace(ticks(1),ticks(2),points));
set(AX(2),'YTick',ticks);
ylabel(AX(1),'Position (mm)');
ylabel(AX(2),'Force (N) and Pressure (kPa)');
xlabel('time (seconds)');
legend('Encoder','LVDT','Load Cell','Pressure');
clear TxtStr_1;
TxtStr_1 = ('Combined data, Only analog filtered');
title({TitleStr,TxtStr_1});
grid on;

% figure
% plot(TimeTrnc,EncATrnc,TimeTrnc,EncBTrnc)
% legend('EncA','EncB','Location','Best')
%
% figure
% plot(TimeTrnc,EncTrnc,TimeTrnc,LvdtFiltTrnc,TimeTrnc,EncATrnc,...
%     TimeTrnc,EncBTrnc);
% xlabel('Time (seconds)');
% ylabel('Position (mm) / Encoder Voltage (V)');
% legend('Encoder','LVDT','Encoder ChanA','Encoder ChanB','Location','Best')
% title('Encoder and LVDT position w/ Encoder Channels A&B');

ABC = length(EncATrnc);
NewMin = -0.1;
```

```
NewMax = 0;
EncATrncDig = zeros(ABC,1);
for i=1:(length(EncATrnc))
   if (EncATrnc(i,1) < 1);
      EncATrncDig(i,1) = NewMin;
   else EncATrncDig(i,1) = NewMax;
   end
end

EncBTrncDig = zeros(ABC,1);
for i=1:(length(EncBTrnc))
   if (EncBTrnc(i,1) < 1);
      EncBTrncDig(i,1) = NewMin;
   else EncBTrncDig(i,1) = NewMax;
   end
end

figure
plot(TimeTrnc,EncTrnc,TimeTrnc,LvdtFiltTrnc,TimeTrnc,EncATrncDig,...
   TimeTrnc,EncBTrncDig);
xlabel('Time (seconds)');
ylabel('Position (mm) / Encoder Voltage (V)');
legend('Encoder','LVDT','Encoder ChanA - shifted','Encoder ChanB -
shifted','Location','Best')
title('Encoder and LVDT position w/ analog Encoder Channels A&B (Digitized)');
grid on
```

1.1.2.5 ST Configurator

ST Configurator is a stand-alone program provided by Applied Motion Products, manufacturer of the stepper motor driver and Q Programmer software. As the name implies, it is used to configure parameters in ST drives (like the ST5-Si drive used in the HyPSTR). Normally, ST Configurator is not used. But, occasionally settings made in Q Programmer and downloaded to the drive can have an effect on the drive's configuration that might require using ST Configurator to re-configure it.

If the stepper and/or driver seem to be responding peculiarly, it does not hurt to re-configure the drive. To do so, with the driver plugged in to the USB-to-serial adaptor and the USB plugged into the laptop, open ST Configurator (Figure 1.58. . From there, click File/Open and choose the file "C:\Program Files\Applied Motion Products\ST Configurator\Configuration_to_use", then click the Download to Drive button. It should acknowledge that the transfer was successfully completed.

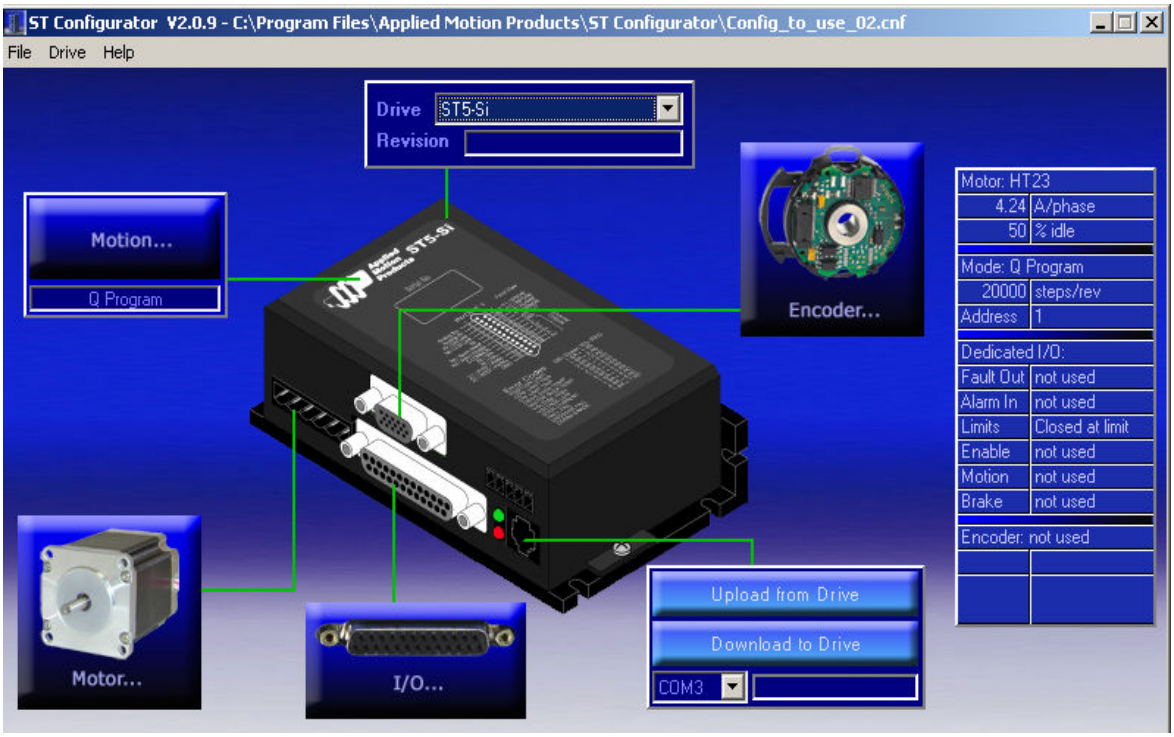

Figure 1.58. ST Configurator user interface

1.2 Testing Patients with the Device

What follows is a thorough, step-by-step procedure to be undergone during human testing in the MRI. The complexity and attention to detail are there to ensure correct functioning of the device, aid someone who is not familiar with the device in using it, and most importantly, to ensure the safety of the test subject. Used improperly, the device has the capability to hurt the test subject or even the operator; **PLEASE USE CAREFULLY!**

1.2.1 Pre-test step

i) Day before: Fill tank ½ full of water and add some food coloring, then leave to sit out overnight or longer

1.2.2 Device set-up

i) Assemble loading jig in MRI imaging room

(1) Slide backboard onto rails

(2) Slide E-stop button onto whichever rail corresponds to the side the test subject would prefer

(3) Slide leg restraint onto appropriate rail, corresponding to which foot is going to be tested

(4) Slide cylinder loading frame onto rails

(5) Don't tighten fasteners down yet; adjustments will need to be made once the person lies in the jig

ii) Wiring connections:

(1) Connect the device's white power supply cord to a wall power outlet

(2) Connect to the white power supply outlet on the device cart:

(a) Main project box's electrical cord (black)

(b) Laptop power supply

(3) Connect to the project laptop:

(a) 100 foot serial cable (for PPU signal output)

(b) USB hub (w/ mouse and USB-to-serial converter for actuator) into top USB port of laptop as tag specifies. Important to ensure COM ports are correctly assigned and Q Programmer won't be confused.

(c) DAQ board USB into bottom USB port of laptop (per the tag)

(d) Laptop power supply

(4) Connect serial-to-fiber optic converter (small gray metal box connected to the 100 foot serial cable) to:

(a) Wall power outlet

(b) CDAS fiber optic inputs – Remove fiber optic cables and connect converter cables (marked with B9 and B10) in their place (Figure 1.59).

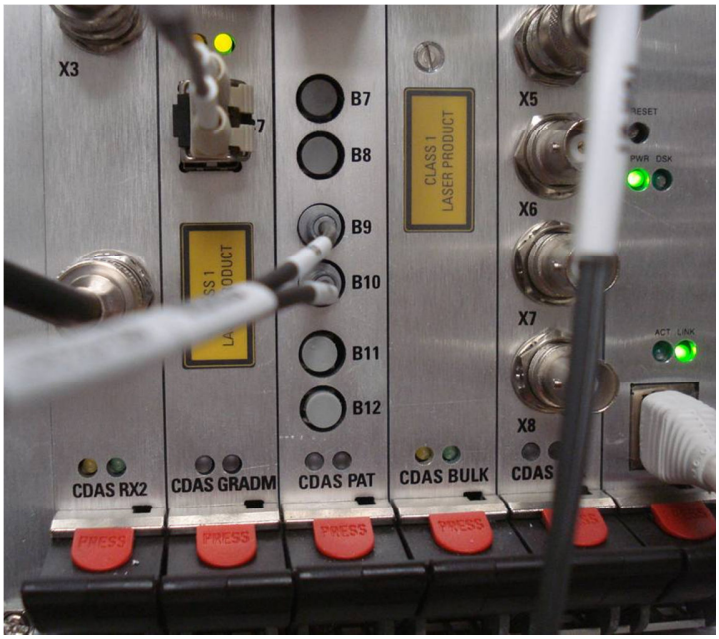

Figure 1.59. Connection to CDAS (picture from Phillips)

(5) Run fiber optic lines for fiber optic E-stop button through wall ports, connect to 2 open ports on fiber optic controller in large project box (either orientation, doesn't matter)

iii) Hydraulic connections

(1) Run hydraulic tubing and water return tubing through the port in the wall
(2) Connect hydraulic tubing to compression fitting on bottom of slave cylinder
(3) Use Velcro straps to secure pressure and drain tubing along with fiber optic cable to one of the side rails of the jig, to ensure it doesn't get caught up in anything when the bed moves.
(4) Use a Velcro strap to keep the syringe over the slave from running into the MRI bore.
(5) Connect fill tubing (big diameter, clear, soft tubing) to spout of fill tank. Use the black plastic clamp to seal the tubing around the brass pipe fitting to prevent water coming back out onto the floor.

1.2.3 User-specific test parameters

i) Power-on the laptop (make sure USB ports and serial cable are connected before starting)

ii) Open programs:

(1) Q Programmer

(2) LabVIEW Master.VI: using shortcut on desktop will start LabVIEW in High Priority execution mode, which is necessary). Do not open block diagram.

(3) Open the Excel pre-processing worksheet

(a) input user-specific displacement and test rate into Input boxes

(b) Click Data tab at top, then Solver

(c) Ensure "Set Objective" is pointing to RMSE cell (yellow highlight)

(d) Object To: MIN (minimize the error)

(e) Ensure “by changing variable cells” is pointing to Solver Variables cells (yellow highlights)

(f) Ensure each variable is constrained to be:

(i) An integer (Q Programmer parameters have a resolution, the variables are set-up to account for that resolution when constrained to be integers)

(ii) > 1

(iii) < 1000

(g) Set solving method to “GRG Nonlinear”, run optimization

(h) Look at resulting graph, make sure you’re in the ballpark

(i) If not, start adjusting the Acceleration/Velocity input cells by hand to get them close

(j) Tighten up the boundaries to more closely envelope the approximate settings, while still giving the optimization algorithm room to move around

(k) Set solving method to “Evolutionary”, re-run optimization

(i) Did it do any better?

(ii) You can also adjust the Solver Variable values by hand to double-check that you’ve found the min RMSE

(iii) Run several iterations if you aren’t sure that you’ve found the global minimum.

(l) Input test subject body weight into the spreadsheet in pounds to:

(i) Calculate user-specific Not-To-Exceed pressure

(ii) Calculate psi setting for mechanical pressure relief valve

(4) LabVIEW

(a) Input filename for datalog files

(b) Input “not-to-exceed Pressure” in kPa

(c) Check that PPU Signal Generation has correct value to trigger once per cycle (10,000 milliseconds = 10 seconds = 0.1 Hz cycling rate)

(d) Make sure that the “Record Data” button is in OFF position

(e) Click Run button

(i) Ensure that encoder graph & numeric indicator and pressure graph & numeric indicator start displaying data

(ii) Ensure that big red EMERGENCY PRESSURE RELEASE button is not depressed. If so, or if unsure, click it. If it goes blank, it is depressed.

1.2.4 Power-on

i) Toggle on the three left-most switches on the main project box (labels are Misc. Power Supply, Actuator Power, Sensor Power Supply)

ii) Did you hear the “ker-thunk” sound of the solenoid valve energizing?

(a) Yes: great, that way the system won’t spew water out when you fill it

(b) No:

(i) Check if red LED light in test operator E-stop button is lit

1. If not, pull up on E-stop button to activate it

(ii) Check if test subject E-stop button is depressed

1. If so, twist button to release, then go to the fourth toggle switch on the main project enclosure (labeled Fiber Optic E-stop Reset) and turn it on for 0.25 – 2.0 seconds and then back off. This resets the fiber optic controller so it’s outputting a voltage to the SSR that drives the solenoid circuit.

(iii) If still not, it means that the DAQ Digital Output is set to LO.

1. Double-check that the big red EMERGENCY PRESSURE RELEASE button is not depressed.

2. Double-check that the not-to-exceed pressure is set to a realistic value (not lower than values the pressure transducer is currently reading)

(iv) If you still haven't heard the solenoid valve engage by this point, there may be bigger problems. Double-check your steps.

1.2.5 Setup and test the safety system

i) Using the values calculated in the Excel spreadsheet, set the not-to-exceed pressure in the LabVIEW VI

ii) Using the mechanical pressure relief valve calculated in the Excel spreadsheet, adjust the mechanical valve. The valve was calibrated against a black marker line drawn on the valve body (circled in red, Figure 1.60)

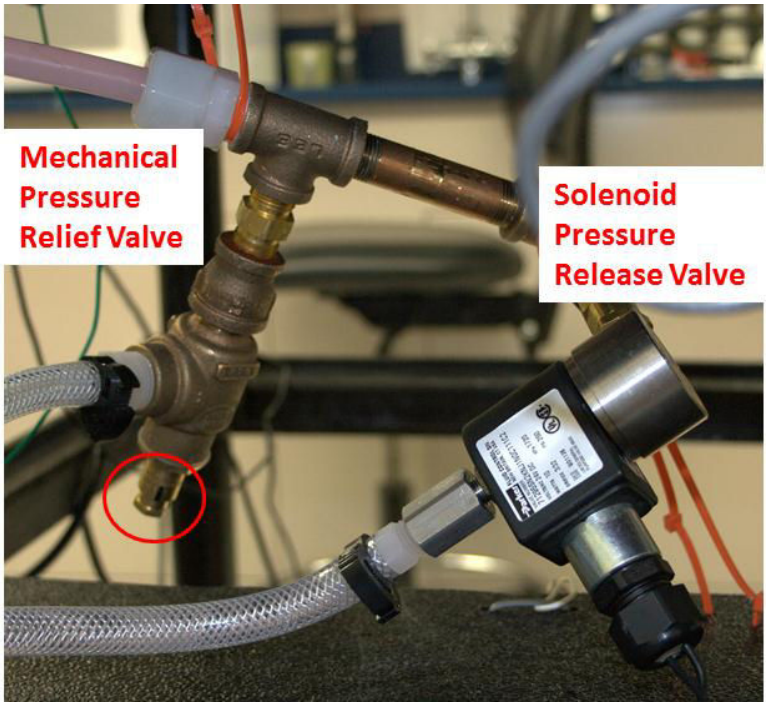

Figure 1.60. Mechanical pressure relief valve and solenoid pressure release valve

iii) Depress the test subject's E-stop button to ensure the solenoid valve opens (listen for it) then reset the button by twisting it and toggling the reset switch on the project box. **It would be best if the test subject can perform the button test, in order to give them an idea of the force required to activate it so that they aren't concerned about resting their hand on the button during testing.**

iv) Depress the test operator's E-stop button (on top of the DAQ box), then reset it

v) Click the red Emergency Pressure Release on the LabVIEW front panel

vi) Ensure the solenoid is re-activated before proceeding

1.2.6 Fill system and bleed

Refer the hydraulic schematic (Figures 1.61, 1.62) and the photos of the valves for filling and bleeding of the hydraulic system.

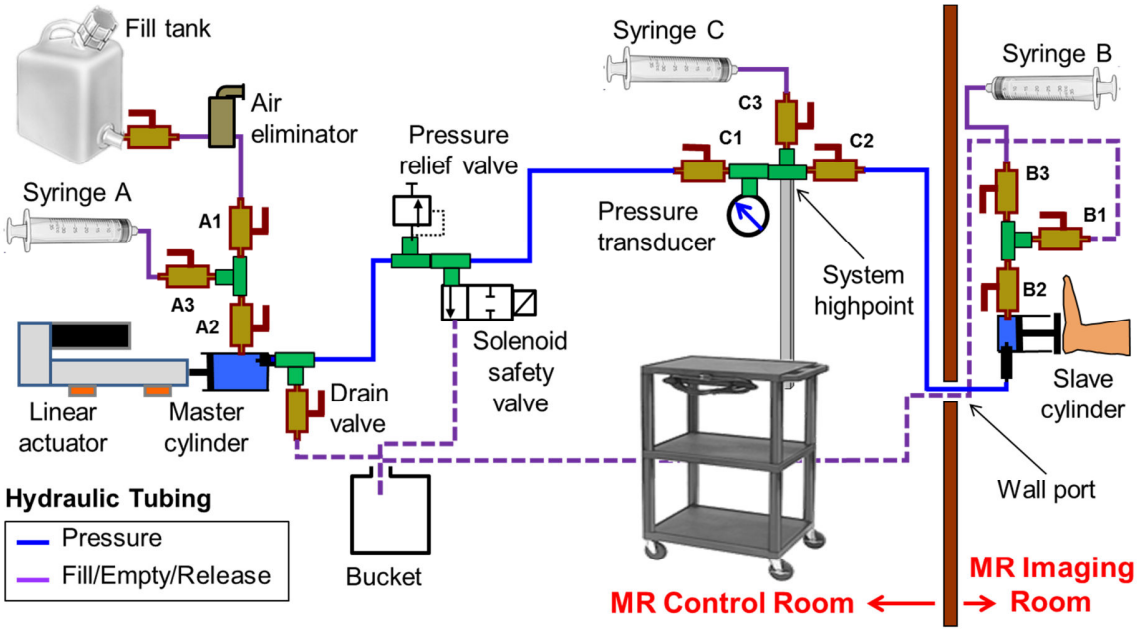

Figure 1.61. Hydraulic schematic showing componentry and location in regards to MRI magnet

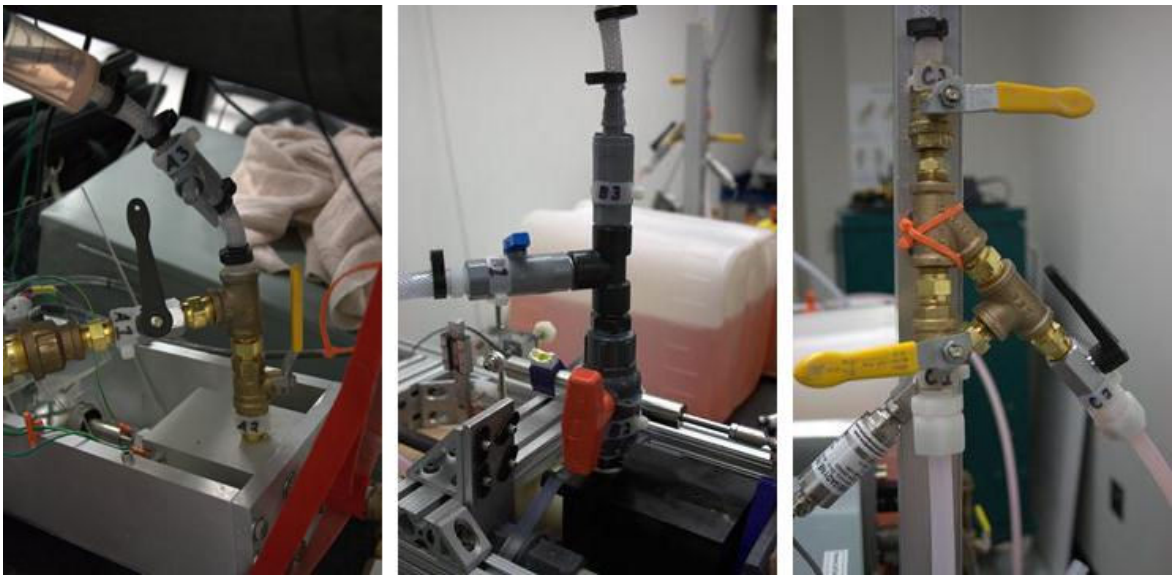

Figure 1.62. From left to right: master cylinder, slave cylinder, and system high point labeled valves

i) Open all valves but B1

ii) Depress all three syringes

iii) Open valve on fill tank to fill line

iv) Pull water through system

(1) Retract Syringe B

(2) While holding Syringe B retracted, close Valve B2 (above slave cylinder)

(3) Open Valve B1, expel Syringe B contents to waste line

(4) Close Valve B1

(5) Open Valve B2

(6) Repeat process, pulling fluid into system line, until you start drawing up mostly fluid into Syringe B

(7) Ensure that you finish this step by closing Valve B1, effectively closing off the far end of the slave end of the system

v) Perform the initial “bubble chase”

(1) Use the MRI-safe titanium adjustable wrench at BMIC to use to tap on components inside the MRI room

(2) Pick a point in the tubing (lowest point, if tubing is stretched out)

(3) From that point, work any bubbles in the fluid to the high point at the slave cylinder by tapping and elevating the tubing, allowing the bubbles to rise towards the slave cylinder end

(4) From that same point but in the other direction, work any bubbles towards the system high point

(5) At point where tubing passes through wall port, it worked best to get air out to high point on one side of the wall port and then pass that tubing through the port, so the tubing that was horizontal in the port is able to be repositioned and air bubbles to rise

(6) Give a quick tap to master cylinder, slave cylinder, valves, and both lines of tubing from master cylinder to valves and from valves to system high point

vi) Repeat pulling water through system to expel air that was just brought to the slave cylinder

vii) Remove air at system high point

(1) Retract Syringe C to draw out air at high point

(2) Close valve C3 (below Syringe C), then unscrew Syringe C's Luer-Lok lock connector and empty the syringe of air to atmosphere

(3) Re-attach Syringe C, open Valve C3, and repeat until air at high point has been removed

viii) Withdraw all three syringes so that they are ⅓ – ½ full of water, with little air inside of them

ix) All Valves to Syringes (A3, B3, C3) should still be open, allowing fluid to circulate

x) Q Programmer on laptop:

(1) Open "advance_to_extension_limit.qpr", Download, then Execute

(2) Open "retract_X_distance_reset_to_zero.qpr", adjust the retraction distance to 400,000, Download, then Execute

(3) Open a 0.1 Hz sine wave file ("Sine_0.1hz_5.0mm.qpr" is an example)

(4) Input a distance parameter in microsteps of 390,000 microsteps

(5) Change number of cycles to 5

(6) Download program, then execute

xi) While system is cycling, tap bubbles out, always trying to move air still residing in system to one of 3 local high points

(1) With end of wrench or something similar, start by tapping master cylinder

(2) At same time, lift up the end of the actuator/cylinder/frame system with the hydraulic line up in the air to ensure that any bubbles being tapped out are flowing up the hydraulic line towards the system high point

(3) Work your way through the hydraulic system, tapping tubing continuously

(4) At valves, move valves around as tapping such that any air trapped inside the valve will find its way to the hydraulic line, and move towards the system high point

(5) Similar to the initial “bubble chase”, starting at lowest point of long run of tubing, tap tubing continuously and move highest point such that bubbles work their way to the slave cylinder

(6) At slave cylinder, force platen to most retracted position (to empty slave cylinder of water) then tap cylinder continuously while rotating around to ensure that bubbles rise to high point (Syringe B)

(7) Starting at same lowest point in long run of tubing, tap tubing continuously, moving highest point so that bubbles work their way to the high point of the system

xii) Push bubbles out (force bubbles that are near or at a high point escape to a syringe)

(1) Close Valve C1, ensure Valve B2 is open and Valve B1 is still closed

(2) Using Syringe C, push fluid through system towards slave, increasing fluid in Syringe B

(3) Then, push fluid from Syringe B into Syringe C

(4) Repeat a few times until you see no bubbles moving into fluid

xiii) Pull bubbles out (use a vacuum to pull bubbles from small cavities of valves/pipe fittings near high points)

(1) Ensure that Syringe B has only a little fluid in it (less than ¼ full); transfer the rest to Syringe C

(2) Close Valve C2

(3) With Valve B1 still closed and Valves B2 and B3 open, pull a vacuum on Syringe B. **Go slowly and cautiously,** as overzealousness will remove the plunger from the syringe and spray water all over.

(4) Slowly let the plunger move back to its initial position, and repeat several times. You will probably see some air bubbles working their way up the tubing to Syringe B.

(5) Once you don't see bubbles rising into the syringe any longer, let plunger retract to initial position

(6) Close Valve C1, open Valve C2, and push fluid from Syringe C to Syringe B such that Syringe C is only about ¼ full.

(7) Close Valve B2.

(8) Repeat process of pulling air from long run of tubing, this time to other end of tubing (the system high point)

(9) Once complete, close Valve C2, open Valve C1.

xiv) Repeat process for short run of tubing

(1) First push water from Syringe C to Syringe A and back, repeatedly.

(2) Then, pull a vacuum on Syringe A with Valve C1 closed.

(3) Finally, pull a vacuum on Syringe C with Valve A2 closed.

xv) Open valve B2 and depress the syringe just enough to extend the slave piston approximately 0.5 – 1.0 from bottomed out in the cylinder. Close Valve B2.

xvi) **When complete, double-check that:**

(1) Valves A2 and B2 are **CLOSED**

(2) Valves C1 and C2 are **OPEN**

(3) Congratulations; you now have a bled, closed system running from the master cylinder to the slave cylinder.

(4) Take the slave cylinder assembly and attach it to the loading frame on the jig

1.2.7 Obtain high-resolution, static scan of the subject

(1) Subject in supine position (Figure 1.63)
(2) Foot itself not touching anything except RF coils (to prevent displacement of the tissue from its unloaded state)
(3) Leg and hip supported with sandbags and cushions to ensure a supported limb, not liable to rotate or shift during the scan
(4) From static scan, obtain unloaded tissue thickness of test subject using MRI software

Figure 1.63. Static scan arrangement showing leg supported but only MRI coils touching foot

1.2.8 Position test subject

i) Place the loading jig onto the MRI bed
ii) IMPORTANT: emphasize to the test subject that depressing the emergency button at this point will require a complete refill/re-bleed of the system, which takes a lot of time. It should only be depressed for painful loading!

iii) Have the test subject lie down on the jig (may require the assistance of someone, as getting on and off the MRI bed with no handles and the loading jig in the way is not easy)

iv) Position pillows/cushions in any place that sharp corners/edges might cause pain on subject

v) Have the subject slide forward until the tested foot is very close to the loading platen

vi) Slide the back board and leg restraints into the proper place, and tighten down the fasteners on the rails

vii) Buckle the backboard straps and gently tighten them down on the test subject's shoulders and mid-section

viii) Add towels under the most distal leg support to raise the heel to roughly the correct position

ix) Adjust the leg restraint webbings until snug, and then slowly tighten them down with the cam mechanism

x) Add additional cross strapping over leg to hold it more firmly

xi) Slide slave end vertically to more precisely position plat ten on heel

xii) Adjust the emergency button so that it is in a position that the subject can easily reach

xiii) Double-check that all fasteners on modular components holding the subject are tight, that the backboard straps are tightened, and that the leg restraint straps are tightened, but that the subject isn't experiencing discomfort (remind them that they might need to be in this position for up to 30 minutes)

xiv) Tell the subject that they cannot move around from this point on,

xv) Finally, adjust the loading platform in the superior/inferior direction and the anterior/posterior directions such that the loading platen just barely touching the plantar surface. Ensure that the loading platen is centered on the heel or

forefoot, and that the volume desired to be imaged is centered (as much as possible) over the loading platen.

xvi) If need be, open valve B2 and use Syringe B to move the platen towards or away from the subject's foot

xvii) Move the MRI bed into the bore, being careful to watch the tubing and cables so they don't catch on anything

1.2.9 Position loading platen

i) Q Programmer:

(1) Open "advance_CCW_incrementally.qpr" file, Download program to driver

(2) With someone watching in the MRI bore, execute the program incrementally at 320 microsteps (0.02mm) each execution until the person watching the loading platen in the MRI imaging room sees definite contact between a significant portion of the subject's foot and the loading platen or when the moving average pressure crosses over 30 kPa

(3) Open sine wave cycling file (example file is "Sine_0.1hz_5.0mm.qpr")

(4) Input acceleration, deceleration, and velocity parameters from Excel worksheet.

(5) Change number of cycles to 5

(6) **IMPORTANT**: Have someone else double-check that the parameters:

(a) Have been input correctly

(b) Check the distance-to-displace field "FP…." (do the math with a calculator: 16,000 microsteps = 1mm)

ii) Close the Excel program

iii) Alert the subject that you will be performing 5 cycles of testing in order to ensure that they are still comfortable

iv) Q Programmer: click Download Program button, then the Execute Program button

v) In LabVIEW, watch the:

(1) Encoder data: did the encoder travel the distance planned for the experiment?

(2) Pressure data, specifically maximum pressure reached: does the value correspond to a load approximately equal to body weight for the test subject?

vi) Confirm with the test subject that everything felt fine (no pain or discomfort). You may even stress that it is easier to deal with any discomfort problems by re-adjusting at this point rather than needing to invalidate the test by using the E-stop button in middle of testing.

vii) If any discomfort exists

(1) Reposition the person in the jig and/or the loading frame

(2) Re-increment the actuator

(3) Re-run 5 cycles and see if the discomfort has been eliminated

1.2.10 Testing

i) Q Programmer:

(1) Enter the appropriate number of cycles into the sine displacement wave file (choose more than the test time says it will take, as the MRI's estimated scan time is not entirely accurate and if displacement stops in the middle of the gated scan, the entire scan is lost. There is no downside to running the actuator longer, as you can always stop the program when the scan completes instead of waiting for all the cycles to complete.

(2) Download Program to the stepper motor driver

ii) Wait for MRI operator to say that they are ready for you to begin.

iii) LabVIEW:

(1) If PPU Signal Status LED is already lit-up, stop VI (by clicking Stop button) and then restart (by clicking the Start VI button)

(2) Zero out the encoder

(3) Zero out the elapsed time

(4) Click Record Data button

(5) Click Arm Trigger? Button

iv) Q Programmer: click the Execute Program button

1.2.11 Test completion

i) LabVIEW: click Stop button on VI (not the Stop Sign in the toolbar, but the button labeled “Stop” on the GUI)

ii) Remove the subject from the loading jig

iii) Q Programmer: close program (to ensure no unintentional movement of the actuator)

iv) Flush water from system

(1) Close valve attached to fill tank, remove fill line from fill tank

(2) Attach fill line to sink in control room, use clamp with light pressure from pliers to secure tubing around sink head

(3) Open Valve B1 and Valve B2, depress syringe B, then close Valve B3

(4) Open Valve C3, empty syringe C, then close Valve C3

(5) Depress syringe A, close Valve A3, open Valves A1 and A2

(6) Turn the sink on and let it run until the red-colored water is gone from the tubing

(7) Turn off the sink, detach the fill line and empty what you can into the sink, then use a Velcro strap to attach the fill line to the cart so it won’t spill

(8) After ensuring that the drain tubing connected to the drain valve near the master cylinder is in the waste bucket, open the drain valve

(9) Remove syringe C from its Luer-Lok, and open valve C3. This should allow water to flow out the low points of the system, now the drain valve and the drain line at the slave cylinder.

v) Disassemble loading jig and put back on cart

vi) Remove laptop and laptop power supply to be taken back to the VA

vii) Store test carts away at BMIC

viii) Post-process data by converting datalog file from PPU signal generation into text and .TDMS file with MATLAB

1.3 Lessons Learned

As in many engineering projects, a great deal of the time spent on this project was in testing and debugging of the system in order to arrive at a workable design. A Gantt chart of my Master's degree, with class work comprising lines 1-6 and the design/build/test work on this device comprising lines 7-46 was constructed (Figure 1.64).

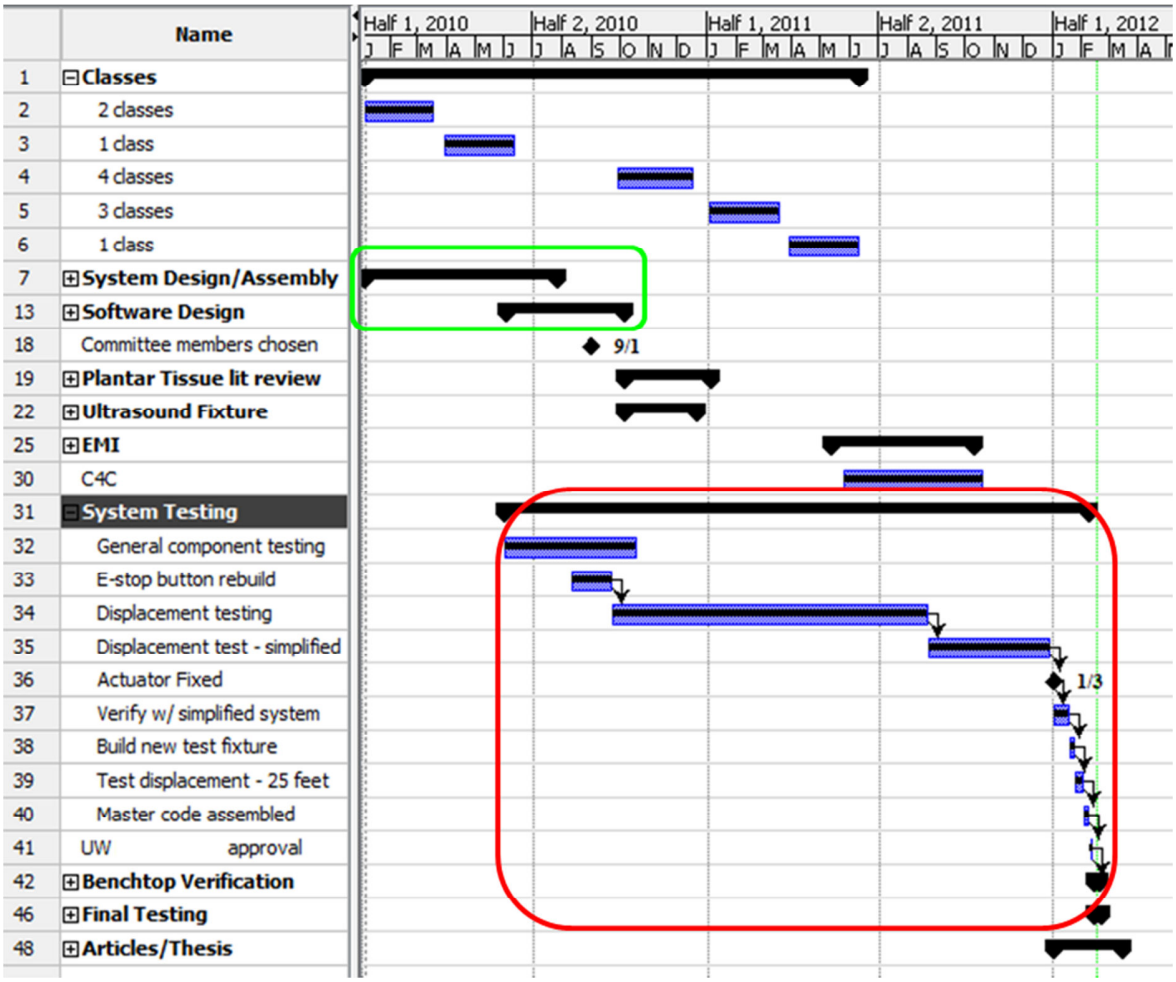

Figure 1.64. Gantt chart of Master's degree (both thesis and classes)

Highlighted in green are the summarized line items representing design and build of the device. As can be seen, this period lasted for approximately 10 months, with some testing work being done in parallel. Highlighted in red are the line items (expanded) representing all of the testing and debugging of the device. This period is approximately 22 months long!

It should be noted that during Autumn quarter of 2010 and Winter quarter of 2011, I was taking a full load of classes, and work on the device was frequently out-prioritized by classwork. But, with that said, it is obvious that taking the device from “built” to “functional” took a great deal of time.

Instead of including the 500+ PowerPoint slides generated during that timeframe documenting hypotheses, tests of hypotheses and outcomes of testing, I have decided to include the following summary list. This might be considered a **"Don't Do This Next Time" list** combined with a **"This Worked Well" list**. See Appendix B for a similar section dealing strictly with the electronics.

- Depending on the time required to disassemble/reassemble the hydraulic system and depending on the ease with which individual components may be tested, any problems with the system's performance at an assembly level should be cause to consider disassembly and component-by-component testing. It wasn't until I had ruled out nearly every other hydraulic component while trying to understand erratic displacements of the slave piston that I tested the linear actuator and rotary encoder with a digital caliper. That simple, component-level test (Figure 1.65) was what determined that my linear actuator, assumed to be operating correctly as it was the most "professionally-designed" part of my entire displacement system, was actually to blame.

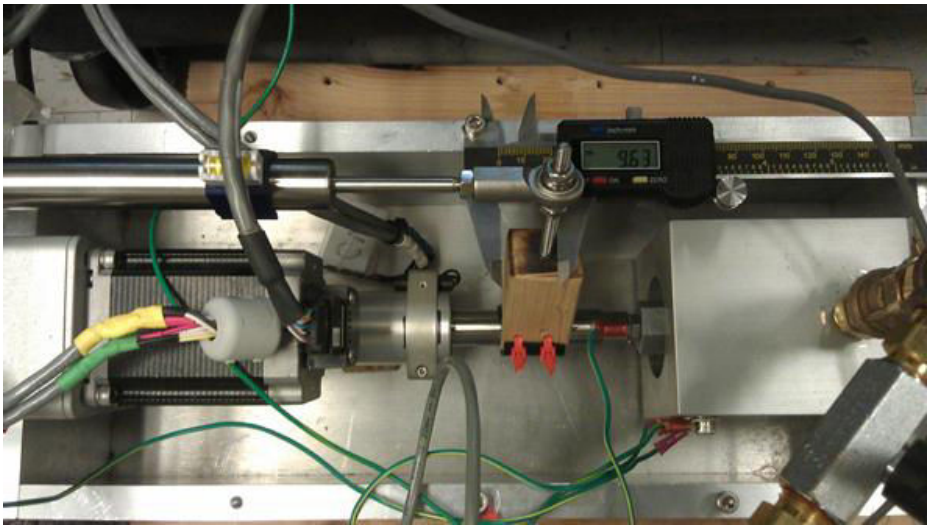

Figure 1.65. Test setup that proved that the linear actuator was not displacing as the encoder claimed

- Do not assume that all design requirements are rigid requirements. This device was designed with a "no-metal in the MRI at all" approach for most of the project. This made sourcing existing hydraulic systems impossible (they all seem to contain at least some non-ferrous metal in the fittings/tubing) and also seemed to eliminate force and displacement measurements inside the MRI. The team thought that we could make do while remaining within these design requirements. Literature that

was discovered late in the project shows experiments with both non-ferrous metals structures and measurement transducers containing metals near the imaged volume in the MRI (Chinzei, 1999). As in many engineering projects, a critical review of the rigidity of all design requirements should have been conducted. It may have led to deeper investigation and/or exploratory experiments regarding metals inside the MRI, and a subsequently larger design space with more existing options.

- Ensure ample airflow behind a contained single-acting piston. The initial slave cylinder design had nowhere for air trapped behind the piston to go to when the piston was extended, so a vent hole was machined in. Much later in the project, it was determined that the vent hole had much too small of a cross-sectional area to effectively move enough air out; the slave cylinder was acting as though there was a pressurized air bladder inside of it. Once several additional, large cross-sectional area vents were machined into the cylinder, air was able to easily escape and the piston was able to move with ease.
- Pressure surges due to a sudden momentum change applied to a nearly-incompressible fluid (aka, “water hammer”) play a large part in water-based hydraulic system design. The pressure in the system (teal-color) under a ramp-and-hold movement of the actuator (blue color) while loading a silicone gel test article is shown (Figure 1.66). As can be seen, the actuator was sitting at position 0mm, then ramped to approximately 3.5 mm at a velocity of approximately 15mm/second and then held in that position. The pressure signal shows a very clear oscillation as the pressure surge travels through the water from one end of the system to the other. The peak pressure reading due to the initial actuator movement is approximately 2x that of the pressure once the move was complete and the silicone gel was placing a load on the system. It is because of this phenomena that the device is cycling at 0.2 Hz (5x slower than the initial design cycling rate) and using a sine displacement wave instead of a triangle (as originally planned).

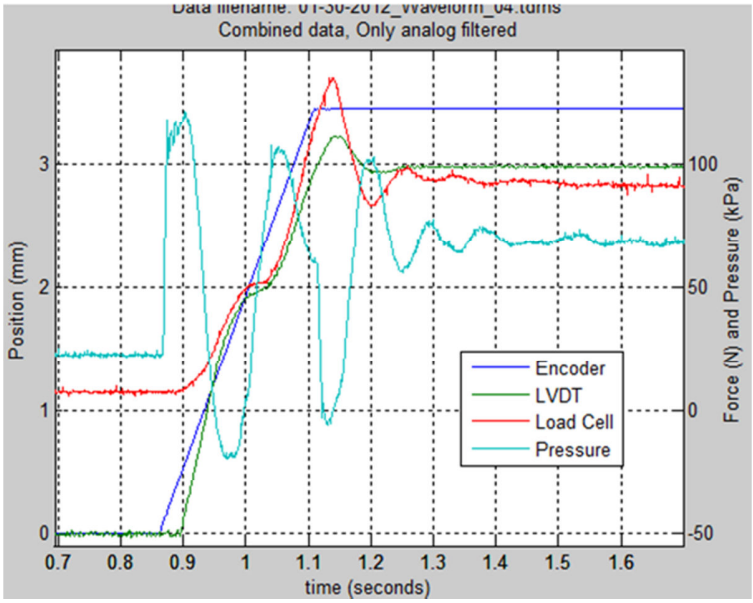

Figure 1.66. Example of water hammer effects in this hydraulic system

- The way that the device will be proven out (the verification testing) should have been considered early in the initial design portion of the project and incorporated into the initial design. Several iterations of support structure were designed and built to mount the LVDT to the slave cylinder and adjust it to be aligned with the piston shaft (Figure 1.67). Finding a relatively simple solution to mounting the LVDT was difficult due to the fact that the rest of the system had been designed without thought to how it might be tested. Additionally, the initial method of mounting the load cell to the slave system was not structurally rigid and could be observed flexing during testing, affecting the test results. Moving forward, any new designs should consider how they will be tested and how that test hardware will integrate with the system.

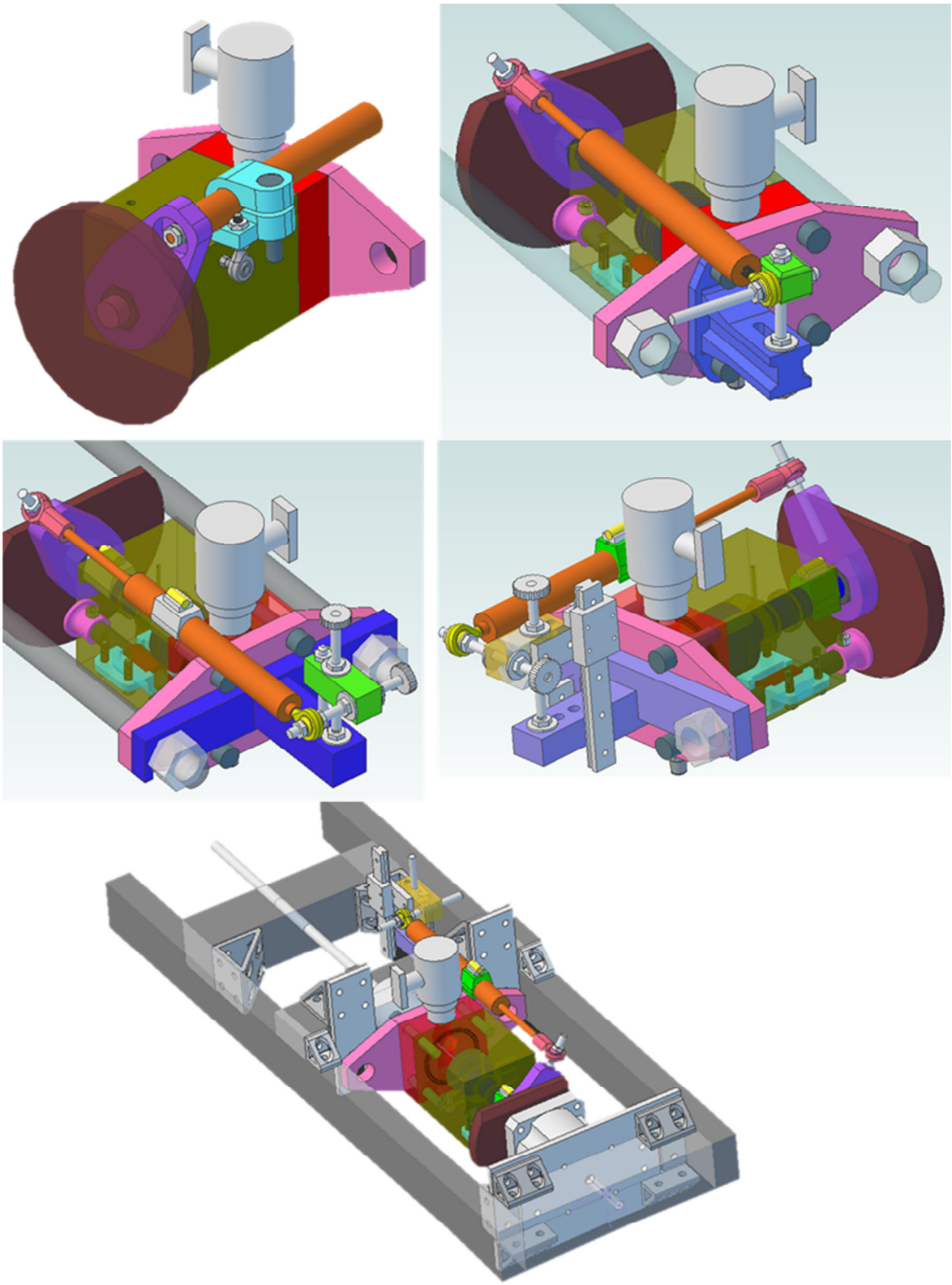

Figure 1.67. Several iterations of LVDT to slave cylinder mounting mechanisms

- When using analog filters to remove noise from signals, start simple and build up to more complicated filter schemes only as necessary. After discovering that a simple 1st order Resistor-Capacitor (RC) filter worked at smoothing out noisy data, but imparted a DC offset to the signal, I moved straight to using complex 8th-order IC (integrated circuit) switched-capacitor filters. While the IC filters were certainly a superior filter from a purely technical point of view, I spent several weeks trying to make them work reliably without offsetting the signal as the RC filters had. More research led me to discover active RC filters; a simple RC filter as I'd used before with an op-amp voltage-follower circuit to reduce the effect of the RC filter on the signal. Much simpler than an IC, and effective, even though it's only 1st order.
- Always apply O-ring lubricant to all O-rings except for the O-rings located inside the tubing compression fittings; they are not designed to be lubricated.
- If purchasing new power supplies in the future, understand how much noise the supply might emit and spend more money if necessary to purchase "quiet" supplies. It can only help prevent EMI issues.

1.4 Future Work

Following is a list of possible future work to be taken in regards to improving this, Version 1 of the device, or in designing and building Version 2. I have tried to arrange them roughly from easy/fast-to-implement to the most costly/time-consuming.

- Test de-gassed water (used in some forms of ultrasound testing) to see if it removes more air from the hydraulic fluid than I have been able to with the methods detailed in this user's manual.
- An optimization of the current fill/bleed procedure in order to reduce time spent in the MRI would be beneficial. Solutions might include different valve/drain tube arrangements and/or some form of pump to move the fluid.
- Test some form of hydraulic oil in order to determine if the higher cycling frequencies made possible due to the reduced pressure shock waves are worth the trade-off for the slightly higher compressibility of the hydraulic fluid.
- Incorporate displacement feedback into the device, in either an iterative-feedback tuning loop (easier to implement) or a closed-loop system (more complicated to implement). Koseki (Koseki et al. 2004)used a charge-coupled device (CCD) laser micrometer just outside of the MRI bore to measure displacement, and another group has used fiber optic linear encoders inside of the MRI (Chinzei et al. 2000).
- Add an MRI-compatible spring into the slave cylinder in order to aid the system in retracting the slave piston to the same position zero during each cycle.
- Move to a double-acting hydraulic slave cylinder using a hydraulic motor, reservoir, and control system located in the MRI control room. This probably requires finding existing hydraulic hoses and fittings that are MRI compatible.
- Add shear loading to the device, to mimic the loading the plantar foot sees during gait. This completely changes most of the slave end of the system, and probably necessitates displacement sensing in the MRI to ensure both degrees of motion are precisely known.

1.5 References

1.5.1 Component User's Manuals

The following is a list of user's manuals that were and still are referenced often by the author in using, testing, and debugging the device's components and software. They can be found in a folder on the Desktop of the project laptop, along with all other pertinent electronic device documentation.

- **Test subject fiber optic E-stop button controller:** Banner Engineering: PICO-GUARD Fiber Optic Safety System Controller Instruction Manual
- **Stepper motor driver software:** Applied Motion Products, Inc.: Host Command Reference, Q and SCL commands for servo and stepper drives
- **Stepper motor driver hardware:** Applied Motion Products, Inc.: ST Hardware Manual
- **Data acquisition board:** DAQ M Series NI USB-6212 User Manual and NI USB-6212 Specifications

1.5.2 Works Cited

Blume, P.A. 2007, *The LabVIEW style book,* Prentice Hall, Upper Saddle River, NJ.

Chinzei, K., Kikinis, R. & Jolesz, F.A. 1999, "MR Compatibility of Mechatronic Devices: Design Criteria", *Lecture notes in computer science.,* , no. 1679, pp. 1020.

Chinzei, K., Hata, N., Jolesz, F. & Kikinis, R. 2000, *MR Compatible Surgical Assist Robot: System Integration and Preliminary Feasibility Study*, Springer Berlin / Heidelberg.

Douglas De Clue 2002, 06-23-2002 08:07 PM-last update*, Re: How can I get labview to record data into excel in time increments that are not multiples of 10 ms.* Available: http://forums.ni.com/t5/LabVIEW/How-can-I-get-labview-to-record-data-into-excel-in-time/m-p/48816/highlight/true#M30770 [2012, 02/27].

Koseki, Y., Kikinis, R., Jolesz, F.A. & Chinzei, K. 2004, "Precise Evaluation of Positioning Repeatability of MR-Compatible Manipulator Inside MRI", *Lecture notes in computer science.,* , no. 3217, pp. 192-199.

Parker Hannifin Corporation 2007, *Parker O-Ring Handbook O-Ring Division 5700,* 50th Anniversary Edition edn, , Lexington, KY.

Yousheng Yang, Semini, C., Guglielmino, E., Tsagarakis, N.G. & Caldwell, D.G. 2009, "Water vs. oil hydraulic actuation for a robot leg", , pp. 1940-1946.

Appendix B. Reduction Of Electromagnetic Interference Noise In Data Signal Acquisition

TABLE OF CONTENTS

1.1 Introduction 178

1.2 EMI Options 178

1.3 Sources and Components of the Noise in this Project 179

1.4 Aliasing 181

1.5 Modifications Made to the Device 183

1.5.1 General Wiring 184

1.5.2 Grounding 187

1.5.3 Hardware and Miscellaneous 187

1.6 Signal Filtering in Data Acquisition 189

1.7 Analog Low Pass Filters 190

1.7.1 Passive Low Pass Filters 190

1.7.2 Active Low Pass Filters 191

1.7.3 Filter Selection 199

1.8 Digital Filters 201

1.9 Signal to DAQ Connections 203

1.10 References 204

LIST OF FIGURES

Figure 1.1. Acquired signal from stationary LVDT at 100 kHz.....179

Figure 1.2. Discrete Fourier Transform of LVDT signal.....180

Figure 1.3. Oscilloscope voltage measurements of (a) the voltage across the terminals ...181

Figure 1.4. Digital sampling of an analog signal with (c) a frequency < $f_s/2$.....182

Figure 1.5. A system that is sampling an input signal at f_s: (a) will identify signals 183

Figure 1.6. Electrical wiring schematic before EMI re-wiring.....185

Figure 1.7. Electrical wiring schematic after EMI re-wiring.....185

Figure 1.8. Re-wiring before (left) and after (right) photos of the main project box.....186

Figure 1.9. Revised instrument cart layout chosen to physically separate noisy. 187

Figure 1.10. Standard data acquisition and filtering system.....189

Figure 1.11. Ideal low pass filter frequency response.....190

Figure 1.12. Passive low pass filter and frequency response calculations.....191

Figure 1.13. Sallen-Key, double pole filter circuit.....192

Figure 1.14. Four pole (2^{nd} order) Sallen-Key low pass filter schematic.....193

Figure 1.15. Parameters for use with the circuit shown in the schematic above.. 193

Figure 1.16. SCF IC dual line low pass filter: (left) circuit wiring schematic.....194

Figure 1.17. (a) Linear variable displacement transducer (LVDT) signal with no filter.....195

Figure 1.18. 1^{st} order active RC filter schematic (from Storr, 2012) 196

Figure 1.19. Step responses of common filter types with a 1 Hz f_c. Plots can be scaled...197

Figure 1.20. Roll-off performance of common filter types with f_c = 1 Hz. 199

Figure 1.21. Comparison of 1 peak and 1 valley of the triangle displacement wave. 202

Figure 1.22. Analog input connections to DAQ board summary 203

1.1 Introduction

Electromagnetic Interference (EMI) is a potential issue encountered in virtually any analog electronic signal acquisition. In biomechanics, as in many other engineering disciplines, the electronic data contained within sensor signals can be an incredibly vital part of the project or device's function. If the data from these sensors are erroneous due to noise, the investigator may draw incorrect conclusions, or even be injured by a device featuring a closed-loop feedback control strategy. With the steadily increasing number of electronic devices surrounding us every day, it's not likely that EMI will become any less of an issue in the near future. Rather, EMI should be anticipated and designed for from the beginning of any electronics or signal acquisition project. This appendix describes my experiences in going from virtually no knowledge whatsoever of EMI to completely revamping my thesis device in an effort to clean up noisy data signals.

1.2 EMI Options

At the highest level, there are three things to do when designing for EMI:

1. First and foremost, determine how much noise you can live with. No analog signal will ever be perfectly free from noise. Moore's law and its effect on price points for instruments with increased sensitivity and analog to digital converters (ADCs) with higher resolution means that if one zooms in tight enough on a signal plot, it will appear to be noisy. Before investing large quantities of time and money on designing an EMI-proof system, an acceptable noise tolerance for the acquired data should be determined in order to prevent the search for "the perfectly quiet signal".
2. Next, reduce the noise output by the system and/or carried by the data signal lines. Some combination of both of these is most likely required.
3. Finally, filter some of the remaining noise from the data. Most likely, no matter how well you do in reducing noise output and noise carried on the signal line, some EMI noise will embed itself into the data. If that amount is more than you can live with, you'll need to filter it out using analog and/or digital filtering, all while working to ensure that you don't lose any of the features of the data that are important to your situation. As might be said about so much in life, nothing in "filtering" is free; you pay a price (in temporal delay, amplitude shifts, reduced feature prominence, undesired frequency attenuation, etc.) for every filter applied to your data.

1.3 Sources and Components of the Noise in this Project

Early testing of both the pressure transducer and the linear variable displacement transducer (LVDT) used in this project showed a large amount of noise in the data. To better understand where the noise was coming from, the sampling rate of the analog voltage channels for the LVDT was raised from 1 kHz (the rate being used in testing at that time) to 100 kHz. Data were acquired with the LVDT held stationary for less than 1 second and then plotted (Figure 1.1). The regularly spaced spikes translated into an erroneous displacement of greater than 2.5 mm in an LVDT that has a total displacement of 30 mm.

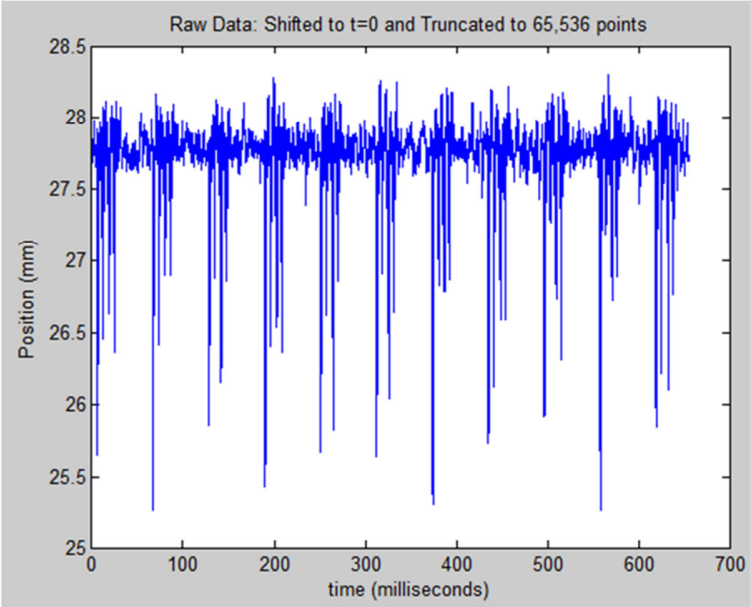

Figure 1.1. Acquired signal from stationary LVDT at 100 kHz

The next step taken was to perform a Discrete Fourier Transform (DFT) on the over-sampled data. The "fft" function in MATLAB was used to break the signal down into the discrete frequency components that it was composed of (Figure 1.2). Very pronounced frequency spikes were observed at 40 kHz, 20 kHz, and to a lesser degree, at 1 kHz, 45 kHz, and 500 Hz, along with general noise less than 100 Hz.

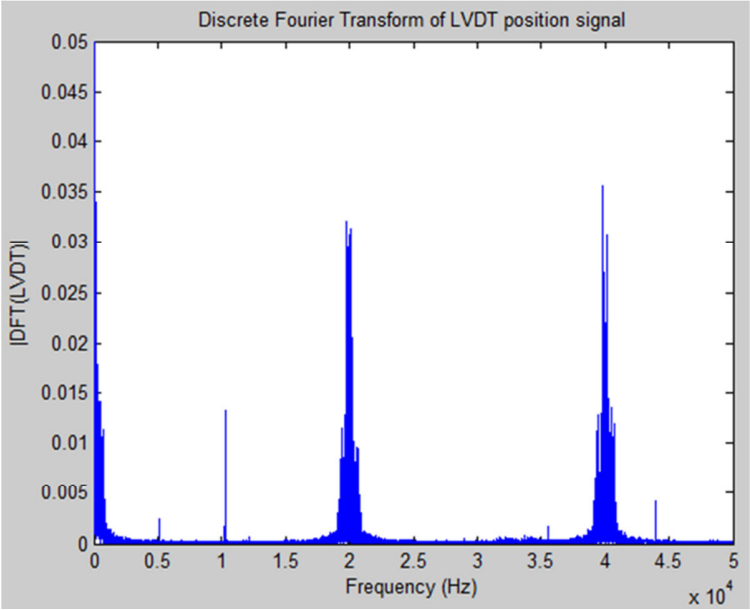

Figure 1.2. Discrete Fourier Transform of LVDT signal

At this point, we sought to determine which one (or several) of the electrical components might be emitting this high-frequency noise. I proceeded to use an oscilloscope attached to several different voltage locations (the LVDT voltage output leads, the DC terminals of the AC-to-DC power supplies, etc.) while powering various combinations of the two power supplies, the components they supply power to, and the stepper motor-driven linear actuator. The purpose was to create a "response surface" of the components' noise in order to determine where to focus my EMI search. Using the oscilloscope proved to be a quick means to observe relative noise levels, as compared to collecting data and post-processing to generate a DFT plot. Two things were observed during testing:

1. The 28 VDC, 224 Watt power supply used to power the stepper motor driver was emitting a lot of noise. This was explored under two different scenarios (Figure 1.3). (a) Shows the voltage output across the 24 VDC power supply with the 28 VDC power supply not powered on. (b) Shows the same voltage measurement as in (a), but with the 28 VDC supply powered on. The 28 VDC supply radiates a great deal of noise into the electronics surrounding it.

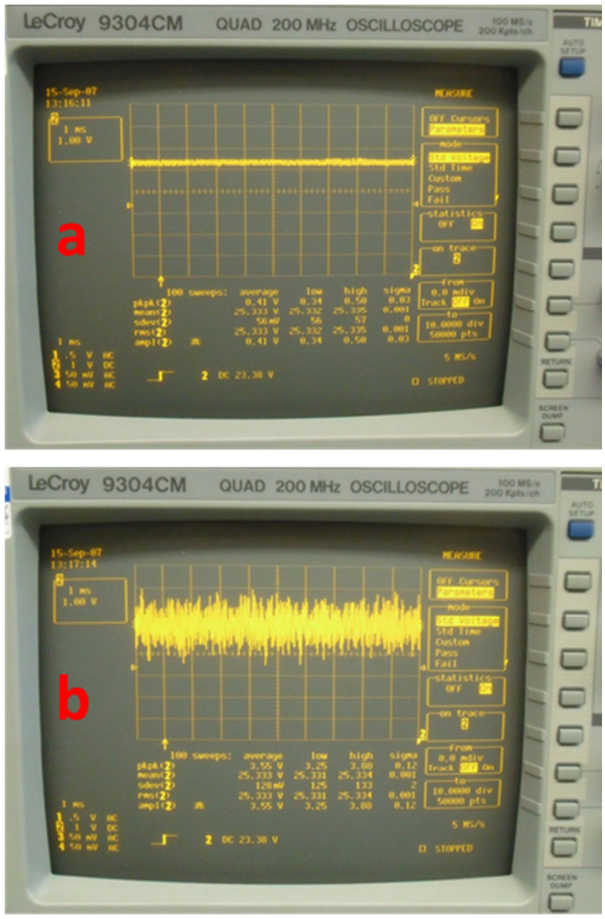

Figure 1.3. Oscilloscope voltage measurements of (a) the voltage across the terminals of the 24V auxiliary power supply (b) the same voltage measurement as in (a) but with the 28V power supply located nearby powered-on.

2. The stepper motor driver powering the stepper motor-driven linear actuator was emitting a great deal of noise itself. This was observed even when the driver was powered by the "quiet" desktop power supply (shown in Figure 1.3c). It was determined that the stepper motor driver uses a digital MOSFET switching at 20 kHz to power the stepper motor. This configuration, known as a current-chopping drive, is potentially very noisy.

1.4 Aliasing

It was determined that the high frequency noise was probably being embedded in my signal via the phenomena of aliasing. Understanding aliasing in signals begins with understanding

the Nyquist frequency. The Nyquist frequency is defined as the highest frequency signal that can be digitized at a given sampling rate in order to be able to determine the period of the signal from the sampled data (Baker, 1999). It is equal to ½ the sampling rate (f_s). A relatively simple example demonstrates what occurs when the frequency being sampled exceeds the Nyquist frequency (Figure 1.4, right side plot). The signal that would be recreated from those digitized samples would be completely different than the analog signal that the points were digitized from.

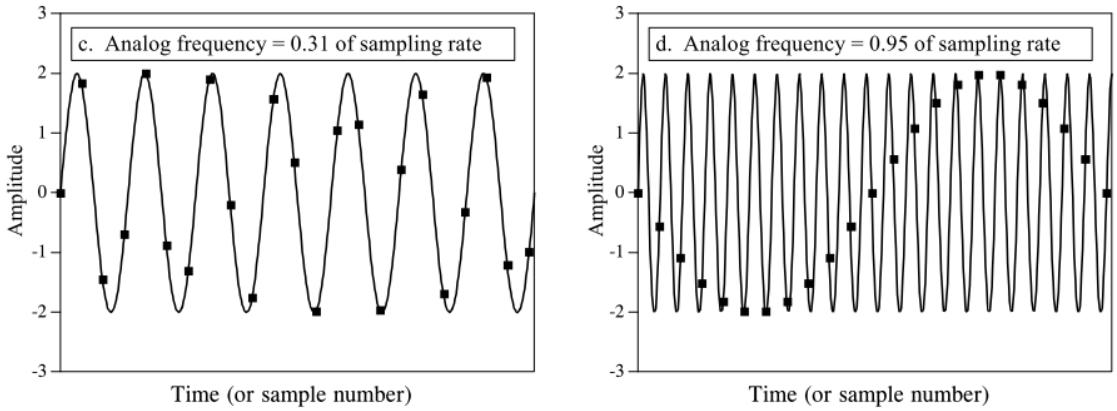

Figure 1.4. Digital sampling of an analog signal with (c) a frequency < $f_s/2$ (d) a frequency > $f_s/2$ (from Smith, 2003)

Aliasing comes in to play when the signal being sampled contains frequency components greater than $f_s/2$. The components of the signal with frequency < $f_s/2$ are reliably digitized, while those components with frequency > $f_s/2$ are aliased, or "folded back into" the bandwidth of interest with the amplitudes preserved.

High frequency signals become aliased into lower frequency signals by folding back into the bandwidth of the ½ times the f_s (Figure 1.5, adapted from Baker, 1999). An analog input consisting of five separate frequency components is sampled at a frequency of f_s. The frequencies of the signal range from less than $f_s/2$ to almost $7f_s/2$. The frequency band is divided into five segments; segment N = 0 spans from DC (a constant signal, frequency = 0) to $f_s/2$, and each subsequent segment is a multiple of f_s past $f_s/2$.

Frequency (1) is less than the Nyquist frequency ($f_s/2$), so it is faithfully sampled (Figure 1.5b). For all frequencies located in segments N > 0, the frequency component will be aliased into the N = 0 segment via the equation:$f_{ALIASED} = |f_{IN} - Nf_s|$ (Baker, 1999).

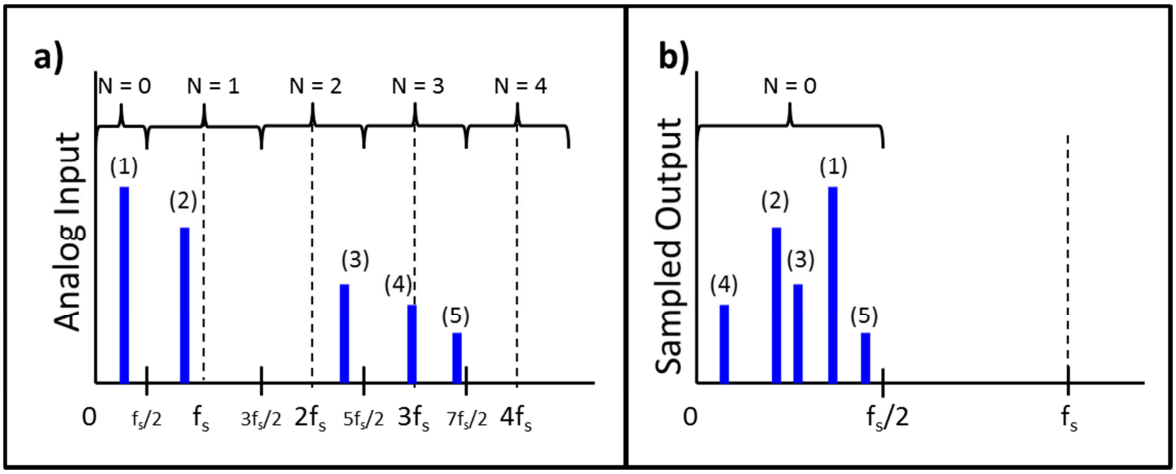

Figure 1.5. A system that is sampling an input signal at f_s: (a) will identify signals with frequencies below $f_s/2$ as well as above. Input signals below $f_s/2$ will be reliably digitized while signals above $f_s/2$ will be folded back and (b) appear as lower frequencies in the digital output. (adapted from Baker, 1999)

1.5 Modifications Made to the Device

As mentioned in Section 1.2, if the noise in an acquired signal is greater than the final application of the data can tolerate, the options are to reduce the noise finding its way into the data and/or filter the noise out of the data.

For this project, once it was determined that there was an EMI issue, I made modifications to the system and investigated data filtering techniques in parallel. There are many best practices that can be applied in the design of a system, in order to reduce the noise generated by the system and the noise carried by the data signals. Most are simple enough from a time and cost-perspective that they should be incorporated into the initial design instead of being retrofitted later, when an EMI problem has been detected and changes are probably harder to make.

What follows is a subdivided list of steps taken. A thorough noise reduction checklist can be found as an appendix in Ott's "Noise Reduction Techniques in Electronic Systems" (Ott, 1988). This list was based on that checklist.

1.5.1 General Wiring

- An electrical schematic of the existing wiring was created (Figure 1.6) and then a new wiring design was drawn in schematic form (Figure 1.7) before any physical re-wiring occurred. These were used to look for:
    - Ground loops, which can be described as an unwanted current carried in a conductor between two points that are supposed to be at the same electrical potential (generally ground), but are in actuality at different potentials. This can occur when one component has more than one path to ground. These are very common generators of noise.
    - Potential EMI radiators, which can be any unshielded wire leaving the main project box that contains the power supplies and stepper motor driver. Each of these was potentially carrying noise outside of the Faraday cage created by the project box.

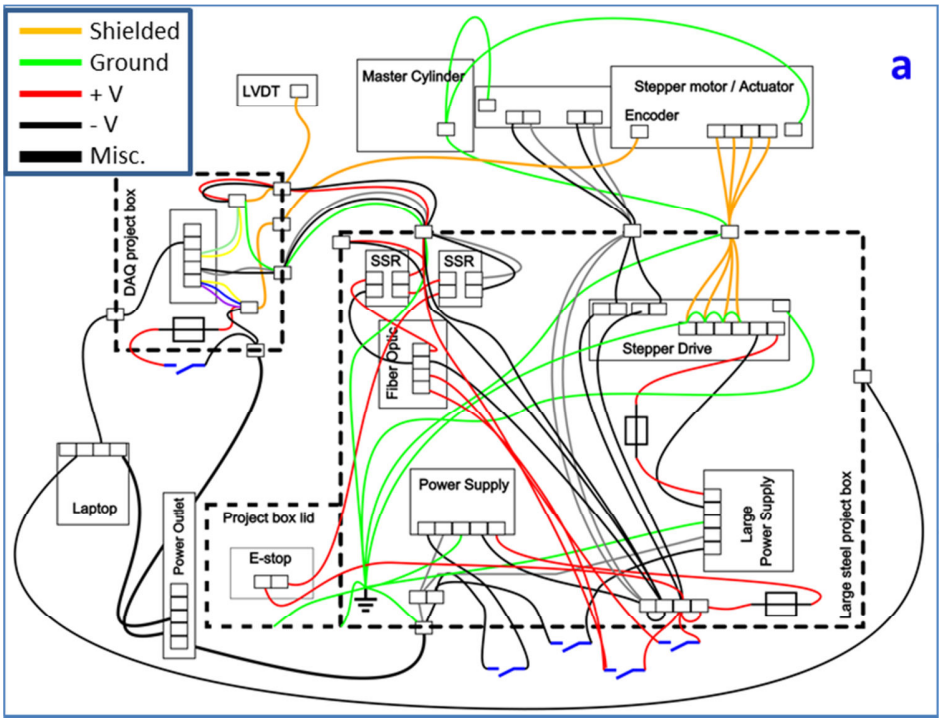

Figure 1.6. Electrical wiring schematic before EMI re-wiring

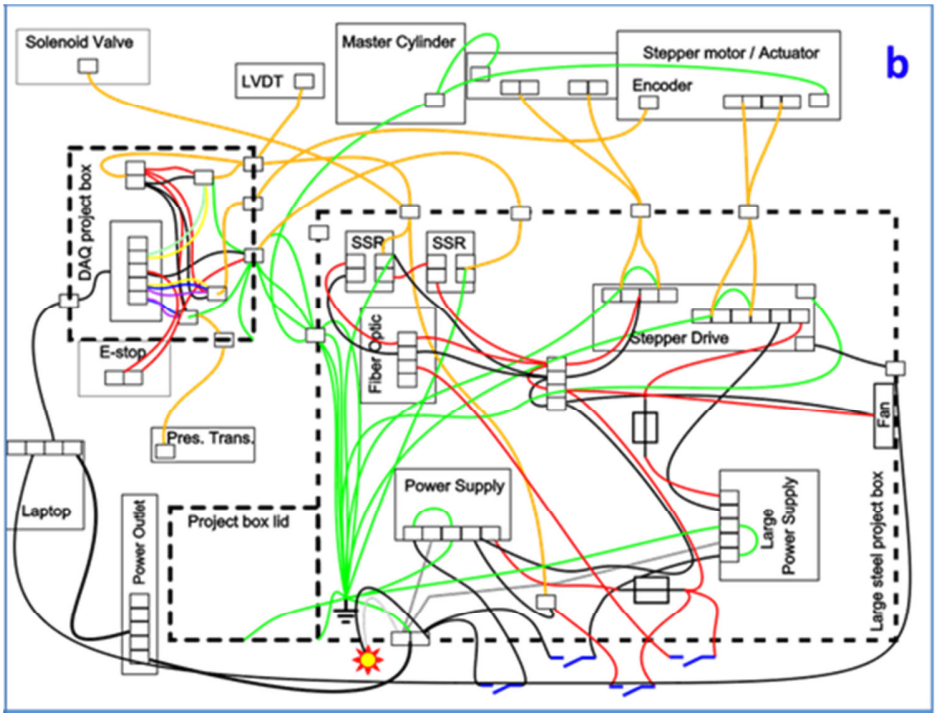

Figure 1.7. Electrical wiring schematic after EMI re-wiring

- Portions of unshielded wire travelling through the large project box to outside of the box were reduced or eliminated.

- Unshielded wiring outside of the project boxes (except for ground lines) was virtually eliminated and replaced with twisted pair shielded wire, with one end of the shielding grounded.
- All unshielded positive/negative power supply wires were twisted together to reduce the magnetic flux produced by current flowing in the lines. The flux fields in the two twisted lines cancel each other out.
- An EMI line filter was installed where the 110VAC mains power enters the project box, before it is directed to the AC-to-DC power supplies. This is to smooth the mains power, which has noise of its own. The EMI line filter also has a whole-system power switch and a fuse, both good from a safety point of view.
- The lengths of the shielded wires running from the stepper motor driver to the stepper motor were made as short as possible. Also, the wires leading directly into the stepper motor coils are unshielded, so the connection between them and the shielded wires was made as close to the stepper motor as possible, to reduce the amount of unshielded wire exposed.
- Ferrite induction beads (commonly called “chokes”) were installed on noisy lines as a means to absorb EMI being radiated from those lines.
- As much as possible, wire runs were kept short and fastened down using zip-ties (Figure 1.8). Wires allowed to move can radiate EMI.

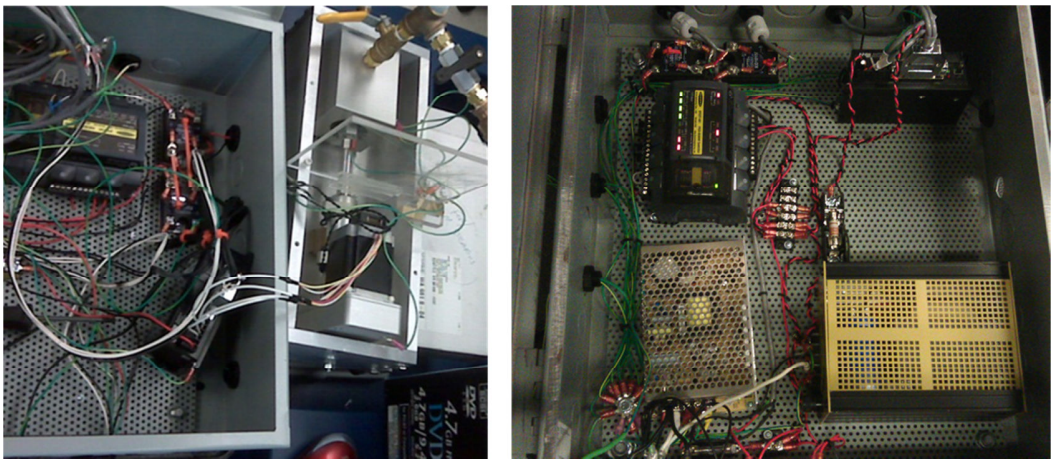

Figure 1.8. Re-wiring before (left) and after (right) photos of the main project box enclosure. Note, before photo represents the system during a state of testing, not the planned final state.

1.5.2 Grounding

- All ground lines run to one common ground point, known as a star ground configuration (Figure 1.8, after image, bottom left corner). This helps reduce potential ground loops. Ground wires were added to all large metal components of the device, even if they were not powered, such as the linear actuator frame and the aluminum rod attached to the instrument cart. These components, while not producing energy of their own, can act as EMI antennas.
- Noisy ground lines (those connected to potentially noisy components) and quiet ground lines (those connected to the DAQ project box or signal lines) were kept physically separated until they were near the connection to the system ground. This prevents noise being carried on the noisy grounds from being transmitted back to the sensitive components.

1.5.3 Hardware and Miscellaneous

- As much as possible, noisy components were re-located as far (physically) away from sensitive components as was possible (Figure 1.9).

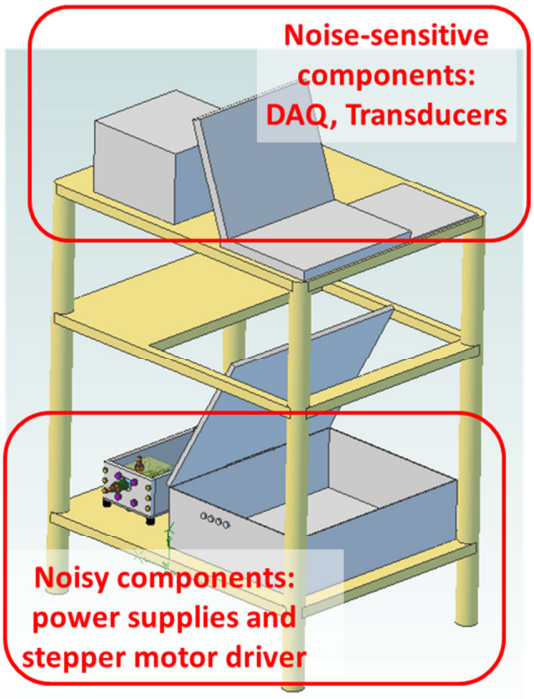

Figure 1.9. Revised instrument cart layout chosen to physically separate noisy components from sensitive data signal acquisition components.

- EMI gaskets were added to both project boxes to eliminate “leaks” in those Faraday cages. The amount of EMI able to pass outside of a Faraday cage is a function of the length of any opening on the surface of that cage (Ott, 1988). For boxes, this means that the entire lid-to-box interface is allowing EMI to pass by in both directions. EMI gaskets were added by using a Dremel tool to remove the paint at the interface and installing the flexible metal gasket to provide a conductive pathway between the two, essentially sealing the leak path.
- Power supply decoupling capacitors were added at both ends of all power supply lines to absorb generated and/or acquired noise and to ensure “clean” power was provided to components.
- The 5V AC-to-DC power supply (commonly called a “wall wart”) that was used to power the rotary encoder was eliminated, and the power was obtained through a voltage step-down from the auxiliary power supply. These inexpensive wall wart supplies are notoriously noisy.
- The power strip that connects the device to a standard wall plug and the laptop AC-to-DC power supply were both moved as far away as possible from sensitive data lines, as they both are potentially noisy.

1.6 Signal Filtering in Data Acquisition

With the information that was presented in Section 1.4, hopefully it is clear that virtually every sampled analog electric signal will have, to some degree, aliased data embedded within it.

While I was redesigning the electrical system of the device to reduce noise output (detailed in Section 1.5), I was also investigating the use of filtering to remove that noise which would still remain.

A standard filtering scheme applied for digital acquisition of an analog signal includes an analog low pass filter in-line before the DAQ board in order to attenuate high-frequency noise, preventing it from becoming aliased into the signal during digitization (Figure 1.10). After the Analog to Digital Conversion (ADC), a digital smoothing filter is used to smooth the output signal. Digital filtering can also remove noise that is injected into the data from the ADC process, but that is of small concern in this project.

While both analog and digital filtering are optional, an important point to note is that once a particular frequency has been aliased into your digitized data, there is no way to remove that frequency from the signal using digital filtering. This demonstrates the importance of an analog filter in-line before the ADC if noise might even potentially be a concern.

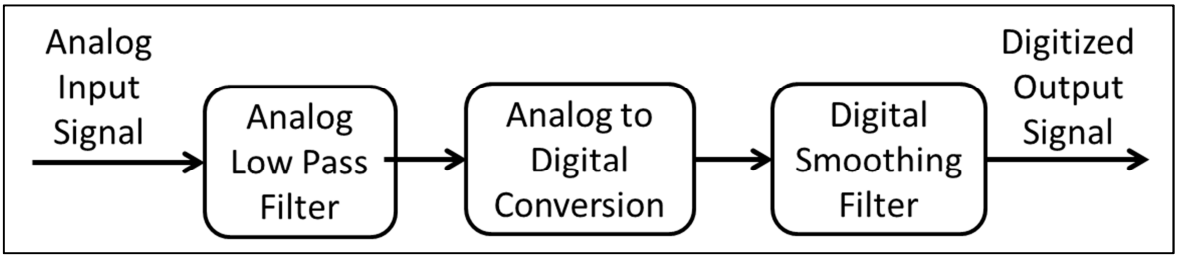

Figure 1.10. Standard data acquisition and filtering system (adapted from Baker, 1999).

1.7 Analog Low Pass Filters

An ideal low pass filter perfectly attenuates frequencies in the stopband (frequencies greater than its cutoff frequency, f_c) while applying a gain of 1 to frequencies in the passband (frequencies less than f_c) (Figure 1.11). An anti-aliasing filter is simply a low pass filter with the sole purpose of eliminating aliased frequencies.

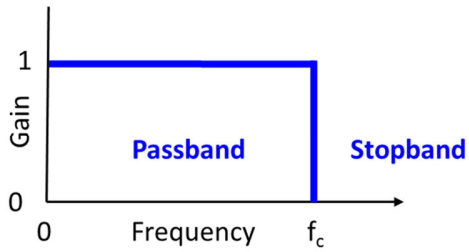

Figure 1.11. Ideal low pass filter frequency response

Following are short descriptions of the types of low pass filters available along with some pros and cons of each. This is by no means an exhaustive study of analog filtering technique; rather, it is the information the author collected through his own research that may prove helpful to others as a filtering starting point.

1.7.1 Passive Low Pass Filters

Passive filters, the simplest of all analog filter types, contain no active components (active components are powered by a separate power supply). Passive filters are composed of passive components alone, generally resistors and capacitors, but occasionally inductors. They feature a simple configuration and calculation for f_c (Figure 1.12).

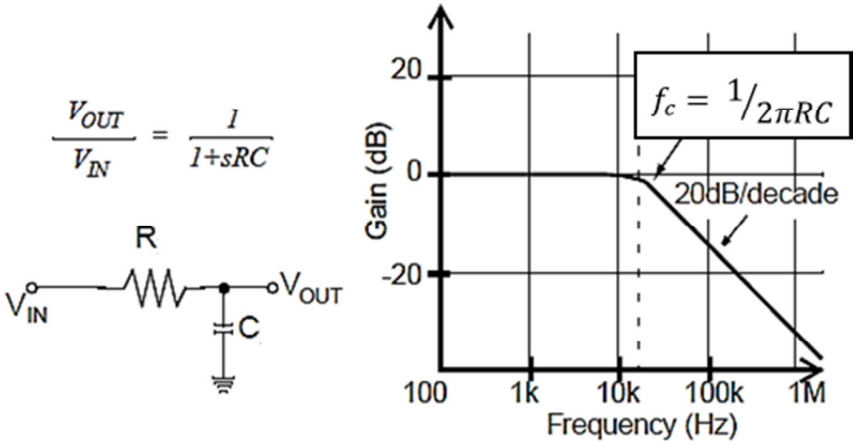

Figure 1.12. Passive low pass filter and frequency response calculations (adapted from Baker, 1999)

Pros:

- Simple to design and implement
- No power supply necessary
- No bandwidth limitations as are found in operational amplifier (op-amp) filters (this means these filters can function at very high frequencies)
- Able to withstand high current/high voltage applications that active filters cannot
- Generate very little noise

Cons:

- No signal gain possible
- Low input impedances and high output impedance can cause an undesirable attenuation in the signal because it acts a voltage divider on the signal voltage
- Once embedded into a permanent circuit (components soldered), it is difficult to change f_c

1.7.2 Active Low Pass Filters

Active filters come in a variety of types and packages, but all use some active components, such as op-amps, and passive components (resistors and capacitors). A common active filter configuration is the Sallen-Key filter (Figure 1.13). Op-amps are a desirable addition to a filter due to two important characteristics:

- High input impedance – the op-amp does not load down the signal source and draws only a minimal current from it, so the input signal is not affected by the device.
- Low output impedance – the op-amp can source a load (the output of the filter) as if it were a perfect voltage source. Voltage output does not vary with current output.

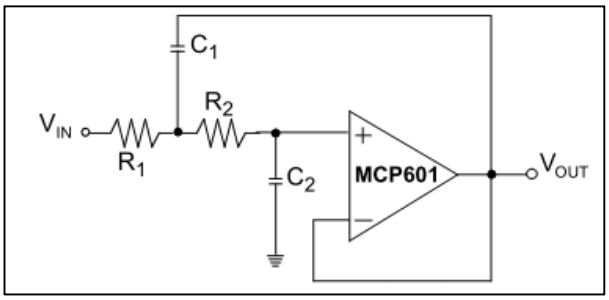

Figure 1.13. Sallen-Key, double pole filter circuit

Other benefits of an active filter include:

- Adjustability of the output amplitude. Different arrangements of the inputs to the op-amp input terminals and the values of the resistors and capacitors used can cause the filter output to be inverting or non-inverting, and almost any gain imaginable, from unity gain, to gain <<1, to gain >>1, is possible.
- Active filters can be cascaded to form multiple pole filters without attenuating the passband signal (as happens when passive filters are cascaded). In general, more poles create a "better" filter performance (more on that in Section 1.7.2.2).

1.7.2.1 Filter Implementations

The same type of active filter may come in different implementation architectures; for instance, a Bessel filter can be constructed on a breadboard using high-tolerance resistors and capacitors or implemented in an Integrated Circuit (IC). Several implementation types are discussed below along with pros and cons.

1.7.2.1.1 Basic Sallen-Key Filter

Numerous books and websites feature schematics and design tables (Figures 1.14 and 1.15) to enable you to build a filter out of common electrical components.

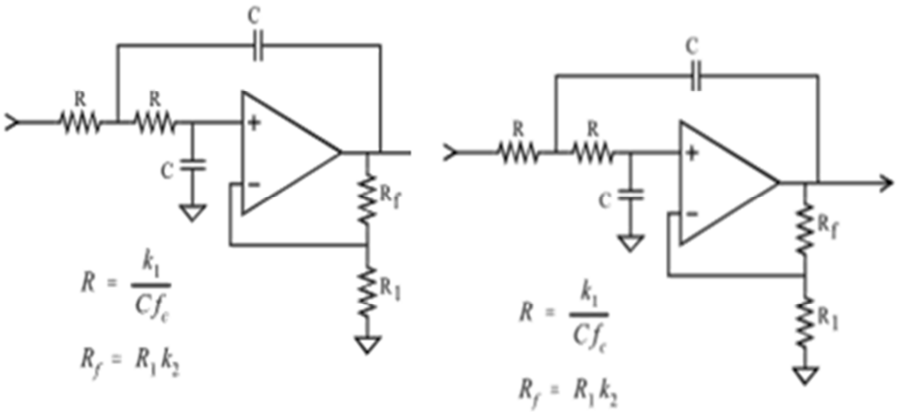

Figure 0.14. Four pole (2nd order) Sallen-Key low pass filter schematic

# poles		Bessel k1	Bessel k2	Butterworth k1	Butterworth k2	Chebyshev k1	Chebyshev k2
2	stage 1	0.1251	0.268	0.1592	0.586	0.1293	0.842
4	stage 1	0.1111	0.084	0.1592	0.152	0.2666	0.582
	stage 2	0.0991	0.759	0.1592	1.235	0.1544	1.660
6	stage 1	0.0990	0.040	0.1592	0.068	0.4019	0.537
	stage 2	0.0941	0.364	0.1592	0.586	0.2072	1.448
	stage 3	0.0834	1.023	0.1592	1.483	0.1574	1.846
8	stage 1	0.0894	0.024	0.1592	0.038	0.5359	0.522
	stage 2	0.0867	0.213	0.1592	0.337	0.2657	1.379
	stage 3	0.0814	0.593	0.1592	0.889	0.1848	1.711
	stage 4	0.0726	1.184	0.1592	1.610	0.1582	1.913

Figure 1.15. Parameters for use with the circuit shown in the schematic above. Note that parameters for a 2nd order, 4 pole Bessel filter are circled in red.

Pros:

- It is a good experience to learn some of the math behind the filter and the specific parameters of the op-amps you choose while building your own filter.
- The filters are easy to prototype and adjust relatively quickly, especially when using a breadboarded circuit and a potentiometer to adjust the gain or f_c.
- They are completely tunable for whatever your application requires (near-infinite f_c values, amplification factors, number of poles, etc.), given the right component values.

Cons:

- It can be difficult to find large varieties of high tolerance capacitors/resistors without buying special kits just for filters. It is recommended to use ≤ 1% resistors as opposed to the commonly available 5% or 10% tolerance resistors.

- If the circuit is permanent (i.e., soldered together on perforated board or a printed circuit board), then adjusting parameters is time-consuming.
- Breadboard and perfboard circuits will introduce noise into the filter due to all the conductive metal attached to the circuit. These noise antennas can decrease filter effectiveness.

1.7.2.1.2 Switched Capacitor IC Filter

Switched capacitor (SC) filters are ICs that use very quickly switching capacitors to replace the resistors in a standard active filter. SCs are used because building resistors out of silicone in an IC is still not feasible. Constructing a circuit featuring SC filters is a straightforward task with perfboard circuit building skills and a soldering iron (Figure1.16).

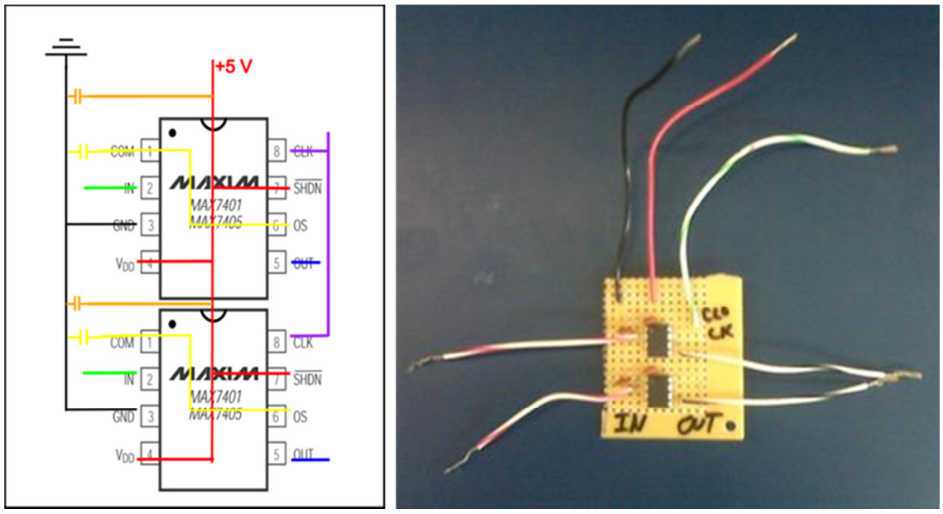

Figure 1.16. SCF IC dual line low pass filter: (left) circuit wiring schematic and (right) final circuit on perfboard

Pros:

- ICs are designed and built by filtering experts
- Inexpensive: IC manufacturers will even generally send a few free samples
- Easy to adjust the cut-off frequency
- Effective at eliminating aliasing (Figure 1.17)
- Available in a variety of configurations, form factors, number of poles, etc.

Cons:

- Overall, not as easy to implement as they might seem to be (my experience)
- Require a square wave, 50% duty cycle clock signal to switch the capacitors
    - Clock signal frequency is generally 100x greater than f_c frequency
    - DAQ Analog Output only capable of ~5 kHz square wave
    - An external, analog comparator-based clock signal circuit is fairly easy to build, but if the signal is not synced with the ADC, beat-frequency noise can appear in the signal

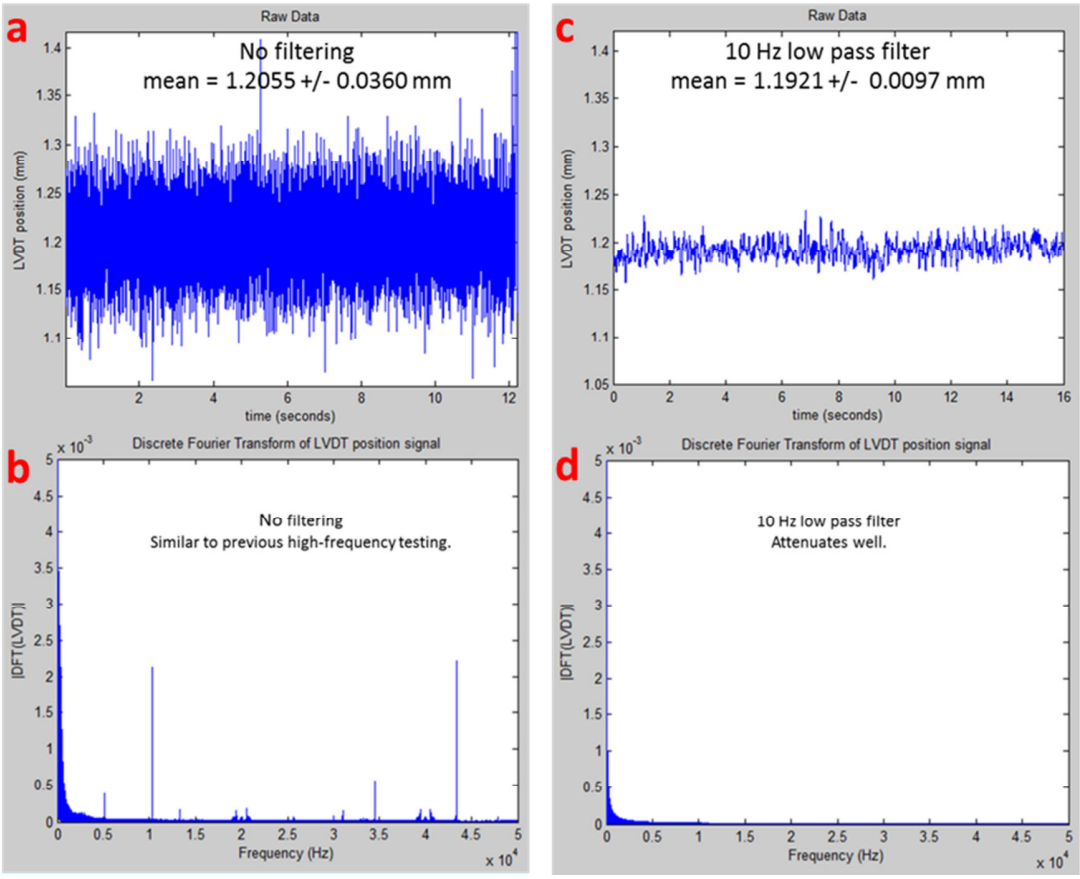

Figure 1.17. (a) Linear variable displacement transducer (LVDT) signal with no filter (b) LVDT signal with 10 Hz SCF (c) Discrete Fourier Transform (DFT) of signal a (d) DFT of signal b. Note that (d) shows none of the spikes seen in (b), which are aliasing into the standard sample rate signal. Note also that the mean value of (c) has shifted from mean value of (a) due to the filter.

1.7.2.1.3 Active RC Filter

This filter is essentially the next step up in complexity from the passive RC low pass filters discussed in Section 1.7.1. It consists of the same passive RC filter but with an op-amp in

voltage-follower configuration placed after the RC filter (Figure 1.18). I experimented with the previous two discussed active filters and had issues with additional noise coming from the filter (Sallen-Key filter implemented on a breadboard) and unexplained, uncorrectable, non-constant DC offsets (SC filter). After coming across a description of this filter and trying it, it was the low pass filter I chose to use for the duration of the project due to its simplicity and affectivity.

Pros:

- All the benefits of a passive RC low pass filter.
- The op-amp's high input impedance prevents excessive loading on the filter's output.
- The op-amp's low output impedance prevents the filter's f_c from being affected by changes in the impedance of the load.

Cons:

- Only a 1st order filter (although cascading for higher-order may be an option, I have not found information on it).
- Only capable of unity gain (no amplification or inversion of signal).
- Because an op-amp's output voltage range is generally narrower than its supply voltages, to output a signal near 0V requires powering the op-amp with +/- 10 VDC (able to be done with two free analog output channels on a DAQ and simple code).

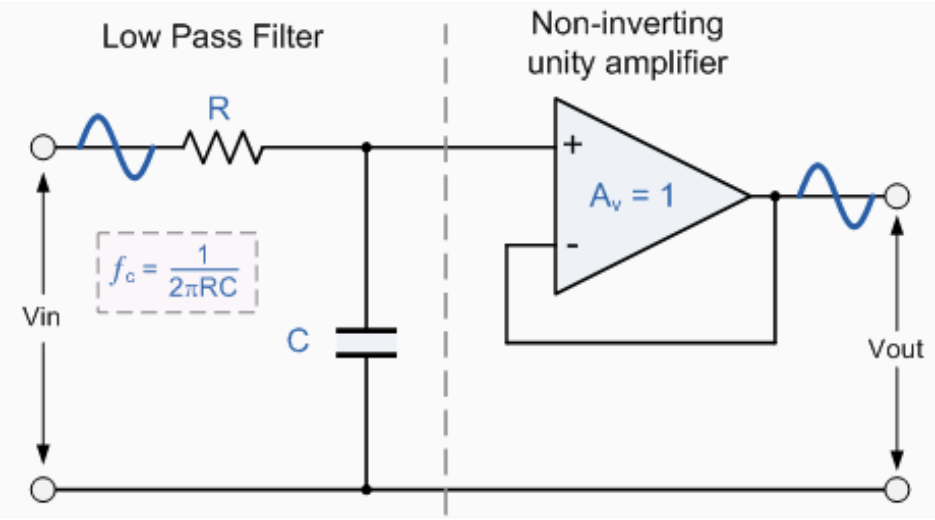

Figure 1.18. 1st order active RC filter schematic (from Storr, 2012)

1.7.2.2 Common Active Filter Types

The component values and arrangements used in the Sallen-Key filter configuration (Figure 1.15) can be tailored to change the filter's performance. Common types include:

- Butterworth – features the sharpest roll-off possible without any passband ripple
- Chebyshev – features a very sharp roll-off at the expense of introduced passband ripple
- Bessel – features relatively poor roll-off but no overshoot or ringing during a step response

The differences in the step responses for the three filter types listed above is substantial (Figure 1.19). For an instantaneous step input from amplitude 0 to 1 occurring at time t = 0 seconds, the Bessel filter shows a fast response and lack of overshoot and passband ripple as compared to the Butterworth and the Chebyshev. Increasing the number of poles of a filter slows the step response of the filter, effectively adding a temporal shift to the data.

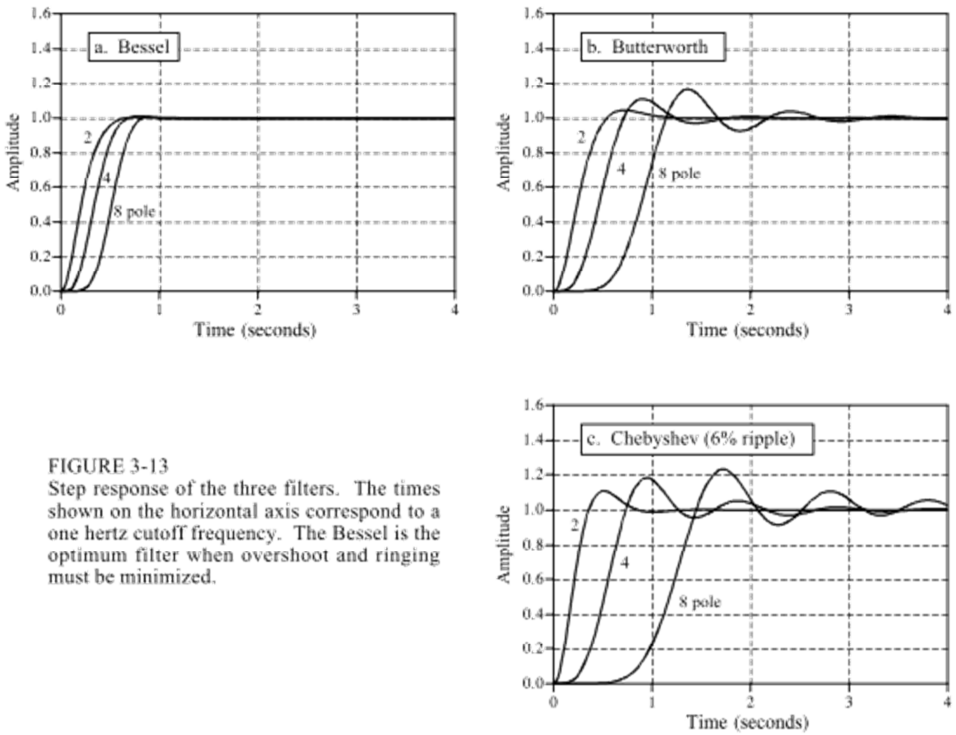

FIGURE 3-13
Step response of the three filters. The times shown on the horizontal axis correspond to a one hertz cutoff frequency. The Bessel is the optimum filter when overshoot and ringing must be minimized.

Figure 1.19. Step responses of common filter types with a 1 Hz f_c. Plots can be scaled (inversely) for higher cutoff frequencies (i.e., a 1000 Hz cutoff frequency would show a step response in milliseconds, rather than seconds. (from Smith, 2003)

The different filter types also have significantly different roll-off characteristics. Roll-off refers to how closely the filter performance matches a theoretically-perfect low pass filter in the stopband. An ideal low pass filter (Figure 1.11) shows a signal gain of 1 through the passband, at which point the gain drops immediately to 0 throughout the stopband. Roll-off is how closely an actual filter matches that drop-off in the stopband (Figure 1.20). The roll-off characteristics of a filter are improved by increasing the number of poles in the filter, thereby improving its performance.

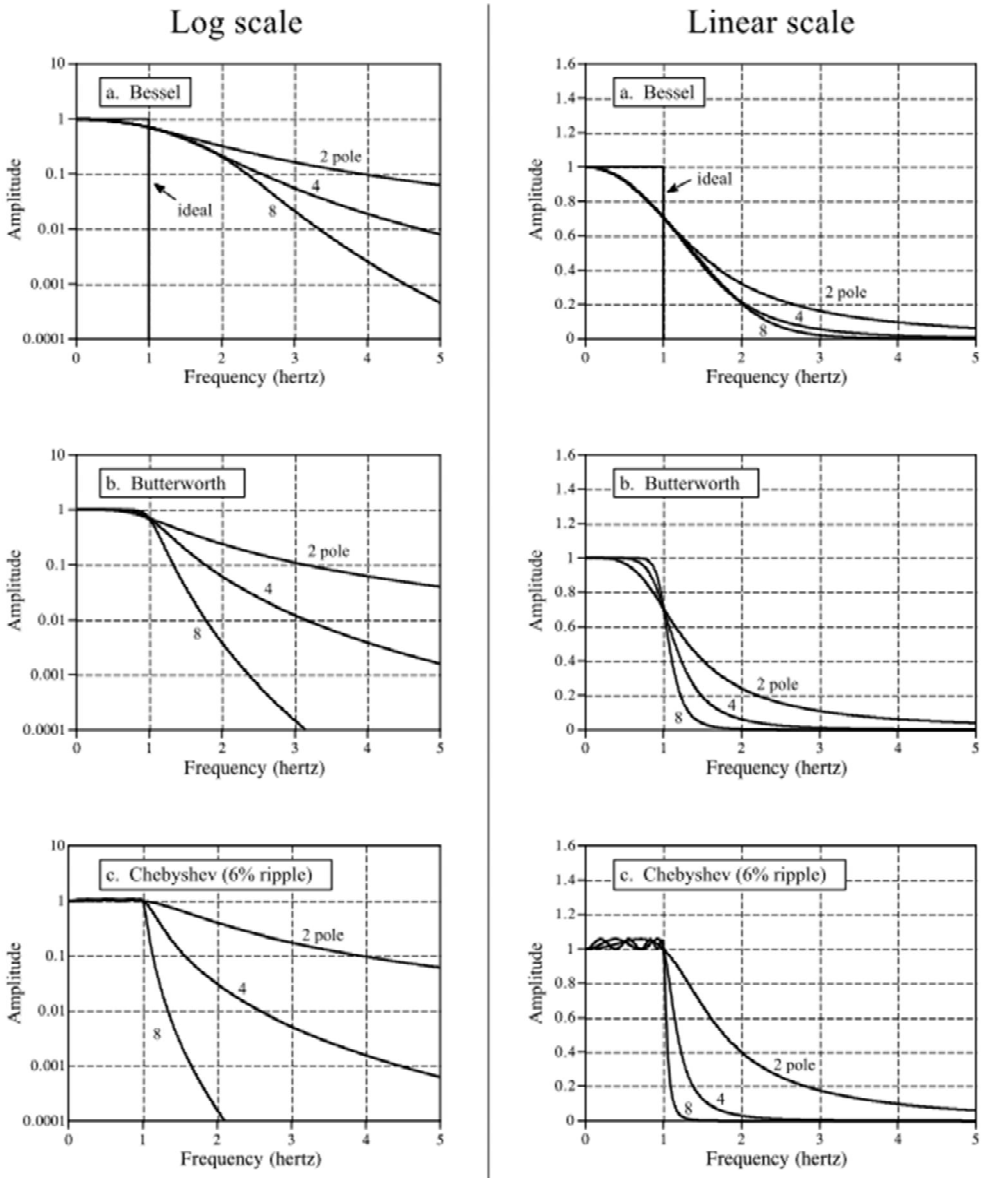

FIGURE 3-11
Frequency response of the three filters on a *logarithmic* scale. The Chebyshev filter has the sharpest roll-off.

FIGURE 3-12
Frequency response of the three filters on a *linear* scale. The Butterworth filter provides the flattest passband.

Figure 1.20. Roll-off performance of common filter types with f_c = 1 Hz. Other frequencies scale directly (from Smith, 2003).

1.7.3 Filter Selection

After reviewing the various performance characteristics of the different active filters, it is apparent that each filter type has pros and cons, and probably also apparent that "you don't get anything for free" when it comes to filtering. Because of this, it is important to consider

the information encoded in the signal being filtered and how those data will be used when selecting a filter type.

1.7.3.1 Frequency domain encoding

In frequency domain encoded signals, the information is stored in sinusoidal waves that combine to form the signal. Audio signals are an example of a frequency domain encoded signal. Since signal aliasing alters the frequency components of a signal, any aliased signal could change the signal significantly. But ripple in the passband does not affect the frequency-encoded data. In this case, a sharp roll-off filter with some passband ripple is probably appropriate.

1.7.3.2 Time domain encoding

In time domain encoded signals, the shape of the signal and how it changes with respect to time is the information stored in the data. An EKG signal is an example. In a time domain encoded signal, any passband ripple or delayed-response to a step input will affect the data, potentially significantly. But, a small amount of aliasing due to a slow roll-off will probably not be as big of an issue. Before I moved away from a true active filter to an active RC filter, I was using an 8^{th} order Bessel filter due to the fact that the temporal response was important for the device data and I desired no overshoot in the passband, which would affect the pressure and LVDT data negatively.

1.7.3.3 Cut-off frequency

As discussed earlier, the Nyquist theorem says we can accurately sample frequencies < $f_s/2$. For most analog filters, the output of the filter in the frequency band of ~0.4 to 0.5 times f_s includes a lot of filter roll-off and aliased signal, so those data are potentially bad. A standard rule of thumb is to set $f_c \leq ¼$ of f_s. This applies to both active and passive filters. It may be tempting, especially in human motion or loading studies where frequencies of interest are generally low, to use a very low f_c in order to avoid any aliased signals in the data. It is important to remember that the time-delay of the filtered signal as compared to

the raw signal is inversely proportional to the f_c of the filter. If accurate temporal data are a high priority, setting f_c too low might incur a relatively large temporal shift into the data.

1.8 Digital Filters

Digital filtering can frequently reduce noise in sampled data while still preserving important characteristics of the data. For this project, the total effort put into digital filtering was much less than the analog filtering effort. For that reason, there is less information presented here.

An important thing to remember if a digital smoothing filter is going to be used is that the sampling rate should probably be increased to account for the averaging that will take place. For this reason, I increased my sampling rate from 1 kHz to 2.5 kHz. This was probably too drastic, but the data files are still a manageable size.

When choosing a smoothing filter, I tested each of the default algorithms in MATLAB:

- Moving average – the simplest, but often very effective smoothing filter
- Lowess – local regression using weighted linear least-squares and a 1st degree polynomial
- Loess – local regression using weighted linear least-squares and a 2nd degree polynomial
- Savitzky-Golay – generalized moving average with filter coefficients determined by an unweighted linear least-squares regression and a polynomial model of specified degree
- Rlowes & Rloess – robust versions of the Lowess and Loess filters, they assign lower weight to outlier data

I ran each filter on sample data obtained while displacing the LVDT with a 1.0 Hz triangle wave. For all filters used, I tested several different window sizes and (when applicable) degrees of polynomial fit. This testing was mostly qualitative in order to narrow down the potential usable filters to a manageable amount to quantitatively test.

For each filter tested in the quantitative round, I:

- Calculated the root mean square (RMS) error between the smoothed data and the raw data.
- Calculated the RMS error between the smoothed data and a triangle wave of the same peak amplitude and frequency.
- Examined the time and location of the maximum and minimum displacement values to ensure they were not shifting in the filtered data (Figure 1.21)

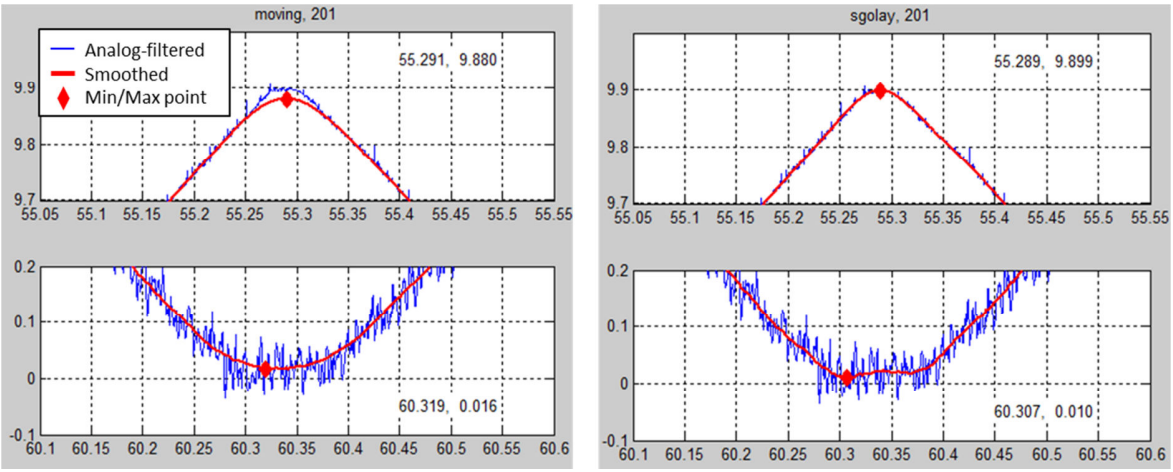

Figure 1.21. Comparison of 1 peak and 1 valley of the triangle displacement wave smoothed with different filters, each = 201 samples window size. (left) Moving average filter (right) Savitzky-Golay 2nd order filter.

The reason behind computing the RMS error from the smoothed data to two different curves was because I noticed that increasing the order of the filters introduced wave shapes into the smoothed data. This gave a smaller RMS error due to the noise in the data, but created smoothed data with unrealistic, wave-filled displacement shape. By calculating the RMS error of the smoothed data to a perfect triangle wave and then optimizing my filter parameters to minimize both RMS error values, I obtained the most realistic smoothed data.

I chose to use a 2nd order Savitzky-Golay filter with a sample window size = 301. This filter is known for its ability to preserve features within data such as relative maxima and minima, which are usually flattened out by other averaging techniques like moving averages (Figure 1.21 left hand image) (Press, 2007).

1.9 Signal to DAQ Connections

The proper connection between the signal wires and the DAQ board should be thoroughly understood before any other signal noise debugging is performed. National Instruments' guide (National Instruments) features a chart that helps identify the proper connection method based on the sensor type and the data acquisition method (Figure 1.22). The entire guide is a worthwhile read for anyone new to analog signal acquisition.

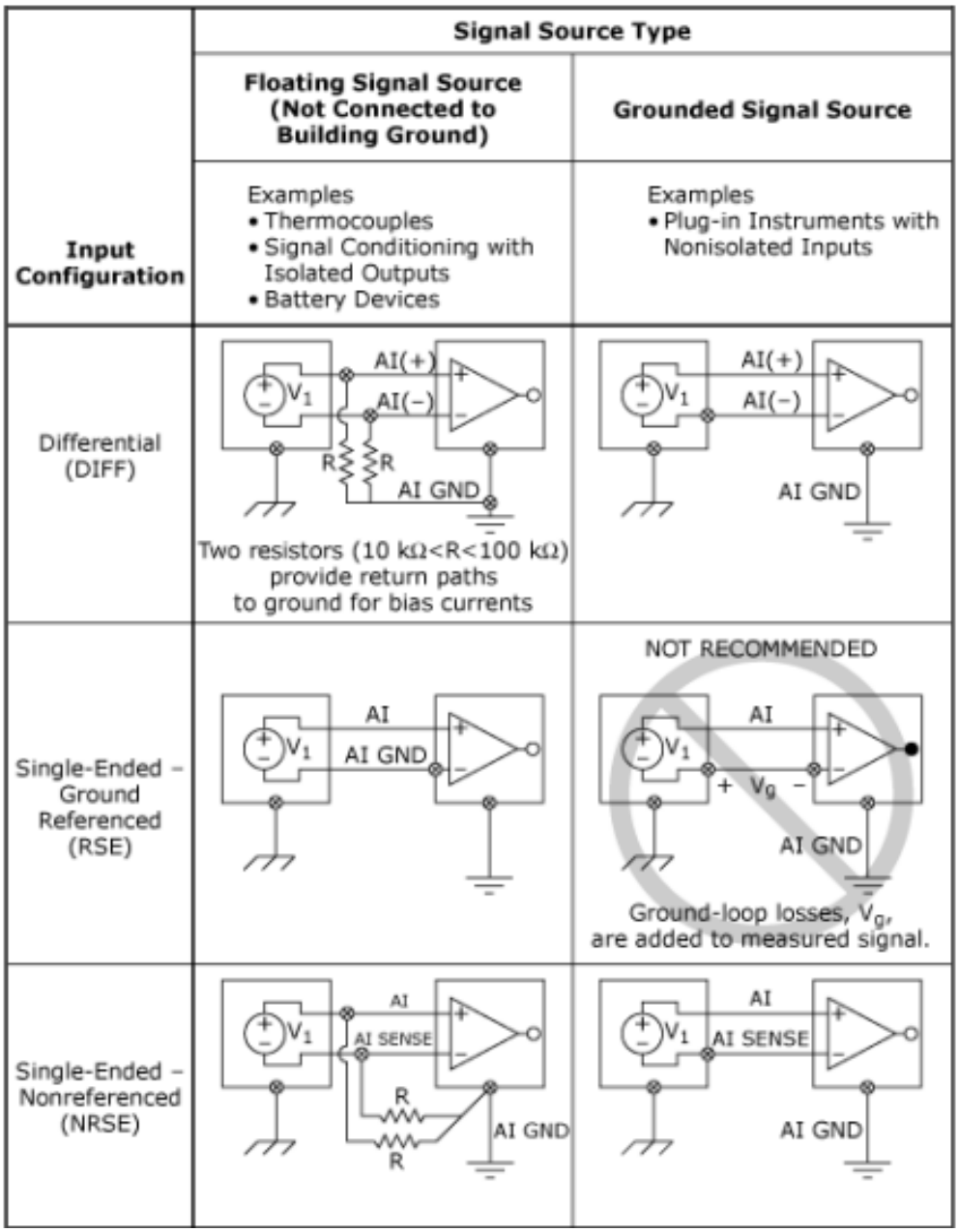

Figure 1.22. Analog input connections to DAQ board summary (from National Instruments)

1.10 References

Baker, B.C. 07/26/99-last update*, Anti-Aliasing, Analog Filters for Data Acquisition Systems*. Available: http://ww1.microchip.com/downloads/en/AppNotes/00699b.pdf [2011, 12/30].

National Instruments, *Field Wiring and Noise Considerations for Analog Signals* [Homepage of National Instruments], [Online]. Available: http://zone.ni.com/devzone/cda/tut/p/id/3344 [2011, 12/30].

Ott, H.W. 1988, *Noise reduction techniques in electronic systems.* Wiley, New York, N.Y.

Press, W.H. 2007, *Numerical recipes: the art of scientific computing,* Cambridge University Press, Cambridge, UK; New York.

Smith, S.W. 2003, *Digital signal processing: a practical guide for engineers and scientists,* Newnes, Amsterdam; Boston.

Storr, W. 2012, 02/2012-last update*, Electronics Tutorial about Active Low Pass Filters*. Available: http://www.electronics-tutorials.ws/filter/filter_5.html [2012, 02/28].

Appendix C. Plantar Tissue Thickness and Strain Under Body Weight Literature Review

TABLE OF CONTENTS

1.1 Introduction 209

1.2 Tabular Data: Subcalcaneus 210

1.3 Tabular Data: Submetatarsal Heads 213

1.4 Charted Data: Subcalcaneus 215

1.5 Charted Data: Submetatarsal Heads 216

1.6 References 221

LIST OF FIGURES

Figure 1.1. Subcalcaneus: Loaded vs. Unloaded Thickness and Strain 215

Figure 1.2. Submetatarsal Heads 1-5 Average: Loaded vs. Unloaded Thickness.....216

Figure 1.3. Submetatarsal Head 1: Loaded vs. Unloaded Thickness and Strain.....217

Figure 1.4. Submetatarsal Head 2: Loaded vs. Unloaded Thickness and Strain.....218

Figure 1.5. Submetatarsal Head 3: Loaded vs. Unloaded Thickness and Strain.....219

Figure 1.6. Submetatarsal Head 4: Loaded vs. Unloaded Thickness and Strain.....220

Figure 1.7. Submetatarsal Head 5: Loaded vs. Unloaded Thickness and Strain.....221

LIST OF TABLES

Table 1.1 Subcalcaneus Plantar Tissue Thickness and Strain 210

Table 1.2. Subcalcaneus Plantar Tissue Thickness and Strain, continued.....211

Table 1.3. Subcalcaneus Plantar Tissue Thickness and Strain, continued.....212

Table 1.4. Submetatarsal Head Plantar Tissue Thickness and Strain 213

Table 1.5. Submetatarsal Head Plantar Tissue Thickness and Strain, continued.....214

1.1 Introduction

This appendix features the results of a literature review undertaken to determine the unloaded and loaded thickness and the strain under load of the plantar soft tissue. The data were collected for both the subcalcaneus and the submetatarsal head regions.

Section 1.2 is comprised of the subcalcaneus and submetatarsal head tissue data in tabular form. Section 1.3 is comprised of charts displaying subcalcaneus tissue data, the averaged submetatarsal head tissue data, and the individual submetatarsal heads tissue data.

An earlier version of this literature review was completed by another member of our group, Dr. Shruti Pai, in 2009. At that time, she did not include data on the strain of the tissue. Approximately one year later, in late 2010, I updated the plantar tissue thickness data with several additional articles, and added all of the strain data to the literature review.

I'd like to express my gratitude to Dr. Pai for providing me such a thorough literature review to begin working from.

1.2 Tabular Data: Subcalcaneus

Table 0.4 Subcalcaneus Plantar Tissue Thickness and Strain

Author	Year	Method	UT* (mm)	ε avg± stdev (range), %	Population	Purpose and Findings	Limitations
Steinbach	1963	Lateral X-ray	17.80	N/A	n=103 (57♀, 46♂) **c**ontrols c_age:17-88yrs c_UT: 17.8±2.0 (13-21mm) n=29 **a**cromegalics a_UT: 25.6 (17-34mm)	Compared normal heel pad thickness with those of acromegaly patients; thickness increased therby validating it as diagnostic paramater.	Weight unknown. Age varied widely. Acromegalic age and standard error unknown.
Fields	1967	Lateral X-ray	20.04 ⓪	N/A	n= 92 (all male, **Cau**casian or **Afr**ican American) age: 20-80yrs UT: 12-27mm Cau_UT: 19.63±3.21mm Afr_UT: 20.44±3.42mm ⓪	Evaluating method as tool for diagnosing acromegaly. Indicates possible differences in skin and plantar tissue thickness due to race (not significant).	Age varied widely. Weight unknown. All controls were at the upper limit of "normal" thickness (intentional for study).
Jackson	1968	Lateral X-ray	22.525 ⓪	N/A	n=20 wgt: 568.9±118.1 N L_UT: 23.15±3.98mm R_UT: 21.90±3.49mm	Measurement of heel pad thickness in obese subjects. Heavier people tend to have thicker heels which does not necessarily signify acromegaly.	Age and gender unknown.
Kho	1969	Lateral X-ray	18.56	N/A	n=52 (28♀, 24♂) ♀age: 46 (17-74yrs) ♂age: 42.8 (15-64yrs) ♀wgt: 689 (374-1326 N) ♂wgt: 725 (507-1322 N) ♀UT: 18.54±2.66 (13-23mm) ♂UT: 18.61±2.51 (15-25mm) UT: 18.56±2.60mm	Evaluating method as tool for diagnosing acromegaly. Heel pad thickness increased with increasing body weight and decreasing age. Weight appeared to be more important in determining thickness than age.	Results are in contrast to later findings that indicate heel pad thickness increases with age.
Kattan	1975	Lateral X-ray	16.57	N/A	n=43 (28♀, 15♂) age: 20-70yrs UT: 16.57 (11-20mm)	Comparing controls to epilepsy patients on drug Dilantin. The drug side effects include heel pad thickening which could lead to false diagnosis of acromegaly.	Weight and standard error unknown. Age varied widely.
Gooding	1985	Ultrasound	16.60	N/A	n=54 (5♀, 5♂=10 **c**ontrols, 38 **d**iabetic patient w/o ulcers) c_age: 28yrs d_age: 62yrs c_UT: 16.6±0.32mm d_UT: 17.8±0.31mm	Evaluation of test method to measure heel pad thickness.	Age varied widely between groups. Weight unknown.
Gooding	1986	Ultrasound	18.62	N/A	n=73 (24 **c**ontrols, 38 **d**iabetic patients, 11 **u**lcered **d**iabetic patients) c_age: 51±3.1yrs d_age: 62±1.2yrs ud_age:60±2.3yrs c_wgt: 845.5±31.2 N d_wgt: 818.8±20.9 N ud_wgt:792.1±33.8 N c_UT: 18.62±0.36mm d_UT: 17.33±0.29mm ud_UT:15.77±0.39mm	Comparison of heel pad and submetatarsal head thickness in three groups: controls, diabetic patients without ulcers, and diabetic patients either with ulcers/ a history of ulcers. Diabetic patients have decreased thickness of sole compared with controls, and diabetic patients prone to ulcers have even thinner soles.	Gender unknown.
DeClerqc	1994	Lateral cineradiographs (fast sequential X-rays)	14.9 ⓪	running shod: 35.6 running barefoot: 60.4 ⓪	n=2 subject_A_age: 22yrs subject_B_age: 21yrs subject_A_wgt: 656 N subject_B_wgt: 695.8 N subject_A_UT: 15.3±0.2mm subject_B_UT: 14.5±0.2mm	Unloaded thickness was the same for barefoot and shod feet in long distance runners. However, maximal deformations of heel pads varied when barefoot vs. shod (60.5±5.5% vs. 35.5±2.5%).	Very small sample population.

*Note: UT= unloaded thickness, LT = loaded thickness, CI = Compressibility Index, BMI = Body Mass Index, US = Ultrasound
c = control, **d** = diabetic patient
⓪ indicates result was not directly provided but was calculated using data from study
₪ indicates strain was calculated from average unloaded thickness and average loaded thickness

Table 0.5. Subcalcaneus Plantar Tissue Thickness and Strain, continued

Author	Year	Method	UT* (mm)	ε avg± stdev (range), %	Population	Purpose and Findings	Limitations
Prichasuka	1994	Lateral X-ray	18.77	w/pain: 41 normal: 48 ⓿	n=200 (100♀, 100♂) age: 20-35 and 40-60yrs ♀UT: 18.12±2.01mm ♂UT: 19.42±2.45mm ♀LT: 9.44±2.13mm ♂LT: 10.26±2.25mm UT: 18.77±2.33mm LT: 9.85±2.22mm	Heel pad thickness appears to be greater in males vs females and older vs younger subjects. Compressibility index is increased in older and heavier subjects, and these people tend to have more heel pain (possibly due to loss of elasticy and increased pressure).	The increased thickness and stiffness with age may be weight related as older people tend to weigh more.
Prichasukb	1994	Lateral X-ray	18.70	47±9 (14-76)	n=400 (200♀, 200♂) age: 36.48±11.54 (20-60yrs) wgt: 571.3±102.8 (343-941 UT: 18.7±2.46 (12-28mm)	Heel pad thickness is greater in males vs females and increases with age.	
Silver	1994	Ultrasound	16.10	N/A	n=21 f vs.n=**f**racture vs.**n**ormal side f_UT: 17.4 (12-23.9mm) n_UT: 16.1 (11.3-19.8mm)	Test of previous belief that heel pad thinning occurs after calcaneal fracture and thereby contributes to pain. Instead, results show a significant increase in thickness for the fractured side.	Weight, age, and gender unknown. Standard error not given.
Rome	1998	Ultrasound	12.47	67.36 ⓿ ₪	n=15, age=25.4yrs (11♀, 4♂ UT: 12.47±4.2mm LT: 4.07±1.8mm	Unloaded and loaded heel pad thicknesses were measured through a plastic platform.	
Zheng	2000	Ultrasound	N/A	N/A	c=controls: n=4 (1♀, 3♂) d=diabetic patients: n=4 (3♀, 1♂) c_age: 22yrs (21-24) d_age: 63yrs (46-74) c_UT: ~16.0±1mm d_UT: ~12.5±2mm	Comparison of 4 older, neuropathic diabetic patients and 4 healthy, younger patients' tissue thickness and Young's modulus at 1st & 2nd metatarsal head, big toe & heel.	Small sample population. UT obtained from bar graph.
Kanatli	2001	Lateral X-ray	19.55	wp: 31 c: 40 ⓿	n=106 (21♀ 26♂=47 controls, 39♀ 20♂=59 **h**eel **p**ain) c_age: 43.88±10.5yrs c_UT: 19.55±2.52mm **hp**_age: 23.47±2.44yrs **hp**_UT: 20.45±2.89mm	Comparison of subjects with heel pain and controls showed no difference between heel pad thickness. No relation was found between compressibility and plantar pressure in either group.	Groups were not age matched.
Rome	2002	Ultrasound		N/A	n=140 (33 **a**thletes **w**/ **p**ain, 107 **a**thletes **n**o **p**ain, 64 control non-athletes no pain) awp_age: 24.6±7.7yrs awp_wgt: 680.6±118.6 N awp_LT: 5.75±1.1mm anp_age: 21.7±5.1yrs anp_wgt: 701±121.5 N anp_LT: 5.02±1.4mm c_age: 23.9±7.4yrs c_wgt: 640.7± 96.0 N c_LT: 5.05±1.5mm	Study done to estimate the effect of BMI on loaded heel pad thickness in young active adults. LT was found to increase proportionally with BMI. Subjects with heel pain were found to be significantly different than other groups regardless of BMI.	Only LT given. Gender unknown.

*Note: UT= unloaded thickness, LT = loaded thickness, CI = Compressibility Index, BMI = Body Mass Index, US = Ultrasound
c = control, **d** = diabetic patient, BMI = Body Mass Index
⓿ indicates result was not directly provided but was calculated using data from study
₪ indicates strain was calculated from average unloaded thickness and average loaded thickness

Table 0.6. Subcalcaneus Plantar Tissue Thickness and Strain, continued

Author	Year	Method	UT* (mm)	ε avg± stdev (range), %	Population	Purpose and Findings	Limitations
Ozdemir	2004	Lateral X-ray	18.13	45.84 ⓪ ₪	n=50 (38♀, 12♂) age: 46.32±11.65 (23-73yrs) wgt: 671.9±122.72 (490-1098 UT: 18.13±3.30 (13-28mm) LT: 9.82±1.64 (7-13mm)	Investigation into possible causes of heel pain (i.e. all subjects had pain). Results show males and older people have thicker heel pads. Obese subjects appeared to have thinner heels.	As spur size increased, UT decreased but not significantly due to small sample population. Conflicting results on obesity factor (see Jackson
Uzel	2005	Ultrasound	18.30	Group1: 39 Group2: 42 Group3: 40 ⓪	n=110 (55♀, 55♂) age: 20-30yrs BMI: 18.5-24.9 ♀UT: 17.0±1.9mm ♂UT: 19.7±1.9mm ♀LT: 10.0±1.6mm ♂LT: 12.0±1.6mm	Comparison of heel pad thickness in three groups: sedentary, active, and athletic young people. Thickness and compressibility index were insignificantly different between all groups.	
Uzel	2006	Ultrasound	19.8	40 ⓪	n=42, (35♀, 7♂) UT: 19.8±2.9mm LT: 12.3±2.9mm Compressibility Index (CI): 0.6±0.09	Measure loaded & unloaded heel pad thickness in 69 feet of patients with plantar heel pad pain with US and direct radiography.	
Garcia	2008	Ultrasound	13.61		n=17, age=25.3±4.4yrs UT: 13.61±1.57mm	Measure thickness w/ US and non-linear stiffness with indenter/load cell.	
Kwan	2010	Ultrasound	21.8		n=60 (46♀, 24♂) age=63.0± (45.1±3.3, 56.4±2.4, 66.6±2.8, 74.3±3.3) yrs UT: 21.81±3.42mm	Healthy volunteers from 41 to 83 yrs. Measured tissue thickness and stiffness to correlate between age and properties.	

*Note: UT= unloaded thickness, LT = loaded thickness, CI = Compressibility Index, BMI = Body Mass Index, US = Ultrasound

c = control, **d** = diabetic patient

⓪ indicates result was not directly provided but was calculated using data from study

₪ indicates strain was calculated from average unloaded thickness and average loaded thickness

1.3 Tabular Data: Submetatarsal Heads

Table 0.7. Submetatarsal Head Plantar Tissue Thickness and Strain

Author	Year	Method	UT* (mm)	ε avg± stdev (range), %	Population	Purpose and Findings	Limitations
Gooding	1986	Ultrasound	13.006 ⓪	N/A	n=73 (24 controls) age: 51±3.1yrs wgt: 845.5±31 N M1_UT: 12.92±0.42mm M2_UT: 14.17±0.26mm M3_UT: 13.56±0.29mm M4_UT: 12.91±0.34mm M5_UT: 11.47±0.27mm	Comparison of heel pad and submetatarsal head thickness in three groups: controls, diabetic patients without ulcers, and diabetic patients either with ulcers/ a history of ulcers. Diabetic patients have decreased thickness of sole compared with controls, and diabetic patients prone to ulcers have even thinner soles.	Gender unknown. Standard errors rather than standard deviations are reported.
Bygrave	1993	Ultrasound	9.25 ⓪	M1: 12.5 M2: 16.2 M3: 12.5 M4: 7.9 M5: 13.2	n=12 age: 33 (21-49yrs) M1_UT: 12.82±3.26mm M2_UT: 10.47±2.40mm M3_UT: 8.58±2.16mm M4_UT: 7.77±1.80mm M5_UT: 6.61±2.26mm	Evaluation of method as a diagnostic tool in foot pathology for loaded and unloaded conditions.Maximum compressive % strain ranged from 7.9 to 19.7%.	Weight and gender unknown. Compressive strain seems low (see Cavanagh 1999).
Cavanagh	1999	Ultrasound	15.20	45.7 (36.8-55.0)	n=5 (2♀, 3♂) age: 36.6±10yrs wgt: 665.4±107.8 N M2_UT: 15.2±1.6 (13.3-17.2mm)	Measurement method of soft tissue deformation during walking. Average maximum compressive % strain was 45.7±6.7%.	Small sample population. Measurements only taken for 2nd submetatarsal head.
Wang	1999	Ultrasound	12.6 ⓪	M1: 44.1 M2: 47.3 M3: 49.2 M4: 47.5 M5: 48.5	n=20 (10♀, 10♂) age=30.2±7.8 (17-44)yrs M1_UT: 15.0±1.6mm M2_UT: 13.6±1.8mm M3_UT: 12.5±1.8mm M4_UT: 11.4±1.7mm M5_UT: 10.4±1.2mm M1_CI: 55.9±5.6 M2_CI: 52.7±5.7 M3_CI: 50.8±5.5 M4_CI: 52.5±5.5 M5_CI: 51.5±6.6	Measure tissue thickness, compressibility index, elastic modulus, and energy dissipation ratio in healthy subjects using an ultrasound transducer and manual displacement mechanism. Strained to pressure = 58.6 kPa.	
Wang	2003	Ultrasound	11.8 ⓪	M1: 25.5 M2: 33.1 M3: 35.3 M4: 32.4 M5: 39.5 ⓪	n=25 (12♀, 13♂) age: 31.0±3.1(24-42yrs) wgt: 588±127.4 N M1_UT: 13.4±2.0mm M2_UT: 12.6±1.8mm M3_UT: 11.8±1.7mm M4_UT: 11.0±1.7mm M5_UT: 10.2±1.3mm	Average submetatarsal head plantar tissue thickness decreased linearly from 1st to 5th ray.	
Zheng	2000	Ultrasound	N/A	N/A	c=controls: n=4 (1♀, 3♂) d=diabetic patients: n=4 (3♀, 1♂) c_age: 22yrs (21-24) d_age: 63yrs (46-74) c_M1_UT: ~12.25±1.5mm c_M2_UT: ~13.6± 0.25mm d_M1_UT: ~6.75±1mm d_M2_UT: ~8.0±2mm	Comparison of 4 older, neuropathic diabetic patients and 4 healthy, younger patients' tissue thickness and Young's modulus at 1st & 2nd metatarsal head, big toe & heel.	Small sample population. UT obtained from bar graph.

*Note: UT= unloaded thickness, LT = loaded thickness, CI = Compressibility Index, BMI = Body Mass Index, US = Ultrasound
c = control, **d** = diabetic patient, M1-5 = Submetatarsal Heads 1-5
⓪ indicates result was not directly provided but was calculated using data from study
₪ indicates strain was calculated from average unloaded thickness and average loaded thickness

Table 0.8. Submetatarsal Head Plantar Tissue Thickness and Strain, continued

Author	Year	Method	UT* (mm)	ε avg± stdev (range), %	Population	Purpose and Findings	Limitations
Abouaesha	2001	Ultrasound	callus:7.45 none: 8.29 ⓪		n=157, age=61.2±10.2yrs diabetes duration: 16.4±10.3yrs M1_L_none_UT: 11.1±1.7mm M1_R_none_UT: 11.0±1.8mm M2_L_none_UT: 9.1±1.8mm M2_R_none_UT: 9.0±2.0mm M3_L_none_UT: 8.1±1.6mm M3_R_none_UT: 8.1±1.9mm M4_L_none_UT: 7.6±1.5mm M4_R_none_UT: 7.4±1.8mm M5_L_none_UT: 5.9±1.4mm M5_R_none_UT: 5.6±1.5mm M1_L_callus_UT: 10.9±1.4mm M1_R_callus_UT: 10.6±1.7mm M2_L_callus_UT: 7.9±1.7mm M2_R_callus_UT: 7.7±1.5mm M3_L_callus_UT: 7.0±1.4mm M3_R_callus_UT: 6.8±1.5mm M4_L_callus_UT: 6.7±1.3mm M4_R_callus_UT: 6.6±1.6mm M5_L_callus_UT: 5.2±1.2mm M5_R_callus_UT: 5.1±1.3mm	Investigate relationship between pressure, tissue thickness, neuropathy, callus,and BMI in diabetic patients.	Lack of sample sizes for callus/no-callus doesn't allow for sample pooling.
Waldecker	2001	Ultrasound	-		n=50 (39♀, 11♂), age=47± M2_UT: 9-17mm M3_UT: 8-15mm	Compare tissue thickness and intermetatarsal angle (1/2) for 50 splay-foot deformity patients.	Only ranges of thickness, no averages reported.
Bus	2004	MRI	6.0 (controls)		c=controls: n=13, age=53.9yrs d_w/o=diabetic patient w/o toe deformity: n=13, age=57.2yrs d_w/=diabetic patient w/ toe deformity: n=13, age=53.9yrs c_UT: 6.0±1.2mm d_w/o_UT: 6.0±1.4mm d_w/_UT: 2.5±1.3mm	High-res MRI images of 2nd & 3rd ray used to measure fat pad thickness and toe angle.	
Weijers	2005	CT	10.4 ⓪	M1: 21.3 M2: 28 M3: 22.6 M4: 19.1 M5: 21.8	n=10 (5♀, 5♂), age=34 (19-51) M1_UT: 13.6, M1_LT: 10.6mm M2_UT: 11.5, M1_LT: 8.2mm M3_UT: 9.9, M1_LT: 7.6mm M4_UT: 9.5, M1_LT: 7.6mm M5_UT: 7.6, M1_LT: 5.9mm	Four phases of healthy gait (unloaded, midstance, heel-rise, toe-off) were simulated, strain at each was calculated.	Subjects told to hold position for ~15 seconds while imaging.
Garcia	2008	Ultrasound	11.64 ⓪		n=17, age=25.3±4.4yrs M1_UT: 13.44±1.86mm M2_UT: 12.61±1.60mm M3_UT: 11.60±1.45mm M5_UT: 8.92±0.81mm	Measure thickness w/ US and non-linear stiffness with indenter/load cell.	
Chao	2010	Ultrasound	11.6 ⓪		**y**=young: n=19, 27.1±4.2yrs **o**=older: n=11, 62.2±5.7yrs M1_y_UT: 12.7±2.1mm M2_y_UT: 13.2±1.8mm M1_o_UT: 9.9±0.9mm M2_o_UT: 10.6±1.8mm	Soft tissue thickness and stiffness of 1st and 2nd met-heads was measured to obtain Young's modulus (linear assumption).	
Kwan	2010	Ultrasound	8.87 ⓪		n=60 (46♀, 24♂) age=63.0± (45.1±3.3, 56.4±2.4, 66.6±2.8, 74.3±3.3) yrs M1_UT: 9.02±2.49 mm ⓪ M3_UT: 9.23±1.66 mm ⓪ M5_UT: 8.36±2.92 mm ⓪	Healthy volunteers from 41 to 83 yrs. Measured tissue thickness and stiffness to correlate btwn age and properties.	

*Note: UT= unloaded thickness, LT = loaded thickness, CI = Compressibility Index, BMI = Body Mass Index, US = Ultrasound

c = control, **d** = diabetic patient, M1-5 = Submetatarsal Heads 1-5

⓪ indicates result was not directly provided but was calculated using data from study

₪ indicates strain was calculated from average unloaded thickness and average loaded thickness

1.4 Charted Data: Subcalcaneus

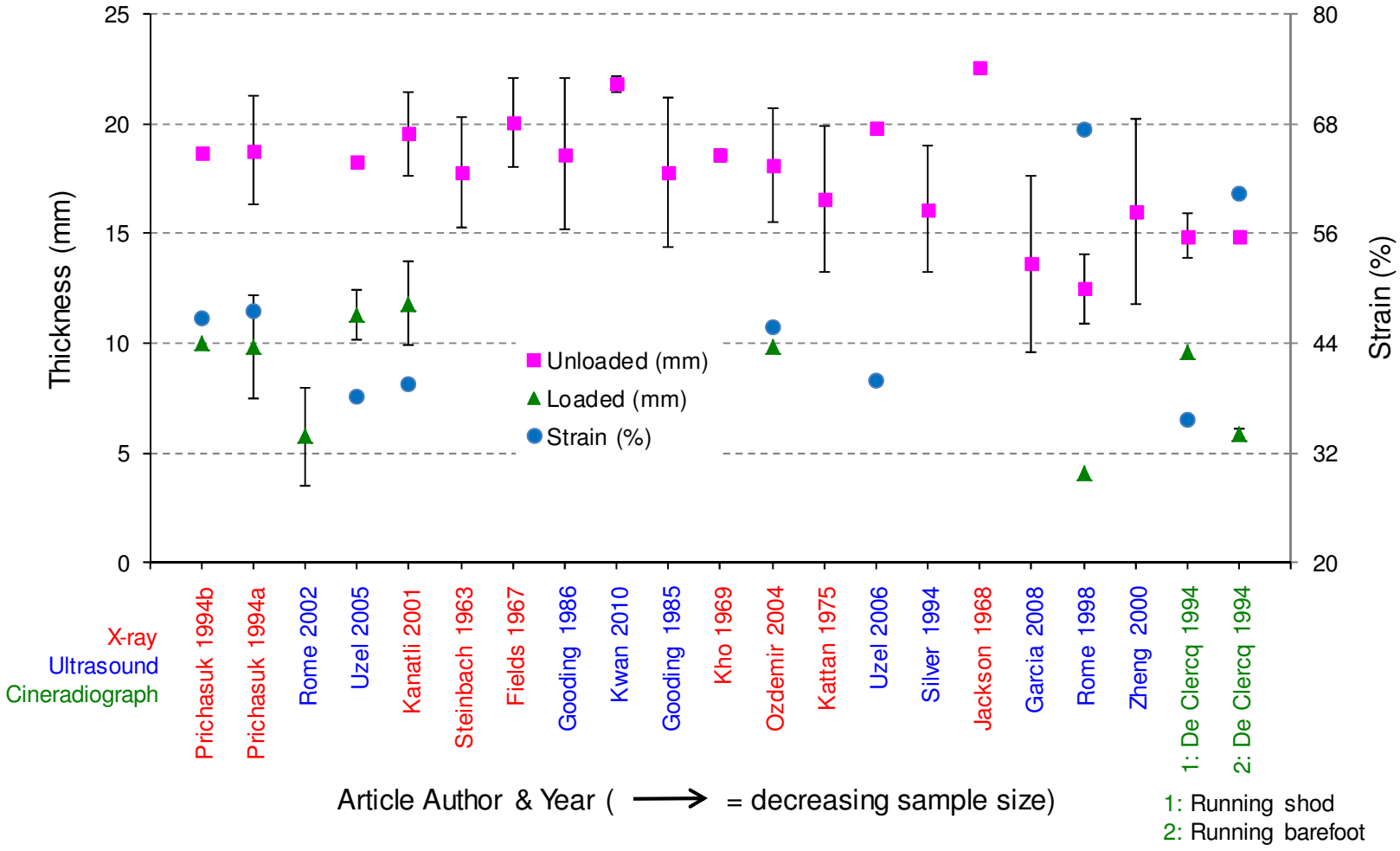

Figure 0.1. Subcalcaneus: Loaded vs. Unloaded Thickness and Strain

1.5 Charted Data: Submetatarsal Heads

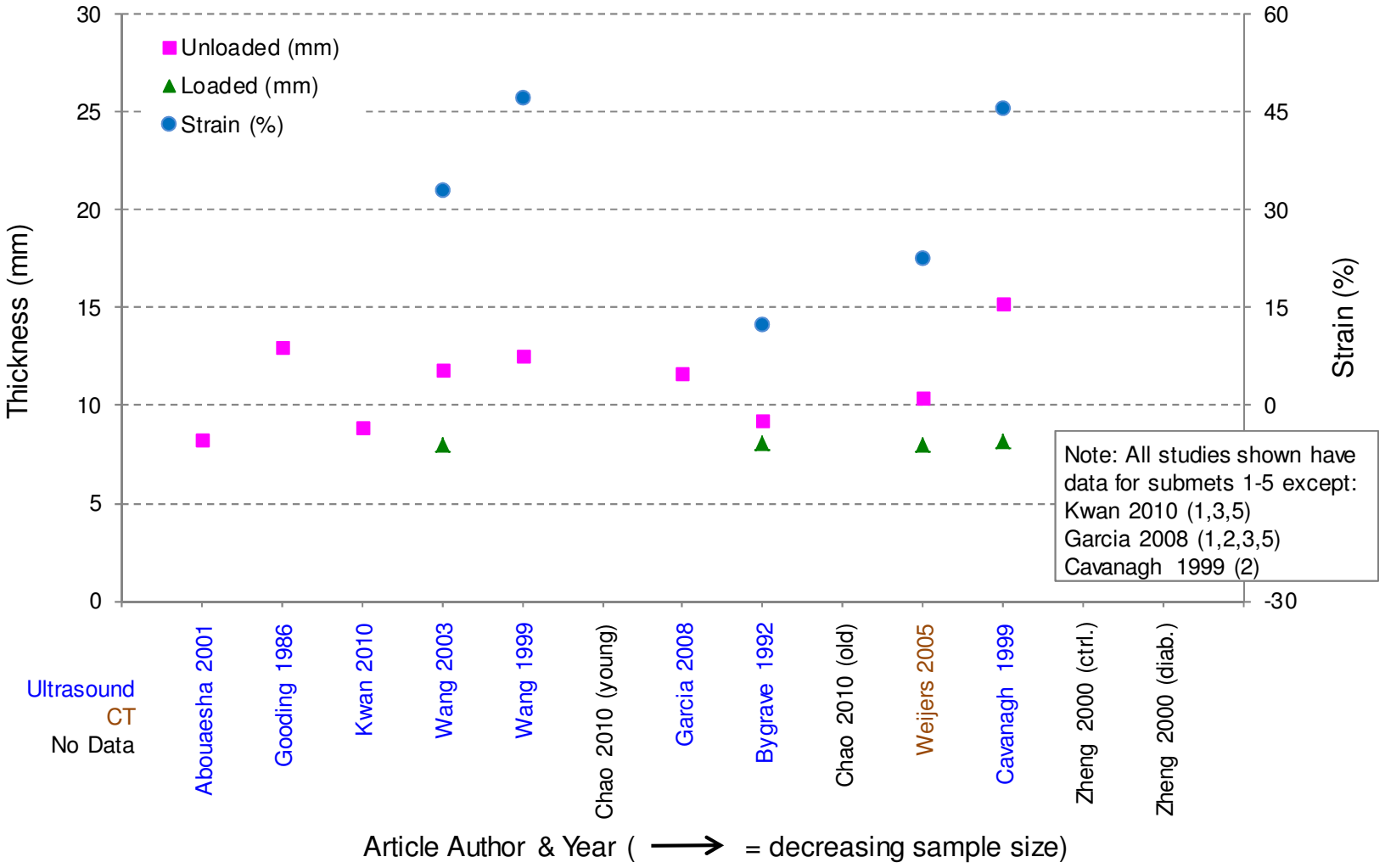

Figure 0.2. Submetatarsal Heads 1-5 Average: Loaded vs. Unloaded Thickness and Strain

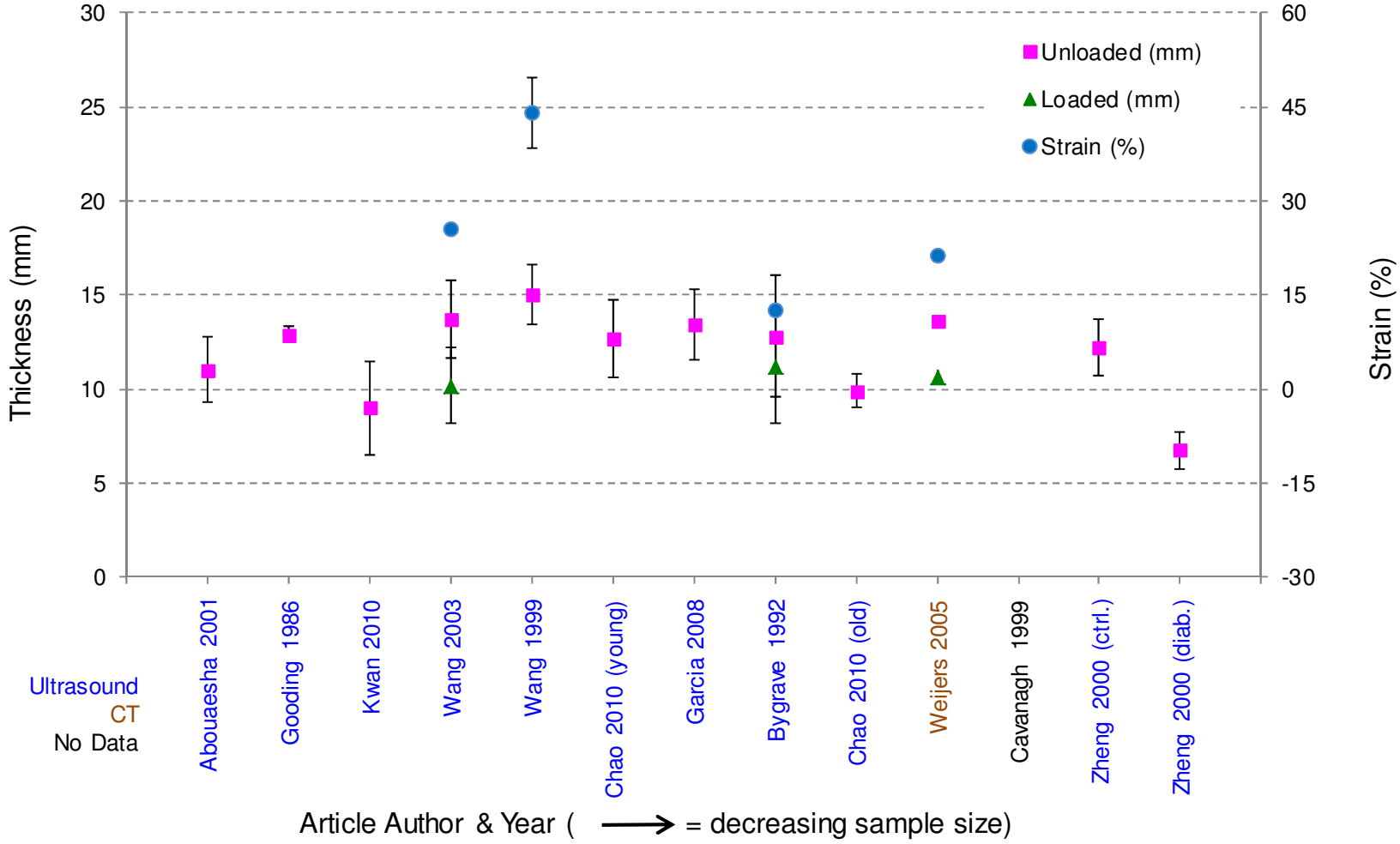

Figure 0.3. Submetatarsal Head 1: Loaded vs. Unloaded Thickness and Strain

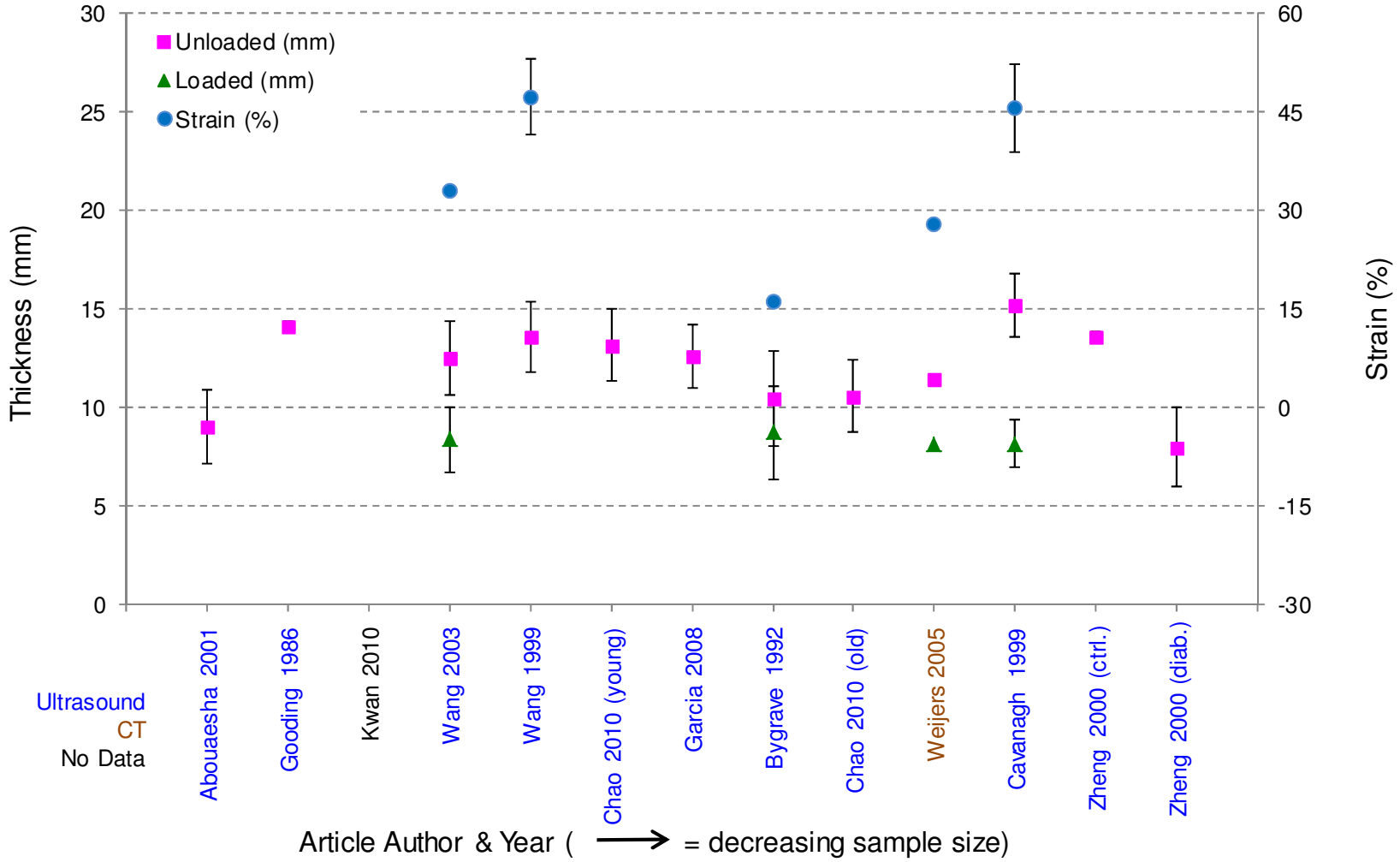

Figure 0.4. Submetatarsal Head 2: Loaded vs. Unloaded Thickness and Strain

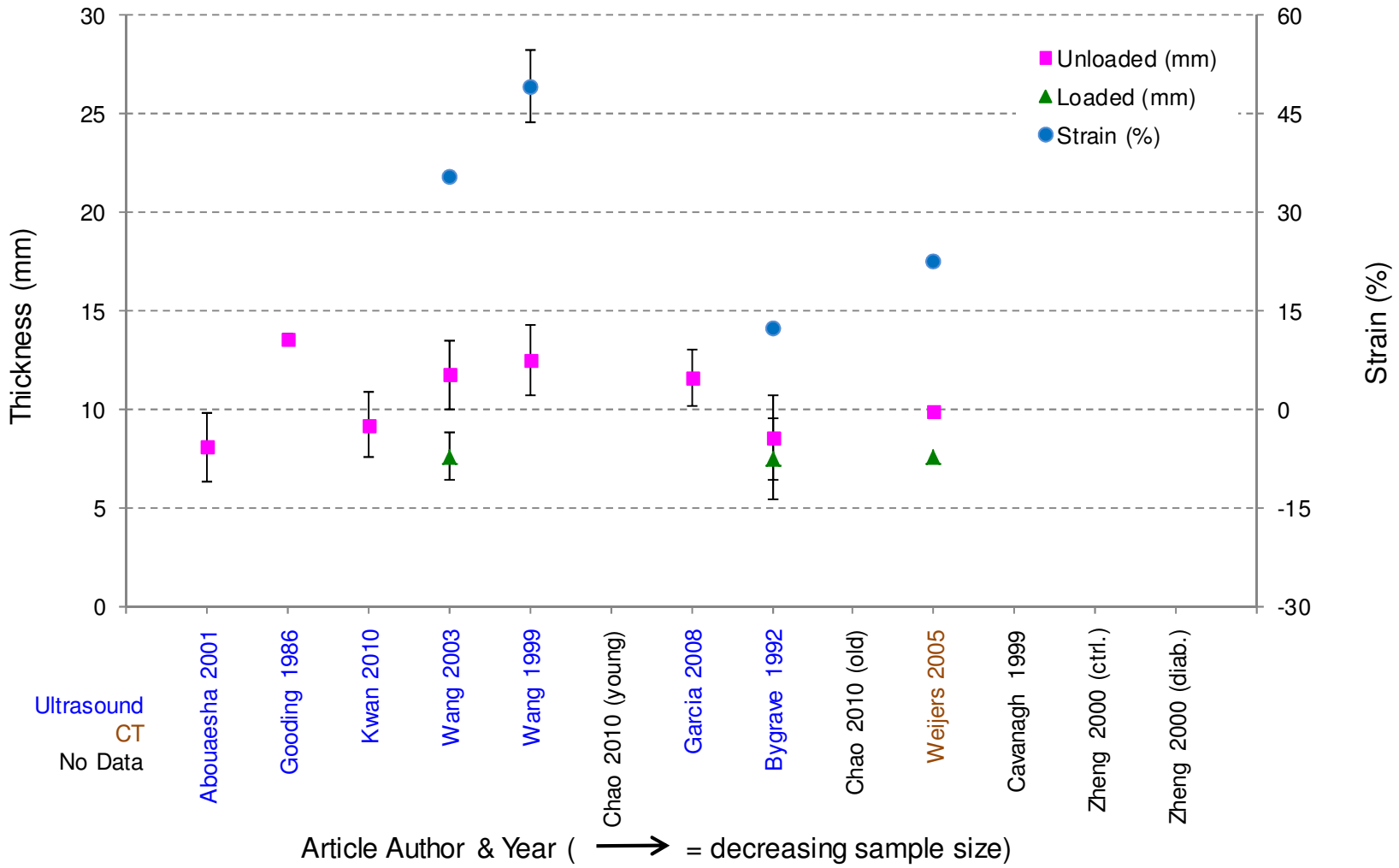

Figure 0.5. Submetatarsal Head 3: Loaded vs. Unloaded Thickness and Strain

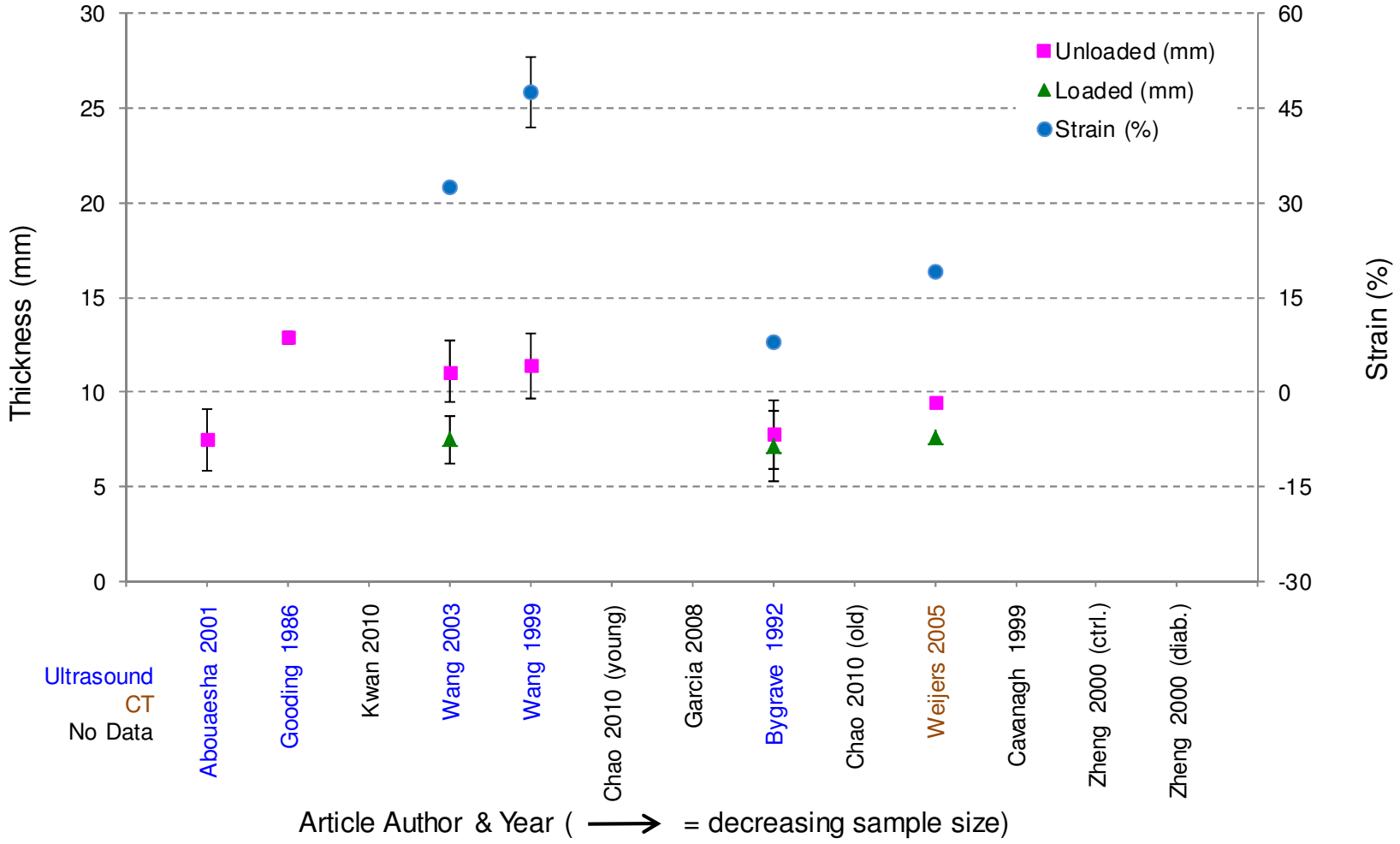

Figure 0.6. Submetatarsal Head 4: Loaded vs. Unloaded Thickness and Strain

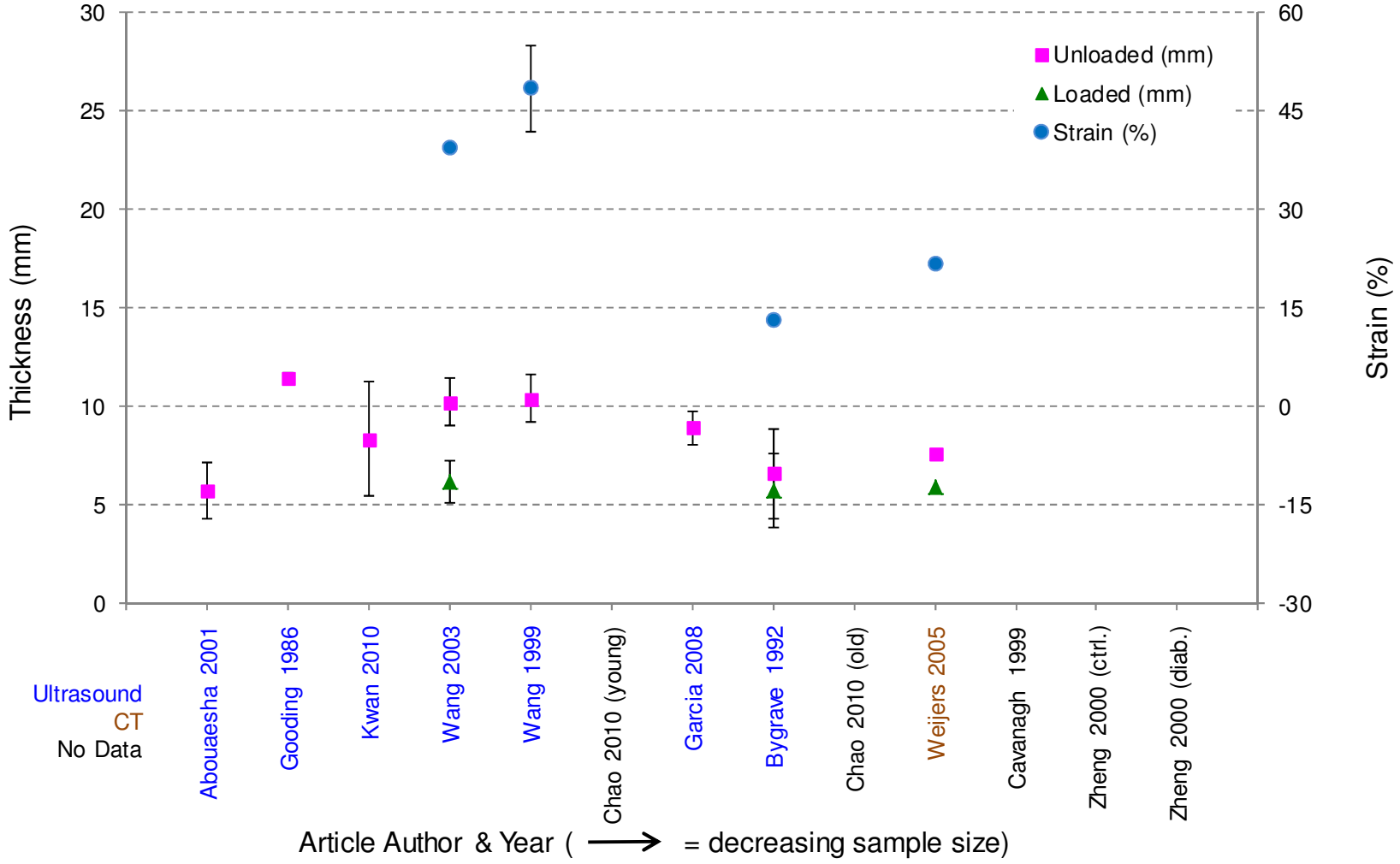

Figure 0.7. Submetatarsal Head 5: Loaded vs. Unloaded Thickness and Strain

1.6 References

Abouaesha F, van Schie CH, Griffths GD, Young RJ & Boulton AJ 2001, "Plantar tissue thickness is related to peak plantar pressure in the high-risk diabetic foot.", *Diabetes care,* vol. 24, no. 7, pp. 1270-4.

Bus SA, Maas M, Cavanagh PR, Michels RP & Levi M 2004, "Plantar fat-pad displacement in neuropathic diabetic patients with toe deformity: a magnetic resonance imaging study.", *Diabetes care,* vol. 27, no. 10, pp. 2376-81.

Bygrave, C.J. & Betts, R.P. 1993, "The plantar tissue thickness in the foot: a new ultrasound technique for loadbearing measurements and a metatarsal head depth study", *The Foot,* vol. 3, no. 2, pp. 71-78.

Cavanagh, P.R. 1999, "Plantar soft tissue thickness during ground contact in walking", *Journal of Biomechanics,* vol. 32, no. 6, pp. 623-628.

Chao, C.Y.L., Zheng, Y.P., Huang, Y.P. & Cheing, G.L.Y. 2010, "Biomechanical properties of the forefoot plantar soft tissue as measured by an optical coherence tomography-based air-jet indentation system and tissue ultrasound palpation system", *Clinical Biomechanics,* vol. 25, no. 6, pp. 594-600.

De Clercq, D., Aerts, P. & Kunnen, M. 1994, "The mechanical characteristics of the human heel pad during foot strike in running: an in vivo cineradiographic study", *Journal of biomechanics.,* vol. 27, no. 10, pp. 1213.

Fields ML, Greenberg BH & Burkett LL 1967, "Roentgenographic measurement of skin and heel-pad thickness in the diagnosis of acromegaly.", *The American Journal of the Medical Sciences,* vol. 254, no. 4, pp. 528-33.

Garcia C.A., Hoffman S.L., Hastings M.K., Klaesner J.W. & Mueller M.J. 2008, "Effect of metatarsal phalangeal joint extension on plantar soft tissue stiffness and thickness", *Foot,* vol. 18, no. 2, pp. 61-67.

Gooding GA, Stess RM, Graf PM, Moss KM, Louie KS & Grunfeld C 1986, "Sonography of the sole of the foot. Evidence for loss of foot pad thickness in diabetes and its relationship to ulceration of the foot.", *Investigative radiology,* vol. 21, no. 1, pp. 45-8.

Gooding GA, Stress RM, Graf PM & Grunfeld C 1985, "Heel pad thickness: determination by high-resolution ultrasonography.", *Journal of ultrasound in medicine : official journal of the American Institute of Ultrasound in Medicine,* vol. 4, no. 4, pp. 173-4.

Jackson DM 1968, "Heel-pad thickness in obese persons.", *Radiology,* vol. 90, no. 1.

Kanatli U, Yetkin H, Simsek A, Besli K & Ozturk A 2001, "The relationship of the heel pad compressibility and plantar pressure distribution.", *Foot & ankle international / American Orthopaedic Foot and Ankle Society [and] Swiss Foot and Ankle Society,* vol. 22, no. 8, pp. 662-5.

Kattan KR 1975, "Thickening of the heel-pad associated with long-term Dilantin therapy.", *The American Journal of Roentgenology, Radium Therapy, and Nuclear Medicine,* vol. 124, no. 1, pp. 52-6.

Kho KM, Wright AD & Doyle FH 1970, "Heel pad thickness in acromegaly.", *The British journal of radiology,* vol. 43, no. 506, pp. 119-25.

Kwan, R.L.C., Zheng, Y.P. & Cheing, G.L.Y. 2010, "The effect of aging on the biomechanical properties of plantar soft tissues", *Clinical Biomechanics,* vol. 25, no. 6, pp. 601-605.

Ozdemir H, Söyüncü Y, Ozgörgen M & Dabak K 2004, "Effects of changes in heel fat pad thickness and elasticity on heel pain.", *Journal of the American Podiatric Medical Association,* vol. 94, no. 1.

Prichasuk S 1994, "The heel pad in plantar heel pain.", *The Journal of bone and joint surgery.British volume,* vol. 76, no. 1, pp. 140-2.

Prichasuk S, Mulpruek P & Siriwongpairat P 1994, "The heel-pad compressibility.", *Clinical orthopaedics and related research,* no. 300, pp. 197-200.

Rome K, Campbell R, Flint A & Haslock I 2002, "Heel pad thickness--a contributing factor associated with plantar heel pain in young adults.", *Foot & ankle international / American Orthopaedic Foot and Ankle Society [and] Swiss Foot and Ankle Society,* vol. 23, no. 2, pp. 142-7.

Rome K, Campbell RS, Flint AA & Haslock I 1998, "Ultrasonic heel pad thickness measurements: a preliminary study.", *The British journal of radiology,* vol. 71, no. 851, pp. 1149-52.

Silver, D.A., Kerr, P.S., Andrews, H.S. & Atkins, R.M. 1994, "Heel pad thickness following calcaneal fractures: ultrasound findings.", *Injury,* vol. 25, no. 1, pp. 39.

Steinbach HL & Russell W 1964, "Measurement of the heel-pad as an aid to diagnosis of acromegaly.", *Radiology,* vol. 82, pp. 418-23.

Tsai WC, Wang CL, Hsu TC, Hsieh FJ & Tang FT 1999, "The mechanical properties of the heel pad in unilateral plantar heel pain syndrome.", *Foot & ankle international / American Orthopaedic Foot and Ankle Society [and] Swiss Foot and Ankle Society,* vol. 20, no. 10, pp. 663-8.

Uzel M, Cetinus E, Ekerbicer HC & Karaoguz A 2006, "Heel pad thickness and athletic activity in healthy young adults: a sonographic study.", *Journal of clinical ultrasound : JCU,* vol. 34, no. 5, pp. 231-6.

Uzel, M., Cetinus, E., Bilgic, E., Ekerbicer, H. & Karaoguz, A. 2006, "Comparison of ultrasonography and radiography in assessment of the heel pad compressibility index of patients with plantar heel pain syndrome. Measurement of the fat pad in plantar heel pain syndrome", *Joint Bone Spine,* vol. 73, no. 2, pp. 196-199.

Waldecker U 2001, "Plantar fat pad atrophy: a cause of metatarsalgia?", *The Journal of foot and ankle surgery : official publication of the American College of Foot and Ankle Surgeons,* vol. 40, no. 1.

Wang, T., Hsiao, T.u., Wang, T., Shau, Y. & Wang, C.i. 2003, "Measurement of vertical alignment of metatarsal heads using a novel ultrasonographic device.", *Ultrasound in medicine & biology,* vol. 29, no. 3.

Weijers RE, Walenkamp GH, Kessels AG, Kemerink GJ & van Mameren H 2005, "Plantar pressure and sole thickness of the forefoot.", *Foot & ankle international / American Orthopaedic Foot and Ankle Society [and] Swiss Foot and Ankle Society,* vol. 26, no. 12, pp. 1049-54.

Zheng, Y.P., Choi, Y.K., Wong, K., Chan, S. & Mak, A.F. 2000, "Biomechanical assessment of plantar foot tissue in diabetic patients using an ultrasound indentation system", U*ltrasound in medicine and biology,* vol. 26, no. 3, pp. 451-456.